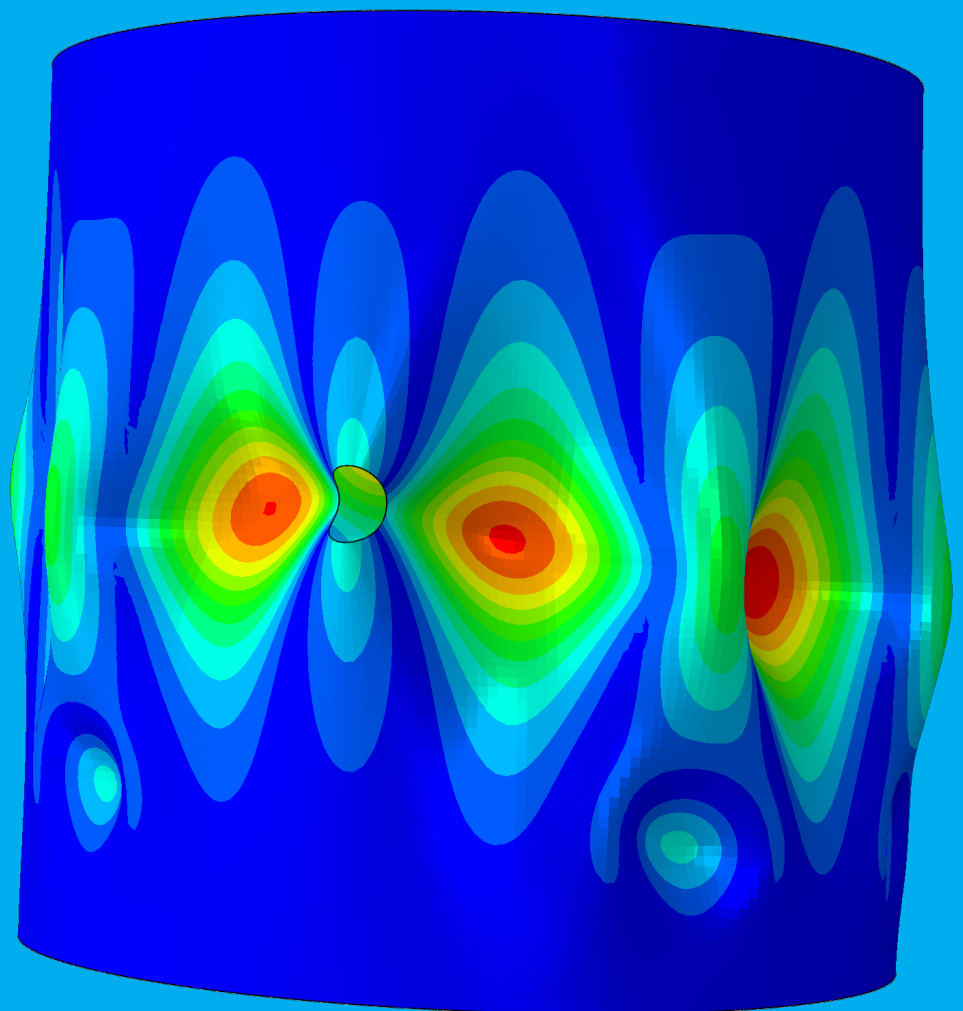


Buckling of Isotropic and Composite Cylindrical Shells with Circular Cutouts

A. Schiller

MSc. Thesis



Buckling of Isotropic and Composite Cylindrical Shells with Circular Cutouts

by

A. Schiller

to obtain the degree of Master of Science
at the Delft University of Technology,
to be defended publicly on February 19, 2021 at 2:30 PM.

Student number:	4807731
Project duration:	December 3, 2019 – February 19, 2021
Thesis committee:	Prof. Dr. C. Bisagni TU Delft, supervisor
	Prof. Dr. C. Kassapoglou TU Delft
	Dr. Ir. O. K. Bergsma TU Delft
	Dr. M. W. Hilburger NASA Langley Research Center

An electronic version of this thesis is available at <http://repository.tudelft.nl/>.

Acknowledgments

Many things have to come together in order to enjoy devoting yourself to a single subject for over a year.

The tasks involved must be challenging and diverse. I can honestly say that studying the intricacies of the buckling behavior of shells with cutouts has been one of the most difficult endeavors I have ever undertaken. Whether it was solving differential equations, automating finite element models, or interpreting results, there was always something interesting to work on.

The research environment must be inspiring. I have learned a lot from the insightful discussions with my supervisor, Prof. Bisagni, and I am incredibly thankful for her guidance. I also want to express my gratitude for the countless conversations with the other members of the ASCM research group who contributed by sharing their expertise, by asking excellent questions to challenge my perception of various problems, and by providing constructive criticism regarding the contents of this document.

The people behind the scenes must be remarkable, especially during a global crisis like the coronavirus pandemic. I would not be where I am today without the support of my parents, and I thank them from the bottom of my heart for giving me the opportunity to follow my own path. I also want to thank my friends from all over the world for being a part of this journey. The experiences, memories, hardships, and victories we share have shaped my life, and I would not want it any other way.

Finally, and perhaps most importantly, there must be a sense of purpose. Understanding the buckling behavior of shells with cutouts is highly relevant for the design of aerospace structures. Hence, I hope that the methods and conclusions presented on the following pages prove to be both use- and helpful for those who want to tackle this challenging task and that they may serve as a starting point for future investigations.

A. Schiller
Delft, January 2021

Abstract

Predicting the critical buckling load of cylindrical shells with circular cutouts subjected to uniform axial compression is an important part of the structural design in the aerospace industry as buckling significantly reduces the load-carrying capability of the structure. A cutout constitutes a major disruption in the shell geometry, and therefore it should be expected that it has a significant effect on the sustainable buckling load.

An analytical solution for estimating the buckling load of isotropic and quasi-isotropic composite cylindrical shells with circular cutouts is developed to assess changes made to the geometry and the material during the preliminary design phase quickly. The Ritz method is employed to minimize the total potential energy of an ideal shell that contains a central opening in order to predict a linear buckling load. Finite element simulations are conducted to verify the accuracy of the analytical solution. In addition, they are used to investigate the evolution of buckling modes, the effects of initial geometric imperfections, as well as the shell failure mode.

The nondimensional curvature parameter α can be used to categorize the buckling behavior of cylindrical shells and is a function of the cutout radius, the shell radius, and the shell thickness. A small cutout has virtually no influence on the buckling load compared to a pristine shell and the displacement pattern at buckling is global. The buckling load decreases rapidly for moderately large cutouts where the stability loss is the result of a local buckling mode that immediately leads to global buckling. Cylindrical shells with large cutouts are again relatively insensitive to an increase of the cutout size, but the buckling load is greatly reduced relative to a shell without a cutout. Large openings also feature a stable local buckling mode where substantial lateral prebuckling displacements emerge before the structure buckles globally.

While the analytical procedure theoretically should not capture the onset of global buckling independent of local buckling, it follows numerical trends for cutouts of moderate and large size regardless. Therefore, it may be used during preliminary design to estimate the impact of changes made to the shell geometry and material. Local buckling is caused by high compressive stresses next to the cutout and, in some cases, large lateral prebuckling displacements. The detrimental effect of the stress field may be partially relieved in composite cylindrical shells by reducing the amount of axial bending stresses that occur. Hence, the chosen stacking sequence can have a significant influence on the buckling load of shells with moderate and large openings.

Contents

List of Figures	ix
List of Tables	xi
List of Abbreviations	xiii
List of Symbols	xv
1 Introduction	1
1.1 Document Organization	2
1.2 Preliminary Note	2
2 Literature Review	3
2.1 Analytical Work	3
2.1.1 Stresses around Cutouts in Plates	3
2.1.2 Stresses around Cutouts in Shells	4
2.1.3 Buckling of Plates with Cutouts	6
2.1.4 Buckling of Shells with Cutouts	8
2.2 Experimental Work	10
2.2.1 Cutout Parameters	10
2.2.2 Reinforcements	13
2.2.3 Imperfections	14
2.3 Numerical Work	14
2.3.1 Cutout Parameters	14
2.3.2 Shell Parameters	17
2.3.3 Reinforcements	18
2.3.4 Imperfections	19
3 Theoretical Prerequisites	21
3.1 General Shell Theory	21
3.2 Shallow Shell Theory	22
3.3 Classical Lamination Theory	24
3.4 Energy Methods	27
3.5 Energy and Equilibrium Equations	27
3.6 Ritz Method	29
3.7 Compatibility Equation	30
3.8 Airy Stress Function	30
3.9 Coordinate Transformation	31
3.9.1 Transformation Matrices	31
3.9.2 Partial Derivatives	32
3.9.3 Integrals	33
3.9.4 In-plane Equilibrium Equations and Airy Stress Function	33
3.10 Classical Buckling Theory	33
4 Buckling Analysis	35
4.1 Geometry and Loading Conditions	35
4.2 Assumptions and Solution Approach	36
4.3 Isotropic Shells	38
4.3.1 Total Potential Energy	38
4.3.2 Coordinate Transformation	38
4.3.3 Prebuckling Stress Distribution	39
4.3.4 Linear Compatibility Equation	39

4.3.5	Complementary and Particular Solution	40
4.3.6	Boundary Value Problem and Stress Resultants	41
4.3.7	Energy Minimization with the Ritz Method	43
4.4	Quasi-Isotropic, Symmetric, Composite Shells	43
4.4.1	Membrane Strain Energy.	43
4.4.2	Bending Strain Energy	45
4.4.3	Energy Contribution of External Forces	45
4.4.4	Final Steps	46
4.5	Shape Function Modification	46
5	Finite Element Models	47
5.1	Geometry	47
5.2	Material Properties	48
5.3	Element Types and Meshing	49
5.4	Boundary Conditions	50
5.5	Analysis Types	51
5.5.1	Linear Eigenvalue Analysis.	51
5.5.2	Nonlinear Static Analysis.	51
5.5.3	Nonlinear Dynamic Analysis.	52
6	Isotropic Cylindrical Shells	53
6.1	Analytical Results	53
6.2	Numerical Results and Verification	57
6.2.1	Comparison of Modeling Alternatives	57
6.2.2	Buckling Loads.	59
6.2.3	Buckling Mode Shapes.	62
6.2.4	Buckling Mode Shape Evolution	63
6.2.5	Initial Geometric Imperfections	65
6.2.6	Shell Failure	68
6.3	Experimental Results and Validation	70
7	Quasi-Isotropic, Symmetric, Composite Cylindrical Shells	73
7.1	Curvature Parameters.	73
7.2	Analytical Results	74
7.3	Numerical Results and Verification	75
7.3.1	Buckling Loads.	75
7.3.2	Buckling Mode Shapes.	79
7.3.3	Buckling Mode Shape Evolution	81
7.3.4	Initial Geometric Imperfections	85
7.3.5	Shell Failure	88
8	Conclusion and Recommendations for Future Work	93
8.1	Conclusion	93
8.1.1	Buckling Behavior of Cylindrical Shells with Circular Cutouts	93
8.1.2	Analytical Solution.	94
8.2	Recommendations for Future Work.	95
A	Expressions Used During the Analysis of an Isotropic Shell With a Circular Cutout	97
A.1	General Stress Resultants	97
A.2	Boundary Value Problem Constants.	98
A.3	Stress Resultant Coefficients	98
A.4	Generalized Eigenvalue Problem Matrices	99
B	Generalized Eigenvalue Problem Matrix Elements for the Quasi-Isotropic Case	101
	Bibliography	103

List of Figures

2.1	Membrane and bending stresses caused by axial tension as predicted by Lekkerkerker [5], ($\delta = t$).	4
2.2	Tangential stress concentration factors along a cutout in an orthotropic cylindrical shell.	5
2.3	Normalized tangential stress resultants around a circular opening in a quasi-isotropic composite shell [14].	6
2.4	Geometry of a plate with a centrally located cutout and integration boundaries [16].	7
2.5	Model of two concentric composite plates [17].	7
2.6	Normalized buckling loads obtained from Starnes' analysis and his experiments [18].	9
2.7	Normalized results of Tennyson's testing campaign [8].	10
2.8	Local buckling of a Mylar shell with $\mu > 2$ [18].	11
2.9	Nondimensional buckling loads as a function of α as well as R/t [24].	12
2.10	Load-displacement curves and measured buckling loads [29].	13
2.11	Displacement pattern at local buckling of a cylindrical shell with a rectangular cutout [37].	15
2.12	Normalized buckling load as a function of the relative cutout location [38].	15
2.13	Prebuckling, buckling, and postbuckling von Mises stress distribution [38].	16
2.14	Numerically predicted local and global buckling loads as well as load-displacement curves [29].	16
2.15	Dependency of the buckling load on the rotation angle of an elliptic cutout [42].	17
2.16	Asymptotic lower bound of the maximum buckling load [25].	17
2.17	Local orthotropic reinforcements around rectangular cutouts [31].	18
2.18	Buckling loads as a function of cutout diameter for two different shell specimens [29].	20
3.1	A general shell with a right-handed curvilinear coordinate system.	21
3.2	A circular cylindrical shell with a curvilinear coordinate system.	23
3.3	Stress resultants and couples acting on an infinitesimal shell element.	25
3.4	Coordinate systems with their origins at the cutout center.	31
4.1	A cylindrical shell loaded by a uniform axial edge load \bar{N}_x	35
4.2	Flow chart outlining the analysis procedure.	37
5.1	A cylindrical shell with a circular cutout in Abaqus.	47
5.2	The discretized shell geometry.	50
5.3	Boundary conditions and different load applications.	50
6.1	Analytical predictions for the normalized buckling stress of isotropic shells.	53
6.2	Normalized buckling stress predictions after modification of the present solution.	54
6.3	Comparison between the different analytical solutions.	55
6.4	Buckling stress τ_{cr} versus decay parameter B	55
6.5	Normalized buckling stress for various values of the Poisson's ratio ν	56
6.6	Relative difference of initial/maximum buckling load estimates for various modeling alternatives considering a LBA.	57
6.7	Relative difference of initial buckling load estimates for various modeling alternatives considering a NLS simulation.	58
6.8	Relative difference of maximum buckling load estimates for various modeling alternatives considering a NLS analysis.	58
6.9	Relative difference of initial buckling load estimates for various modeling alternatives considering a NLD simulation.	59
6.10	Relative difference of maximum buckling load estimates for various modeling alternatives considering a NLD analysis.	59
6.11	Normalized buckling loads of isotropic shells.	60

6.12	Prebuckling distribution of the von Mises stress as computed by geometrically linear and non-linear procedures.	61
6.13	Effect of the Poisson's ratio on the normalized maximum buckling loads.	62
6.14	Initial buckling patterns of isotropic shells.	63
6.15	Normalized load-displacement curves for various isotropic shells.	64
6.16	Radial displacements amplified by factor 5 during loading (A), at stable local buckling (B), before (C), and after (D) global buckling of isotropic shells.	65
6.17	Normalized load-displacement curves considering an imperfect geometry of shell I1.4 ($\mu = 0.364$).	66
6.18	Normalized load-displacement curves considering an imperfect geometry of shell I1.6 ($\mu = 0.728$).	66
6.19	Normalized load-displacement curves considering an imperfection in the shape of the local buckling mode for shell I1.10 ($\mu = 1.45$).	67
6.20	Normalized load-displacement curves considering an imperfection in the shape of the global buckling mode for shell I1.10 ($\mu = 1.45$).	67
6.21	Von Mises stress distribution in isotropic shells during loading (A), at local buckling (B), before (C), and after (D) global buckling.	69
6.22	Normalized buckling loads of isotropic shells including experimental data.	70
7.1	Analytically predicted normalized buckling stresses for quasi-isotropic laminates.	74
7.2	Absolute buckling stresses for quasi-isotropic composite shells predicted by the analytical solution.	75
7.3	Normalized buckling loads for various stacking sequences predicted with a LBA.	76
7.4	Normalized initial buckling loads for various stacking sequences predicted with a NLD analysis.	77
7.5	Normalized maximum buckling loads for various stacking sequences predicted with a NLD analysis.	77
7.6	Normalized (initial) buckling loads of quasi-isotropic shells for $R/t = 400$	78
7.7	Normalized (maximum) buckling loads of quasi-isotropic shells for $R/t = 400$	78
7.8	Absolute buckling loads of quasi-isotropic shells for $R/t = 400$	79
7.9	Initial buckling patterns of the $[0, \pm 45, 90]_S$ layup.	80
7.10	Initial buckling patterns of the $[\pm 45, 0, 90]_S$ layup.	80
7.11	Initial buckling patterns of the $[90, \pm 45, 0]_S$ layup.	80
7.12	Load-displacement curves for some configurations of the $[0, \pm 45, 90]_S$ laminate.	81
7.13	Load-displacement curves for some configurations of the $[\pm 45, 0, 90]_S$ laminate.	82
7.14	Load-displacement curves for some configurations of the $[90, \pm 45, 0]_S$ laminate.	82
7.15	Radial displacements of a $[0, \pm 45, 90]_S$ laminate calculated with a NLD analysis during loading (A), at local buckling (B), before (C), and after (D) global buckling. Amplification factor 5.	83
7.16	Radial displacements of a $[\pm 45, 0, 90]_S$ laminate calculated with a NLD analysis during loading (A), at local buckling (B), before (C), and after (D) global buckling. Amplification factor 5.	84
7.17	Radial displacements of a $[90, \pm 45, 0]_S$ laminate calculated with a NLD analysis during loading (A), at local buckling (B), before (C), and after (D) global buckling. Amplification factor 5.	85
7.18	Normalized load-displacement curves for shell QI1.3 with a $[0, \pm 45, 90]_S$ layup and varying imperfection amplitudes.	86
7.19	Normalized load-displacement curves for shell QI3.3 with a $[\pm 45, 0, 90]_S$ layup and varying imperfection amplitudes.	86
7.20	Normalized load-displacement curves for shell QI3.5 with a $[90, \pm 45, 0]_S$ layup and varying local mid-surface imperfection amplitudes.	87
7.21	Normalized load-displacement curves for shell QI3.5 with a $[90, \pm 45, 0]_S$ layup and a combination of local and global mid-surface imperfections at varying amplitudes.	87
7.22	Stresses along the fiber direction of the innermost ply in a $[0, \pm 45, 90]_S$ laminate during loading (A), at local buckling (B), before (C), and after (D) global buckling.	90
7.23	Stresses in fiber direction in the innermost ply of a $[\pm 45, 0, 90]_S$ laminate during loading (A), at local buckling (B), before (C), and after (D) global buckling.	91
7.24	Stresses in fiber direction in the innermost ply of a $[90, \pm 45, 0]_S$ laminate during loading (A), at local buckling (B), before (C), and after (D) global buckling.	92

List of Tables

2.1	Buckling loads predicted for various imperfections and measured test results [34].	19
5.1	Geometric parameters for isotropic cylindrical shells.	48
5.2	Geometric parameters for composite shells.	48
5.3	Material properties of Mylar.	49
5.4	Material properties of Hexcel IM7-8552.	49
6.1	Normalized and relative maximum buckling loads for several isotropic shells and imperfection amplitudes.	68
6.2	Maximum von Mises stress during loading (A), at local buckling (B), before (C), and after (D) global buckling.	70
7.1	Number of buckling waves m and n as well as the corresponding buckling stresses for pristine composite shells.	74
7.2	Normalized and relative maximum buckling loads for a $[0, \pm 45, 90]_S$ laminate considering mid-surface imperfections.	88
7.3	Normalized and relative maximum buckling loads for a $[\pm 45, 0, 90]_S$ laminate considering mid-surface imperfections.	88
7.4	Normalized and relative maximum buckling loads for a $[90, \pm 45, 0]_S$ laminate considering mid-surface imperfections.	88
7.5	Average stress allowables of Hexcel IM7-8552 [74].	89

List of Abbreviations

DOF	Degree of Freedom
FE	Finite Element
FEM	Finite Element Method
LBA	Linear Buckling Analysis
NASA	National Aeronautics and Space Administration
NLD	Nonlinear Dynamic
NLS	Nonlinear Static
NR	Newton-Raphson
ODE	Ordinary Differential Equation
PDE	Partial Differential Equation
STAGS	Structural Analysis of General Shells
UD	Unidirectional

List of Symbols

The list below contains symbols as well as the associated descriptions as they are utilized in this document. Many of them were taken from publications whose authors naturally employed different notations. It was attempted to remain consistent with respect to these references while simultaneously being as unambiguous as possible. Hence, there may be occasional discrepancies in notation between some sources and the document at hand. For the same reason, a symbol may refer to more than a single concept, but the appropriate meaning can always be derived from context.

0	Zero vector
a	Extensional compliance matrix
a	Acceleration vector
a'	Transformed extensional compliance matrix
abd	Compliance matrix based on the classical lamination theory
<i>a</i>	Cutout radius
<i>a, b</i>	Shell dimensions
<i>a_n, a'_n, b_n, ...</i>	Constants of the complementary solution in equation (4.7)
<i>a_{ij}</i>	Extensional compliance matrix elements
<i>a'_{ij}</i>	Transformed extensional compliance matrix elements
A	Extensional stiffness matrix
A'	Transformed extensional stiffness matrix
ABD	Stiffness matrix based on the classical lamination theory
ABD'	Transformed stiffness matrix
<i>A</i>	Area
<i>A, B</i>	Lamé parameters
<i>A_n, B_n, C_n, ...</i>	Coefficients
<i>A_{ij}</i>	Extensional stiffness matrix elements
b	Coupling compliance matrix
<i>b</i>	Circumferential width of a rectangular cutout
<i>b_{ij}</i>	Coupling compliance matrix elements
B	Coupling stiffness matrix
B	Strain-displacement matrix
B₁, B₂, B₃	Matrices introduced by Starnes, see equation (2.16)
B'	Transformed coupling stiffness matrix
<i>B</i>	Decay parameter
<i>B_{ij}</i>	Coupling stiffness matrix elements
<i>c</i>	Circumferential cutout width
C	Stiffness tensor
C	Damping matrix
<i>C</i>	Curvature parameter introduced by Hilburger, see equation (2.19)
<i>C</i>	Extensional stiffness of an isotropic material
<i>C_{ij}</i>	Stiffness tensor components in Voigt notation
<i>C_{mn}</i>	Integration constants
d	Flexural compliance matrix
<i>d</i>	Cutout diameter
<i>d_{ij}</i>	Flexural compliance matrix elements
D	Flexural stiffness matrix
<i>D</i>	Bending stiffness of an isotropic material
<i>D_{ij}</i>	Flexural stiffness matrix elements
<i>D'_{ij}</i>	Transformed flexural stiffness matrix elements

E	Young's modulus
E_m	Equivalent membrane Young's modulus
E_i	Young's modulus along axis i
\mathbf{f}	Force vector
f	Function
F	Functional
F_{cl}	Linear shell buckling load corresponding to τ_{cl}
F_{cr}	Buckling load of a cylindrical shell with a circular cutout
g_0, g_2, g_4	Disturbance function terms in equation (4.11)
G_{ij}	Shear modulus in the ij -plane
h_0, h_2, h_4	Particular solution terms in equation (4.14)
\mathbf{I}	Identity matrix
k_{ij}	Coefficients of the stress resultants at buckling
\mathbf{K}	Stiffness matrix
\mathbf{K}^G	Geometric stiffness matrix
\mathbf{K}^M	Material stiffness matrix
K_x, K_y, K_{xy}	Buckling coefficients
K_{ij}^G	Geometric stiffness matrix elements
K_{ij}^M	Material stiffness matrix elements
l	Axial cutout length
L	Shell length
m	Number of axial buckling half-waves
\mathbf{M}	Mass matrix
M_x, M_y, M_{xy}, M_{yx}	Stress couples
n	Number of circumferential buckling waves
$N_r, N_\theta, N_{r\theta}$	Stress resultants
N_x, N_y, N_{xy}, N_{yx}	Stress resultants
$N_r^0, N_\theta^0, N_{r\theta}^0$	Prebuckling stress resultants
N_x^0, N_y^0, N_{xy}^0	Transformed prebuckling stress resultants
\bar{N}_x	Shell edge load
p	Pressure
\tilde{p}	Nondimensional loading parameter
q_{mn}, q_n	Ritz coefficients
\mathbf{Q}	Lamina stiffness matrix
$\bar{\mathbf{Q}}$	Lamina stiffness matrix aligned with the global coordinate system
Q_x, Q_y	Transverse shear stress resultants
Q_{ij}	Lamina stiffness matrix elements
r, θ	Radial and angular coordinates
r	Characteristic cutout size
\bar{r}	Curvature parameter introduced by Montague et al., see equation (2.22)
\bar{r}	Curvature parameter introduced by Jullien et al., see equation (2.24)
R	Shell radius
R_i	Shell radius with respect to axis i
\mathbf{S}	Compliance tensor
S	Slenderness ratio
S_{ij}	Compliance tensor components in Voigt notation
t	Shell thickness
t	Time
t_b	Equivalent bending thickness
t_i	Direction cosines in Voigt notation
\mathbf{T}	Transformation matrix
\mathbf{T}_{iD}	Transformation matrix for tensor of dimension i
\mathbf{u}	Displacement vector
u, v, w	Displacements corresponding to the coordinates x, y, z
u_{cl}	Linear shell buckling displacement corresponding to τ_{cl}

U	Strain energy
U_b	Bending strain energy
U_m	Membrane strain energy
\mathbf{v}	Velocity vector
V	Potential energy due to external forces
V	Volume
w	Displacement function
W	Nondimensional out-of-plane displacement
W	Weight added by local cutout reinforcements
W_0	Weight removed by a cutout
W_{mn}, W_m	Wronskian
x, y, z	Axial, circumferential/transverse, and lateral coordinates
x', y'	Transformed coordinates
X, Y, Z	Nondimensional coordinates
X_T, X_C, Y_T, Y_C, S	Lamina stress allowables
z_i	Complex numbers
z_n	z -coordinates of the lamina boundaries
Z	Batdorf parameter
α	Curvature parameter introduced by Lur'e, see equation (2.3)
$\alpha_b, \gamma_b, \mu', \delta_b$	Nondimensional bending parameters
$\alpha_m, \gamma_m, \beta', \delta_m$	Nondimensional membrane parameters
β	Curvature parameter introduced by Van Dyke, see equation (2.7)
γ	Weight ratio
γ	Euler-Mascheroni constant
γ_{opt}	Optimal weight ratio
δ	Variational operator
Δt	Time increment
$\boldsymbol{\varepsilon}$	Strain tensor
ε_{ij}	Strain tensor components
ε_{ij}^0	In-plane contribution to the strain tensor components
Θ	Circumferential cutout angle
κ_{ij}	Curvature contribution to the strain tensor components
λ	Eigenvalue
μ	Curvature parameter introduced by Lekkerkerker, see equation (2.5)
μ_i	Principal roots of the characteristic equation of an anisotropic plate
ν	Poisson's ratio
ν_{ij}	Poisson's ratio, contraction along axis j due to an extension of axis i
ξ, ϕ	Nondimensional Cartesian coordinates
Π	Total energy
ρ	Density
$\boldsymbol{\tau}$	Stress tensor
τ_∞	Applied far-field stress
τ_{cl}	Buckling stress of a pristine cylindrical shell
τ_{cr}	Buckling stress of a cylindrical shell with a circular cutout
τ_{ij}	Stress tensor components
ϕ	Test function
φ_i	Complex potential functions introduced by Lekhnitskii, see equation (2.2)
Φ	Airy stress function
Ψ	Dimensionless complex function introduced by Lekkerkerker, see equation (2.4)
$\bar{\nabla}$	Dimensionless gradient operator
∇^4	Biharmonic operator

1

Introduction

Thin shells are frequently used as structural elements when the application requires a design that can carry loads efficiently while at the same time being lightweight. Hence, shell designs are often employed in the aerospace industry in the form of cylindrical shells, for example as aircraft fuselages, rocket (inter-) stages, and even as modules of the International Space Station. The defining characteristic of a shell is its curvature which is simultaneously the reason for the coupling between the structure's in-plane and out-of-plane response. As a consequence, shells are able to transfer loads as membrane stresses that would cause a pure bending response in plates. This is advantageous because stressing the material in a given cross-section equally through the thickness is one aspect of design optimization. In addition, the thinness of the shell reduces the relative bending contribution by decreasing the corresponding stiffness properties. Thus, it also promotes the more efficient membrane response.

To further improve the design, optimized structures should carry section forces and moments in every direction as close to the respective limit loads as possible. From this perspective isotropic materials like steel and aluminum alloys are a poor choice because a single load case and cross-section are often critical for sizing. Consequently, other parts of the structure do not contribute as much to the load transfer as they could. Composite materials on the other hand enable the engineer to tailor strength and stiffness properties to a much larger degree. Typical composites are created by embedding fibers in a matrix material. The fibers provide high strength and stiffness along their longitudinal orientation while the matrix transfers load to the fibers and protects them from the environment. As a result, shell designs made from composites are highly relevant due to the beneficial properties of both shape and material.

Despite their otherwise attractive characteristics, cylindrical shells are susceptible to buckling which describes the phenomenon where a body undergoes a sudden and drastic deformation when subjected to a critical load. While some structural elements can sustain their integrity during and after buckling, shell buckling is particularly disadvantageous because the load-carrying capability of the structure is greatly reduced in the process. Therefore, the design of shells against buckling is extremely important. Even though the theoretical buckling resistance of cylindrical shells is reasonably high, their real counterparts buckle at comparatively low stress levels. The reason for this discrepancy is the presence of initial geometric imperfections, especially mid-surface variations, which are an unwanted result of inherently imperfect manufacturing processes. In contrast, cutouts are added much more deliberately to shell designs because they may serve as access points during assembly and inspection, as a simple means of weight reduction, or as aesthetic features like windows. Since the opening creates a disruption in the geometry of the cylindrical shell, it can be expected that it also has a significant influence on the shell buckling behavior. Hence, the engineer must be able to estimate the critical load at which cylindrical shells with cutouts buckle.

Generally speaking, there are three ways to predict or determine the mechanical response of any type of structure to loads, namely analytical, numerical, and experimental methods. Naturally, experiments are the most realistic, but they are expensive in terms of both time and money. For this reason, it is not feasible to test all conceivable design permutations to select the one that performs best. Numerical approaches like the Finite Element Method (FEM) get rid of the monetary cost issue since simulations do not require the manufacturing of specimens. Nonetheless, the time it takes to conduct parametric studies is still significant as models become more and more detailed even though the available computing power increases at a rapid pace.

Analytical solutions on the other hand provide reasonably accurate predictions in very little time at almost no cost. Consequently, they are especially suitable for preliminary design where they immediately enable their users to assess the consequences of certain design choices. Furthermore, analytical solutions are easily customized to perform parametric studies. From an academic perspective they are valuable because they grant insights regarding the interplay of the various mechanisms that cause structural phenomena like buckling and help to determine which variables are the most influential. On the downside, analytical solutions are often only obtainable for simple geometries and load cases because solving the governing differential equations tends to be rather complex.

Clearly, predicting the buckling load of composite shells that contain cutouts with an analytical approach is highly relevant, both from an academic and an industrial point of view. Therefore, the goal of this thesis is to develop such a solution, to verify its accuracy with Finite Element (FE) simulations, and to investigate the mechanisms that govern the phenomenon.

1.1. Document Organization

This thesis is divided into eight chapters. After a brief introduction in Chapter 1, the literature on the subject of the buckling behavior of cylindrical shells with cutouts is reviewed and summarized in Chapter 2. Subsequently, Chapter 3 discusses the theoretical foundations of a shell buckling analysis by revisiting, inter alia, shell theory to describe cylindrical shells mathematically, classical lamination theory to account for composite materials, and energy methods to quantify the shell response. These tools are applied in Chapter 4 to derive an analytical solution for the linear buckling load of cylindrical shells with circular cutouts considering the constitutive relations that describe isotropic and quasi-isotropic, symmetric, composite materials. Afterwards, the setup of the FE models, which are used for verification purposes, is presented in Chapter 5. The next two segments of the thesis, Chapters 6 and 7, are concerned with evaluating the analytical and numerical results regarding isotropic and quasi-isotropic composite cylindrical shells, respectively. Finally, a critical assessment of the outcomes is available in Chapter 8 together with recommendations for future work.

1.2. Preliminary Note

A structure may buckle due to a variety of applied loads and cylindrical shells can appear in many shapes. Naturally, this document cannot provide analytical solutions for every combination of load and shape. In fact, the buckling analysis in Chapter 4 is restricted to circular cylindrical shells with circular cutouts subjected to a uniform axial compressive edge load. To reduce the number of words required to describe the problem, three naming conventions are introduced. First, shell and cylindrical shell will be taken to mean circular cylindrical shell. Second, it can be assumed that buckling is caused by the aforementioned uniform axial edge load. Additionally, the word cutout refers to a circular opening. Exceptions from these naming conventions are clearly specified.

2

Literature Review

This chapter contains a summary of publications that relate to analyzing and understanding the buckling phenomenon of cylindrical shells with cutouts. The historical development of analytical methods is presented in Section 2.1. Experiments and the interpretation of their results are covered in Section 2.2. The last part of this chapter, Section 2.3, discusses numerical analyses of cylindrical shells with cutouts, i.e. predominantly results obtained with FEM.

2.1. Analytical Work

Before buckling of shells with cutouts can be studied, it is first necessary to be able to predict the stress field in the structure due to external loads. The simplest case is the shell with zero curvature, i.e. a plate, after which the more complex case of the cylindrical shell is examined. Even though the buckling response of shells and plates differ, some analysis choices and their consequences are well illustrated in papers on the latter subject which is why a short excursion to plate buckling is undertaken. Finally, methods for determining the buckling load of shells with cutouts are discussed. Semi-analytical approaches are treated as a subset of analytical methods on the following pages.

2.1.1. Stresses around Cutouts in Plates

Kirsch [1] showed that the stress distribution around a circular opening in an infinite isotropic flat plate subjected to an axial load is described by equation (2.1). The stress tensor components τ_{ij} are a function of the radial coordinate r , the angular coordinate θ , the cutout radius a , and the applied far-field stress τ_{∞} . Equation (2.1) is valid when the applied load is aligned with $\theta = 0^\circ$.

$$\begin{aligned}\tau_{rr} &= \frac{\tau_{\infty}}{2} \left[1 - \left(\frac{a}{r} \right)^2 \right] + \frac{\tau_{\infty}}{2} \left[1 - 4 \left(\frac{a}{r} \right)^2 + 3 \left(\frac{a}{r} \right)^4 \right] \cos 2\theta \\ \tau_{\theta\theta} &= \frac{\tau_{\infty}}{2} \left[1 + \left(\frac{a}{r} \right)^2 \right] - \frac{\tau_{\infty}}{2} \left[1 + 3 \left(\frac{a}{r} \right)^4 \right] \cos 2\theta \\ \tau_{r\theta} &= -\frac{\tau_{\infty}}{2} \left[1 + 2 \left(\frac{a}{r} \right)^2 - 3 \left(\frac{a}{r} \right)^4 \right] \sin 2\theta\end{aligned}\tag{2.1}$$

A solution for the stress field in an orthotropic flat plate containing an elliptic opening was presented by Lekhnitskii [2]. Later, Savin [3] published Lekhnitskii's method in a compendium about stress distributions around cutouts in plates and shells. First, the elliptic opening is transformed onto a unit circle in the complex plane. Using an inverse mapping function and complex potential functions, equation (2.2) allows calculating stress components at discrete points. μ_i ($i = 1, 2$) denotes the principal complex roots of the characteristic equation for an anisotropic plate, φ'_i refers to the derivatives of the potential functions, and z_i indicates complex coordinates.

$$\begin{aligned}\tau_{xx} &= 2\text{Re} \left[\mu_1^2 \varphi'_1(z_1) + \mu_2^2 \varphi'_2(z_2) \right] + \tau_{xx,\infty} \\ \tau_{yy} &= 2\text{Re} \left[\varphi'_1(z_1) + \varphi'_2(z_2) \right] + \tau_{yy,\infty} \\ \tau_{xy} &= -2\text{Re} \left[\mu_1 \varphi'_1(z_1) + \mu_2 \varphi'_2(z_2) \right] + \tau_{xy,\infty}\end{aligned}\tag{2.2}$$

2.1.2. Stresses around Cutouts in Shells

An early examination of the stress distribution around a circular opening in an isotropic cylindrical shell was conducted by Lur'e [4] who derived an equation similar to (2.4) which satisfies the equilibrium equations of an unsymmetrically loaded cylindrical shell. Taking R as the shell radius and t as the shell thickness, he assumed $R/a \ll \sqrt{t/a}$ so that higher order terms of his complex stress function could be dismissed. Lur'e defined the curvature parameter α as shown in equation (2.3).

$$\alpha = \frac{a}{\sqrt{Rt}} \quad (2.3)$$

The problem was more rigorously approached by Lekkerkerker [5] and Van Dyke [6] who independently concluded that Lur'e's results were only valid for small values of α as a direct consequence of the aforementioned simplification and furthermore incorrect by a factor of 0.5.

Lekkerkerker idealized the shell geometry as a spiral shell with infinite length in the circumferential direction, applied the principle of superposition, arrived at the same governing equation as Lur'e, but also nondimensionalized it by introducing a dimensionless gradient operator $\bar{\nabla}$.

$$\bar{\nabla}^4 \Psi - 4\mu^2 i \frac{\partial^2 \Psi}{\partial x^2} = 0 \quad (2.4)$$

The dimensionless complex function Ψ contains both a stress function Φ as well as the out-of-plane deflection w . μ is an alternative curvature parameter that also depends on the Poisson's ratio ν .

$$\mu = \frac{1}{2} \sqrt[4]{12(1-\nu^2)} \frac{a}{\sqrt{Rt}} \quad (2.5)$$

Lekkerkerker solved the partial differential equation (2.4) by separating the variables and subsequently assuming a solution in terms of Hankel functions (Bessel functions of the third kind) and exponentials. The final result is expressed as a Fourier series where $2n$ coefficients, A_n and B_n , are determined from the boundary conditions. Some stress distributions based on equation (2.6) are plotted in Figure 2.1. The stress field changes drastically with the curvature parameter μ . It can be seen that cylindrical shells experience bending stresses which are not present in axially loaded flat plates ($\mu = 0$).

$$\Psi = \sum_{m=0}^{\infty} \sum_{n=0}^{\infty} (A_n + iB_n) f(m, n, \mu r) \cos 2m\theta \quad (2.6)$$

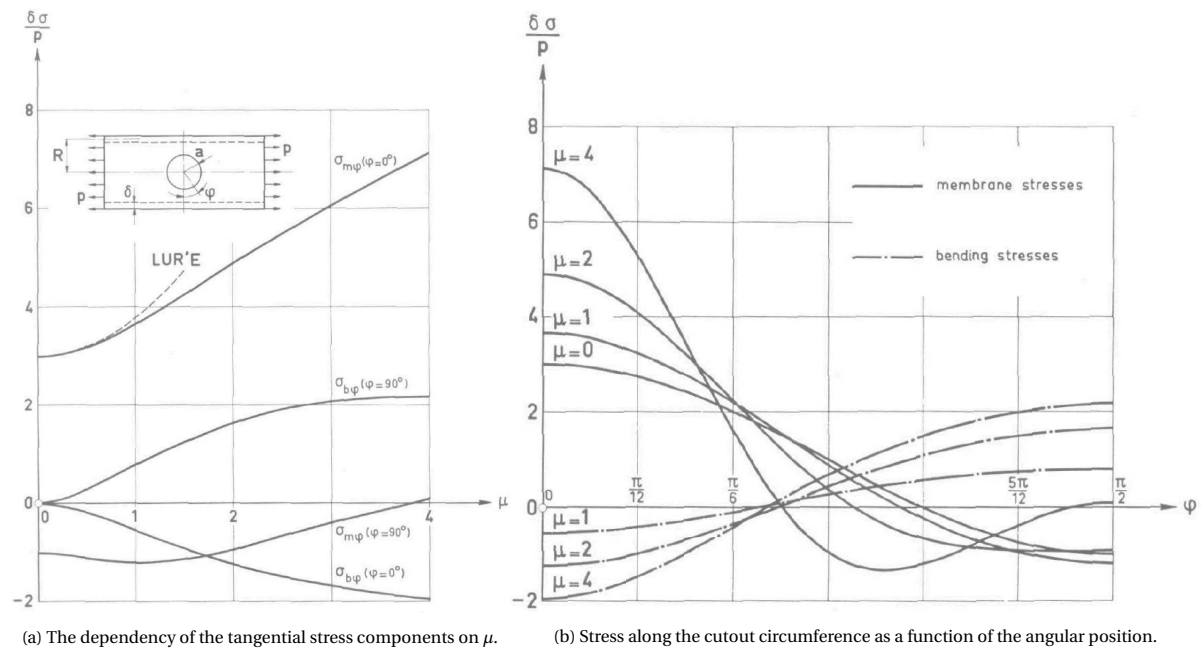


Figure 2.1: Membrane and bending stresses caused by axial tension as predicted by Lekkerkerker [5], ($\delta = t$).

Van Dyke introduced his own curvature parameter β which relates to μ by $\mu = \sqrt{2}\beta$. A major difference between Lekkerkerker's and Van Dyke's approach is the calculation of the coefficients A_n and B_n . While every term in Lekkerkerker's Fourier series fulfills the boundary conditions exactly, only the sum of all terms in Van Dyke's solution accomplishes the same. Lekkerkerker showed that his analysis is always accurate as long as a/R is small compared to unity. Van Dyke derived the inequality (2.7) for the same purpose.

$$\frac{a}{R} < \frac{\beta}{4.6 + 2\beta} \quad (2.7)$$

Adams [7] attempted to simplify the relatively complicated solutions derived by Lekkerkerker and Van Dyke by finding an approximate solution with Galerkin's method. D_n , E_n , X_n , and Y_n in equation (2.8) are undetermined coefficients. Adams' test functions for the out-of-plane displacement w and the Airy stress function Φ were obviously inspired by Kirsch's solution for the flat plate. The stress distribution calculated with this approach differs significantly from Lekkerkerker's and Van Dyke's predictions which were validated by third parties, for example Tennyson [8].

$$w = \sum_{n=1}^N E_n \alpha^2 \left[X_n \left(\frac{a}{r}\right)^{n+1} + Y_n \left(\frac{a}{r}\right)^{n+2} + \left(\frac{a}{r}\right)^{n+3} \right] \cos 2n\theta$$

$$\Phi = \tau_\infty \left\{ \frac{r^2}{4} - \frac{a^2 \ln(r)}{2} + \left(\frac{a^2}{2} - \frac{r^2}{4} - \frac{a^4}{4r^2} \right) \cos 2\theta + \sum_{n=1}^N D_n \alpha^2 \left[\left(\frac{a}{r}\right)^{n+1} - 2\left(\frac{a}{r}\right)^{n+2} + \left(\frac{a}{r}\right)^{n+3} \right] \cos 2n\theta \right\} \quad (2.8)$$

Murthy et al. [9] considered an isotropic shell with an elliptic cutout. Instead of Bessel functions, they developed their solution in terms of Mathieu functions. The coefficients A_n and B_n were determined with the Newton-Raphson (NR) method for a given set of boundary conditions. The authors published stress concentration factors, but their approach can probably be extended to calculate stress distributions around elliptic openings as a function of the radial coordinate as well. Furthermore, the publication covers the extreme cases of circular cutouts as well as circumferential and axial cracks.

One of the first to study stresses around openings in orthotropic cylindrical shells was Guz [10] who assumed the cutout edges to be clamped. The more common case of a freely displaceable cutout boundary was treated by Ashmarin [11]. Expressing the governing equation in a polar semi-geodesic coordinate system, he applied the Galerkin method by prescribing shape functions for the displacements and calculated the corresponding stress resultants. The unknown coefficients were determined with the help of a computer.

Another approach was presented by Guz (a namesake) et al. [12]. They summarized solutions for stress concentration factors of various types of orthotropic shells. The governing equation for the case of a cylindrical shell assuming linear strains and neglecting lateral shear was solved with cylindrical and Krylov functions. Interestingly enough, the stresses predicted by Ashmarin and Guz et al. agree quite well as Figure 2.2 shows. The Roman numeral I indicates a free cutout edge while II denotes a clamped cutout boundary. Furthermore, solid lines refer to a Young's modulus ratio of $E_1/E_2 = 2$, dashed ones to $E_1/E_2 = 1$, and dot-dashed lines symbolize a ratio of $E_1/E_2 = 0.5$.

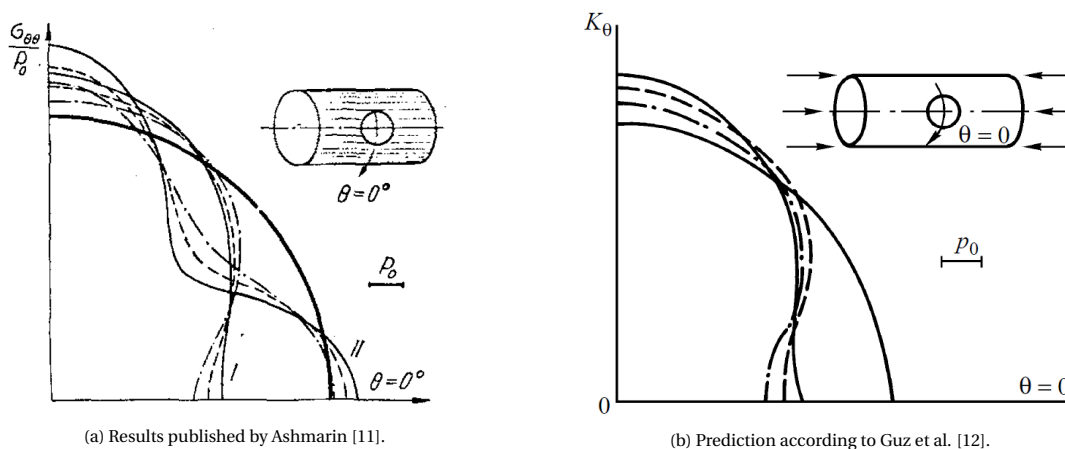


Figure 2.2: Tangential stress concentration factors along a cutout in an orthotropic cylindrical shell.

Lekkerkerker's approach [5] was modified by van Tooren et al. [13] to investigate the stress distribution around circular openings in composite sandwich shells. They replaced the Young's modulus of the isotropic material with an equivalent membrane property E_m of the sandwich structure, calculated a new bending thickness t_b for the analysis to match the composite's bending stiffness, and then solved for the coefficients A_n and B_n twice, i.e. once for the in-plane and once for the out-of-plane response. Adding the bending stress field corrected for the artificial bending thickness to the in-plane and the far-field stresses yields the final solution for the stress distribution in the shell.

Oterkus et al. [14] modified a methodology proposed by Madenci et al. [15], see Subsection 2.1.4, to compute stresses in thin composite cylindrical shells with an elliptic cutout. Considered variables are the cutout size, its shape and orientation, shell wall-thickness variations, cross-section eccentricity, as well as external loading parameters. The elliptic cutout shape and cross-section were described in Cartesian coordinates using mapping functions. Model properties were quantified in terms of their total potential energy. A system of springs connected the actual geometry and a virtual rigid end ring to which all boundary conditions and external loads were applied. The authors argued that this enabled them to select more versatile shape functions. Eventually, a material stiffness matrix \mathbf{K} and a force vector \mathbf{f} were derived. Subsequently,

$$\mathbf{K}\mathbf{u} = \mathbf{f} \quad (2.9)$$

was solved through matrix inversion by a computer for the unknown displacement vector \mathbf{u} . Figure 2.3 depicts the estimated stress distribution around a circular cutout in a quasi-isotropic composite cylindrical shell. The calculated stress field for small openings and curvatures, i.e. small values of the curvature parameter μ from equation (2.5), approaches the flat plate solution derived by Kirsch [1].

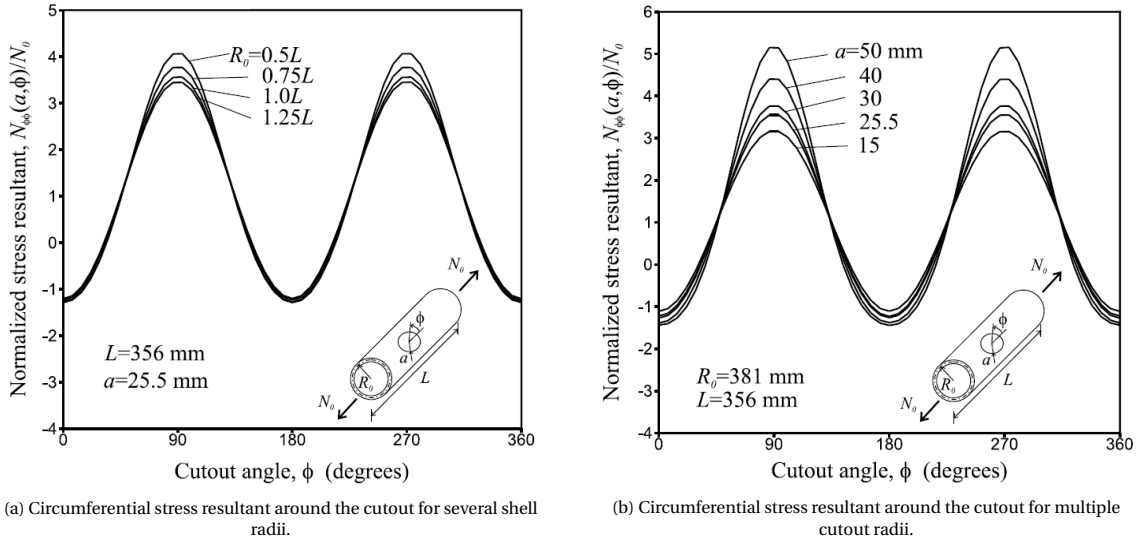


Figure 2.3: Normalized tangential stress resultants around a circular opening in a quasi-isotropic composite shell [14].

2.1.3. Buckling of Plates with Cutouts

Two different methods for determining the buckling load of axially compressed plates with centrally located cutouts are showcased in this subsection. Nemeth et al. [16] investigated the buckling of a finite orthotropic plate containing a circular opening. Following the Kantorovich method, they reduced the problem from a two-dimensional problem to a one-dimensional one. Displacement functions for the prebuckling response of the structure were assumed and the principle of minimum potential energy was applied to approximate the stress distribution before buckling occurs. The buckling load was then estimated by minimizing the second variation of the total potential energy while prescribing a shape function for the out-of-plane deflection. The governing differential equations were solved with a computer where the Fourier series expressing the displacements is truncated at $N = 3$. Since displacement loading is applied, the generalized eigenvalue problem

$$\mathbf{K}^M \mathbf{u} = \lambda \mathbf{K}^G \mathbf{u} \quad (2.10)$$

yields the axial buckling displacement as the eigenvalues λ which may be converted to a buckling load. \mathbf{K}^M denotes the material stiffness matrix and \mathbf{K}^G refers to the geometric stiffness matrix in equation (2.10). Figure 2.4 illustrates the idealized geometry. Choosing a Cartesian reference frame enables using familiar and convenient stress-strain relations. However, the authors had to account for the opening by modifying the displacement functions and integrating from the curved path $f(x)$ to b in the width direction. This results in a complex problem formulation and probably necessitates a computer to determine solutions.

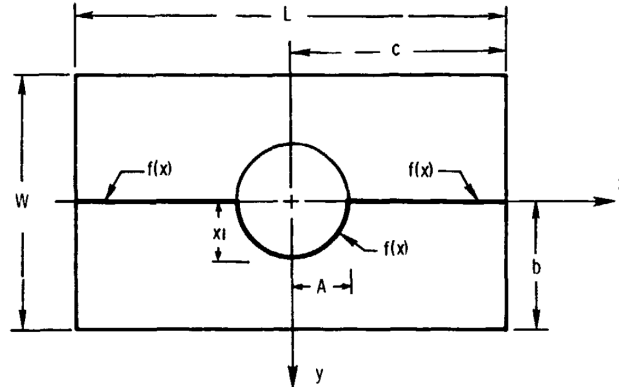


Figure 2.4: Geometry of a plate with a centrally located cutout and integration boundaries [16].

Kassapoglou [17] predicted the buckling load of a composite plate with two concentric rectangular layups, see Figure 2.5. When assigning zero stiffness to the smaller one of the two, it can be interpreted as a cutout. The buckling load is obtained by minimizing the total potential energy, this time with the Rayleigh-Ritz method. Kassapoglou chose the shape function

$$w = \sum_{m=1}^M \sum_{n=1}^N q_{mn} \sin m\pi\xi \sin n\pi\phi \quad (2.11)$$

The coefficients q_{mn} are to be determined with the Rayleigh-Ritz method. The integration over the whole domain is performed with the normalized coordinates ξ and ϕ as defined in Figure 2.5. The variables in the shape function were selected accordingly. Solving the generalized eigenvalue problem from equation (2.10) gives the buckling load as a multiple of the applied distributed edge load.

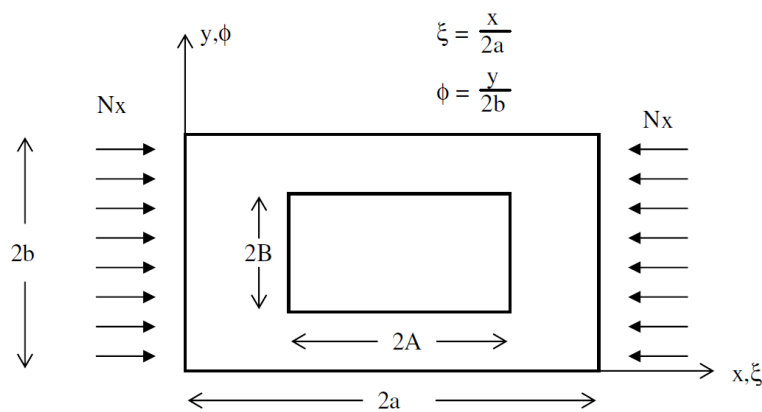


Figure 2.5: Model of two concentric composite plates [17].

The simplicity of Kassapoglou's approach compared to that of Nemeth et al. is apparent and at least partly the result of selecting a Cartesian coordinate system for a rectangular cutout. However, Nemeth et al. were able to truncate their Fourier series at $N = 3$, whereas the stiffness discontinuity caused by the opening combined with Kassapoglou's shape function requires many terms of the Fourier series (2.11) to achieve convergence. In fact, Kassapoglou reported that for the vast majority of cases between 15 and 20 terms in each direction, i.e. 225 to 400 total terms, were needed to account for the large difference in stiffness.

2.1.4. Buckling of Shells with Cutouts

Starnes [18] was probably the first to present an analytical solution for the buckling load of isotropic cylindrical shells with circular cutouts. Assumptions and simplifications made during his analysis are based on an extensive testing campaign featuring Mylar, a thermoplastic, and copper shells. He argued that nonlinear events do not significantly influence the buckling behavior of the shells with cutouts and thus linearized the problem. Furthermore, Starnes noted that the global loss of stiffness appeared to be caused by local buckling so that this phenomenon should be investigated. Consequently, changes in the displacement and stress field far away from the opening were assumed to be small enough to be dismissed. Based on Lekkerkerker's results, Starnes proposed that the influence of bending stresses could be neglected and that the membrane stresses could be approximated with the flat plate solution from Kirsch for small values of the curvature parameter μ .

The specimens in Starnes' experiments featured two seemingly symmetric buckles when a sudden loss of stiffness occurred which he modeled with the displacement function

$$w(r, \theta) = e^{-Br} [(A_0 + rC_0) + (A_2 + rC_2) \cos 2\theta] \quad (2.12)$$

Here, A_0 , A_2 , C_0 , and C_2 are undetermined coefficients while B represents a decay parameter. Defining the total potential energy as

$$\Pi = U_m + U_b + V \quad (2.13)$$

where U_m denotes the membrane strain energy, U_b indicates the bending strain energy, and V stands for the energy due to external forces, Starnes transformed the expressions from curvilinear orthogonal coordinates to a new curvilinear polar reference frame in accordance with equation (2.12). The bending strain energy was calculated by substituting equation (2.12) while the prebuckling stress distribution for the external applied load could be approximated with the flat plate stress distribution. To integrate U_m , the linear compatibility equation in polar coordinates had to be solved. The boundary conditions for the stress resultants N_r , N_θ , and $N_{r\theta}$ are given by

$$\begin{aligned} N_r = N_{r\theta} = 0 & \quad \text{for } r = a \\ N_r = N_\theta = N_{r\theta} = 0 & \quad \text{for } r \rightarrow \infty \end{aligned} \quad (2.14)$$

In a next step, the Rayleigh-Ritz procedure was applied to minimize (2.13) which yielded

$$[\mathbf{B}_1 - \lambda \mathbf{B}_2] \begin{Bmatrix} A_0 \\ A_2 \\ C_0 \\ C_2 \end{Bmatrix} = \mathbf{0} \quad (2.15)$$

where \mathbf{B}_1 and \mathbf{B}_2 are 4x4 matrices whose entries depend on U_m , U_b , and V . The eigenvalues λ of the first term in equation (2.15) provide the buckling load as a multiple of the applied far-field stress. Starnes calculated these eigenvalues by pre-multiplying equation (2.15) with \mathbf{B}_2^{-1} and then examining

$$\det(\mathbf{B}_3 - \lambda \mathbf{I}) = 0 \quad (2.16)$$

\mathbf{B}_3 is a function of a , B , R , t , E , and ν when an isotropic material is considered. In a last step, the eigenvalues were minimized with respect to B . A computer is needed for this step due to the presence of unsolved integrals which had to be evaluated numerically.

Figure 2.6 shows the buckling stress predicted by Starnes' analysis in comparison with the buckling stress measured during his experiments. It can be seen that the analytical results all fall onto a single curve when normalizing the computed buckling stress of the cylindrical shell with the classical solution (3.63) and plotting this against the curvature parameter μ . The same graph with different numerical values on the horizontal axis is obtained when the normalized buckling stress is plotted against α instead. Initially, it had been predicted by Starnes that the analysis would only deliver meaningful results for small values of μ . However, the analytical solution follows the trend of the experimental measurements between $0.4 \leq \mu \leq 2.5$ reasonably well, while major discrepancies are apparent for small μ .

Starnes argued that this was caused by the shells' sensitivity to initial geometric imperfections which were not considered in the analysis. Another explanation could be that assuming a displacement function for a local buckling pattern does not accurately represent the structural response of the shell when a conventional global buckling mode independent of the cutout is observed for small cutout sizes. Assumptions related to the smallness of μ seem to hold longer than anticipated which could explain reasonable predictions up to $\mu = 2.5$. Furthermore, Starnes observed that large prebuckling displacements occurred when the cutout exceeded a certain size. This implies a nonlinear material response which is obviously neglected in a linear buckling analysis.

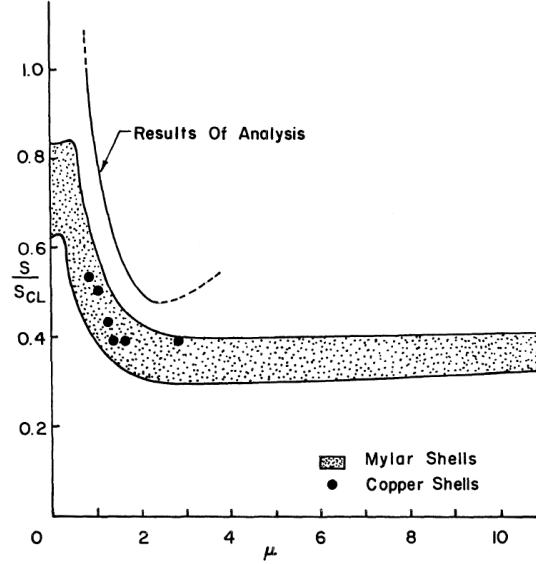


Figure 2.6: Normalized buckling loads obtained from Starnes' analysis and his experiments [18].

Starnes also pointed out some aspects for reducing the discrepancy between his analytical predictions and experimental measurements. He suggested adding additional degrees of freedom (DOFs) to the shape function as the Rayleigh-Ritz method provides overly large buckling load estimates if the assumed displacement function is not sufficiently general. Additionally, he noted that incorporating a prebuckling stress distribution that accounts for the neglected bending stresses should increase the accuracy of the analysis.

Composite cylindrical shells with rectangular cutouts were treated by Hilburger [19] in his Ph.D. dissertation. He derived nondimensionalized equilibrium (2.17) and compatibility (2.18) equations using the method of adjacent equilibrium starting from the Donnell-Mushtari-Vlasov nonlinear theory of thin shells. In the equations below, X and Y are nondimensional coordinates, α_b , β' , γ_b , δ_b , α_m , μ' , γ_m , as well as δ_m represent nondimensional bending and membrane parameters, whereas K_x , K_y , and K_{xy} denote nondimensional buckling coefficients.

$$\begin{aligned} \alpha_b^2 \frac{\partial^4 W}{\partial X^4} + 4\alpha_b \gamma_b \frac{\partial^4 W}{\partial X^3 \partial Y} + 2\beta' \frac{\partial^4 W}{\partial X^2 \partial Y^2} + 4 \frac{\delta_b}{\alpha_b} \frac{\partial^4 W}{\partial X \partial Y^3} + \frac{1}{\alpha_b^2} \frac{\partial^4 W}{\partial Y^4} + \sqrt{12}C \frac{\partial^2 \Phi}{\partial X^2} \\ - K_x \pi^2 \frac{\partial^2 W}{\partial X^2} - K_y \pi^2 \frac{\partial^2 W}{\partial Y^2} - 2 \frac{K_{xy} \pi^2}{\alpha_b^2} \frac{\partial^2 W}{\partial X \partial Y} = 0 \end{aligned} \quad (2.17)$$

$$\alpha_m^2 \frac{\partial^4 \Phi}{\partial X^4} + 2\alpha_m \gamma_m \frac{\partial^4 \Phi}{\partial X^3 \partial Y} + 2\mu' \frac{\partial^4 \Phi}{\partial X^2 \partial Y^2} + 2 \frac{\delta_m}{\alpha_m} \frac{\partial^4 \Phi}{\partial X \partial Y^3} + \frac{1}{\alpha_m^2} \frac{\partial^4 \Phi}{\partial Y^4} = \sqrt{12}C \frac{\partial^2 W}{\partial X^2} \quad (2.18)$$

The formulas above are also available in reference [20] together with the definitions of the nondimensional parameters. It should be noted that Hilburger's β' and μ' are not equivalent to the curvature parameters introduced earlier in this chapter. Instead, C fulfills a similar function. b indicates the circumferential cutout width, A_{ij} refers to extensional, and D_{ij} to flexural stiffness matrix elements.

$$C = \frac{b^2}{R} \left(\frac{A_{11}A_{22} - A_{12}^2}{12\sqrt{A_{11}A_{22}D_{11}D_{22}}} \right)^{1/2} \quad (2.19)$$

The stress analysis of Oterkus et al. [14] is based on a framework proposed by Madenci et al. [15] who studied the linear buckling of composite shells containing elliptic openings. The main difference compared to the already presented paper by Oterkus et al. is that Madenci et al. considered the nonlinear version of the Love-Timoshenko strains to capture the buckling behavior of the shell. Thus, an analytical equivalent of the geometric stiffness matrix \mathbf{K}^G in addition to the material stiffness matrix \mathbf{K}^M was derived. The eigenvalue problem

$$\left(\mathbf{K}^M + \lambda \mathbf{K}^G\right) \mathbf{u} = \mathbf{0} \quad (2.20)$$

was solved with a numerical algorithm for the eigenvalues and eigenmodes of the structure.

2.2. Experimental Work

Naturally, studying the buckling behavior of shells with cutouts in a real-world setting is invaluable and provides essential insights as analytical models are often based on observations from experiments. Additionally, performing tests to check the accuracy of models is useful for validation purposes. In this context, the present section first provides some information regarding the influence of cutout parameters such as size, shape, number, and position on the buckling of shells that contain cutouts. Subsequently, a short overview of the effects of local isotropic and orthotropic reinforcements is given. The section concludes with a discussion of initial geometric imperfections.

2.2.1. Cutout Parameters

Motivated by research on the instability of plates with cutouts, Tennyson [8] investigated the buckling behavior of "near-perfect" epoxy cylindrical shells with one central circular cutout. Effectively providing clamped boundary conditions with two end plates and dealing with the parametric ranges $0 \leq a/R \leq 0.189$ as well as $0 \leq \beta^2 \leq 2.58$, Tennyson summarized his buckling load measurements as illustrated in Figure 2.7. It should be noted that the buckling load of the shell containing an opening is normalized with the experimental buckling load of the same shell before an opening was cut into it. This value is plotted against a/R , and not against one of the previously introduced curvature parameters.

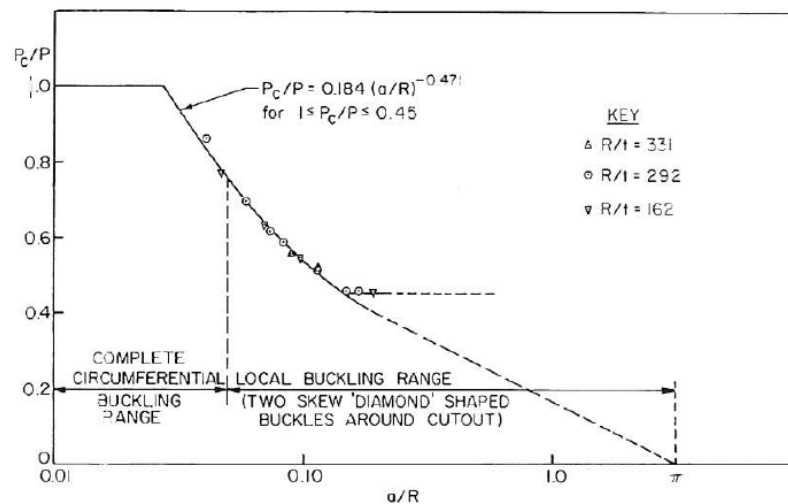


Figure 2.7: Normalized results of Tennyson's testing campaign [8].

Tennyson observed two distinct buckling patterns. Global buckling occurred for small openings and local buckling was observed after the cutout size had been sufficiently increased. A corresponding drop in the normalized buckling load was measured which leveled out at some value of a/R . The author argued that since an opening of size $a = \pi R$ corresponds to a buckling load of zero, there should be another critical point after which the buckling load resumes to decrease. Tennyson suspected that the local buckling pattern was a result of "the growing imperfection in shape in the region of the cutout".

Starnes [18], who was already mentioned in Subsection 2.1.4, conducted an extensive series of experiments on Mylar and copper shells which he manufactured himself. During testing the specimens were

clamped on both edges. While the Mylar shells were force-loaded, the copper shells were subjected to a prescribed displacement until global buckling occurred. Figure 2.8 shows a typical local buckling pattern around a circular cutout in a Mylar shell. Based on his analysis, Starnes argued that a nondimensional geometry parameter should be proportional to a/\sqrt{Rt} instead of simply a/R . For that purpose, he chose Lekkerkerker's μ . Starnes normalized the obtained buckling loads with the classical buckling formula for cylindrical shells.

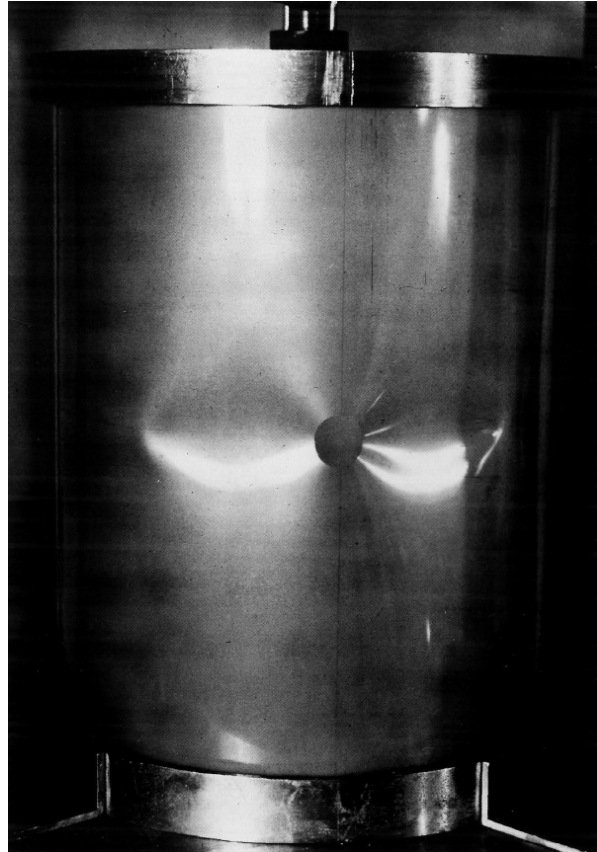


Figure 2.8: Local buckling of a Mylar shell with $\mu > 2$ [18].

He divided the tested shells into four different groups. For values of μ smaller than 0.4, a diamond buckling pattern was observed while the buckling load was similar to that of a pristine reference shell, i.e. heavily dependent on initial geometric imperfections. In the range $0.4 \leq \mu \leq 1.0$ the normalized buckling load decreased rapidly and the diamond displacement pattern appeared to originate from the cutout. This led Starnes to believe that local buckling and the sensitivity to the corresponding stress redistribution caused the shell instability. Shells with $1.0 \leq \mu \leq 2.0$ showed the same behavior, but the buckling load did not decrease as drastically with increasing cutout size. Finally, specimens that had a μ -value larger than 2.0 deformed significantly in the lateral direction resulting in a stable local buckling configuration. However, this buckling event was not unstable as the load could be increased further until the shell eventually buckled globally. The corresponding maximum buckling load was virtually constant regardless of cutout size.

Later, Starnes [21] also reported that slots at the horizontal opening boundaries increased the sustainable buckling load of the structure. He suggested that the slots disrupted the bending stress field around the cutout and therefore delayed the onset of buckling.

Toda [22] varied both size and shape (circular, rectangular, and elliptic) of cutouts in Mylar shells. He obtained a scatter band of buckling loads comparable to that published by Starnes. Toda adjusted the nondimensional parameter α to include the area A of the cutout since he expected the amount of removed material to be indicative of the shell response.

$$\alpha = \frac{a}{\sqrt{Rt}} = \sqrt{\frac{\pi a^2}{\pi R t}} = \sqrt{\frac{A}{\pi R t}} \quad (2.21)$$

He also regrouped the different buckling behavior ranges proposed by Starnes as a function of α , specifically to $\alpha < 0.5$, $0.5 \leq \alpha \leq 2.0$, and $\alpha > 2.0$. Obviously, the actual shell response does not change. Hence, the main difference is that Toda merged $0.4 \leq \mu \leq 1.0$ with $1.0 \leq \mu \leq 2.0$ into one category.

Montague et al. [23] tested cylindrical shells made from aluminum with axially elongated cutouts. They introduced the curvature parameter

$$\bar{r} = \frac{r}{\sqrt{Rt}} \quad (2.22)$$

where r is a characteristic value for a given cutout shape. If the opening was circular, Montague et al. set $r = a$ so that $\bar{r} = \alpha$. For a rectangular cutout, they proposed $r = 0.25(b + l)$, i.e. an eighth of its perimeter. An interesting result of their testing campaign was that almost tripling the cutout length l only resulted in a buckling load reduction of about 10%. Thus, they showed that the removed shell area incorporated into α by Toda is not a relevant factor for the buckling load prediction. Furthermore, Montague et al. noticed two different failure modes. Relatively thick cylindrical shells yielded before they buckled locally while others featured a stable local buckling load along the cutout edge in the form of cosine waves. Since \bar{r} was not indicative of which behavior was to be expected, the researchers defined a slenderness ratio S . Low slenderness ratios corresponded to yielding followed by buckling whereas a high slenderness ratio implied stable local buckling.

$$S = \sqrt[3]{\frac{t^4}{R^2 l^2}} \quad (2.23)$$

Toda [24] revisited his previous research in 1983 when he experimented on Mylar shells with circular cutouts. The results are plotted in Figure 2.9 and illustrate the different characteristic parameter ranges for α . Moreover, one can see that the virtually constant normalized buckling loads branch off at varying values of α depending on the ratio R/t which had been predicted by Tennyson.

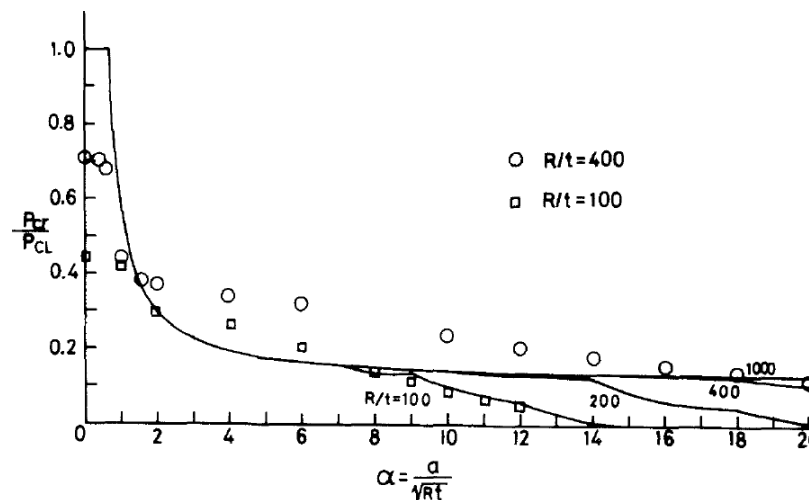


Figure 2.9: Nondimensional buckling loads as a function of α as well as R/t [24].

The most comprehensive experimental study on the buckling of cylindrical shells with cutouts was probably conducted by Jullien et al. [25] who tested more than 100 steel specimens. They investigated the effects of cutout size, shape, location, and number. The authors confirmed that the axial cutout dimension has a negligible influence on the buckling load and found that the circumferential opening size dominates the shell response. Both varying the cutout shape as well as the cutout location did not significantly alter the buckling load which suggests that the stress field above and below the shell is, if at all, of little importance. However, the buckling mode of rectangular and circular cutouts was different in so far as that the displacement pattern depicted in Figure 2.8 was skewed towards the corners of the rectangular opening. When multiple openings were cut into the specimens, the measured buckling loads were the same as for a single cutout of the same size if the displacement patterns around the openings did not interfere. When an interaction of the stress and displacement fields occurred, the buckling load dropped, but not as much as the sum of the individual cutout parameters would suggest. As a measure for the shell response, Jullien et al. proposed

$$\bar{r} = \frac{c}{\sqrt{Rt}} = \frac{R\Theta}{\sqrt{Rt}} \quad (2.24)$$

where Θ denotes the circumferential opening angle of the cutout and c is the circumferential cutout width regardless of the shape of the opening.

Aluminum shells with a single and two opposing openings were investigated by Zhao et al. [26]. They noted that the global buckling load of the specimens with two cutouts was not half as big as that of shells with only one opening where all cutouts have the same radius. Instead, the solid curve in Figure 2.9 represents the relation between the two configurations more accurately.

More recently, Bisagni [27] studied composite sandwich shells with a $[90/-19/19/\text{CORE}/90/-19/19]$ stacking sequence where the facesheets were manufactured from Hexcel IM7-8552 unidirectional (UD) carbon fiber pre-impregnated laminas. The core material was Evonik Rohacell WF200. A large cutout was drilled on one side of the cylindrical shell while two smaller ones were cut on the opposing side. Bisagni reported that the response of the shell was linear elastic until buckling occurred and measured a buckling load reduction of approximately 30% compared to a pristine specimen.

Shirkavand et al. [28] conducted experiments on seven composite cylindrical shells with cutouts. The specimens were made from E-glass fibers embedded in an epoxy resin where a $[90/\mp 23/90]$ layup was considered. The authors chose to plot the normalized buckling loads against the a/R instead of α . Hence, the effects of varying shell thicknesses could not be quantified. Anyhow, increasing the cutout size lead to lower buckling loads just like for isotropic cylindrical shells. Shirkavand et al. also measured linear elastic material behavior before buckling occurred.

Khakimova et al. [29] studied the buckling response CFRP cylindrical shells with a central circular cutout made from the Hexcel IM7-8552. A layup of $[\pm 34/0_2/\pm 53]$ was selected. The obtained load-displacement curves and the buckling load are plotted as a function of the cutout diameter (and therefore as a function of α since neither shell radius nor shell thickness were changed) in Figure 2.10. These graphs agree well with the observations reported by the aforementioned researchers.

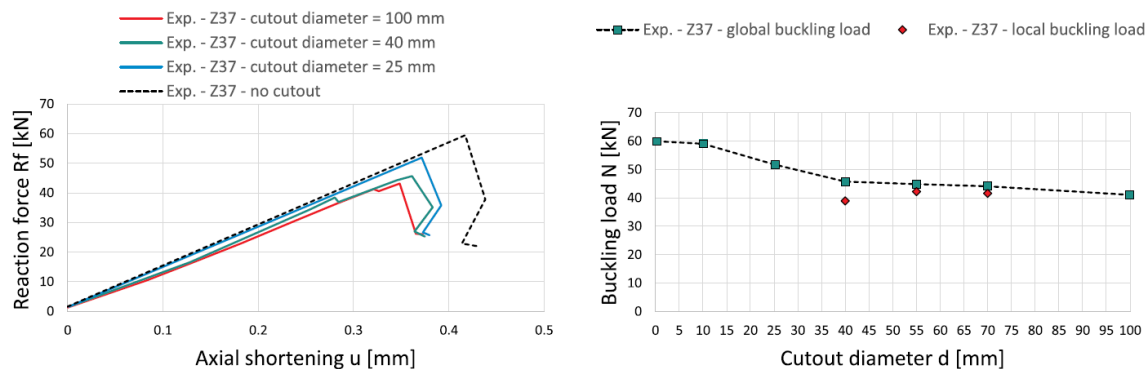


Figure 2.10: Load-displacement curves and measured buckling loads [29].

2.2.2. Reinforcements

Shells can be stiffened in many different ways. This subsection is limited to reinforcements where material is added in the vicinity of the opening, i.e. local reinforcements.

In his second referenced publication, Toda [24] defined the parameter

$$\gamma = \frac{W}{W_0} \quad (2.25)$$

to quantify the ratio between the mass of material added by any stiffeners W and the mass of the material removed by creating the cutout W_0 in an isotropic cylindrical shell. He suggested that for every α , there is an optimal ratio γ_{opt} for which a maximum buckling load is achieved given a single reinforcement design. Toda determined that this value of γ_{opt} decreases with increasing α . Furthermore, he reported that it was not possible to restore the full load-carrying capability of the pristine shell after introducing an opening in the structure. However, the larger the cutout, the more beneficial it was to add more local reinforcements

because the onset of the stable local buckling configuration was delayed. This also resulted in a higher global buckling load. Similar conclusions were drawn by Jiao et al. [30] who placed ringed stiffeners around circular cutouts in mild steel cylindrical shells.

Investigations on local orthotropic reinforcements were published by Hilburger in collaboration with Starnes [31], Hilburger together with Nemeth [32] and Hilburger by himself [33]. Shells manufactured from UD graphite-epoxy tape with stacking sequences of $[\mp 45/0_2]_s$, $[\mp 45/0/90]_s$, and $[\mp 45/90_2]_s$ were considered. Both pristine as well as cylindrical shells with rectangular cutouts of various sizes were tested. Regarding the buckling of the pristine specimens, Hilburger, Starnes, and Nemeth stated that instability is caused by a "non-linear coupling between localized destabilizing compressive axial and circumferential stress resultants and the radial deformations that occur in the shell near the cutout". Hence, by mitigating one or both reasons for buckling, it should be possible to delay its onset. The authors also noted that these large radial displacements resulted in a stress redistribution away from the opening reducing the effective load-carrying width of the shell and thus explaining a measured loss of axial stiffness.

Groups of 0° and 90° plies were placed along the cutout edges to stiffen the structure. The experimental buckling loads indicated that the thickness increase and consequently the added bending stiffness played the largest role in retarding buckling. However, the more plies were added, the less efficient each new one was. On average, 90° reinforcements were 4.5% more effective than 0° ones. Using additional 0° plies increased axial stress concentrations near the cutout while reducing circumferential ones. Stiffeners consisting out of 90° plies had the opposite effect. While the local buckling displacement pattern for rectangular cutouts was the same as previously described regardless of the number of added plies, the local buckling mode became unstable for some critical amount of reinforcing plies resulting in immediate global buckling. Hilburger and Nemeth noted that the shells seemed to become more imperfection-sensitive when thicker stiffeners were used which was also concluded by Toda during his experiments on isotropic reinforcements.

2.2.3. Imperfections

The buckling load of a cylindrical shell without cutouts is significantly reduced by initial geometric imperfections, especially by mid-surface variations. Hence, it can be expected that deviations from the ideal geometry and material properties have some influence on the response of shells that contain openings. Since it is impossible to create perfect structures as manufacturing processes are inherently flawed, examining imperfections based on experimental work only is a rather futile endeavor. Instead, the geometric and physical properties of real specimens are measured and compared with perfect computer models. Therefore, imperfections are predominantly discussed in Subsection 2.3.4.

Anyhow, investigations targeted specifically at determining the influence of initial imperfections on the buckling of circular cylindrical shells with cutouts were conducted by Starnes et al. [34]. Starnes and his co-authors studied composite shells made from graphite-epoxy prepregs which were modified by cutting rectangular openings into them. They considered mid-surface imperfections, wall-thickness variations, corresponding thickness-adjusted lamina properties, shell-end imperfections, as well as nonuniform loading. Taheri et al. [35] focused on mid-surface imperfections. They manufactured their asymmetric composite shell with a circular opening from E-glass fibers and an epoxy resin. In both cases, the shell edges were potted, and the testing machines were operated in displacement-control mode.

2.3. Numerical Work

The availability of analytical models is often restricted to relatively simple geometries and material combinations while experiments tend to be expensive in terms of both time and money. Complex structures are therefore often analyzed by employing approximate numerical methods, usually FEM. Insights obtained by applying this approach are covered on the following pages. First, the effects of cutout parameters are revisited and expanded upon. The next part deals with the influence of shell parameters such as shell length and wall thickness. Afterwards, numerical predictions of structures with reinforcements are evaluated. Finally, the relevance of initial geometric imperfections on the buckling of cylindrical shells with cutouts is outlined.

2.3.1. Cutout Parameters

Some of the first numerical work was conducted by Brogan and Almroth who, amongst others, developed early iterations of the computer code STAGS (SStructural Analysis of General Shells). Equipped with this tool, Almroth et al. [36] verified Tennyson's hypothesis that the curvature parameter α is not sufficient to quantify the structural response of cylindrical shells with large cutouts as shown in Figure 2.9. Furthermore, they noted

that the global buckling load of shells that contain circular and square cutouts is practically identical if the circumferential cutout dimension is the same.

Hilburger et al. reported on the structural response of quasi-isotropic cylindrical shells with rectangular cutouts subjected to axial loading and internal pressure in 1998 [20] as well as 1999 [37]. They modeled and analyzed the cylindrical shell with STAGS. Radial and circumferential displacements at and near the shell edges were restricted to simulate the potting encountered in real experiments. An arc-length solver was used which switched automatically between nonlinear static and nonlinear dynamic algorithms depending on the amount of kinetic energy present in the simulation.

The first local buckling mode for this structure is displayed in Figure 2.11. It features an elliptic displacement pattern where the major and minor semi-axes are oriented along the cutout diagonals. Buckling was caused by the previously mentioned interaction of destabilizing biaxial stresses as well as large radial displacements. The latter leads to a stress redistribution away from the cutout and a loss of axial stiffness. For small openings, the stress redistribution is enough of a disturbance to immediately trigger global buckling whereas larger openings feature stable local buckling modes. Adding internal pressure introduces tensile stresses which relieves the severity of the biaxial stress state and thus delays the onset of local buckling.

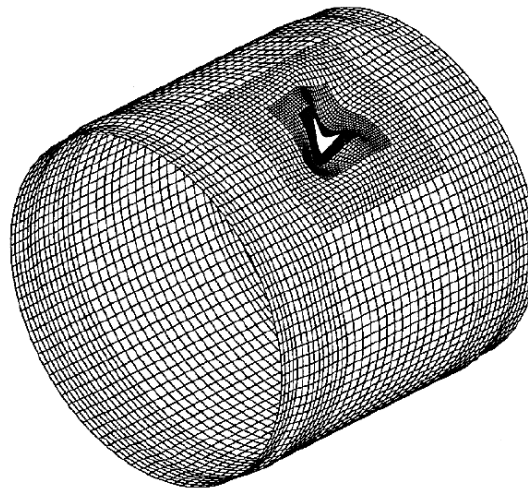


Figure 2.11: Displacement pattern at local buckling of a cylindrical shell with a rectangular cutout [37].

Shariati et al. [38] considered steel shells with elliptic cutouts and varied their position along the longitudinal shell axis. The authors included imperfections in the shape of the first three eigenmodes from a linear buckling analysis and the effects of plasticity in their models. Rigid plates were connected to the shell edges out of which only one could displace axially. The ensuing nonlinear static system of equations was solved with the Riks method in Abaqus.

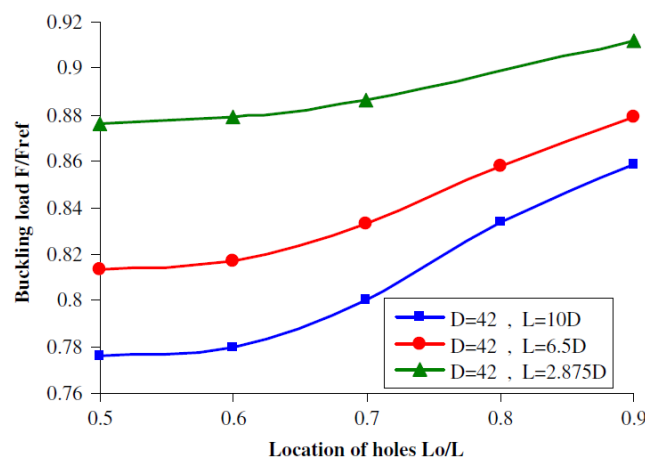


Figure 2.12: Normalized buckling load as a function of the relative cutout location [38].

Figure 2.12 indicates that there is some dependency of the buckling load on the cutout location. Moving the center of the opening towards one of the shell edges slightly increases the buckling load. When shells are longer, the benefit of changing the cutout location is more pronounced. However, the influence is relatively small which is probably the reason why Jullien et al. [25] stated that there was no effect of the cutout location on the buckling load during their experiments.

Shariati et al. argued that the positioning effect may be explained with the stress field in the cylindrical shell. The stress distribution just before, at, and after buckling is visualized in Figure 2.13 for two different cutout positions. It is clearly visible that the material below and above the cutout carries less load. This effect is apparently reduced once the cutout is moved towards one of the shell edges. Figure 2.13 also provides an intuitive explanation for the importance of the circumferential cutout size as the area of reduced stresses seems to be limited by the cutout width. A different reasoning for the trends in Figure 2.12 was proposed by Han et al. [39]. They noted that cutouts closer to the shell edges appeared to promote higher order buckling modes and therefore larger buckling loads.

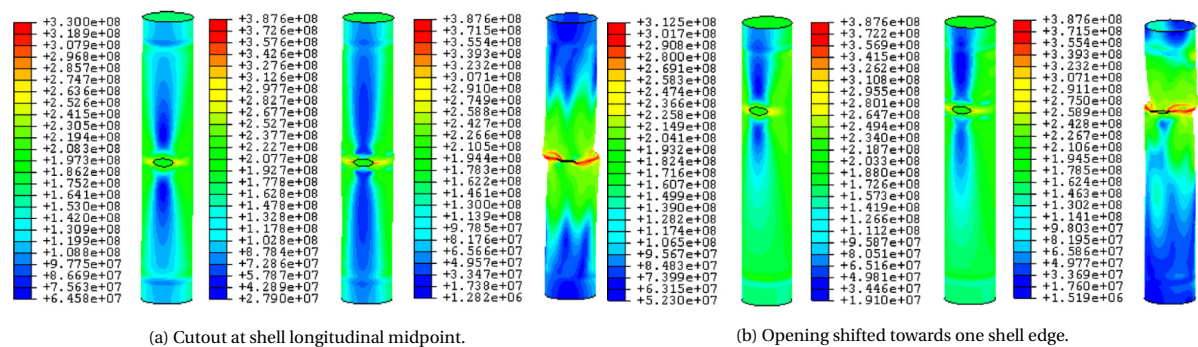


Figure 2.13: Prebuckling, buckling, and postbuckling von Mises stress distribution [38].

The results obtained by Shariati and his co-authors were confirmed by Salloomi et al. [40] who discussed the same problem. Furthermore, Shariati et al. conducted a small validation study which suggested that buckling loads and modes were predicted accurately, whereas the shell-end shortening at buckling was underestimated.

In addition to their own experiments, Shirkavand et al. [28] simulated the structural response of their specimens in Abaqus. Like Shariati et al., they introduced imperfections in the shape of eigenmodes from a linear buckling analysis. Results were obtained with a nonlinear dynamic implicit procedure. While the researchers reported their findings as a function of a/R , converting them to equivalent α values suggests that they are in agreement with the characteristic ranges identified by Starnes and Toda.

Likewise, Khakimova et al. [29] performed numerical analyses in conjunction with their experiments. The curves in Figure 2.14 were generated with Abaqus. The buckling load versus cutout diameter plot suggests that no local buckling event occurred for $d = 40$ mm, but the load-displacement graph on the left features a reaction force drop that is typical for this event. However, Khakimova et al. studied a $[\pm 34, 0_2, \pm 53]$ layup which might respond differently than isotropic or quasi-isotropic composite cylindrical shells.

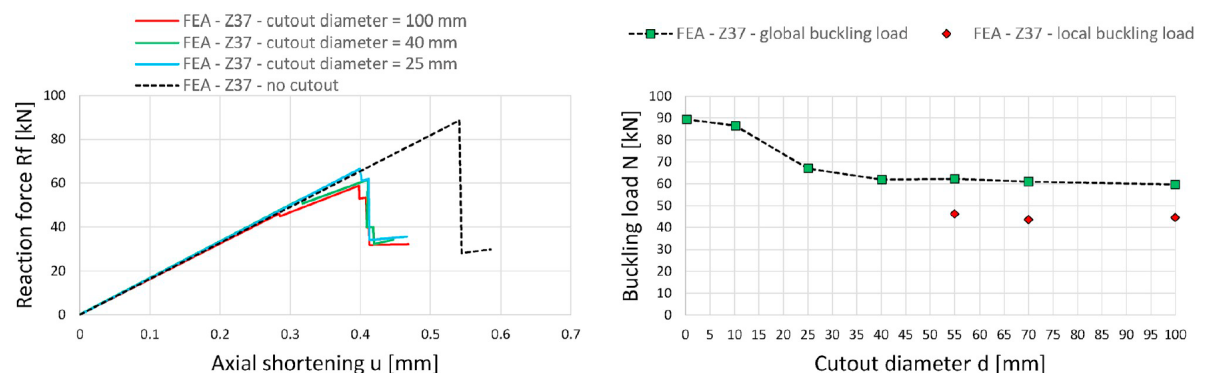


Figure 2.14: Numerically predicted local and global buckling loads as well as load-displacement curves [29].

Shariati et al. [41], Wang et al. [42], and Salloomi et al. [40] all investigated the influence of cutout shape and orientation on the buckling behavior of isotropic cylindrical shells. Shariati et al. employed a nonlinear static analysis with the Riks method in Abaqus, Wang et al. selected the Abaqus linear eigenvalue procedure, and Salloomi et al. resorted to a solver in Ansys. All parties reported that changing the cutout shape by varying the lengths of the ellipse semi-axes was more detrimental when it resulted in a larger circumferential cutout size. On the other hand, altering the axial dimension of the cutout had very little influence on the buckling load. Of course, this is expected based on previous discussions. Figure 2.15 was created by rotating the major and minor ellipse axes. Again, it can be seen increasing the circumferential cutout size decreases the obtainable maximum load as an angle of $\theta = 0^\circ$ corresponds to the major ellipse semi-axis being aligned with the longitudinal shell axis.

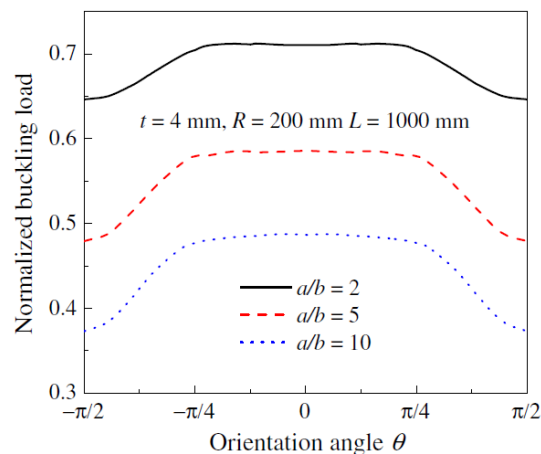


Figure 2.15: Dependency of the buckling load on the rotation angle of an elliptic cutout [42].

2.3.2. Shell Parameters

Jullien et al. [25] also modeled cylindrical shells with the FE code CASTEM 2000 in addition to their testing campaign. They accounted for nonlinear geometric and material effects. Figure 2.16 shows that the maximum buckling load approaches a lower bound when the cutout parameters are kept constant and the shell length-to-radius ratio L/R is increased.

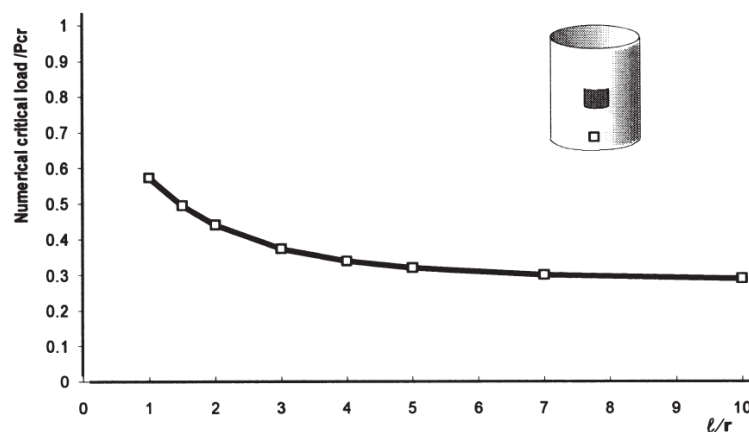


Figure 2.16: Asymptotic lower bound of the maximum buckling load [25].

In their first publication, Shariati et al. [38] stated that the buckling load of the structure is more sensitive to the cutout position if the shell is longer, see Figure 2.12. Their second paper [41] suggests that clamping both shell edges changes the curve in Figure 2.16 only in so far as that the asymptotic limit is reached later, i.e. for a higher value of L/R .

Han et al. [39] simulated the buckling behavior of isotropic cylindrical shells with rectangular cutouts that were either thin or moderately thick. They performed their numerical analyses with Ansys and considered large displacements as well as multi-linear isotropic hardening. The cylindrical shells were subjected to a uniform axial shell-end load. Otherwise, the DOFs of the shell edges were completely constrained.

Thin shells always buckled in the same way and at similar load levels regardless of whether plasticity was included in the analysis or not. On the other hand, thicker shells yielded first, causing a chain reaction of local and then global buckling. The global buckling configuration was more reminiscent of column buckling than of the displacement pattern observed for thin shells. The fact that thick shells tend to yield before an instability occurs is probably one of the reasons Montague et al. [23] reported the behavior that is described in Subsection 2.2.1.

2.3.3. Reinforcements

Relatively early, Brogan and Almroth [43] discussed the effects of placing two isotropic stringers parallel to the vertical edges of a rectangular cutout. Regardless of the geometric proportions they chose, they were not able to reach the buckling load of an equivalent cylindrical shell without a cutout. Like Toda, they found that adding stiffener mass was only beneficial up to a certain threshold ratio of γ .

Later, Almroth et al. [44] investigated the effects of an isotropic rectangular frame positioned around the cutout. Surprisingly, the reinforced structure performed worse than an unreinforced one. The authors attributed this to stress concentrations caused by the additional frame stiffness. Despite obtaining unfavorable results, Almroth et al. suggested that reinforcements should be optimized for maximum bending stiffness to reduce the large radial displacements that occur at local buckling.

Shi et al. [45] compared seven different isotropic reinforcement configurations around circular and rectangular cutouts in composite shells with quasi-isotropic layups. The FE models were created in Nastran and the analysis procedure accounted for large displacements. It was determined that stiffener designs which redirect stresses smoothly around the cutout are preferable to those that promote unevenly distributed stresses. Since the stress fields around circular and rectangular openings are different, distinct reinforcement configurations are required. Again, it was suggested that a higher bending stiffness delays the onset of local buckling and therefore increases the maximum sustainable load carried by the structure.

Jiao et al. [30] reproduced their experiments in Abaqus where they considered initial geometric imperfections measured during testing. A linear buckling analysis was used to determine an optimal ringed stiffener thickness which approximately corresponded to a weight ratio of $\gamma = 1$.

The publications by Hilburger, Starnes, and Nemeth [31–33] also discuss numerical analyses of the tested laminates. The models were set up similar to the already presented work by Hilburger [37]. Initial geometric imperfections were not considered. The data points in Figure 2.17 illustrate the conclusions drawn from the experiments, i.e. that additional material is less effective in terms of increasing the buckling load and that 90° ply reinforcements are generally more efficient than 0° ones.

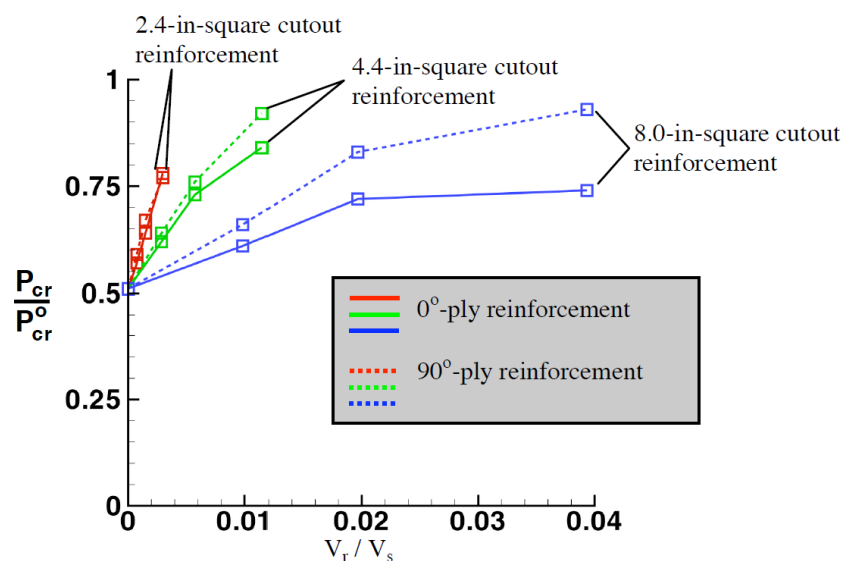


Figure 2.17: Local orthotropic reinforcements around rectangular cutouts [31].

2.3.4. Imperfections

Starnes, Hilburger, and Nemeth [34] conducted an extensive examination of the influence of various imperfections on the buckling behavior of composite cylindrical shells with a rectangular cutout by comparing experimental measurements with numerical predictions from STAGS. The solver was modified such that a nonlinear static response was considered when neither instabilities nor modal interactions were detected. When zero tangent stiffnesses were encountered, an arc-length algorithm was used instead of the standard NR method.

By comparing the coordinates of the inner and outer shell walls, mid-surface imperfections were estimated and linearly interpolated so that nodes in the FE model could be moved accordingly. Wall thickness variations were furthermore used to adjust the lamina properties based on the rule of mixtures assuming a constant fiber volume fraction. Finally, the shell edge nodes were modified to represent the effects of nonuniform loading during testing.

The results of various linear and nonlinear analyses considering different combinations of imperfections as well as experimentally measured buckling loads are summarized in Table 2.1. Specimens C1 to C3 are reference shells without cutouts. The effects of mid-surface imperfections on the buckling load are more pronounced in these shells than in the specimens that contain openings, i.e. C4 to C6. For the latter group, the authors concluded that linear buckling analyses provide reasonable estimates when knockdown factors are applied to account for imperfections. The specimens did not appear to be disproportionately sensitive to a certain kind of imperfection with the exception of shell C4. The discrepancy between the numerical results and the experimental measurements was explained with material failure that had not been modeled.

No.	Bifurcation Buckling [kN]	Nonlinear [kN]					Experiment [kN]
		Without Imperfections	Mid-Surface Imperfections	Thickness Variations	Nonuniform Loading	All	
C1	148.8	142.7	140.5	142.3	141.5	136.5	123.6
C2	215.4	200.3	182.6	199.3	195.9	184.9	152.0
C3	189.6	180.3	170.9	180.4	179.5	170.0	142.0
C4	108.9	105.4	108.9	106.1	74.9	75.3	74.8
C5	118.3	106.4	101.9	108.1	103.8	102.7	91.2
C6	106.8	105.4	106.9	105.4	105.4	105.0	95.7

Table 2.1: Buckling loads predicted for various imperfections and measured test results [34].

The idealized shells featured two diamond-shaped buckles with inversion symmetry around the cutout center. Naturally, the presence of imperfections removed this symmetry. For the real structure, a single elliptic buckle on one side of the cutout was observed. Starnes and his co-authors noted that a stable local buckling mode was encountered for the imperfect cylindrical shells which changed shape multiple times. Each buckling mode jump was accompanied by larger radial displacements that resulted in a loss of axial stiffness with every jump.

Jullien et al. [25] provided several plots in which they showed that the obtainable buckling load of isotropic cylindrical shells with cutouts greatly depends on the boundary conditions. If the loaded shell edge was allowed to deform freely, the buckling load dropped considerably in comparison with a specimen where a uniform displacement was prescribed. Starnes [18] had proposed that initial geometric imperfections dominate the shell response for very small openings as the buckling load is independent of the cutout size in this domain. Jullien et al. suggested that the threshold for this behavior was reached when the cutout dimensions were equal to one half-wave of the Yoshimura buckling pattern. Brunesi et al. [46] reproduced parts of the study by Jullien et al. in Nastran NX 10 and verified the numerical results.

Tafreshi [47] built up on Hilburger's [37] work and included imperfections in the shape of eigenmodes from a linear buckling analysis in Abaqus. The nonlinear static solver computed that this did not lower the buckling load significantly which was explained with the presence of sufficiently large cutouts.

Schenk et al. [48] introduced random boundary conditions and imperfections in isotropic shells using the theory of random fields. They performed linear and nonlinear buckling analyses in STAGS where they noticed that the results from linear bifurcation analyses were much lower than those of nonlinear ones. This was justified with the fact that the linear analysis could not account for the stress redistribution caused by the large radial displacements and therefore overestimated stresses which consequently leads to an underestimation

of the linearized buckling load.

Orifici and Bisagni [49] used Abaqus to apply the concept of a single perturbation load to quasi-isotropic and cross-ply laminates as well as to thin and thick sandwich composites. The shells were subjected to the transverse perturbation force in a first load step which simulated initial geometric imperfections. A subsequent nonlinear dynamic step provided an estimate for the buckling load. When large cutouts were considered, the authors could not detect any influence of the perturbation force on the buckling load and concluded that the opening itself could be considered as a dominant imperfection. In contrast, there was some dependency of the buckling load on the perturbation load when smaller cutouts were modeled which lead Orifici and Bisagni to believe that some imperfection interaction occurred. Arbelo et al. [50] published results that agree well with Orifici and Bisagni.

Alfano and Bisagni [51] incorporated chaos theory in an imperfection sensitivity study on composite cylindrical shells with and without cutouts. By defining control parameters related to mid-surface imperfections, an integrity measure was calculated. Simulations of the structural response were performed with a nonlinear dynamic procedure in Abaqus. A reduction of the integrity measure characterized the onset of buckling. When comparing shells with and without cutouts, this integrity measure eroded earlier for pristine shells, thus verifying that cylindrical shells with cutouts are less sensitive to mid-surface imperfections.

Taheri et al. [35] used a probability density function to determine which imperfections in the shape of eigenmodes were most likely to be present in a real structure. They incorporated them in their Abaqus models and compared the predictions of the nonlinear buckling analysis with one where imperfections were simulated with a single perturbation load. Overall, the differences between the two approaches were negligible. The concept of a probability density function was adopted by Shirkavand et al. [28] who estimated buckling loads for different a/R ratios. Like other researchers, they observed that the effects of initial geometric imperfections are reduced with increasing cutout size.

In the same year, Alfano and Bisagni [52] employed a probabilistic approach and increased the number of considered imperfections compared to their previous investigation. Namely, they incorporated longitudinal stiffness variations, ply misalignment, and shell-end imperfections in their study. Latin Hypercube sampling in conjunction with the Strength-Stress Interference method was used to check representative data points with an Abaqus nonlinear dynamic buckling analysis. Again, imperfections played less of a role for shells with cutouts compared to pristine reference shells.

Khakimova et al. [29] modified their perfect shell models with imperfection data measured during their experiments. Considering mid-surface imperfections and thickness-adjusted lamina properties, they reran their nonlinear static analyses in Abaqus. Figure 2.18 illustrates how the buckling loads change when different shell configurations and cutout sizes are considered. Accounting for imperfections clearly reduces the discrepancy between perfect shells and experiments. However, the gap is not fully closed suggesting that some disregarded imperfection types or material failure could provide alternative explanations for the difference between theory and practice. Finally, Khakimova et al. identified ranges of the curvature parameter α where the characteristic shell response defined by Starnes and Toda can be observed. Of course, the limited number of data points makes it difficult to determine threshold values. Hence, the exact boundary values indicated in Figure 2.18 are debatable.

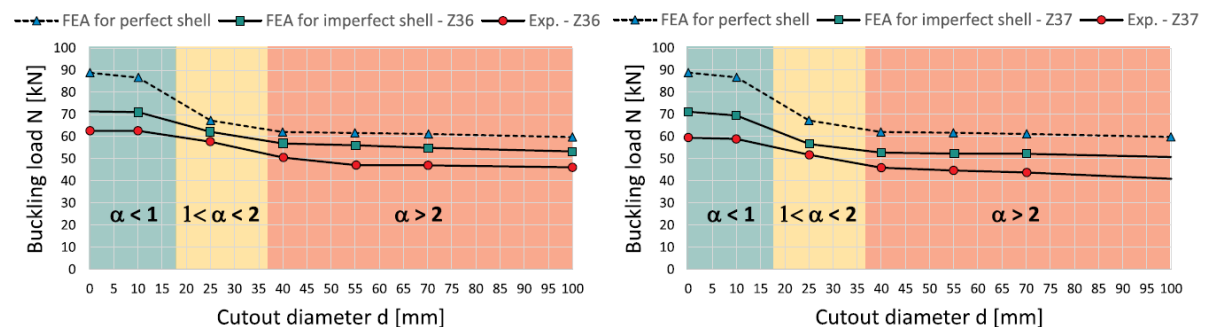


Figure 2.18: Buckling loads as a function of cutout diameter for two different shell specimens [29].

3

Theoretical Prerequisites

The analysis described in Chapter 4 necessitates prior knowledge of various concepts and theories. These are revisited on the following pages. First, general shell theory is presented in Section 3.1 and, by adding further assumptions, adjusted for shallow shells in Section 3.2. Section 3.3 discusses the classical lamination theory to incorporate composite laminates. Subsequently, energy methods are introduced to quantify the structural response in Sections 3.4 and 3.5. The Ritz method as an approximate solution procedure is described in Section 3.6. Afterwards, the compatibility equation and the Airy stress function are evaluated as tools to reduce the number of variables in the analysis. Some aspects of coordinate transformations are reviewed in Section 3.9. Finally, Section 3.10 examines the derivation of buckling stresses of pristine cylindrical shells as reference values.

3.1. General Shell Theory

A shell is a body that is bounded by two curved surfaces where the distance between its boundaries, the thickness t , is small in relation to its other dimensions a and b . Curvature allows shells to carry loads efficiently because their stretching and bending response is coupled. Figure 3.1 illustrates a general shell where the displacements u, v, w correspond to the curvilinear coordinates x, y, z . The radii R_x and R_y are equal to the inverse of the curvature with respect to the corresponding axis.

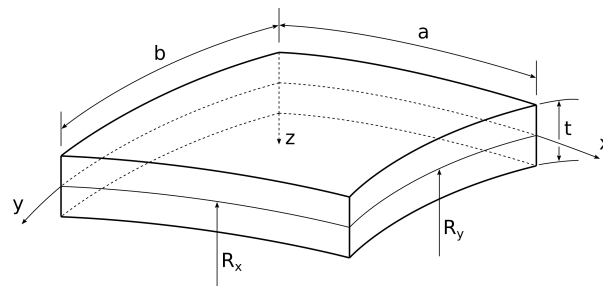


Figure 3.1: A general shell with a right-handed curvilinear coordinate system.

An early mathematical description of shells was derived by Love [53] who added the assumptions of thinness and small deflections to Kirchhoff's plate bending theory. The combined set of their premises is known as the Kirchhoff-Love hypothesis which entails four main considerations:

1. Lines normal to shell's middle surface remain straight, orthogonal and do not extend after deformation.
2. The normal stress τ_{zz} is negligible compared to the other stress components.
3. Shells are thin, i.e. $t \ll a, b$.
4. Displacements are small compared to the shell thickness.

The first two assumptions constitute the so-called Kirchhoff hypothesis. From point 1 it follows that out-of-plane elongations and shortenings cannot occur which implies a state of plane strain.

Combining assumptions 1 and 2 suggests a state of plane stress. This introduces two formal contradictions. Hooke's law for isotropic materials states that shear stresses normal to the shell mid-surface are solely caused by out-of-plane shear strains. Consequently, the shear stresses τ_{yz} and τ_{xz} must be equal to zero. However, the corresponding stress resultants Q_x and Q_y are required for the force equilibrium of a shell differential element. Additionally, plane strain and plane stress cannot exist simultaneously unless the material's Poisson's ratio is equal to zero which is generally not the case. Nonetheless, the Kirchhoff hypothesis manages to accurately predict the structural response of both plates and shells. In fact, Novozhilov [54] showed that the error introduced by Kirchhoff's assumptions is of the order t/R_i ($i = x, y$) relative to unity.

Various rules of thumb are used to estimate whether the thinness criterion 3 is fulfilled. A popular one is given by Ventsel and Krauthammer [55] on page 294.

$$\max\left(\frac{t}{R_i}\right) \leq \frac{1}{20} \quad (3.1)$$

From assumption 4 it follows that all nonlinear strain-displacement relations must vanish since first-order derivatives are much larger than higher order ones.

The linear strain tensor components ε_{ij} in equation (3.2) are then obtained for the coordinate system illustrated in Figure 3.1. A detailed derivation is available in Chapters 11 and 12 of reference [55].

$$\begin{aligned} \varepsilon_{xx} &= \frac{1}{1 - \frac{z}{R_x}} \left(\varepsilon_{xx}^0 + z\kappa_{xx} \right) \\ \varepsilon_{yy} &= \frac{1}{1 - \frac{z}{R_y}} \left(\varepsilon_{yy}^0 + z\kappa_{yy} \right) \\ \varepsilon_{xy} &= \frac{1}{\left(1 - \frac{z}{R_x}\right)\left(1 - \frac{z}{R_y}\right)} \left\{ \varepsilon_{xy}^0 \left(1 - \frac{z^2}{R_x R_y}\right) + z\kappa_{xy} \left[1 - \frac{z}{2} \left(\frac{1}{R_x} + \frac{1}{R_y}\right)\right] \right\} \end{aligned} \quad (3.2)$$

The superscript 0 denotes mid-plane strains while κ indicates the curvature contribution. A and B symbolize the Lamé parameters which relate the change in arc length on the shell surface to the variation of the corresponding curvilinear coordinate.

$$\begin{aligned} \varepsilon_{xx}^0 &= \frac{1}{A} \frac{\partial u}{\partial x} + \frac{1}{AB} \frac{\partial A}{\partial y} v - \frac{w}{R_x} \\ \varepsilon_{yy}^0 &= \frac{1}{B} \frac{\partial v}{\partial y} + \frac{1}{AB} \frac{\partial B}{\partial x} u - \frac{w}{R_y} \\ \varepsilon_{xy}^0 &= \frac{1}{2} \left[\frac{B}{A} \frac{\partial}{\partial x} \left(\frac{v}{B} \right) + \frac{A}{B} \frac{\partial}{\partial y} \left(\frac{u}{A} \right) \right] \\ \kappa_{xx} &= - \left[\frac{1}{A} \frac{\partial}{\partial x} \left(\frac{u}{R_x} + \frac{1}{A} \frac{\partial w}{\partial x} \right) + \frac{1}{AB} \frac{\partial A}{\partial y} \left(\frac{v}{R_y} + \frac{1}{B} \frac{\partial w}{\partial y} \right) \right] \\ \kappa_{yy} &= - \left[\frac{1}{B} \frac{\partial}{\partial y} \left(\frac{v}{R_y} + \frac{1}{B} \frac{\partial w}{\partial y} \right) + \frac{1}{AB} \frac{\partial B}{\partial x} \left(\frac{u}{R_x} + \frac{1}{A} \frac{\partial w}{\partial x} \right) \right] \\ \kappa_{xy} &= - \left[\frac{1}{AB} \left(-\frac{1}{A} \frac{\partial A}{\partial y} \frac{\partial w}{\partial x} - \frac{1}{B} \frac{\partial B}{\partial x} \frac{\partial w}{\partial y} + \frac{\partial^2 w}{\partial x \partial y} \right) + \frac{1}{R_x} \frac{A}{B} \frac{\partial}{\partial y} \left(\frac{u}{A} \right) + \frac{1}{R_y} \frac{B}{A} \frac{\partial}{\partial x} \left(\frac{v}{B} \right) \right] \end{aligned} \quad (3.3)$$

3.2. Shallow Shell Theory

Equations (3.2) and (3.3) are relatively complex and therefore difficult to implement in a buckling analysis. Donnell [56], Mushtari [57], and Vlasov [58] were able to simplify the strain-displacement relations by incorporating two additional assumptions.

1. The transverse shear forces Q_x and Q_y have a negligible influence on the in-plane equilibrium.
2. The out-of-plane displacement w dominates the shell bending response.

It is interesting to note that the first assumption takes care of one of the contradictions from the Kirchhoff hypothesis. Anyhow, restricting the permissible shell response means that only shells with certain properties meet the new requirements. Novozhilov [54] identified these as shells with rapidly varying stress gradients in the direction of at least one in-plane coordinate as well as the so-called shallow shells.

Ventsel and Krauthammer [55] provide the inequalities

$$\left(\frac{\partial z}{\partial x}\right)^2 < 0.05 \quad \text{and} \quad \left(\frac{\partial z}{\partial y}\right)^2 < 0.05 \quad (3.4)$$

to determine whether a given thin shell also fulfills the shallowness criterion. The numerical values in equation (3.4) correspond to a maximum angle of 13° between the x - y -plane and a plane tangent to the shell mid-surface. Most shells used in modern designs can be idealized as thin and shallow. Unfortunately, the term "shallow" is frequently omitted when talking about this type of shell even though the structural response of shells and shallow shells is not necessarily identical.

It can be shown that the Lamé parameters of shallow shells are reasonably well approximated by $A = B = 1$. The same result is also obtained for flat plates. Considering a circular cylindrical shell where $R_x = \infty$ and $R_y = R$ as depicted in Figure 3.2, equations (3.2) and (3.3) simplify considerably, see (3.5) and (3.6). Due to the thinness constraint, the z/R_i terms are discarded. Furthermore, all partial derivatives of A and B disappear and the curvature expressions become a function of w only.

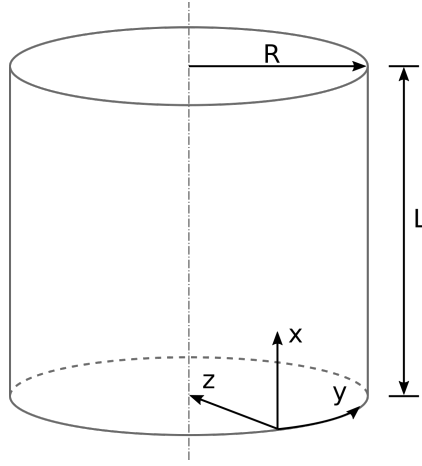


Figure 3.2: A circular cylindrical shell with a curvilinear coordinate system.

The out-of-plane displacements are not small when the phenomenon of buckling is studied. This violates one of the assumptions introduced by Love. Hence, nonlinear strain terms are added back into the strain expressions. Starting from the general nonlinear Green strains for shallow shells, the squares of certain rotational terms may be dismissed when requiring the out-of-plane deflection w to be bounded by $|w| \leq 5t$. The resulting nonlinear strain-displacement relations for thin, shallow shells are then given by equations (3.5) and (3.6). They are identical with the nonlinear strains for the flat plate except for the inclusion of a w/R term in ε_{yy} . A comprehensive discussion of this derivation is given in Subsection 18.2.2 of reference [55].

$$\begin{aligned} \varepsilon_{xx} &= \varepsilon_{xx}^0 + z\kappa_{xx} \\ \varepsilon_{yy} &= \varepsilon_{yy}^0 + z\kappa_{yy} \\ \varepsilon_{xy} &= \varepsilon_{xy}^0 + z\kappa_{xy} \end{aligned} \quad (3.5)$$

$$\begin{aligned} \varepsilon_{xx}^0 &= \frac{\partial u}{\partial x} + \frac{1}{2} \left(\frac{\partial w}{\partial x} \right)^2 & \kappa_{xx} &= -\frac{\partial^2 w}{\partial x^2} \\ \varepsilon_{yy}^0 &= \frac{\partial v}{\partial y} - \frac{w}{R} + \frac{1}{2} \left(\frac{\partial w}{\partial y} \right)^2 & \kappa_{yy} &= -\frac{\partial^2 w}{\partial y^2} \\ \varepsilon_{xy}^0 &= \frac{1}{2} \left(\frac{\partial u}{\partial y} + \frac{\partial v}{\partial x} + \frac{\partial w}{\partial x} \frac{\partial w}{\partial y} \right) & \kappa_{xy} &= -\frac{\partial^2 w}{\partial x \partial y} \end{aligned} \quad (3.6)$$

3.3. Classical Lamination Theory

An arbitrary composite material is unlikely to feature any symmetries. Therefore, it usually classifies as an anisotropic body, i.e. there is a directional dependency between the stresses τ_{ij} and the strains ε_{ij} . As long as the material is loaded in the elastic domain, the generalized Hooke's law for this constitutive model is given by equation (3.7) in Voigt notation. Here, the stiffness tensor \mathbf{C} is symmetric so that $C_{ij} = C_{ji}$ when it is written in matrix form. The number of independent elastic constants is 21.

$$\begin{Bmatrix} \tau_{xx} \\ \tau_{yy} \\ \tau_{zz} \\ \tau_{yz} \\ \tau_{xz} \\ \tau_{xy} \end{Bmatrix} = \begin{bmatrix} C_{11} & C_{12} & C_{13} & C_{14} & C_{15} & C_{16} \\ C_{21} & C_{22} & C_{23} & C_{24} & C_{25} & C_{26} \\ C_{31} & C_{32} & C_{33} & C_{34} & C_{35} & C_{36} \\ C_{41} & C_{42} & C_{43} & C_{44} & C_{45} & C_{46} \\ C_{51} & C_{52} & C_{53} & C_{54} & C_{55} & C_{56} \\ C_{61} & C_{62} & C_{63} & C_{64} & C_{65} & C_{66} \end{bmatrix} \begin{Bmatrix} \varepsilon_{xx} \\ \varepsilon_{yy} \\ \varepsilon_{zz} \\ 2\varepsilon_{yz} \\ 2\varepsilon_{xz} \\ 2\varepsilon_{xy} \end{Bmatrix} \quad (3.7)$$

Orthotropic materials have three symmetry planes that are all perpendicular to one another. A consequence of this symmetry is that there is no coupling between shear strains and normal stresses. Also, shear strains in one plane do not cause shear stresses in any other plane. The number of independent elastic constants reduces to 9 and the new stiffness tensor is formulated as shown in equation (3.8).

$$\begin{Bmatrix} \tau_{xx} \\ \tau_{yy} \\ \tau_{zz} \\ \tau_{yz} \\ \tau_{xz} \\ \tau_{xy} \end{Bmatrix} = \begin{bmatrix} C_{11} & C_{12} & C_{13} & 0 & 0 & 0 \\ C_{12} & C_{22} & C_{23} & 0 & 0 & 0 \\ C_{13} & C_{23} & C_{33} & 0 & 0 & 0 \\ 0 & 0 & 0 & C_{44} & 0 & 0 \\ 0 & 0 & 0 & 0 & C_{55} & 0 \\ 0 & 0 & 0 & 0 & 0 & C_{66} \end{bmatrix} \begin{Bmatrix} \varepsilon_{xx} \\ \varepsilon_{yy} \\ \varepsilon_{zz} \\ 2\varepsilon_{yz} \\ 2\varepsilon_{xz} \\ 2\varepsilon_{xy} \end{Bmatrix} \quad (3.8)$$

Of course, strains can also be expressed as a function of stresses. The inverse of the stiffness tensor \mathbf{C} is the compliance tensor \mathbf{S} which is specified in equation (3.9) for an orthotropic material.

$$\begin{Bmatrix} \varepsilon_{xx} \\ \varepsilon_{yy} \\ \varepsilon_{zz} \\ 2\varepsilon_{yz} \\ 2\varepsilon_{xz} \\ 2\varepsilon_{xy} \end{Bmatrix} = \begin{bmatrix} S_{11} & S_{12} & S_{13} & 0 & 0 & 0 \\ S_{12} & S_{22} & S_{23} & 0 & 0 & 0 \\ S_{13} & S_{23} & S_{33} & 0 & 0 & 0 \\ 0 & 0 & 0 & S_{44} & 0 & 0 \\ 0 & 0 & 0 & 0 & S_{55} & 0 \\ 0 & 0 & 0 & 0 & 0 & S_{66} \end{bmatrix} \begin{Bmatrix} \tau_{xx} \\ \tau_{yy} \\ \tau_{zz} \\ \tau_{yz} \\ \tau_{xz} \\ \tau_{xy} \end{Bmatrix} \quad (3.9)$$

Composite plies may be idealized as orthotropic materials. As mentioned before, the Kirchhoff-Love hypothesis assumes a state of plane stress in the shell. Hence, equation (3.8) reduces to (3.10) assuming that the fiber orientation in the lamina coincides with the x -axis in Figure 3.2. The resulting stiffness matrix is often referred to as the \mathbf{Q} matrix with components Q_{ij} . If the coordinate axis and the fiber orientation do not align, the entries Q_{xs} and Q_{ys} become nonzero. Equation (3.10) is also valid for local lamina coordinate systems. In such a case it is common to replace the indices x, y, s with 1, 2, 6 to denote the local reference frame.

$$\begin{Bmatrix} \tau_{xx} \\ \tau_{yy} \\ \tau_{xy} \end{Bmatrix} = \begin{bmatrix} Q_{xx} & Q_{xy} & 0 \\ Q_{xy} & Q_{yy} & 0 \\ 0 & 0 & Q_{ss} \end{bmatrix} \begin{Bmatrix} \varepsilon_{xx} \\ \varepsilon_{yy} \\ 2\varepsilon_{xy} \end{Bmatrix} \quad (3.10)$$

Equation (3.11) may be used to calculate the components of \mathbf{Q} . E_i is the Young's modulus along the direction i , G_{ij} represents the shear modulus in the ij -plane, and ν_{ij} refers to the Poisson's ratio as the quotient of the contraction along the j -axis relative to the extension in i -direction.

$$\begin{aligned} Q_{xx} &= \frac{E_x}{(1 - \nu_{xy}\nu_{yx})} & Q_{xy} &= \frac{\nu_{xy}E_y}{(1 - \nu_{xy}\nu_{yx})} \\ Q_{yy} &= \frac{E_y}{(1 - \nu_{xy}\nu_{yx})} & Q_{ss} &= G_{xy} \end{aligned} \quad (3.11)$$

If the local and global reference frames do not align, the transformation matrix \mathbf{T} as defined in (3.12) may be used to rotate \mathbf{Q} to the global coordinate system in which case it is denoted as $\bar{\mathbf{Q}}$. \mathbf{T} in equation (3.13) is given for a conventional orthogonal coordinate system, e.g. the one depicted in Figure 2.5.

$$\bar{\mathbf{Q}} = \mathbf{T}^T \mathbf{Q} \mathbf{T} \quad (3.12)$$

$$\mathbf{T} = \begin{bmatrix} \cos^2\theta & \sin^2\theta & \sin\theta\cos\theta \\ \sin^2\theta & \cos^2\theta & -\sin\theta\cos\theta \\ -2\sin\theta\cos\theta & 2\sin\theta\cos\theta & \cos^2\theta - \sin^2\theta \end{bmatrix} \quad (3.13)$$

The section forces and moments, or stress resultants and couples, N , Q , and M are helpful to describe the structural response of a laminate. They are illustrated in Figure 3.3 and are defined in equation (3.14) for a cylindrical shell.

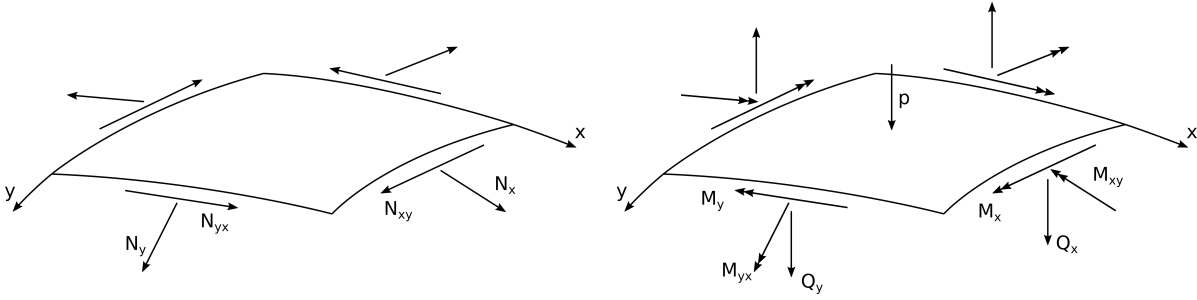


Figure 3.3: Stress resultants and couples acting on an infinitesimal shell element.

$$\begin{aligned} N_x &= \int_{-t/2}^{+t/2} \left[\tau_{xx} \left(1 - \frac{z}{R} \right) \right] dz & N_y &= \int_{-t/2}^{+t/2} \left[\tau_{yy} \right] dz \\ N_{xy} &= \int_{-t/2}^{+t/2} \left[\tau_{xy} \left(1 - \frac{z}{R} \right) \right] dz & N_{yx} &= \int_{-t/2}^{+t/2} \left[\tau_{yx} \right] dz \\ Q_x &= \int_{-t/2}^{+t/2} \left[\tau_{xz} \left(1 - \frac{z}{R} \right) \right] dz & Q_y &= \int_{-t/2}^{+t/2} \left[\tau_{yz} \right] dz \\ M_x &= \int_{-t/2}^{+t/2} \left[\tau_{xx} z \left(1 - \frac{z}{R} \right) \right] dz & M_y &= \int_{-t/2}^{+t/2} \left[\tau_{yy} z \right] dz \\ M_{xy} &= \int_{-t/2}^{+t/2} \left[\tau_{xy} z \left(1 - \frac{z}{R} \right) \right] dz & M_{yx} &= \int_{-t/2}^{+t/2} \left[\tau_{yx} z \right] dz \end{aligned} \quad (3.14)$$

Even though the stress tensor is symmetric, the shear forces N_{xy} and N_{yx} as well as the twisting moments M_{xy} and M_{yx} are not necessarily of equal magnitude because of the dependency on R . However, as stated previously, the z/R terms are negligible if the shell is thin. Hence, a distinction between the two shear forces and twisting moments is not required. With this in mind, the laminate is characterized by first rotating individual plies in the direction of the global coordinate system with equation (3.12), then substituting the stress-strain relations (3.10), subsequently the strain-displacement relations (3.5) and (3.6), integrating the relevant section forces and moments from (3.14) over the thickness, and finally summing everything up to arrive at the well-known **ABD** matrix presented in equation (3.15).

$$\begin{Bmatrix} N_x \\ N_y \\ N_{xy} \\ M_x \\ M_y \\ M_{xy} \end{Bmatrix} = \begin{bmatrix} A_{11} & A_{12} & A_{16} & B_{11} & B_{12} & B_{16} \\ A_{12} & A_{22} & A_{26} & B_{12} & B_{22} & B_{26} \\ A_{16} & A_{26} & A_{66} & B_{16} & B_{26} & B_{66} \\ B_{11} & B_{12} & B_{16} & D_{11} & D_{12} & D_{16} \\ B_{12} & B_{22} & B_{26} & D_{12} & D_{22} & D_{26} \\ B_{16} & B_{26} & B_{66} & D_{16} & D_{26} & D_{66} \end{bmatrix} \begin{Bmatrix} \varepsilon_{xx}^0 \\ \varepsilon_{yy}^0 \\ 2\varepsilon_{xy}^0 \\ \kappa_{xx} \\ \kappa_{yy} \\ 2\kappa_{xy} \end{Bmatrix} \quad (3.15)$$

In a more compact form, one may also write

$$\begin{bmatrix} \mathbf{A} & \mathbf{B} \\ \mathbf{B} & \mathbf{D} \end{bmatrix} = \begin{bmatrix} A_{11} & A_{12} & A_{16} & B_{11} & B_{12} & B_{16} \\ A_{12} & A_{22} & A_{26} & B_{12} & B_{22} & B_{26} \\ A_{16} & A_{26} & A_{66} & B_{16} & B_{26} & B_{66} \\ B_{11} & B_{12} & B_{16} & D_{11} & D_{12} & D_{16} \\ B_{12} & B_{22} & B_{26} & D_{12} & D_{22} & D_{26} \\ B_{16} & B_{26} & B_{66} & D_{16} & D_{26} & D_{66} \end{bmatrix} \quad (3.16)$$

\mathbf{A} , \mathbf{B} , and \mathbf{D} , each with elements A_{ij} , B_{ij} , and D_{ij} , refer to the extensional, coupling, and flexural stiffness matrices which are readily calculated as

$$\begin{aligned} \mathbf{A} &= \sum_{n=1}^N \bar{\mathbf{Q}}_n (z_n - z_{n-1}) \\ \mathbf{B} &= \sum_{n=1}^N \bar{\mathbf{Q}}_n \frac{1}{2} (z_n^2 - z_{n-1}^2) \\ \mathbf{D} &= \sum_{n=1}^N \bar{\mathbf{Q}}_n \frac{1}{3} (z_n^3 - z_{n-1}^3) \end{aligned} \quad (3.17)$$

where n indicates the lamina number and z_n refers to the corresponding ply boundary coordinates.

Strains may also be expressed in terms of section forces and moments. The inverse of the \mathbf{ABD} matrix is the \mathbf{abd} matrix given in equation (3.18) which may be interpreted as a compliance matrix with elements a_{ij} , b_{ij} , and d_{ij} .

$$\begin{Bmatrix} \varepsilon_{xx}^0 \\ \varepsilon_{yy}^0 \\ 2\varepsilon_{xy}^0 \\ \kappa_{xx} \\ \kappa_{yy} \\ 2\kappa_{xy} \end{Bmatrix} = \begin{bmatrix} a_{11} & a_{12} & a_{16} & b_{11} & b_{12} & b_{16} \\ a_{12} & a_{22} & a_{26} & b_{12} & b_{22} & b_{26} \\ a_{16} & a_{26} & a_{66} & b_{16} & b_{26} & b_{66} \\ b_{11} & b_{12} & b_{16} & d_{11} & d_{12} & d_{16} \\ b_{12} & b_{22} & b_{26} & d_{12} & d_{22} & d_{26} \\ b_{16} & b_{26} & b_{66} & d_{16} & d_{26} & d_{66} \end{bmatrix} \begin{Bmatrix} N_x \\ N_y \\ N_{xy} \\ M_x \\ M_y \\ M_{xy} \end{Bmatrix} \quad (3.18)$$

Shell structures are often designed with laminates that are symmetric and balanced. Symmetric layups do not feature any coupling between the in-plane and the out-of-plane response of the laminate which means that all elements of \mathbf{B} and \mathbf{b} are equal to 0. Furthermore, a symmetric and balanced laminate is not subject to in-plane extension-shear coupling, i.e. $A_{16} = A_{26} = a_{16} = a_{26} = 0$. The fact that these terms are zero is advantageous in so far as that the complexity of the structural response is reduced and that analytical solutions are easier to develop.

The stress-strain relations of isotropic materials can also be described with the \mathbf{ABD} matrix because isotropy is a special case of orthotropy. An isotropic material does not exhibit coupling between in-plane and out-of-plane, extension and shear, or bending and twisting quantities. Thus, the corresponding matrix elements are given in equation (3.19) where C represents the extensional and D the bending stiffness.

$$\begin{aligned} A_{11} = C = \frac{Et}{1-\nu^2} & \quad B_{11} = 0 & \quad D_{11} = D = \frac{Et^3}{12(1-\nu^2)} \\ A_{12} = \nu C = \frac{\nu Et}{1-\nu^2} & \quad B_{12} = 0 & \quad D_{12} = \nu D = \frac{\nu Et^3}{12(1-\nu^2)} \\ A_{16} = 0 & \quad B_{16} = 0 & \quad D_{16} = 0 \\ A_{22} = C = \frac{Et}{1-\nu^2} & \quad B_{22} = 0 & \quad D_{22} = D = \frac{Et^3}{12(1-\nu^2)} \\ A_{26} = 0 & \quad B_{26} = 0 & \quad D_{26} = 0 \\ A_{66} = \frac{1-\nu}{2} C = \frac{Et}{2(1+\nu)} & \quad B_{66} = 0 & \quad D_{66} = \frac{1-\nu}{2} D = \frac{Et^3}{24(1+\nu)} \end{aligned} \quad (3.19)$$

3.4. Energy Methods

Energy methods constitute a powerful procedure for the analysis of structures because the former can be used to approximate the response of the latter to loads by applying the Ritz method. Therefore, the concept of energy methods is illustrated here and expressions for certain types of energy are derived in Section 3.5.

The state of a structure can be quantified through the total energy Π of its current configuration. A structure is said to be in equilibrium when its energy level corresponds to a relative extremum. Using the variational operator δ , this is written as

$$\delta\Pi = 0 \quad (3.20)$$

All configurations that satisfy equation (3.20) lie on a so-called equilibrium path. The stability of an equilibrium path is determined by the type of the local extremum of Π . Minima indicate a stable configuration whereas maxima characterize an unstable one. At the transition point between these two states a structure is susceptible to the loss of stability. Hence, buckling can occur when

$$\delta^2\Pi = 0 \quad (3.21)$$

For the purpose of a general buckling analysis it is reasonable to dismiss all energy contributions except for the strain energy U and the energy added by external forces V . There are two different ways to quantify these energies. When describing energy as a function of strains, and therefore displacements, one speaks of total potential energy. In this case the geometric boundary conditions have to be fulfilled. When the dynamic boundary conditions are satisfied and the energy is given in terms of stresses, one speaks of total complementary energy. In any case, the total energy is given by

$$\Pi = U + V \quad (3.22)$$

A simplified procedure for estimating the buckling load is a linear bifurcation analysis. By prescribing displacements in the shape of typical buckling patterns it is possible to determine the point on the equilibrium path where the assumed deformation pattern emerges. Hence, one can estimate the buckling load by evaluating equation (3.20) and solving an eigenvalue problem without considering (3.21). A drawback of this procedure is that there is no unique solution for the buckling displacements because they are represented by the eigenmodes that correspond to the calculated eigenvalues which relate to the buckling loads.

3.5. Energy and Equilibrium Equations

The formula for the strain energy U that is stored in a linear elastic body is

$$U = \frac{1}{2} \int_V \left(\tau_{xx}\varepsilon_{xx} + \tau_{yy}\varepsilon_{yy} + \tau_{zz}\varepsilon_{zz} + 2\tau_{xy}\varepsilon_{xy} + 2\tau_{xz}\varepsilon_{xz} + 2\tau_{yz}\varepsilon_{yz} \right) dV \quad (3.23)$$

Substituting the strain expressions from equation (3.5) yields

$$U = \frac{1}{2} \int_V \left[\tau_{xx} \left(\varepsilon_{xx}^0 + z\kappa_{xx} \right) + \tau_{yy} \left(\varepsilon_{yy}^0 + z\kappa_{yy} \right) + 2\tau_{xy} \left(\varepsilon_{xy}^0 + z\kappa_{xy} \right) \right] dV \quad (3.24)$$

Integration over the thickness allows converting stresses to section forces and moments as defined in equation (3.14).

$$U = \frac{1}{2} \int_A \left[N_x \varepsilon_{xx}^0 + M_x \kappa_{xx} + N_y \varepsilon_{yy}^0 + M_y \kappa_{yy} + 2N_{xy} \varepsilon_{xy}^0 + 2M_{xy} \kappa_{xy} \right] dA \quad (3.25)$$

Equation (3.26) is then obtained by incorporating the **ABD** matrix relations from (3.15).

$$\begin{aligned} U = & \frac{1}{2} \int_A \left[A_{11} \left(\varepsilon_{xx}^0 \right)^2 + 2A_{12} \varepsilon_{xx}^0 \varepsilon_{yy}^0 + 4A_{16} \varepsilon_{xx}^0 \varepsilon_{xy}^0 + A_{22} \left(\varepsilon_{yy}^0 \right)^2 + 4A_{26} \varepsilon_{yy}^0 \varepsilon_{xy}^0 + 4A_{66} \left(\varepsilon_{xy}^0 \right)^2 \right] dA \\ & + \int_A \left[B_{11} \varepsilon_{xx}^0 \kappa_{xx} + B_{12} \left(\varepsilon_{xx}^0 \kappa_{yy} + \varepsilon_{yy}^0 \kappa_{xx} \right) + 2B_{16} \left(\varepsilon_{xx}^0 \kappa_{xy} + \varepsilon_{xy}^0 \kappa_{xx} \right) \right. \\ & + B_{22} \varepsilon_{yy}^0 \kappa_{yy} + 2B_{26} \left(\varepsilon_{yy}^0 \kappa_{xy} + \varepsilon_{xy}^0 \kappa_{yy} \right) + 4B_{66} \varepsilon_{xy}^0 \kappa_{xy} \left. \right] dA \\ & + \frac{1}{2} \int_A \left[D_{11} \kappa_{xx}^2 + 2D_{12} \kappa_{xx} \kappa_{yy} + 4D_{16} \kappa_{xx} \kappa_{xy} + D_{22} \kappa_{yy}^2 + 4D_{26} \kappa_{yy} \kappa_{xy} + 4D_{66} \kappa_{xy}^2 \right] dA \end{aligned} \quad (3.26)$$

Now, the strain-displacement relations from equation (3.5) are implemented in (3.26) alongside the simplifications associated with a symmetric laminate. Furthermore, the strain energy is split up into the membrane strain energy U_m and the bending strain energy U_b .

$$U = U_m + U_b \quad (3.27)$$

$$\begin{aligned} U_m &= \frac{1}{2} \int_0^L \int_0^{2\pi R} \left\{ A_{11} \left[\frac{\partial u}{\partial x} + \frac{1}{2} \left(\frac{\partial w}{\partial x} \right)^2 \right]^2 + 2A_{12} \left[\frac{\partial u}{\partial x} + \frac{1}{2} \left(\frac{\partial w}{\partial x} \right)^2 \right] \left[\frac{\partial v}{\partial y} - \frac{w}{R} + \frac{1}{2} \left(\frac{\partial w}{\partial y} \right)^2 \right] \right. \\ &\quad + 2A_{16} \left[\frac{\partial u}{\partial x} + \frac{1}{2} \left(\frac{\partial w}{\partial x} \right)^2 \right] \left[\frac{\partial u}{\partial y} + \frac{\partial v}{\partial x} + \frac{\partial w}{\partial x} \frac{\partial w}{\partial y} \right] + A_{22} \left[\frac{\partial v}{\partial y} - \frac{w}{R} + \frac{1}{2} \left(\frac{\partial w}{\partial y} \right)^2 \right]^2 \\ &\quad \left. + 2A_{26} \left[\frac{\partial v}{\partial y} - \frac{w}{R} + \frac{1}{2} \left(\frac{\partial w}{\partial y} \right)^2 \right] \left[\frac{\partial u}{\partial y} + \frac{\partial v}{\partial x} + \frac{\partial w}{\partial x} \frac{\partial w}{\partial y} \right] + A_{66} \left[\frac{\partial u}{\partial y} + \frac{\partial v}{\partial x} + \frac{\partial w}{\partial x} \frac{\partial w}{\partial y} \right]^2 \right\} dy dx \quad (3.28) \\ U_b &= \frac{1}{2} \int_0^L \int_0^{2\pi R} \left[D_{11} \left(\frac{\partial^2 w}{\partial x^2} \right)^2 + 2D_{12} \frac{\partial^2 w}{\partial x^2} \frac{\partial^2 w}{\partial y^2} + 4D_{16} \frac{\partial^2 w}{\partial x^2} \frac{\partial^2 w}{\partial x \partial y} + D_{22} \left(\frac{\partial^2 w}{\partial y^2} \right)^2 \right. \\ &\quad \left. + 4D_{26} \frac{\partial^2 w}{\partial y^2} \frac{\partial^2 w}{\partial x \partial y} + 4D_{66} \left(\frac{\partial^2 w}{\partial x \partial y} \right)^2 \right] dy dx \end{aligned}$$

Since the \mathbf{B} matrix elements are equal to zero, there are no displacement terms with odd powers which tend to be considerable obstacles when deriving closed-form solutions for the governing differential equations as noted by Nemeth [59]. Closed-form solutions are desirable results of analyses because their evaluation is computationally inexpensive.

V denotes the potential energy added due to external forces which is quantified in equation (3.29) where certain terms are dismissed. The lateral pressure p acts on the outside of the shell as illustrated in Figure 3.3.

$$V = - \int_0^L \int_0^{2\pi R} \left[(pw) - (N_x \epsilon_{xx}^0 + N_y \epsilon_{yy}^0 + 2N_{xy} \epsilon_{xy}^0) + (M_x \kappa_{xx} + M_y \kappa_{yy}) \right] dy dx \quad (3.29)$$

By evaluating the Euler-Lagrange equations (3.30) it is then possible to determine the nonlinear equilibrium equations of shallow shells. The functional F only includes the internal strain energy U and the potential energy added by the external pressure term as explained by Jones [60].

$$\begin{aligned} \frac{\partial F}{\partial u} - \frac{\partial}{\partial x} \left[\frac{\partial F}{\partial \left(\frac{\partial u}{\partial x} \right)} \right] - \frac{\partial}{\partial y} \left[\frac{\partial F}{\partial \left(\frac{\partial u}{\partial y} \right)} \right] &= 0 \\ \frac{\partial F}{\partial v} - \frac{\partial}{\partial x} \left[\frac{\partial F}{\partial \left(\frac{\partial v}{\partial x} \right)} \right] - \frac{\partial}{\partial y} \left[\frac{\partial F}{\partial \left(\frac{\partial v}{\partial y} \right)} \right] &= 0 \quad (3.30) \\ \frac{\partial F}{\partial w} - \frac{\partial}{\partial x} \left[\frac{\partial F}{\partial \left(\frac{\partial w}{\partial x} \right)} \right] - \frac{\partial}{\partial y} \left[\frac{\partial F}{\partial \left(\frac{\partial w}{\partial y} \right)} \right] + \frac{\partial^2}{\partial x^2} \left[\frac{\partial F}{\partial \left(\frac{\partial^2 w}{\partial x^2} \right)} \right] + \frac{\partial^2}{\partial x \partial y} \left[\frac{\partial F}{\partial \left(\frac{\partial^2 w}{\partial x \partial y} \right)} \right] + \frac{\partial^2}{\partial y^2} \left[\frac{\partial F}{\partial \left(\frac{\partial^2 w}{\partial y^2} \right)} \right] &= 0 \end{aligned}$$

Comparing the results of (3.30) with (3.15) yields

$$\begin{aligned} \frac{\partial N_x}{\partial x} + \frac{\partial N_{xy}}{\partial y} &= 0 \\ \frac{\partial N_{xy}}{\partial x} + \frac{\partial N_y}{\partial y} &= 0 \quad (3.31) \\ \frac{\partial^2 M_x}{\partial x^2} + 2 \frac{\partial^2 M_{xy}}{\partial x \partial y} + \frac{\partial^2 M_y}{\partial y^2} + N_x \frac{\partial^2 w}{\partial x^2} + 2N_{xy} \frac{\partial^2 w}{\partial x \partial y} + N_y \frac{\partial^2 w}{\partial y^2} + \frac{N_y}{R} + p &= 0 \end{aligned}$$

3.6. Ritz Method

Solving boundary value problems for differential equations such as (3.31) exactly tends to be quite difficult. The previously discussed energy methods are employed as an alternative framework. The biggest obstacle of this approach is usually the minimization of the total energy of the system. For this purpose, approximate procedures like the Ritz method [61] have been developed.

If the total energy of a structure is described by a functional F where

$$\Pi = \int_V \left[F \left(f, \frac{\partial f}{\partial x}, \dots, \frac{\partial^m f}{\partial x^m} \right) \right] dV \quad (3.32)$$

then the function f can be substituted with the infinite series

$$f^* (x, y, z) = \sum_{n=1}^N q_n \phi_n (x, y, z) \quad (3.33)$$

Here, q_n are yet undetermined coefficients which are sometimes called Ritz coefficients. ϕ is a test function that should fulfill the following criteria:

1. ϕ is a complete series.
2. ϕ is continuous and derivable up to the power of m in equation (3.32).
3. ϕ satisfies the appropriate boundary conditions which depend on the chosen energy formulation.

The energy is minimized by evaluating

$$\frac{\partial \Pi}{\partial q_n} = 0 \quad \text{where } n = 1, 2, \dots, N \quad (3.34)$$

which yields N expressions for as many undetermined coefficients. Solving the corresponding system of equations allows the resubstitution of q_n in (3.33). It can be shown that the total energy given by $\Pi [F(f^*)]$ approaches the energy of the exact solution $\Pi [F(f)]$ when N goes to infinity assuming that conditions 1, 2, and 3 are satisfied.

Obviously, the series (3.33) has to be truncated at some point. In this case, the Ritz method overestimates the stiffness of the structure. Convergence of the two energy states is achieved by choosing ϕ so that the displacement or the stress field of the structure is accurately described. If ϕ is not selected carefully, an approximate solution may be imprecise at best or completely incorrect at worst. When a complex response must be modeled, the amount of DOFs in the infinite series can be increased through the modification of f^* by extending its definition according to equation (3.35).

$$f^* = \sum_{n=1}^N q_{1n} \phi_{1n} + \sum_{p=1}^P q_{2p} \phi_{2p} + \dots + \sum_{r=1}^R q_{sr} \phi_{sr} \quad (3.35)$$

As a consequence, the convergence rate is increased but the system of equations that has to be solved to determine the Ritz coefficients becomes more complicated since minimization now requires

$$\frac{\partial \Pi}{\partial q_{1n}} = 0 \quad \frac{\partial \Pi}{\partial q_{2p}} = 0 \quad \dots \quad \frac{\partial \Pi}{\partial q_{sr}} = 0 \quad \text{for } n, p, r = 1, 2, \dots, N, P, R \quad (3.36)$$

In any case, it is convenient to write the derivatives in matrix form which is showcased in Chapter 4.

$$\begin{Bmatrix} \frac{\partial \Pi}{\partial q_{1n}} \\ \vdots \\ \frac{\partial \Pi}{\partial q_{2p}} \\ \vdots \\ \frac{\partial \Pi}{\partial q_{rs}} \end{Bmatrix} = \begin{bmatrix} K_{1n1n} & \dots & K_{1n2p} & \dots & K_{1nrs} \\ \vdots & \ddots & \vdots & \ddots & \vdots \\ K_{2p1n} & \dots & K_{2p2p} & \dots & K_{2prs} \\ \vdots & \ddots & \vdots & \ddots & \vdots \\ K_{rs1n} & \dots & K_{rs2p} & \dots & K_{rsrs} \end{bmatrix} \begin{Bmatrix} q_{1n} \\ \vdots \\ q_{2p} \\ \vdots \\ q_{rs} \end{Bmatrix} = \begin{Bmatrix} 0 \\ \vdots \\ 0 \\ \vdots \\ 0 \end{Bmatrix} \quad (3.37)$$

3.7. Compatibility Equation

As suggested by the third equilibrium equation in (3.31), the shell membrane and bending response is coupled. Consequently, the in-plane displacement fields u and v are not necessarily compatible with arbitrary out-of-plane deflections w . Admissible configurations satisfy the compatibility equation. The membrane strains from equation (3.6) are differentiated such that

$$\begin{aligned}\frac{\partial^2 \varepsilon_{xx}^0}{\partial y^2} &= \frac{\partial^3 u}{\partial x \partial y^2} + \frac{\partial^2}{\partial y^2} \left[\frac{1}{2} \left(\frac{\partial w}{\partial x} \right)^2 \right] \\ \frac{\partial^2 \varepsilon_{yy}^0}{\partial y^2} &= \frac{\partial^3 v}{\partial x^2 \partial y} - \frac{1}{R} \frac{\partial^2 w}{\partial x^2} + \frac{\partial^2}{\partial x^2} \left[\frac{1}{2} \left(\frac{\partial w}{\partial y} \right)^2 \right] \\ \frac{\partial^2 \varepsilon_{xy}^0}{\partial x \partial y} &= \frac{1}{2} \left[\frac{\partial^3 u}{\partial x \partial y^2} + \frac{\partial^3 v}{\partial x^2 \partial y} + \frac{\partial^2 w}{\partial x \partial y} \left(\frac{\partial w}{\partial x} \frac{\partial w}{\partial y} \right) \right]\end{aligned}\quad (3.38)$$

is obtained. The last term in each expression is evaluated with the product rule.

$$\frac{\partial^2}{\partial y^2} \left[\frac{1}{2} \left(\frac{\partial w}{\partial x} \right)^2 \right] = \frac{\partial^3 w}{\partial x \partial y^2} \frac{\partial w}{\partial x} + \left(\frac{\partial^2 w}{\partial x \partial y} \right)^2 \quad (3.39a)$$

$$\frac{\partial^2}{\partial x^2} \left[\frac{1}{2} \left(\frac{\partial w}{\partial y} \right)^2 \right] = \frac{\partial^3 w}{\partial x^2 \partial y} \frac{\partial w}{\partial y} + \left(\frac{\partial^2 w}{\partial x \partial y} \right)^2 \quad (3.39b)$$

$$\frac{\partial^2 w}{\partial x \partial y} \left(\frac{\partial w}{\partial x} \frac{\partial w}{\partial y} \right) = \frac{\partial^3 w}{\partial x \partial y^2} \frac{\partial w}{\partial x} + \frac{\partial^3 w}{\partial x^2 \partial y} \frac{\partial w}{\partial y} + \left(\frac{\partial^2 w}{\partial x \partial y} \right)^2 + \frac{\partial^2 w}{\partial x^2} \frac{\partial^2 w}{\partial y^2} \quad (3.39c)$$

Adding (3.39a) and (3.39b) while subtracting (3.39c) twice eliminates the in-plane displacements u and v . The result is the nonlinear compatibility equation for circular cylindrical shells given by equation (3.40). An implicit consequence of these operations is that u and v become functions of w .

$$\frac{\partial^2 \varepsilon_{xx}^0}{\partial y^2} + \frac{\partial^2 \varepsilon_{yy}^0}{\partial x^2} - 2 \frac{\partial^2 \varepsilon_{xy}^0}{\partial x \partial y} = \left(\frac{\partial^2 w}{\partial x \partial y} \right)^2 - \frac{1}{R} \frac{\partial^2 w}{\partial x^2} - \frac{\partial^2 w}{\partial x^2} \frac{\partial^2 w}{\partial y^2} \quad (3.40)$$

3.8. Airy Stress Function

The Airy stress function Φ is introduced to reduce the number of variables that need to be considered during an analysis. If the stress resultants are formulated in accordance with equation (3.41), they always fulfill the requirements for the in-plane equilibrium according to (3.31).

$$N_x = \frac{\partial^2 \Phi}{\partial y^2} \quad N_y = \frac{\partial^2 \Phi}{\partial x^2} \quad N_{xy} = -\frac{\partial^2 \Phi}{\partial x \partial y} \quad (3.41)$$

Strictly speaking, the Airy stress function can only be applied to materials with symmetries that prohibit stress gradients through the thickness as a dependency on z is missing in equation (3.41). When evaluating composites this means that the stress resultants are averaged over the laminate thickness, i.e. ply stresses are not accurately modeled. Using (3.41), the out-of-plane equilibrium equation is rewritten as

$$D_{11} \frac{\partial^4 w}{\partial x^4} + (2D_{12} + 4D_{66}) \frac{\partial^4 w}{\partial x^2 \partial y^2} + D_{22} \frac{\partial^4 w}{\partial y^4} - \frac{\partial^2 \Phi}{\partial y^2} \frac{\partial^2 w}{\partial x^2} + 2 \frac{\partial^2 \Phi}{\partial x \partial y} \frac{\partial^2 w}{\partial x \partial y} - \frac{\partial^2 \Phi}{\partial x^2} \frac{\partial^2 w}{\partial y^2} - \frac{1}{R} \frac{\partial^2 \Phi}{\partial x^2} = p \quad (3.42)$$

where the bending stiffness terms D_{16} and D_{26} have been neglected. This is a common assumption as they are usually small compared to the other components of the \mathbf{D} matrix. By applying the relations from the **abd** matrix (3.18) for a symmetric and balanced laminate, the nonlinear compatibility equation becomes

$$a_{22} \frac{\partial^4 \Phi}{\partial x^4} + (2a_{12} + a_{66}) \frac{\partial^4 \Phi}{\partial x^2 \partial y^2} + a_{11} \frac{\partial^4 \Phi}{\partial y^4} = \left(\frac{\partial^2 w}{\partial x \partial y} \right)^2 - \frac{1}{R} \frac{\partial^2 w}{\partial x^2} - \frac{\partial^2 w}{\partial x^2} \frac{\partial^2 w}{\partial y^2} \quad (3.43)$$

The structural response of a shell is fully defined when both the out-of-plane deflection w and the Airy stress function Φ are known. In fact, if a displacement field w is given, then the corresponding stress distribution in the shell can be determined by solving the partial differential equation (3.43) for Φ .

The relations (3.42) and (3.42) simplify significantly when an isotropic material is considered.

$$D\nabla^4 w - \frac{\partial^2 \Phi}{\partial y^2} \frac{\partial^2 w}{\partial x^2} + 2 \frac{\partial^2 \Phi}{\partial x \partial y} \frac{\partial^2 w}{\partial x \partial y} - \frac{\partial^2 \Phi}{\partial x^2} \frac{\partial^2 w}{\partial y^2} - \frac{1}{R} \frac{\partial^2 \Phi}{\partial x^2} = p \quad (3.44)$$

$$\nabla^4 \Phi = Et \left[\left(\frac{\partial^2 w}{\partial x \partial y} \right)^2 - \frac{1}{R} \frac{\partial^2 w}{\partial x^2} - \frac{\partial^2 w}{\partial x^2} \frac{\partial^2 w}{\partial y^2} \right] \quad (3.45)$$

3.9. Coordinate Transformation

The equations and derivations discussed up to this point are mostly valid for the curvilinear reference frame displayed in Figure 3.2. Just like a rectangular cutout should be expressed in Cartesian coordinates, which has been showcased in Subsection 2.1.3, a circular opening in a cylindrical shell is more conveniently described with a semi-geodesic polar coordinate system as illustrated in Figure 3.4a. Hence, some coordinate transformations are required to adjust the previous expressions.

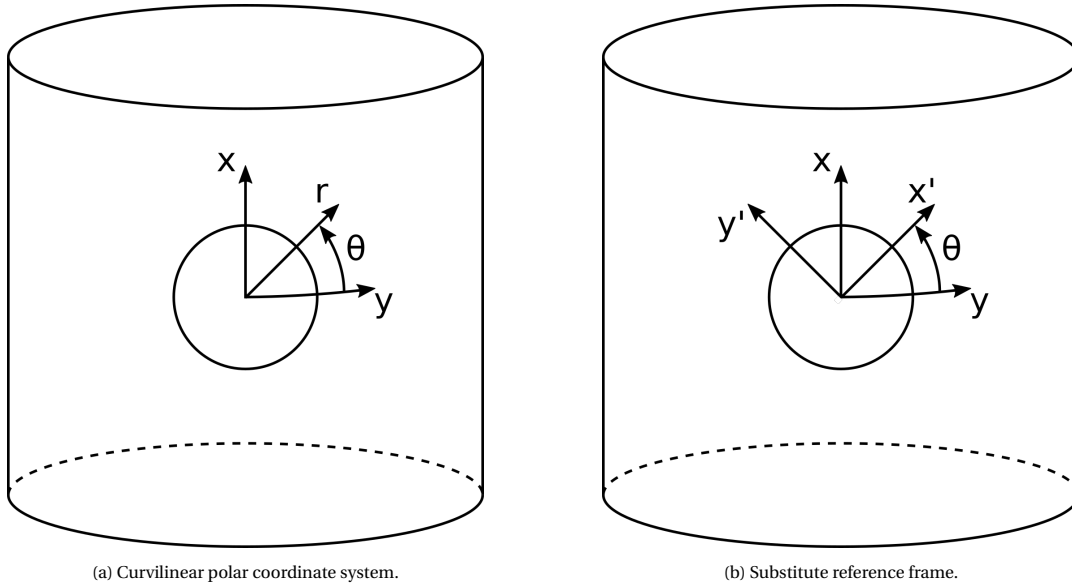


Figure 3.4: Coordinate systems with their origins at the cutout center.

Comparing Figures 3.4a and 3.4b shows that the r, θ coordinates are identical to the transformed x', y' if the latter are rotated appropriately. Since the Lamé parameters of shallow shells are approximated as $A = B = 1$ and the through-the-thickness-coordinate remains the same, the coordinate transformation from the curvilinear system in Figure 3.2 to semi-geodesic polar coordinates in Figure 3.4a is equivalent to the transformation from Cartesian to polar coordinates in two dimensions. Consequently, the relations between x, y and x', y' are

$$\begin{Bmatrix} x \\ y \end{Bmatrix} = \begin{bmatrix} \sin\theta & \cos\theta \\ \cos\theta & -\sin\theta \end{bmatrix} \begin{Bmatrix} x' \\ y' \end{Bmatrix} \quad \begin{Bmatrix} x' \\ y' \end{Bmatrix} = \begin{bmatrix} -\sin\theta & \cos\theta \\ \cos\theta & \sin\theta \end{bmatrix} \begin{Bmatrix} x \\ y \end{Bmatrix} \quad (3.46)$$

Inversion is easily achieved by substituting $-\theta$ for the angle in equation (3.46).

3.9.1. Transformation Matrices

Directional quantities are transformed from one coordinate system to another by evaluating the direction cosines t_{ij} between them. The formulas for 1D- (coordinates and displacements), 2D- (strain and stress

tensors), as well as 4D-quantities (stiffness and compliance tensors) are presented in equation (3.47). Transformed values are marked with a prime.

$$\begin{aligned} x'_i &= t_{im} x_m & u'_i &= t_{im} u_m \\ \varepsilon'_{ij} &= t_{im} t_{jn} \varepsilon_{mn} & \tau'_{ij} &= t_{im} t_{jn} \tau_{mn} \\ C'_{ijkl} &= t_{im} t_{jn} t_{kp} t_{lq} C_{mnpq} & S'_{ijkl} &= t_{im} t_{jn} t_{kp} t_{lq} S_{mnpq} \end{aligned} \quad (3.47)$$

In matrix form, one may write

$$\mathbf{x}' = \mathbf{T}_{1D} \mathbf{x} \quad \boldsymbol{\varepsilon}' = \mathbf{T}_{2D} \boldsymbol{\varepsilon} \quad \mathbf{C}' = \mathbf{T}_{4D} \mathbf{C} \quad (3.48)$$

with

$$\mathbf{T}_{1D} = \begin{bmatrix} t_1 & t_3 \\ t_4 & t_2 \end{bmatrix} \quad (3.49a)$$

$$\mathbf{T}_{2D} = \begin{bmatrix} t_1^2 & t_3^2 & 2t_1 t_3 \\ t_4^2 & t_2^2 & 2t_4 t_2 \\ t_1 t_4 & t_3 t_2 & t_1 t_2 + t_3 t_4 \end{bmatrix} \quad (3.49b)$$

$$\mathbf{T}_{4D} = \begin{bmatrix} t_1^4 & 2t_1^2 t_3^2 & 4t_1^3 t_3 & t_3^4 & 4t_1 t_3^3 & 4t_1^2 t_3^2 \\ t_4^4 & 2t_4^2 t_2^2 & 4t_4^3 t_2 & t_2^4 & 4t_4 t_2^3 & 4t_4^2 t_2^2 \\ t_1^2 t_4^2 & 2t_1 t_3 t_4 t_2 & 2t_1^2 t_4 t_2 + 2t_1 t_3 t_4^2 & t_3^2 t_2^2 & 2t_1 t_3 t_2^2 + 2t_3^2 t_4 t_2 & t_1^2 t_2^2 + t_3^2 t_4^2 + 2t_1 t_3 t_4 t_2 \\ t_1 t_4^3 & t_1 t_4 t_2^2 + t_3 t_4^2 t_2 & 3t_1 t_4^2 t_2 + t_3 t_4^3 & t_3 t_2^3 & 3t_3 t_4 t_2^2 + t_1 t_2^3 & 2t_1 t_4 t_2^2 + 2t_3 t_4^2 t_2 \\ t_1^3 t_4 & t_1^2 t_3 t_2 + t_1 t_3^2 t_4 & 3t_1^2 t_3 t_4 + t_1^3 t_2 & t_3^3 t_2 & 3t_1 t_3^2 t_2 + t_3^3 t_4 & 2t_1^2 t_3 t_2 + 2t_1 t_3^2 t_4 \\ t_1^2 t_4^2 & t_1^2 t_2^2 + t_3^2 t_4^2 & 2t_1^2 t_4 t_2 + 2t_1 t_3 t_4^2 & t_3^2 t_2^2 & 2t_1 t_3 t_2^2 + 2t_3^2 t_4 t_2 & 4t_1 t_3 t_4 t_2 \end{bmatrix} \quad (3.49c)$$

where Voigt notation has been applied. Every transformation matrix \mathbf{T} is valid for a tensor of a certain dimension. Tensor strains are the only type of strain measure that is correctly converted without further modification of \mathbf{T}_{2D} . By comparing the general one-dimensional transformation matrix \mathbf{T}_{1D} from (3.49a) with the special case in equation (3.46), components of higher order transformation matrices may be determined.

3.9.2. Partial Derivatives

A function $f(r(x, y), \theta(x, y))$ can be differentiated with respect to x (or y) by applying the chain rule.

$$\frac{\partial f}{\partial x} = \frac{\partial f}{\partial r} \frac{\partial r}{\partial x} + \frac{\partial f}{\partial \theta} \frac{\partial \theta}{\partial x} \quad (3.50)$$

Mapping functions that define r and θ in terms of x and y are derived from Figure 3.4a.

$$r = \sqrt{x^2 + y^2} \quad \theta = \arctan \frac{x}{y} \quad (3.51)$$

Equation (3.50) is divided by f . Expressions for the partial derivatives $\partial r / \partial x$ and $\partial \theta / \partial x$ in (3.50) are found by differentiating the mapping functions in (3.51).

$$\frac{\partial}{\partial x} = \sin \theta \frac{\partial}{\partial r} + \frac{1}{r} \cos \theta \frac{\partial}{\partial \theta} \quad (3.52)$$

The partial derivative with respect to y is determined in a similar fashion.

$$\frac{\partial}{\partial y} = \cos \theta \frac{\partial}{\partial r} - \frac{1}{r} \sin \theta \frac{\partial}{\partial \theta} \quad (3.53)$$

One may write the second partial derivative as

$$\frac{\partial^2 f}{\partial x^2} = \frac{\partial}{\partial x} \left(\frac{\partial f}{\partial x} \right) \quad (3.54)$$

and the first partial derivative is already known. It is substituted and after applying the product as well as the chain rule, the resulting expression is simplified.

$$\frac{\partial^2 f}{\partial x^2} = \left(\frac{\partial r}{\partial x} \right)^2 \frac{\partial^2 f}{\partial r^2} + \frac{\partial^2 r}{\partial x^2} \frac{\partial f}{\partial r} + 2 \frac{\partial r}{\partial x} \frac{\partial \theta}{\partial x} \frac{\partial^2 f}{\partial r \partial \theta} + \left(\frac{\partial \theta}{\partial x} \right)^2 \frac{\partial^2 f}{\partial \theta^2} + \frac{\partial^2 \theta}{\partial x^2} \frac{\partial f}{\partial \theta} \quad (3.55)$$

Again, (3.55) is divided by f while the mapping functions are used to calculate partial derivatives.

$$\frac{\partial^2}{\partial x^2} = \sin^2 \theta \frac{\partial^2}{\partial r^2} + \cos^2 \theta \left(\frac{1}{r} \frac{\partial}{\partial r} + \frac{1}{r^2} \frac{\partial^2}{\partial \theta^2} \right) - \sin 2\theta \left(\frac{1}{r^2} \frac{\partial}{\partial \theta} - \frac{1}{r} \frac{\partial^2}{\partial r \partial \theta} \right) \quad (3.56)$$

The same procedure is applied to obtain the other two possible partial derivatives.

$$\frac{\partial^2}{\partial y^2} = \cos^2 \theta \frac{\partial^2}{\partial r^2} + \sin^2 \theta \left(\frac{1}{r} \frac{\partial}{\partial r} + \frac{1}{r^2} \frac{\partial^2}{\partial \theta^2} \right) + \sin 2\theta \left(\frac{1}{r^2} \frac{\partial}{\partial \theta} - \frac{1}{r} \frac{\partial^2}{\partial r \partial \theta} \right) \quad (3.57)$$

$$\frac{\partial^2}{\partial x \partial y} = \frac{1}{2} \sin 2\theta \left(\frac{\partial^2}{\partial r^2} - \frac{1}{r} \frac{\partial}{\partial r} - \frac{1}{r^2} \frac{\partial^2}{\partial \theta^2} \right) - \cos 2\theta \left(\frac{1}{r^2} \frac{\partial}{\partial \theta} - \frac{1}{r} \frac{\partial^2}{\partial r \partial \theta} \right) \quad (3.58)$$

Alternatively, one could have also multiplied the first order partial derivatives (3.52) and (3.53) with each other to arrive at the same results. Fourth-order partial derivatives are needed for the analysis in Chapter 4 as well. However, they are not presented in detail here due to their size. Anyhow, they can be easily calculated by applying the procedure just described.

3.9.3. Integrals

The change of the reference system requires an adjustment of both the integration limits as well as the integration variables.

$$\int_{x_0}^{x_1} \int_{y_0}^{y_1} dy dx = \iint_A dA = \int_{\theta_0}^{\theta_1} \int_{r_0}^{r_1} r dr d\theta \quad (3.59)$$

3.9.4. In-plane Equilibrium Equations and Airy Stress Function

The in-plane equilibrium equations in the new reference frame are given by

$$\frac{1}{r} \frac{\partial (r N_r)}{\partial r} + \frac{1}{r} \frac{\partial N_{r\theta}}{\partial \theta} - \frac{N_\theta}{r} = 0 \quad \frac{1}{r^2} \frac{\partial (r^2 N_{r\theta})}{\partial r} + \frac{1}{r} \frac{\partial N_\theta}{\partial \theta} = 0 \quad (3.60)$$

As a consequence, the relation between the section forces and the Airy stress function must change so that equation (3.60) is always fulfilled. The validity of the new expressions may be confirmed through direct substitution of (3.61) in (3.60).

$$N_r = \frac{1}{r} \frac{\partial \Phi}{\partial r} + \frac{1}{r^2} \frac{\partial^2 \Phi}{\partial \theta^2} \quad N_\theta = \frac{\partial^2 \Phi}{\partial r^2} \quad N_{r\theta} = -\frac{\partial}{\partial r} \left(\frac{1}{r} \frac{\partial \Phi}{\partial \theta} \right) \quad (3.61)$$

3.10. Classical Buckling Theory

Donnell [62] is often credited with the first formulation of a single governing equation that describes the buckling behavior of isotropic circular cylindrical shells. He eliminated the coupling between in-plane and out-of-plane displacements as described in Section 3.7. When employing the method of adjacent equilibrium, equations (3.44) and (3.45) can be combined such that (3.62) is obtained.

$$D \nabla^8 \delta w + \frac{E t}{R^2} \frac{\partial^4 \delta w}{\partial x^4} - \nabla^4 \left(N_x \frac{\partial^2 \delta w}{\partial x^2} + 2 N_{xy} \frac{\partial^2 \delta w}{\partial x \partial y} + N_y \frac{\partial^2 \delta w}{\partial y^2} \right) = 0 \quad (3.62)$$

Batdorf [63] modified equation (3.62) by multiplying it with ∇^{-4} which removes some mathematical inconsistencies when clamped boundary conditions are part of the problem formulation. The first term in the ensuing equation can be interpreted as the shell bending stiffness, the second one as its extensional resistance, and the third one as a measure of the applied load. Batdorf solved the modified buckling equation assuming an axisymmetric displacement pattern and derived the classical expression for the buckling stress of an isotropic cylindrical shell τ_{cl} .

$$\tau_{cl} = \frac{E}{\sqrt{3(1-\nu^2)}} \frac{t}{R} \quad (3.63)$$

He defined the parameter Z , now named after Batdorf himself, as

$$Z = \sqrt{1-\nu^2} \frac{L^2}{Rt} \quad (3.64)$$

Equation (3.63) is valid for $Z \geq 2.85$, that is for cylindrical shells which qualify as moderately long. Even though obtaining an expression like (3.63) was most definitely a great achievement, it was also soon discovered that isotropic shells never reached the theoretical buckling loads in experiments.

Koiter [64] resolved the apparent discrepancy with the publication of his Ph.D. dissertation in 1945 where he included initial geometric imperfections in his analytical model of cylindrical shells. The scientific community was mostly unaware of this breakthrough until Koiter's dissertation was translated from Dutch to English in the 1960s. In the meantime, Donnell and Wan [65] had included imperfections in the shape of eigenmodes obtained from a linear buckling analysis in a numerical approach. Realizing the implications of these results, and to some extent certainly motivated by the "space race", the National Aeronautics and Space Administration (NASA) conducted an extensive testing campaign to quantify the effects of initial imperfections. As a result, the well-known NASA SP-8007 [66] was published which provides knock-down factors for the design of shells against buckling.

While structures have been designed with isotropic materials in the past, composites are popular today because they offer the possibility to tailor strength and stiffness properties in every direction to optimize material usage. The previously presented buckling formula is of course not valid for composite cylindrical shells which is why Nemeth et al. [67] published equations for determining the buckling load of laminated shells. Neglecting the influence of all coupling terms in equation (3.15) and allowing buckling waves in both the axial (m) as well as the circumferential (n) direction, the buckling stress is approximated by minimizing

$$\tilde{p}\pi^2 = \frac{n^4 \alpha_b^2}{m^2 \pi^2} + 2\beta' n^2 + \frac{m^2 \pi^2}{\alpha_b^2} + \frac{12\rho^2}{\frac{n^4 \alpha_m^2}{m^2 \pi^2} + 2\mu' n^2 + \frac{m^2 \pi^2}{\alpha_m^2}} \quad (3.65)$$

All terms in equation (3.65) are known for a given laminate with the exception of the number of buckling waves. The definitions of the nondimensional stiffness parameters are given in reference [67] and the constants β' and μ' should not be confused with the curvature parameters β and μ . The buckling stress τ_{cl} of a pristine cylindrical shell relates to the nondimensional loading parameter \tilde{p} by

$$\tau_{cl} = \tilde{p}\pi^2 \sqrt{D_{11}D_{22}} \frac{t}{R^2} \quad (3.66)$$

4

Buckling Analysis

A linear bifurcation analysis for estimating the buckling load of cylindrical shells with circular cutouts is presented. After introducing the geometry and loading conditions in Section 4.1, major assumptions as well as the general solution approach are highlighted in Section 4.2. Next, the methodology is demonstrated for the case of isotropic shells in Section 4.3. The analytical formulation is subsequently derived for quasi-isotropic, symmetric, composite laminates in Section 4.4. Modifications to the shape function as well as the corresponding effects on the solution procedure are investigated in the last part of the chapter, Section 4.5.

4.1. Geometry and Loading Conditions

The buckling analysis is developed for a cylindrical shell with a circular cutout of radius a subjected to a uniform axial shell edge load \bar{N}_x as shown in Figure 4.1. A polar semi-geodesic coordinate system r, θ with its origin at the center of the opening is employed to quantify the response of the cylindrical shell mathematically. The reference frame r, θ is chosen over x, y from Figure 3.2, which is also illustrated below, because it is more convenient to describe a circular cutout in a polar coordinate system.

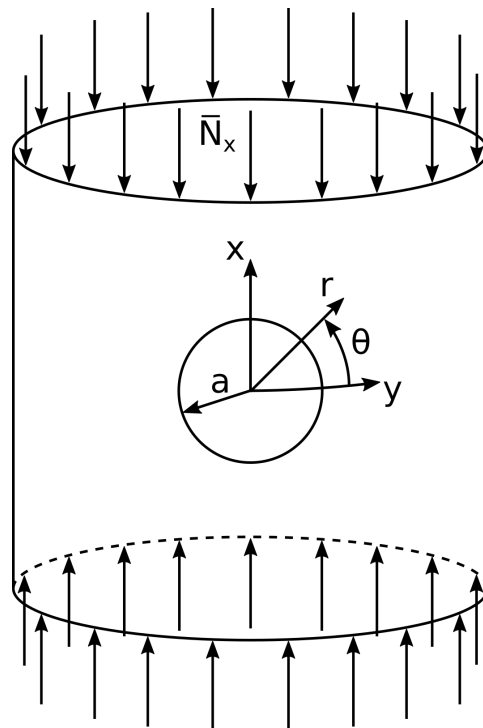


Figure 4.1: A cylindrical shell loaded by a uniform axial edge load \bar{N}_x .

4.2. Assumptions and Solution Approach

Several assumptions are made during the linear buckling analysis of the cylindrical shell. They are divided into two categories, namely assumptions that relate to shell buckling in general, as well as assumptions that are specific to the buckling of cylindrical shells with circular cutouts. The first group entails the following considerations:

- The premises of the Kirchhoff-Love hypothesis, with the exception of the assumption of small displacements compared to the shell thickness, are valid.
- The shell is of constant thickness t and features a constant radius R .
- The shell curvature is small which means that the strain-displacement relations for shallow shells apply.
- The shell is idealized as a perfect structure, i.e. geometric and material imperfections are not modeled.
- The shell is not stiffened.
- The orthotropic plies of the composite shell are perfectly bonded.
- There are no large prebuckling displacements such that a linear eigenvalue analysis can be performed to estimate the buckling load.
- Buckling occurs while the material behavior is linear elastic. This is justified with observations made by Starnes [18], Bisagni [27], and Shirkavand et al. [28] for isotropic and composite shells, respectively.

Even though the last assumption is motivated with conclusions from investigations on the buckling of shells with cutouts, it is also employed during the derivation of the classical buckling load for pristine cylindrical shells. The remaining assumptions are specific to shells with circular openings:

- The shell instability originates from local buckling in the area around the cutout which is true as long as the curvature parameter μ is larger than approximately 0.5 according to Starnes [18]. The local nature of the buckling event was also confirmed by Hilburger, Starnes, and Nemeth [31–33].
- Thus, the effects of displacements, strains, and stresses are small everywhere but in the vicinity of the opening.
- The prebuckling stress distribution in the shell is approximated with the flat plate solution by Kirsch [1] as the effects of bending stresses and higher shell membrane stresses are considered to be negligible.

The solution procedure illustrated in Figure 4.2 is inspired by the approach presented by Starnes [18] in his Ph.D. dissertation where he investigated the buckling behavior of isotropic shells with circular cutouts analytically and experimentally. He validated the analytical results with buckling tests of Mylar specimens. This provides the opportunity to reuse Starnes' data for the verification of numerical simulations, and the experimental results for the validation of the modified analytical solution for the isotropic shell.

The shell response is quantified with the method of total potential energy and therefore a displacement function has to be prescribed. Since the structural behavior is expressed in the r, θ reference frame, so is the shape function. It must produce negligible displacements far away from the cutout due to the localized nature of the buckling event which suggests the use of an exponential function with a negative exponent. Additionally, the shape function has to provide a smooth transition at the origin of the coordinate system when the cutout radius is almost zero. Hence, its derivative with respect to r must approach zero for small values of the radial coordinate. This can be achieved by multiplying the negative exponent with r . Of course, the shape function must also accurately describe the buckling displacement pattern around the opening. A function that satisfies all of these conditions was proposed by Starnes based on his extensive experimental studies. It is given in equation (4.1) where A_0 , A_2 , C_0 , and C_2 denote undetermined Ritz coefficients and B is a decay parameter.

$$w(r, \theta) = e^{-Br} [(A_0 + rC_0) + (A_2 + rC_2) \cos 2\theta] \quad (4.1)$$

As shown in equation (3.22), the total potential energy Π can be written as the sum of the membrane strain energy U_m , the bending strain energy U_b , and the potential energy due to external forces V . Expressions for

these quantities are originally derived in the curvilinear coordinate system x, y in Chapter 3. Consequently, they have to be transformed into the r, θ reference frame. The contribution of U_b can be evaluated as soon as a displacement function is assumed. After approximating the prebuckling stress distribution with the flat plate solution, it is also possible to determine the energy contribution of V . The calculation of U_m is more complicated because the stress resultants at buckling are not known. To work them out, the linear shell compatibility equation is solved for the Airy stress function Φ .

Having obtained an expression for Π , the total potential energy is minimized with the Ritz method. This yields two matrices which set up the generalized eigenvalue problem. Minimum eigenvalues are computed as a function of B using a numerical algorithm. Finally, the buckling load is given as the product of the minimum eigenvalue and the applied load. The eigenvectors that correspond to the minimum eigenvalues are interpreted as the buckling mode shapes.

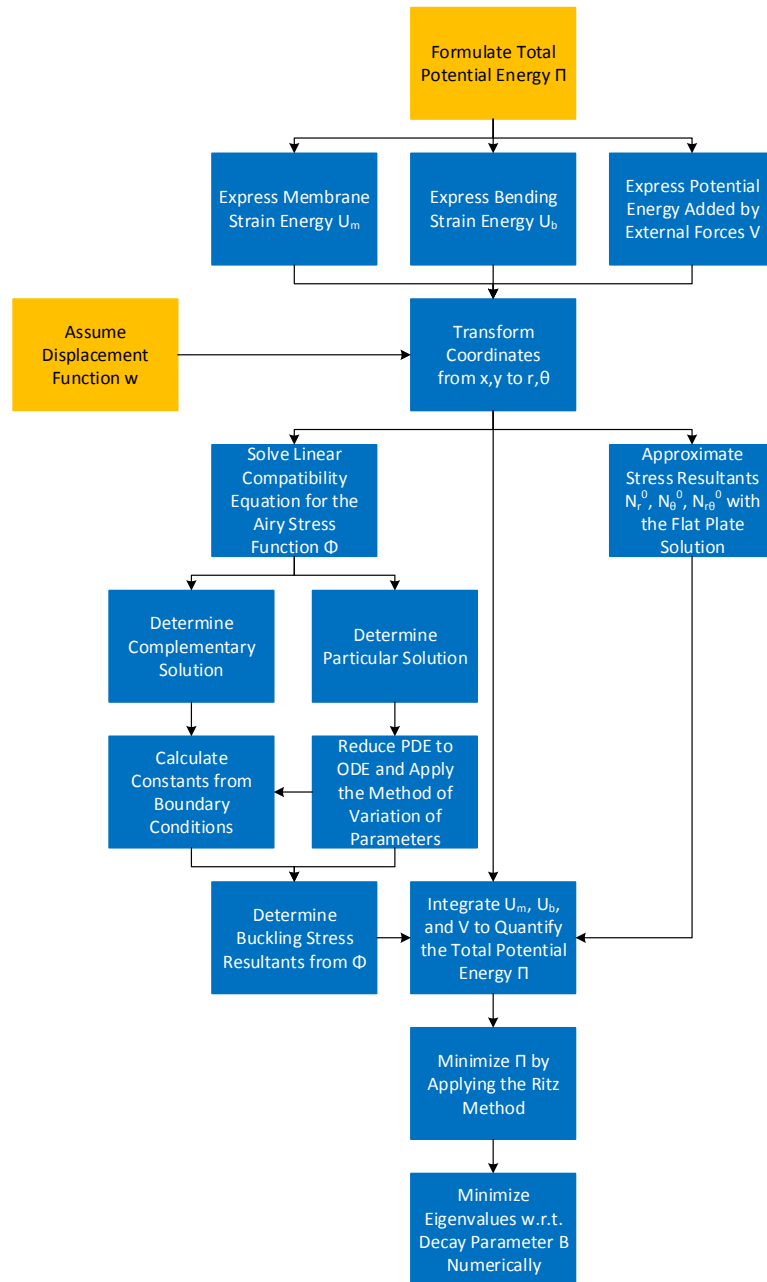


Figure 4.2: Flow chart outlining the analysis procedure.

4.3. Isotropic Shells

As mentioned at the beginning of the chapter, the solution approach visualized in Figure 4.2 is described in detail based on the special case of an isotropic shell with a circular cutout. The following subsections are concerned with explaining individual blocks of the above flow chart. Section 4.4 then focuses on the changes made to the respective solution steps in order to adapt the procedure for quasi-isotropic, composite, symmetric cylindrical shells.

4.3.1. Total Potential Energy

The total potential energy of the shell amounts to

$$\Pi = U_m + U_b + V \quad (4.2)$$

where U_m and U_b have been defined in equation (3.28) while V is specified in (3.29). Substituting the equivalent **ABD** matrix components for isotropic materials from (3.19), applying the von Kármán approximation to the expression for V since out-of-plane displacements are large, and denoting the prebuckling stress resultants with the superscript 0, the respective energy contributions may be rewritten as

$$\begin{aligned} U_m &= \frac{1}{2Et} \iint \left[N_x^2 + N_y^2 - 2\nu N_x N_y + 2(1+\nu) N_{xy}^2 \right] dx dy \\ U_b &= \frac{D}{2} \iint \left\{ \left(\frac{\partial^2 w}{\partial x^2} + \frac{\partial^2 w}{\partial y^2} \right)^2 - 2(1-\nu) \left[\frac{\partial^2 w}{\partial x^2} \frac{\partial^2 w}{\partial y^2} - \left(\frac{\partial^2 w}{\partial x \partial y} \right)^2 \right] \right\} dx dy \\ V &= \frac{1}{2} \iint \left[N_x^0 \left(\frac{\partial w}{\partial x} \right)^2 + N_y^0 \left(\frac{\partial w}{\partial y} \right)^2 + 2N_{xy}^0 \frac{\partial w}{\partial x} \frac{\partial w}{\partial y} \right] dx dy \end{aligned} \quad (4.3)$$

4.3.2. Coordinate Transformation

Since the formulas in equation (4.3) are developed for the reference frame depicted in Figure 3.2, some coordinate transformations are required. First, the derivation of U_m in Section 3.5 would have been equally valid with the subscripts r, θ instead of x, y . Also acknowledging the change of the integration variables, see Subsection 3.9.3, this immediately becomes

$$U_m = \frac{1}{2Et} \iint \left\{ \left[N_r^2 + N_\theta^2 - 2\nu N_r N_\theta + 2(1+\nu) N_{r\theta}^2 \right] r \right\} dr d\theta \quad (4.4)$$

Considering the transformations for the partial derivatives described in (3.56) through (3.58), the bending strain energy U_b is expressed as

$$\begin{aligned} U_b &= \frac{D}{2} \iint \left\{ \left[\left(\frac{\partial^2 w}{\partial r^2} \right)^2 + \frac{1}{r^2} \left(\frac{\partial w}{\partial r} \right)^2 + \frac{2}{r^3} \frac{\partial w}{\partial r} \frac{\partial^2 w}{\partial \theta^2} + \frac{1}{r^4} \left(\frac{\partial^2 w}{\partial \theta^2} \right)^2 \right] \right. \\ &\quad \left. + 2(1-\nu) \left[\frac{1}{r^2} \left(\frac{\partial^2 w}{\partial r \partial \theta} \right)^2 - \frac{2}{r^3} \frac{\partial w}{\partial \theta} \frac{\partial^2 w}{\partial r \partial \theta} + \frac{1}{r^4} \left(\frac{\partial w}{\partial \theta} \right)^2 \right] + 2\nu \left[\frac{1}{r} \frac{\partial w}{\partial r} \frac{\partial^2 w}{\partial r^2} + \frac{1}{r^2} \frac{\partial^2 w}{\partial r^2} \frac{\partial^2 w}{\partial \theta^2} \right] \right\} r \, dr d\theta \end{aligned} \quad (4.5)$$

Likewise, the total potential energy due to external forces is converted by substituting the partial derivatives (3.52) and (3.53) as well as the 2D transformation matrix (3.49b).

$$\begin{aligned} V &= \frac{1}{4} \iint \left\{ \left[\left(N_r^0 + N_\theta^0 \right) + \left(N_r^0 - N_\theta^0 \right) \cos 4\theta + 2N_{r\theta}^0 \sin 4\theta \right] \left(\frac{\partial w}{\partial r} \right)^2 + \frac{2}{r} \left(N_\theta^0 - N_r^0 \right) \left(\frac{\partial w}{\partial r} \frac{\partial w}{\partial \theta} \right) \right. \\ &\quad \left. + \frac{4}{r} N_{r\theta}^0 \cos 4\theta \left(\frac{\partial w}{\partial r} \frac{\partial w}{\partial \theta} \right) + \frac{1}{r^2} \left[\left(N_r^0 + N_\theta^0 \right) - \left(N_r^0 - N_\theta^0 \right) \cos 4\theta - 2N_{r\theta}^0 \sin 4\theta \right] \left(\frac{\partial w}{\partial \theta} \right)^2 \right\} r \, dr d\theta \end{aligned} \quad (4.6)$$

Since the linear version of the compatibility equation (3.45) is needed in Subsection 4.3.4, it also has to be converted. Again, the second-order partial derivatives (3.56) and (3.57) are used to obtain

$$\nabla^4 \Phi = -\frac{Et}{R} \left[\sin^2 \theta \frac{\partial^2 w}{\partial r^2} + \cos^2 \theta \left(\frac{1}{r} \frac{\partial w}{\partial r} + \frac{1}{r^2} \frac{\partial^2 w}{\partial \theta^2} \right) - \sin 2\theta \left(\frac{1}{r^2} \frac{\partial w}{\partial \theta} - \frac{1}{r} \frac{\partial^2 w}{\partial r \partial \theta} \right) \right] \quad (4.7)$$

The biharmonic operator ∇^4 in polar coordinates may be written as

$$\nabla^4 = \left(\frac{\partial^2}{\partial r^2} + \frac{1}{r} \frac{\partial}{\partial r} + \frac{1}{r^2} \frac{\partial^2}{\partial \theta^2} \right) \left(\frac{\partial^2}{\partial r^2} + \frac{1}{r} \frac{\partial}{\partial r} + \frac{1}{r^2} \frac{\partial^2}{\partial \theta^2} \right) \quad (4.8)$$

4.3.3. Prebuckling Stress Distribution

The most accurate formulation of the stress field in an isotropic cylindrical shell with a circular cutout prior to buckling has probably been derived by Lekkerkerker [5]. However, his solution is computationally expensive to implement because stresses can only be computed in concentric circles around the opening. Furthermore, it does not extend to composite shells. Like the solution proposed by Van Dyke [6] for isotropic cylindrical shells, Ashmarin's [11] result for the stress distribution in an orthotropic shell is determined by solving the governing equations numerically. Since the goal is to derive an analytical solution, these alternatives are dismissed. The publication by Guz et al. [12] covers the stress field in an orthotropic shell, but it suffers from similar restrictions as Lekkerkerker's approach.

It is much more convenient to approximate the stress distribution in a cylindrical shell with that of the flat plate which is a reasonable assumption as long as the curvature parameter μ is small, see Figure 2.1. While Lekhnitskii's [2] solution for the orthotropic plate can yield results for stress concentration factors as suggested by Kassapoglou [68], obtaining stress distributions is more difficult because the dependency on the radial coordinate also has to be accounted for. Moreover, multiple aspects of the solution procedure change depending on the equivalent elastic properties of the laminate, for example the equation for the transformation from real to complex coordinates mentioned in Subsection 2.1.1, which increases the complexity of determining stress resultants considerably.

In contrast, the solution for the stress distribution around a circular cutout in a flat isotropic plate derived by Kirsch [1] is available in closed-form and furthermore extends to the quasi-isotropic case. Multiplying equation (2.1) with t yields an expression for the in-plane stress resultants. Assuming a compressive stress τ_∞ and considering the different definition of the reference frame in the aforementioned equation, the pre-buckling section force components N_r^0 , N_θ^0 , and $N_{r\theta}^0$ are given by

$$\begin{aligned} N_r^0 &= -\frac{\tau_\infty t}{2} \left[1 - \left(\frac{a}{r} \right)^2 \right] + \frac{\tau_\infty t}{2} \left[1 - 4 \left(\frac{a}{r} \right)^2 + 3 \left(\frac{a}{r} \right)^4 \right] \cos 2\theta \\ N_\theta^0 &= -\frac{\tau_\infty t}{2} \left[1 + \left(\frac{a}{r} \right)^2 \right] - \frac{\tau_\infty t}{2} \left[1 + 3 \left(\frac{a}{r} \right)^4 \right] \cos 2\theta \\ N_{r\theta}^0 &= -\frac{\tau_\infty t}{2} \left[1 + 2 \left(\frac{a}{r} \right)^2 - 3 \left(\frac{a}{r} \right)^4 \right] \sin 2\theta \end{aligned} \quad (4.9)$$

These expressions are substituted in equation (4.6) which yields

$$\begin{aligned} V = -\frac{1}{4} \tau_\infty t \iint \left\{ \left[2 \sin^2 \theta + \frac{a^2}{r^2} (4 \cos 2\theta - 1) - 3 \frac{a^4}{r^4} \cos 2\theta \right] \left(\frac{\partial w}{\partial r} \right)^2 \right. \\ \left. + \left[\left(\frac{2}{r} + 4 \frac{a^2}{r^3} - 6 \frac{a^4}{r^5} \right) \sin 2\theta \right] \left(\frac{\partial w}{\partial r} \frac{\partial w}{\partial \theta} \right) + \left[\frac{2}{r^2} \cos^2 \theta + \frac{a^2}{r^4} + 3 \frac{a^4}{r^6} \cos 2\theta \right] \left(\frac{\partial w}{\partial \theta} \right)^2 \right\} r \, dr \, d\theta \end{aligned} \quad (4.10)$$

4.3.4. Linear Compatibility Equation

In Section 3.8 it was shown that the introduction of the Airy stress function Φ reduces the number of variables that have to be considered during an analysis. Additionally, Φ can be used to determine the stress resultants by solving the compatibility equation (3.45) which is desirable because N_r , N_θ , and $N_{r\theta}$ in (4.4) are unknowns. Since a linear eigenvalue analysis is performed, it is sufficient to solve the linear version of the compatibility equation. Substituting the shape function (4.1) on the right-hand side (RHS) of (4.7) gives

$$\nabla^4 \Phi = g_0(r) + g_2(r) \cos 2\theta + g_4(r) \cos 4\theta \quad (4.11)$$

where g_m ($m = 0, 2, 4$) in (4.12) are disturbance function terms of a partial differential equation (PDE). To be precise, (4.11) is a fourth-order inhomogeneous PDE with constant coefficients.

$$\begin{aligned}
g_0 &= -\frac{Et}{2R} e^{-Br} \left[A_0 \left(B^2 - \frac{B}{r} \right) + A_2 \left(-\frac{1}{2} B^2 + \frac{3B}{2r} \right) + C_0 \left(B^2 r - 3B + \frac{1}{r} \right) + C_2 \left(-\frac{1}{2} B^2 r \frac{5}{2} B - \frac{3}{2} \frac{1}{r} \right) \right] \\
g_2 &= -\frac{Et}{2R} e^{-Br} \left[A_0 \left(-B^2 - \frac{B}{r} \right) + A_2 \left(B^2 - \frac{B}{r} - \frac{4}{r^2} \right) + C_0 \left(-B^2 r + B + \frac{1}{r} \right) + C_2 \left(B^2 r - 3B - \frac{3}{r} \right) \right] \\
g_4 &= \frac{Et}{2R} e^{-Br} \left[A_2 \left(\frac{1}{2} B^2 + \frac{5B}{2r} + \frac{4}{r^2} \right) + C_2 \left(\frac{1}{2} B^2 r + \frac{3}{2} B + \frac{3}{2} \frac{1}{r} \right) \right]
\end{aligned} \tag{4.12}$$

4.3.5. Complementary and Particular Solution

An inhomogeneous differential equation is solved by determining the complementary (Φ_c) as well as the particular (Φ_p) part of its solution. One solution for Φ_c was derived by J.H. Mitchell in 1899 and can be found on page 246 in reference [69].

$$\begin{aligned}
\Phi_c &= a_0 \ln r + b_0 r^2 + c_0 r^2 \ln r + d_0 r^2 \theta + a'_0 \theta \\
&\quad + \frac{a''_1}{2} r \theta \sin \theta + \left(a_1 r + b_1 r^3 + a'_1 r^{-1} + b'_1 r \ln r \right) \cos \theta \\
&\quad + \frac{c''_1}{2} r \theta \cos \theta + \left(c_1 r + d_1 r^3 + c'_1 r^{-1} + d'_1 r \ln r \right) \sin \theta \\
&\quad + \sum_{n=2}^{\infty} \left[\left(a_n r^n + b_n r^{n+2} + a'_n r^{-n} + b'_n r^{-n+2} \right) \cos n \theta \right] \\
&\quad + \sum_{n=2}^{\infty} \left[\left(c_n r^n + d_n r^{n+2} + c'_n r^{-n} + d'_n r^{-n+2} \right) \sin n \theta \right]
\end{aligned} \tag{4.13}$$

The method of variation of parameters is employed to compute Φ_p . However, this procedure only works for ordinary differential equations (ODEs). Separating the variables in a traditional sense is not possible without considerable effort because of mixed partial derivatives originating from $\nabla^4 \Phi$. Hence, the cosine pattern in (4.11) inspires an educated guess for the particular solution.

$$\Phi_p = h_0(r) + h_2(r) \cos 2\theta + h_4(r) \cos 4\theta \tag{4.14}$$

In a more general way, one may write

$$\Phi_{pm} = h_m(r) \cos m\theta \tag{4.15}$$

Substituting (4.15) on the left-hand side (LHS) of equation (4.11) results in

$$\frac{d^4 h_m}{dr^4} + \frac{2}{r} \frac{d^3 h_m}{dr^3} - \frac{2m^2 + 1}{r^2} \frac{d^2 h_m}{dr^2} + \frac{2m^2 + 1}{r^3} \frac{dh_m}{dr} + \frac{m^4 - 4m^2}{r^4} h_m = g_m \tag{4.16}$$

after dividing by $\cos m\theta$ which is permissible due to the linear independence of the cosine function. Consequently, the problem is reduced to an ODE and the complete particular solution of (4.11) is the sum of all h_m terms ($m = 0, 2, 4$). The complementary solution for the ODE that corresponds to a certain m in (4.16) needed for applying the method of variation of parameters is simply the sum of the factors in front of the respective $\cos m\theta$ term in (4.13) when neglecting θ .

For example, the ODE for $m = 0$ is

$$\frac{d^4 h_0}{dr^4} + \frac{2}{r} \frac{d^3 h_0}{dr^3} - \frac{1}{r^2} \frac{d^2 h_0}{dr^2} + \frac{1}{r^3} \frac{dh_0}{dr} = g_0 \tag{4.17}$$

with the homogeneous solution

$$h_{0c} = C_{01} \ln r + C_{02} r^2 \ln r + C_{03} r^2 + C_{04} \tag{4.18}$$

A particular solution can be determined by evaluating

$$h_m = \sum_{n=1}^N h_{mn}(r) \int \left\{ \frac{g_m(r) W_{mn}(r)}{W_m(r)} \right\} dr \tag{4.19}$$

h_{mn} refers to the variables in the n -th term of the m -th complementary solution and W_m is their Wronskian. W_{mn} is equal to W_m where the n -th column of the corresponding matrix is replaced by zeros except for the last row which contains a one. The disturbance function g_m is already known. For the chosen shape function there will always be four terms in (4.18) as well as in (4.21), and therefore the summation terminates at $N = 4$. Computing (4.19) for $m = 0$ yields

$$h_0 = -\frac{Et}{8RB^3} \left\{ A_0 \left[4Be^{-Br} + 4BEi_1(Br) \right] - A_2 \left[e^{-Br} (B^2r + B) - B^3r^2 Ei_1(Br) \right] + C_0 \left[e^{-Br} (4Br + 12) + 8Ei_1(Br) \right] - C_2 \left[e^{-Br} (2Br + 2) \right] \right\} \quad (4.20)$$

The complementary solutions for $m = 2$ and $m = 4$ are given by

$$\begin{aligned} h_{2c} &= C_{21}r^2 + C_{22}r^4 + C_{23}r^{-2} + C_{24} \\ h_{4c} &= C_{41}r^4 + C_{42}r^6 + C_{43}r^{-4} + C_{44}r^{-2} \end{aligned} \quad (4.21)$$

The particular solutions for h_2 and h_4 are obtained by applying (4.19) again.

$$\begin{aligned} h_2 &= \frac{Et}{8RB^5r^2} e^{-Br} \left\{ A_0 \left[4B^3r^2 + 12B^2r + 12B \right] - A_2 \left[B^4r^3 + 3B^3r^2 + 6B^2r + 6B - B^5r^4 e^{Br} Ei_1(Br) \right] + C_0 \left[4B^3r^3 + 20B^2r^2 + 48Br + 48 \right] - C_2 \left[4B^3r^3 + 12B^2r^2 + 24Br + 24 \right] \right\} \\ h_4 &= \frac{Et}{4RB^7r^4} e^{-Br} \left[A_2 \left(B^5r^4 + 7B^4r^3 + 27B^3r^2 + 60B^2r + 60B \right) + C_2 \left(B^5r^5 + 9B^4r^4 + 48B^3r^3 + 168B^2r^2 + 360Br + 360 \right) \right] \end{aligned} \quad (4.22)$$

Resubstitution of h_m in (4.14) and subsequently in (4.11) satisfies the original PDE. Hence, assuming a particular solution of the type $h_m(r) \cos m\theta$ is appropriate. $Ei_1(Br)$ in equations (4.20) and (4.22) denotes the exponential integral as given in [70] on page 228. Definition 5.1.1 is equivalent to equation (4.23) with a slightly different notation.

$$Ei_1(z) = \int_z^\infty \frac{e^{-t}}{t} dt \quad (4.23)$$

4.3.6. Boundary Value Problem and Stress Resultants

The sum of (4.13) and (4.14) yields the complete solution of the PDE (4.11).

$$\Phi = \Phi_c + \Phi_p \quad (4.24)$$

Boundary conditions provide constraints for the unknown constants in (4.13). These are:

1. Stresses must be periodical with respect to the angular coordinate θ .
2. The strain energy must be bounded, i.e. it cannot go to infinity.
3. Stress components normal to the cutout edge must be equal to zero.

$$N_r(r = a) = 0 \quad (4.25a)$$

$$N_{r\theta}(r = a) = 0 \quad (4.25b)$$

4. Since the analysis is concerned with a local buckling phenomenon, it is assumed that the stress resultants far away from the cutout are negligible.

$$N_r(r \rightarrow \infty) = 0 \quad (4.26a)$$

$$N_\theta(r \rightarrow \infty) = 0 \quad (4.26b)$$

$$N_{r\theta}(r \rightarrow \infty) = 0 \quad (4.26c)$$

Equation (3.61) provides information on how the Airy stress function Φ relates to the stress resultants. The corresponding partial derivatives of Φ are computed, see Appendix A.1, and are assessed with the above requirements in mind. In some cases, there are multiple reasons why a certain constant is dismissible. One argument is obviously sufficient and therefore it is acceptable that the following list is not exhaustive.

I. From (4.26a): r^n terms with $n \geq 0$ are not admissible.

$$b_0 = c_0 = d_0 = b_1 = d_1 = 0$$

II. From (4.26b): r^n terms with $n \geq 0$ are not admissible.

$$a_n = b_n = c_n = d_n = 0 \quad (n \geq 2)$$

III. The constants a_1 and c_1 do not appear in the expressions for the stress resultants. Thus, they may be discarded without loss of generality.

$$a_1 = c_1 = 0$$

IV. From (4.25a): Only $\cos m\theta$ terms may be nonzero.

$$c'_2 = d'_2 = a'_3 = b'_3 = c'_3 = d'_3 = c'_4 = d'_4 = a'_n = b'_n = c'_n = d'_n = 0 \quad (n \geq 5)$$

V. From (4.25b): Only $\cos m\theta$ terms may be nonzero.

$$a'_0 = 0$$

VI. Condition IV. is also satisfied when

$$\begin{aligned} a''_1 r^{-1} - 2a'_1 r^{-3} + b'_1 r^{-1} &= 0 \\ -c''_1 r^{-1} - 2c'_1 r^{-3} + d'_1 r^{-1} &= 0 \end{aligned}$$

After factoring out the squares of the stress resultants according to equation (4.4), a''_1 and b'_1 retain a factor of r^{-1} . The integration limits in the polar reference frame are taken as a and ∞ . It is known that

$$\int_a^\infty r^{-1} dr = [\ln r]_a^\infty = \infty$$

which means that the strain energy becomes unbounded unless all six constants are zero.

$$a''_1 = a'_1 = b'_1 = c''_1 = c'_1 = d'_1 = 0$$

Consequently, the Airy stress function simplifies to

$$\Phi = [a_0 \ln r + h_0(r)] + [a'_2 r^{-2} + b'_2 + h_2(r)] \cos 2\theta + [a'_4 r^{-4} + b'_4 r^{-2} + h_4(r)] \cos 4\theta \quad (4.27)$$

The remaining constants are determined from the boundary conditions (4.25a) and (4.25b) which must hold for all θ . In other words: the factors of $\cos m\theta$ of the stress resultants in Appendix A.1 have to be equal to zero. This yields five equations for five unknowns as a_0 does not appear in the expression for $N_{r\theta}$. The values of a_0 , a'_2 , b'_2 , a'_4 , and b'_4 are presented in Appendix A.2.

Having calculated all constants, the compatibility equation is solved and it is possible to compute explicit functions for the stress resultants in the buckled configuration using equations (3.61) and (4.27).

$$\begin{aligned} N_r &= k_{11}(r) + k_{12}(r) \cos 2\theta + k_{13}(r) \cos 4\theta \\ N_\theta &= k_{21}(r) + k_{22}(r) \cos 2\theta + k_{23}(r) \cos 4\theta \\ N_{r\theta} &= k_{31}(r) + k_{32}(r) \sin 2\theta + k_{33}(r) \sin 4\theta \end{aligned} \quad (4.28)$$

The coefficients k_{ij} are specified in Appendix A.3.

4.3.7. Energy Minimization with the Ritz Method

Now that all terms in equations (4.4), (4.5), and (4.6) are known, the total potential energy of the shell may be determined through integration. Terms with trigonometric functions that are orthogonal in the interval $[0, 2\pi]$ can be removed because their integrals are zero. $B, r \leq 0$ does not make any physical sense and therefore the product of these variables must be positive. Thus, an alternative formulation of the exponential integral, namely definition 5.1.2 from [70], can be substituted.

$$\text{Ei}_1(Br) = -\text{Ei}(-Br) \quad (4.29)$$

This makes it possible to evaluate some additional definite integrals in equation (4.4) so that any type of numerical integration as in Starnes' solution is avoided. After completing the integration, the original exponential integral (4.23) is resubstituted by applying (4.29) again.

The buckling load of the cylindrical shell is subsequently approximated by minimizing the total potential energy with the Ritz method which is discussed in Subsection 3.6. The presence of four undetermined coefficients requires taking four partial derivatives and setting each of them equal to zero.

$$\frac{\partial \Pi}{\partial A_0} = 0 \quad \frac{\partial \Pi}{\partial A_2} = 0 \quad \frac{\partial \Pi}{\partial C_0} = 0 \quad \frac{\partial \Pi}{\partial C_2} = 0 \quad (4.30)$$

Like terms are collected and assembled to form the matrices in (4.31).

$$\mathbf{K}^M \begin{Bmatrix} A_0 \\ A_2 \\ C_0 \\ C_2 \end{Bmatrix} = \tau_{\text{cr}} \mathbf{K}^G \begin{Bmatrix} A_0 \\ A_2 \\ C_0 \\ C_2 \end{Bmatrix} \quad (4.31)$$

Equation (4.31) is recognized as the generalized eigenvalue problem where the buckling stress τ_{cr} is a multiple of the applied far-field stress τ_{∞} which is conveniently chosen as 1 MPa. The components of \mathbf{K}^M and \mathbf{K}^G are given in Appendix A.4. Both matrices are symmetric because the expression for the total potential energy Π only contains second-order terms of the undetermined Ritz coefficients. Furthermore, \mathbf{K}^M scales with the material stiffness while \mathbf{K}^G depends on the applied load, i.e. there is some resemblance of features present in the material and the geometric stiffness matrices from a linear buckling analysis in FEM.

Unfortunately, the presence of the exponential integral prohibits the analytical calculation of the eigenvalues of (4.31). Moreover, they are still a function of B and need to be minimized with respect to this parameter as well. Hence, a numerical procedure is adopted. The function "eig" from the Matlab software package automatically solves the generalized eigenvalue problem with a Choleksy factorization of the matrix on the RHS of (4.31). This is a standard algorithm when the both matrices in equation (4.31) are symmetric [71]. Minimization of τ_{cr} with respect to B is subsequently achieved with a brute force approach.

4.4. Quasi-Isotropic, Symmetric, Composite Shells

The analytical solution for isotropic shells is extended to quasi-isotropic, symmetric, composite cylindrical shells by accounting for the more general formulation of the corresponding constitutive relations. The approach outlined in Figure 4.2 is still applicable, but the derivation of the membrane strain energy in Subsection 4.4.1 requires deriving the shell compatibility equation in a different manner. Furthermore, the formulation of the bending strain energy in Subsection 4.4.2 becomes more complex because both the strain and the stiffness tensor depend on the orientation of the reference frame while the number of bending stiffness terms increases. Subsections 4.4.3 and 4.4.4 discuss the remaining procedure which remains mostly unchanged.

4.4.1. Membrane Strain Energy

An equation for the membrane strain energy U_m is derived by combining (3.18) and (3.25) considering the subscripts of the semi-geodesic polar coordinates which yields

$$U_m = \frac{1}{2} \iint \left[\left(a'_{11} N_r^2 + 2a'_{12} N_r N_\theta + 2a'_{16} N_r N_{r\theta} + a'_{22} N_\theta^2 + 2a'_{26} N_\theta N_{r\theta} + a'_{66} N_{r\theta}^2 \right) r \right] dr d\theta \quad (4.32)$$

where a'_{ij} represent the compliance matrix elements expressed in the coordinate system r, θ . They are determined by inverting the transformed extensional stiffness matrix \mathbf{A}' instead of the converted \mathbf{ABD}' matrix because all elements of \mathbf{B}' are zero for symmetric laminates. Since the laminate stiffness properties are

often calculated in the x, y reference frame illustrated in Figure 4.1, it is desirable to express the solution in such coordinates. Thus, the transformation for fourth-order tensors from Section 3.9 must be applied to the original extensional stiffness matrix \mathbf{A} . Before doing so, \mathbf{A} is simplified by noting that the relations between the individual elements of \mathbf{A} are the same for quasi-isotropic laminates and isotropic materials, i.e. there are only 2 independent elastic constants.

$$A_{11} = A_{22} \quad A_{16} = A_{26} = 0 \quad A_{66} = \frac{A_{11} - A_{12}}{2} \quad (4.33)$$

Substituting these expressions in \mathbf{A} , considering Voigt notation, and multiplying the obtained vector with the transformation matrix \mathbf{T}_{4D} from (3.49c) returns

$$\mathbf{A} = \mathbf{A}' = \begin{bmatrix} A_{11} & A_{12} & 0 \\ A_{12} & A_{11} & 0 \\ 0 & 0 & \frac{A_{11} - A_{12}}{2} \end{bmatrix} \quad (4.34)$$

This result is expected because the in-plane stiffness properties of isotropic materials and quasi-isotropic laminates are identical in every direction and consequently do not change when switching between different reference frames. Due to $\mathbf{A} = \mathbf{A}'$, the compliance matrices \mathbf{a} and \mathbf{a}' obtained through inversion are also equal.

$$\mathbf{a} = \mathbf{a}' = \begin{bmatrix} \frac{A_{11}}{A_{11}^2 - A_{12}^2} & -\frac{A_{12}}{A_{11}^2 - A_{12}^2} & 0 \\ -\frac{A_{12}}{A_{11}^2 - A_{12}^2} & \frac{A_{11}}{A_{11}^2 - A_{12}^2} & 0 \\ 0 & 0 & \frac{2}{A_{11} - A_{12}} \end{bmatrix} \quad (4.35)$$

Substituting the entries of (4.35) in equation (4.32) yields

$$U_m = \frac{1}{2} \iint \left\{ \left[\frac{A_{11}}{A_{11}^2 - A_{12}^2} (N_r^2 + N_\theta^2 + 2N_r N_\theta) - 2 \frac{A_{12}}{A_{11}^2 - A_{12}^2} (N_r N_\theta - N_{r\theta}^2) \right] r \right\} dr d\theta \quad (4.36)$$

Just as in Section 4.3, the next step is to determine the stress resultants of U_m in (4.36) for integration. Again, the linear version of the compatibility equation (3.43) is formulated, and the compliance matrix elements are replaced with expressions from (4.35). Furthermore, the fourth-order derivatives are transformed to the polar semi-geodesic coordinate system. Because the laminate is quasi-isotropic, the stiffness terms in equation (4.37) are constant. If this was not the case, the governing PDE would have variable coefficients in which case determining a solution is substantially more complex.

$$\frac{A_{11}}{A_{11}^2 - A_{12}^2} \left(\frac{\partial^2}{\partial r^2} + \frac{1}{r} \frac{\partial}{\partial r} + \frac{1}{r^2} \frac{\partial^2}{\partial \theta^2} \right) \left(\frac{\partial^2 \Phi}{\partial r^2} + \frac{1}{r} \frac{\partial \Phi}{\partial r} + \frac{1}{r^2} \frac{\partial^2 \Phi}{\partial \theta^2} \right) = -\frac{1}{R} \frac{\partial^2 w}{\partial x^2} \quad (4.37)$$

The two terms in parentheses on the LHS of equation (4.37) may be rewritten as $\nabla^4 \Phi$. Bringing the \mathbf{A} matrix entries to the RHS and converting the partial derivative there as well yields

$$\nabla^4 \Phi = -\frac{1}{R} \frac{A_{11}^2 - A_{12}^2}{A_{11}} \left[\sin^2 \theta \frac{\partial^2 w}{\partial r^2} + \cos^2 \theta \left(\frac{1}{r} \frac{\partial w}{\partial r} + \frac{1}{r^2} \frac{\partial^2 w}{\partial \theta^2} \right) - \sin 2\theta \left(\frac{1}{r^2} \frac{\partial w}{\partial \theta} - \frac{1}{r} \frac{\partial^2 w}{\partial r \partial \theta} \right) \right] \quad (4.38)$$

The only difference between the compatibility equations (4.11) and (4.38) are the respective stiffness terms. In fact, it would have been equally valid to substitute the Young's modulus of the isotropic material with the equivalent in-plane laminate stiffness property of a quasi-isotropic composite E_m , which is defined in equation (4.39), to arrive at the expression in (4.38).

$$E_m = \frac{A_{11}^2 - A_{12}^2}{t A_{11}} \quad (4.39)$$

Consequently, the solution to the compatibility equation for the quasi-isotropic composite is given by substituting equation (4.39) in the particular solution terms h_0 , h_2 , and h_4 in (4.20) and (4.22) as well as modifying the constants a_0 , a'_2 , b'_2 , a'_4 , and b'_4 of the complementary solution in Appendix A.2 accordingly.

4.4.2. Bending Strain Energy

A new expression for the bending strain energy contribution U_b is obtained by following the derivation of U in Section 3.4, but with the subscripts r, θ instead of x, y .

$$U_b = \frac{1}{2} \iint \left[\left(D'_{11} \kappa_{rr}^2 + 2D'_{12} \kappa_{rr} \kappa_{\theta\theta} + 4D'_{16} \kappa_{rr} \kappa_{r\theta} + D'_{22} \kappa_{\theta\theta}^2 + 4D'_{26} \kappa_{\theta\theta} \kappa_{r\theta} + 4D'_{66} \kappa_{r\theta}^2 \right) r \right] dr d\theta \quad (4.40)$$

Like in the previous segment, the stiffness tensor is rotated such that one can formulate the transformed bending stiffness matrix components D'_{ij} as a function of D_{ij} . Additional relations between the bending stiffness elements of quasi-isotropic laminates do not exist, so a simplification analogous to (4.33) is not possible. As a consequence, the following transformation equations are more complex than those for the in-plane relations. It is noted that they also incorporate the bending-twisting coupling terms D_{16} and D_{26} which are often neglected in analytical solutions for reasons of simplicity as indicated by Kassapoglou [72].

$$\begin{aligned} D'_{11} &= \frac{1}{8} (3D_{11} + 2D_{12} + 3D_{22} + 4D_{66}) - (D_{16} + D_{26}) \sin 2\theta - \frac{1}{2} (D_{11} - D_{22}) \cos 2\theta \\ &\quad + \frac{1}{2} (D_{16} - D_{26}) \sin 4\theta + \frac{1}{8} (D_{11} - 2D_{12} + D_{22} - 4D_{66}) \cos 4\theta \\ D'_{12} &= \frac{1}{8} (D_{11} + 6D_{12} + D_{22} - 4D_{66}) - \frac{1}{2} (D_{16} - D_{26}) \sin 4\theta - \frac{1}{8} (D_{11} - 2D_{12} + D_{22} - 4D_{66}) \cos 4\theta \\ D'_{16} &= -\frac{1}{4} (D_{11} - D_{22}) \sin 2\theta + \frac{1}{2} (D_{16} + D_{26}) \cos 2\theta \\ &\quad + \frac{1}{8} (D_{11} - 2D_{12} + D_{22} - 4D_{66}) \sin 4\theta - \frac{1}{2} (D_{16} - D_{26}) \cos 4\theta \\ D'_{22} &= \frac{1}{8} (3D_{11} + 2D_{12} + 3D_{22} + 4D_{66}) + (D_{16} + D_{26}) \sin 2\theta + \frac{1}{2} (D_{11} - D_{22}) \cos 2\theta \\ &\quad + \frac{1}{2} (D_{16} - D_{26}) \sin 4\theta + \frac{1}{8} (D_{11} - 2D_{12} + D_{22} - 4D_{66}) \cos 4\theta \\ D'_{26} &= -\frac{1}{4} (D_{11} - D_{22}) \sin 2\theta + \frac{1}{2} (D_{16} + D_{26}) \cos 2\theta \\ &\quad - \frac{1}{8} (D_{11} - 2D_{12} + D_{22} - 4D_{66}) \sin 4\theta + \frac{1}{2} (D_{16} - D_{26}) \cos 4\theta \\ D'_{66} &= \frac{1}{8} (D_{11} - 2D_{12} + D_{22} + 4D_{66}) - \frac{1}{2} (D_{16} - D_{26}) \sin 4\theta - \frac{1}{8} (D_{11} - 2D_{12} + D_{22} - 4D_{66}) \cos 4\theta \end{aligned} \quad (4.41)$$

Combining the transformation matrix \mathbf{T}_{2D} , the strain-displacement relations (3.6), as well as the partial derivatives (3.56), (3.57), and (3.58) allows determining expressions for the curvature contribution of the strains in the polar semi-geodesic coordinate system.

$$\begin{aligned} \kappa_{rr} &= -\frac{1}{2} \left(\frac{\partial^2 w}{\partial r^2} + \frac{1}{r} \frac{\partial w}{\partial r} + \frac{1}{r^2} \frac{\partial^2 w}{\partial \theta^2} \right) + \left(\frac{1}{r} \frac{\partial^2 w}{\partial r \partial \theta} - \frac{1}{r^2} \frac{\partial w}{\partial \theta} \right) \sin 4\theta - \frac{1}{2} \left(\frac{\partial^2 w}{\partial r^2} - \frac{1}{r} \frac{\partial w}{\partial r} - \frac{1}{r^2} \frac{\partial^2 w}{\partial \theta^2} \right) \cos 4\theta \\ \kappa_{\theta\theta} &= -\frac{1}{2} \left(\frac{\partial^2 w}{\partial r^2} + \frac{1}{r} \frac{\partial w}{\partial r} + \frac{1}{r^2} \frac{\partial^2 w}{\partial \theta^2} \right) - \left(\frac{1}{r} \frac{\partial^2 w}{\partial r \partial \theta} - \frac{1}{r^2} \frac{\partial w}{\partial \theta} \right) \sin 4\theta + \frac{1}{2} \left(\frac{\partial^2 w}{\partial r^2} - \frac{1}{r} \frac{\partial w}{\partial r} - \frac{1}{r^2} \frac{\partial^2 w}{\partial \theta^2} \right) \cos 4\theta \\ \kappa_{r\theta} &= -\frac{1}{2} \left(\frac{\partial^2 w}{\partial r^2} - \frac{1}{r} \frac{\partial w}{\partial r} - \frac{1}{r^2} \frac{\partial^2 w}{\partial \theta^2} \right) \sin 4\theta - \left(\frac{1}{r} \frac{\partial^2 w}{\partial r \partial \theta} - \frac{1}{r^2} \frac{\partial w}{\partial \theta} \right) \cos 4\theta \end{aligned} \quad (4.42)$$

Substituting equations (4.41) and (4.42) back into (4.40) yields an equation that describes the bending strain energy contribution with known terms that may be integrated.

4.4.3. Energy Contribution of External Forces

The most accurate quantification of the prebuckling membrane stress distribution contribution to the total potential energy for a laminated composite would consist of calculating V for every ply and subsequently adding up the energy of all laminas. However, the fact that the laminate is quasi-isotropic means that computing V as expressed in equation (4.10) provides the same final energy quantity due to the assumption of a pure membrane stress state in the prebuckling domain. Hence, equation (4.10) may be reused for the quasi-isotropic case.

4.4.4. Final Steps

At this point, expressions for U_m , U_b , and V with known terms are available which can be integrated as described in Subsection 4.3.7 to determine the total potential energy of the structure. Afterwards, the final steps, i.e. the energy minimization with the Ritz method and the calculation of the eigenvalues with Matlab, remain unchanged. Naturally, \mathbf{K}^M and \mathbf{K}^G feature different entries than for the isotropic shell. These are presented in Appendix B. They simplify to the matrix elements of the isotropic solution when the equivalent stiffness terms from equation (3.19) are substituted.

4.5. Shape Function Modification

It is desirable to define the shape function (4.1) in a more general form in order to capture structural behavior that is more complex. This is useful when describing buckling modes of composite shells. Consequently, the displacement function may be converted into a Fourier series in θ . Furthermore, Figure 2.8 suggests that higher order terms of r may be required to describe the displacement field, so an improved shape function should feature a power series in r . An appropriate double series is given by

$$w(r, \theta) = e^{-Br} \sum_{m=0}^M \sum_{n=0}^N [A_{2n}(m) r^m \cos 2n\theta] \quad (4.43)$$

where $A_{2n}(m) = A_{2n}, C_{2n}, E_{2n}, \dots$ for $m, n = 0, 1, 2, \dots$. The original shape function is then obtained by setting $M = N = 1$. As mentioned earlier, the energy of the system approximated with the Ritz method approaches the energy of the real solution if M and N tend to infinity. As such, solutions for displacement functions that correspond to larger M and N are of interest for convergence studies.

First, it is assumed that $N = 1 = \text{const.}$ so that the consequences of increasing M can be investigated. Larger M result in higher powers of r in $w(r, \theta)$ and introduce additional undetermined Ritz coefficients. Thus, the partial derivatives of the transformed equations for U_b and V contain higher order terms of r . The same effect is observed for the RHS of the linear compatibility equation (4.11). Hence, the expressions for g_m change which in turn yields a new particular solution h_m for the PDE as suggested by equation (4.19). The complementary solution is only modified in so far as that the constants $a_0, a'_2, b'_2, a'_4, b'_4$ have to offset the new h_m . Consequently, the coefficients k_{ij} in equation (4.28) differ from their previous formulation. The increased number of Ritz coefficients requires calculating more partial derivatives when minimizing the total potential energy of the structure. Therefore, the dimensions of \mathbf{K}^M and \mathbf{K}^G grow depending on the value of N . More specifically, these matrices are of the size $(M + N + 2) \times (M + N + 2)$. Overall, the solution procedure does not require elaborate modifications if M is increased. However, one has to pay a higher price for the calculation of eigenvalues and eigenvectors as the computational complexity of this procedure is of the order $O(n^3)$ where n is the dimension of the matrices \mathbf{K}^M and \mathbf{K}^G .

Additional cosine terms are considered by setting $M = 1 = \text{const.}$ while modifying N . Most of the observations made for the previous case hold true. A major difference is the fact that raising N by one adds another g_m term due to the nature of the disturbance function in the compatibility equation (4.11). Thus, the homogeneous solution (4.13) has to provide additional constants such that the force equilibrium at the cutout edge is satisfied, i.e. one further k_{ij} term is needed to define each stress resultant. Consequently, the difficulty of determining the definite integrals increases significantly as a larger number of more complex integrals have to be solved. For example,

$$\int_a^\infty \left[e^{-Br} \text{Ei}(-Br) r^{-3} \right] dr \quad (4.44)$$

does not appear to be solvable analytically. Furthermore, the solution of

$$\int_a^\infty \left[\text{Ei}(-Br) r^{-1} \right] dr \quad (4.45)$$

contains the generalized hypergeometric function $\text{hypergeom}(i, j, k)$ as well as the Euler-Mascheroni constant γ . Even though these integrals can be evaluated numerically, they significantly add to the cost of the analytical solution. Technically, they are also present when the shape function only features $\cos 2\theta$, but they do not appear in the final expression of the membrane strain energy because of identical terms with opposite signs. Moreover, their inclusion leads to a very large equation for U_m and consequently the size of the matrix entries of \mathbf{K}^M increases considerably. As a result, the quality of the solution cannot be assessed in a feasible manner which is why only the modification of the shape function with respect to r is discussed in Chapters 6 and 7.

5

Finite Element Models

This chapter describes the design of the FE models that are used for the verification of the analysis presented in Chapter 4. Section 5.1 focuses on the generation of the shell geometry including the cutout. Material properties of isotropic and composite cylindrical shells are presented in Section 5.2. The element type selection as well as the shell discretization are subject of Section 5.3 while Section 5.4 covers the considered boundary conditions. Finally, the three FE analysis procedures employed to predict the buckling of cylindrical shells with circular cutouts are discussed in Section 5.5.

5.1. Geometry

The software Abaqus by Dassault Systèmes was chosen for all stages of a typical numerical analysis with FEM, i.e. solving the governing matrix equations as well as pre- and post-processing.

Naturally, the first step is to create the geometry of the shell considering the circular opening. For this purpose, a 3D cylindrical shell is generated by extruding a circle. Next, the body is cut with a solid tube whose base is a circle the size of the cutout. Even though this does not result in a perfect curvilinear circular opening which is modeled with the semi-geodesic polar coordinate system in the analytical solution, it is nonetheless a very good approximation. An exemplary shell is depicted in Figure 5.1 where the partitions for meshing are already visible.

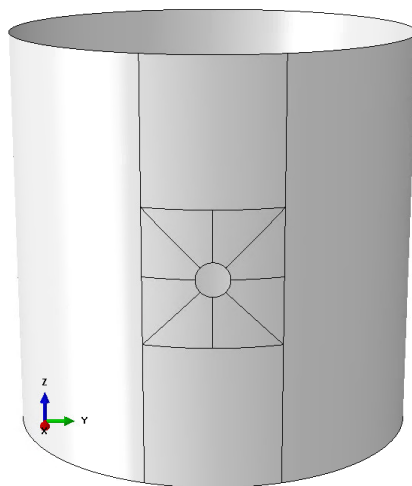


Figure 5.1: A cylindrical shell with a circular cutout in Abaqus.

The buckling loads predicted by the analysis are compared with the results from Abaqus for certain shell and cutout dimensions. Two different sets of geometric parameters are considered, one for the isotropic cylindrical shells and one for the quasi-isotropic shells. Starnes [18] reported both experimental as well as analytical results in his Ph.D. dissertation. These constitute a valuable data set for verification and validation

purposes. Hence, it makes sense to size the FE cylindrical shells so that they match Starnes' specimens. His Mylar shells, which accounted for the vast majority of tested cylindrical shells, had a diameter of 8 inches. A shell length of 203.2 mm is assumed so that a length-to-radius ratio of $L/R = 2$ is obtained. Table IV in Starnes' dissertation provides further geometric properties which are used to compute the remaining geometric parameters. All configurations considered for isotropic cylindrical shells are summarized in Table 5.1.

$L = 203.2 \text{ mm}, R = 101.6 \text{ mm}$											
$R/t = 100$			$R/t = 200$			$R/t = 400$			$R/t = 800$		
No.	a [mm]	α [-]	No.	a [mm]	α [-]	No.	a [mm]	α [-]	No.	a [mm]	α [-]
I1.1	1.017	0.1	I2.1	1.012	0.14	I3.1	1.017	0.2	I4.1	1.016	0.28
I1.2	2.034	0.2	I2.2	2.031	0.28	I3.2	2.034	0.4	I4.2	2.035	0.57
I1.3	3.052	0.3	I2.3	3.051	0.42	I3.3	4.069	0.8	I4.3	3.051	0.85
I1.4	4.069	0.4	I2.4	4.071	0.57	I3.4	6.092	1.2	I4.4	4.071	1.13
I1.5	6.103	0.6	I2.5	6.102	0.85	I3.5	8.104	1.6	I4.5	6.086	1.69
I1.6	8.138	0.8	I2.6	8.141	1.13	I3.6	10.17	2.0	I4.6	8.141	2.27
I1.7	10.17	1.0	I2.7	10.12	1.41	I3.7	14.25	2.8	I4.7	10.20	2.84
I1.8	12.18	1.2	I2.8	12.17	1.69	I3.8	16.26	3.2	I4.8	12.17	3.39
I1.9	14.20	1.4	I2.9	14.23	1.98	I3.9	18.28	3.6	I4.9	14.23	3.96
I1.10	16.21	1.6	I2.10	16.28	2.27	I3.10	20.34	4.0			
I1.11	18.33	1.8	I2.11	18.26	2.54						
I1.12	20.34	2.0	I2.12	20.39	2.84						

Table 5.1: Geometric parameters for isotropic cylindrical shells.

The verification of the analytical results for quasi-isotropic, symmetric laminates is performed with the shell dimensions that are presented in Table 5.2. They are practically identical to those listed in the previous table but rounded to more appealing numbers.

$L = 200 \text{ mm}, R = 100 \text{ mm}$											
$R/t = 100$			$R/t = 200$			$R/t = 400$			$R/t = 800$		
No.	a [mm]	α [-]	No.	a [mm]	α [-]	No.	a [mm]	α [-]	No.	a [mm]	α [-]
QI1.1	1.0	0.1	QI2.1	1.0	0.14	QI3.1	1.0	0.2	QI4.1	1.0	0.28
QI1.2	2.0	0.2	QI2.2	2.0	0.28	QI3.2	2.0	0.4	QI4.2	2.0	0.57
QI1.3	3.0	0.3	QI2.3	3.0	0.42	QI3.3	4.0	0.8	QI4.3	3.0	0.85
QI1.4	4.0	0.4	QI2.4	4.0	0.57	QI3.4	6.0	1.2	QI4.4	4.0	1.13
QI1.5	6.0	0.6	QI2.5	6.0	0.85	QI3.5	8.0	1.6	QI4.5	6.0	1.69
QI1.6	8.0	0.8	QI2.6	8.0	1.13	QI3.6	10.0	2.0	QI4.6	8.0	2.27
QI1.7	10.0	1.0	QI2.7	10.0	1.41	QI3.7	14.0	2.8	QI4.7	10.0	2.83
QI1.8	12.0	1.2	QI2.8	12.0	1.69	QI3.8	16.0	3.2	QI4.8	12.0	3.39
QI1.9	14.0	1.4	QI2.9	14.0	1.98	QI3.9	18.0	3.6	QI4.9	14.0	3.96
QI1.10	16.0	1.6	QI2.10	16.0	2.26	QI3.10	20.0	4.0			
QI1.11	18.0	1.8	QI2.11	18.0	2.55						
QI1.12	20.0	2.0	QI2.12	20.0	2.83						

Table 5.2: Geometric parameters for composite shells.

5.2. Material Properties

The analysis in Chapter 4 is capable of estimating the buckling load for isotropic and quasi-isotropic composite shells. Mylar is selected to represent the isotropic material in accordance with Starnes' buckling tests, whereas Hexcel IM7-8552 is the material of choice for the composite plies.

Starnes determined the modulus of elasticity of his Mylar specimens through experiments in a tensile testing machine. He reported an average Young's modulus of $7.25 \cdot 10^5$ psi. No measurements were conducted

to specify the Poisson's ratio ν . Instead, Starnes assumed $\nu = 0.3$. Since he did not document the density of the material, a value of $\rho_{\text{Mylar}} = 1.38 \text{ g/cm}^3$ [73] is presumed. Even though Mylar does not feature all the typical characteristics of an isotropic material, it will be idealized as one to remain consistent with Starnes' assumptions. The material properties of the thermoplastic are given in Table 5.3.

E [MPa]	ν [-]	ρ [g/cm ³]
4998.7	0.3	1.38

Table 5.3: Material properties of Mylar.

Hexcel IM7-8552 is a frequently used composite where carbon fibers are embedded in an epoxy matrix. Its material properties were determined by Camanho et al. [74] according to ASTM standards as part of an investigation on the damage propagation in notched laminates. They reported mean values for the elastic in-plane properties but did not include any value for the average laminate density. However, they stated that the average fiber volume fraction of their specimens was equal to 59.1%. Thus, the average ply density may be approximated by assuming $\rho_{CF} = 1.9 \text{ g/cm}^3$ and $\rho_{\text{Epoxy}} = 1.3 \text{ g/cm}^3$ for the density of carbon fiber and epoxy, respectively. Furthermore, the definition of composite plies with engineering constants in Abaqus requires information about out-of-plane properties. These are also not available and therefore estimated with the relations in equation (5.1).

$$E_2 = E_3 \quad G_{12} = G_{13} \quad G_{23} = \frac{G_{12}}{2} \quad \nu_{12} = \nu_{13} \quad \nu_{23} = 2\nu_{12} \quad (5.1)$$

Even if the elastic out-of-plane properties are only approximated, their influence on the final buckling load is negligible as explained in Section 5.3. Anyhow, the relevant material properties of Hexcel IM7-8552 are summarized in Table 5.4.

E_1 [MPa]	E_2 [MPa]	E_3 [MPa]	G_{12} [MPa]	G_{13} [MPa]	G_{23} [MPa]
171000	9080	9080	5300	5300	2650
	ν_{12} [-]	ν_{13} [-]	ν_{23} [-]	ρ [g/cm ³]	
	0.32	0.32	0.64	1.654	

Table 5.4: Material properties of Hexcel IM7-8552.

5.3. Element Types and Meshing

The shell geometry is idealized with S4R elements from the Abaqus element library. A number of cylindrical shells are also discretized with S4 elements to evaluate its influence on the buckling load in Subsection 6.2.1. S4 and S4R are general-purpose, conventional, finite-strain shell elements where each of the four nodes features six DOFs. Their strain-displacement formulation approximates the Koiters-Sanders shell theory [75]. While the S4 element features four integration points, this number reduces to one for S4R elements. Consequently, the S4 element is more computationally expensive, but in return not prone to hourglassing. However, hourglass control is available for elements with reduced integration. In any case, both elements provide accurate solutions to problems where thin and thick shells are modeled [76]. Transverse shear deformations are negligible in thin shells, i.e. corresponding stiffness properties have little influence on the structural response. Furthermore, conventional shell elements make use of the plane stress assumption which further reduces the effect of out-of-plane stiffness properties.

To set up the calculation of the matrices presented in Section 5.5, the shell geometry has to be discretized. From earlier discussions it is clear that rapidly varying stresses can be expected in the vicinity of the cutout. Consequently, this area must feature a relatively fine mesh. Depending on the dimensions of the opening, a square partition with an edge length of three or four times the size of the cutout diameter is created. The vertical boundaries are extended until they intersect with the curves of the shell edges and the square partition is split into eight parts as shown in Figure 5.1. Mesh seeds are introduced at the shell edges as well as on all visible curves in the cutout vicinity. Seeds on lines that connect the boundary of the opening to the edges of

the square partition feature a single bias of five towards the opening. All other mesh seeds are not biased. The entire pre-processing is automated with custom Python scripts for all combinations of geometry, material properties, element types, boundary conditions, and analysis procedures. Consequently, the exact number of elements for a given seed can be calculated such that a prescribed mesh size is obtained at the edges of the square partition. A structured mesh is created for the partition around the cutout while the mesh control is set to 'free' for the remaining shell geometry.

The final result is presented in Figure 5.2 considering a characteristic mesh size of 4.5 mm. The elements in the vicinity of the cutout are small enough to capture the high stress gradients, and the remaining geometry is meshed with sufficiently large elements as to not increase computational cost needlessly.

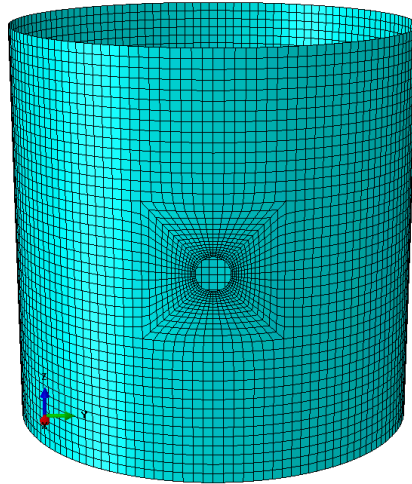


Figure 5.2: The discretized shell geometry.

5.4. Boundary Conditions

The boundary conditions applied to the shell are shown in Figure 5.3 for displacement- as well as force-controlled loading. Clamped shell edges are modeled. Consequently, all nodal DOFs at the two shell edges are restricted with the exception of U_3 at the upper shell edge. The same is true for the reference point in the case of force loading. In contrast, the cutout boundaries are not constrained and therefore they are able to deform freely.

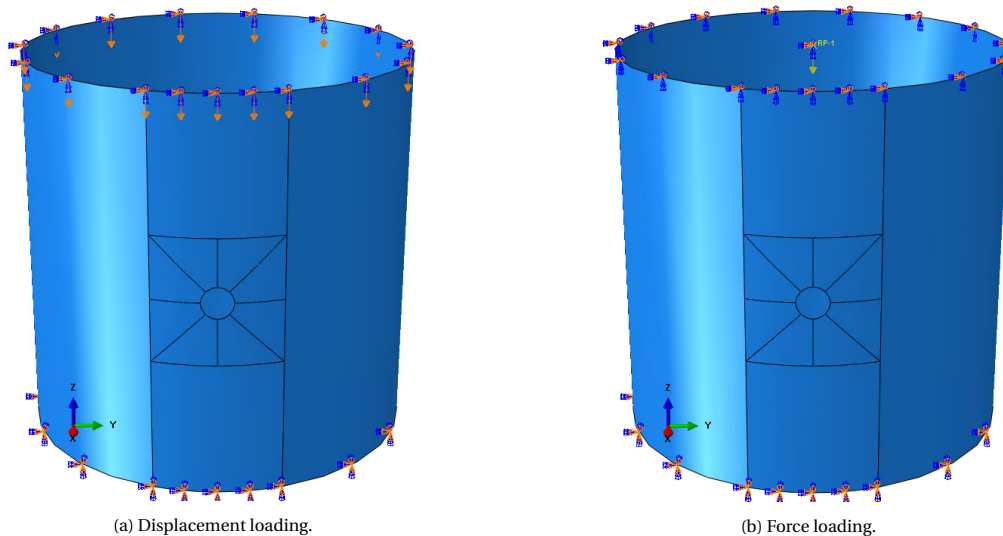


Figure 5.3: Boundary conditions and different load applications.

Usually, structures are loaded in displacement control mode so that more conclusive load-displacement curves can be obtained. However, the analysis in Chapter 4 assumes a force control setting. Hence, both load applications are modeled to investigate possible differences. Displacement-controlled loading is achieved by applying a uniform displacement at the topmost row of nodes of the shell. In contrast, force loading is realized by prescribing a concentrated force on a centrally located reference point and subsequently distributing the load equally to the aforementioned node set with a kinematic coupling constraint. For both cases the load application is purely axial, i.e. in negative z -direction in Figure 5.3.

5.5. Analysis Types

Several different numerical algorithms are available to predict buckling, each one of them with their distinct advantages and drawbacks. To evaluate the performance of the solution procedure presented in Chapter 4, a linear eigenvalue analysis is performed for direct comparison. Some shortcomings of a linear eigenvalue analysis can be overcome with either a nonlinear static or a nonlinear dynamic simulation. Hence, these are also considered. Furthermore, evaluating the predictions from the nonlinear procedures can provide additional insights regarding the mechanisms governing the buckling behavior of cylindrical shells with circular cutouts.

5.5.1. Linear Eigenvalue Analysis

As stated earlier, a linear bifurcation analysis may be performed by solving an eigenvalue problem. Its output is the point on the load-displacement curve where the equilibrium path bifurcates.

$$\left(\mathbf{K}^M + \lambda_{cr}^n \mathbf{K}^G \right) \mathbf{u}^n = \mathbf{0} \quad (5.2)$$

The variables in equation (5.2) are the material stiffness matrix \mathbf{K}^M , the n -th eigenvalues λ_{cr}^n , the geometric stiffness matrix \mathbf{K}^G , and the n -th eigenvectors \mathbf{u}^n . The components of \mathbf{K}^M are determined with the strain-displacement matrix \mathbf{B} and the stiffness tensor \mathbf{C} . \mathbf{B} is constant for a given geometry when linear strains, i.e. small displacements, are assumed. \mathbf{K}^G scales linearly with the applied load.

The problem is solved when an eigenvalue λ_{cr}^n causes the term in parentheses $\mathbf{K}^M + \lambda_{cr}^n \mathbf{K}^G$, which is equal to the stiffness matrix \mathbf{K} , to become singular. The critical buckling load is then given by multiplying λ_{cr}^n with the applied load. Hence, an arbitrary displacement or concentrated force may be prescribed, and the buckling load can almost always be calculated. The eigenvectors \mathbf{u}^n that correspond to the eigenvalues λ_{cr}^n can be interpreted as the mode shapes of the buckled structure.

A limitation of the procedure is that buckling loads tend to be overestimated because a linear prebuckling response is assumed. This is not necessarily the case for real structures, especially not for imperfection-sensitive ones. Moreover, eigenvectors are not unique and therefore the displacement field, and as a result the stress field, of the buckled structure can only be predicted as normalized quantities with unknown magnitudes. Additionally, a linear buckling analysis is by definition not able to capture nonlinear effects.

Abaqus provides two eigenvalues extraction algorithms that approximate λ_{cr}^n , namely the Lanczos and the subspace method. For most considered simulations less than 20 eigenvalues are requested in which case it is recommended to use the subspace procedure [76].

5.5.2. Nonlinear Static Analysis

A static analysis is governed by

$$\mathbf{K}\mathbf{u} = \mathbf{f} \quad (5.3)$$

where $\mathbf{K} = \mathbf{K}^M + \mathbf{K}^G$ is the tangent stiffness matrix, while \mathbf{u} and \mathbf{f} denote the displacement and external force vector, respectively. Nonlinear behavior is modeled when \mathbf{B} and \mathbf{C} are not assumed to be constant. The strain-displacement matrix then becomes a function of the displacement vector and the stiffness tensor depends on the stress tensor $\boldsymbol{\tau}$. From the first modification it follows that the equilibrium equations are satisfied on the deformed structure. The second nonlinearity allows modeling effects like plasticity. As a result, displacement and stress fields obtained from nonlinear analyses are reasonably accurate if the model accounts for the effects that govern the structural response.

Stating the obvious, the main difference between the linear eigenvalue and the nonlinear static analysis is that nonlinear effects are considered. Any static or dynamic solver computes the structural response until the initially prescribed load is reached, even if buckling has not occurred yet. Thus, the buckling load prediction

from the linear eigenvalue analysis is typically used as an input for the nonlinear procedure to guarantee that unstable behavior on the equilibrium path is encountered.

When predicting the buckling of cylindrical shells with nonlinear procedures, it is common practice to introduce initial geometric imperfections in the shape of the eigenmodes from the linear eigenvalue analyses into the model. Unless specifically mentioned, these are not included.

Again, one may choose between two algorithms that solve the nonlinear equation (5.3) for the displacement vector \mathbf{u} . The NR method is a gradient-based algorithm whereas the Riks method searches for new equilibrium states in a circular arc around the base configuration. Both algorithms are initiated by applying a load increment to the undeformed structure. Once the convergence criteria are met, i.e. as soon as the force residual and the relative change of the displacement vector \mathbf{u} are sufficiently small, the geometry is updated, and the computation of the next increment commences. When the NR algorithm is used, individual increments are calculated as a fraction of the prescribed load. In contrast, an increment is computed in terms of the arc length for the Riks method. Due to the gradient-based approach, the NR algorithm has difficulties overcoming zero tangents, but the relation between the applied load and the current increment is straightforward. On the other hand, the Riks method can follow an equilibrium path regardless of any tangents with the drawback that the relation between the applied load and a given increment cannot be known a priori. Despite its shortcomings, the NR algorithm is chosen because the dynamic solver does not support the Riks method.

Since static analyses do not account for time-dependent quantities, dynamic effects such as buckling mode jumps or modal interactions cannot be captured. These also tend to prevent convergence unless additional measures are taken, for example the inclusion of artificial damping mechanisms. To reduce the number of required convergence studies, numerical stabilization in nonlinear static analyses is not considered.

5.5.3. Nonlinear Dynamic Analysis

Any structural response may be described with the equation of motion in its most general form.

$$\mathbf{M}\mathbf{a} + \mathbf{C}\mathbf{v} + \mathbf{K}\mathbf{u} = \mathbf{f} \quad (5.4)$$

In addition to the terms present in the static procedure, the mass matrix \mathbf{M} , the damping matrix \mathbf{C} , the acceleration vector \mathbf{a} , and the velocity vector \mathbf{v} are introduced. Consequently, the effects of inertia and damping can be quantified which can stabilize the structural response.

The algorithms that are available to solve equation (5.4) are usually classified as implicit and explicit. An implicit nonlinear dynamic analysis solves the governing nonlinear equation through matrix inversion at time $t + \Delta t$ with information from $t + \Delta t$. As a result, implicit algorithms are unconditionally stable, but the calculation of each time step is quite expensive. In contrast, the structural response at $t + \Delta t$ is computed with information from only t when an explicit scheme is employed. Therefore, errors are introduced which may add up over time unless the time increment Δt is sufficiently small. The advantage of an explicit procedure is the reduced computational cost per time step. Since the maximum allowable Δt is "approximately equal to the time for an elastic wave to cross the smallest element dimension in the model" [75], and the element size close to the cutout is very small, an implicit procedure is chosen because the time increment required for convergence of the explicit algorithm becomes unreasonably small.

Time integration in Abaqus is by default based on a subset of the generalized α -scheme, namely the Hilber-Hughes-Taylor method. When a quasi-static application is prescribed, the backward Euler operator is employed. Damping can be incorporated by specifying \mathbf{C} as a function of mass, stiffness, internal forces, or by defining the parameters that control numerical damping. The approach mentioned last is the simplest one and is therefore selected. Two different damping settings are considered to determine convergence, namely a quasi-static application with linearly ramped loads and default damping properties as well as a moderate dissipation application with linearly ramped loads in combination with maximum numerical damping for the high frequency response, i.e. $\alpha = -1/3$.

Since equation (5.4) contains the time derivatives \mathbf{a} and \mathbf{v} , structural behavior that previously led to convergence problems can now be captured. In other words, buckling mode jumps and modal interactions are accurately predicted for the modeled geometry.

6

Isotropic Cylindrical Shells

Chapter 6 deals with the buckling behavior of isotropic cylindrical shells that contain circular cutouts. Results obtained from the analytical procedure developed in Chapter 4 are presented in Section 6.1 and are compared with predictions of Starnes [18]. Section 6.2 is concerned with evaluating numerical analyses for verification purposes. In particular, buckling loads and mode shapes from FE simulations are contrasted with the analytical model. Additionally, the effects of initial geometric imperfections on the shell buckling resistance as well as shell failure are investigated. The last part of the chapter, Section 6.3, relates both analytical and numerical buckling load estimates to the experimental measurements published by Starnes.

6.1. Analytical Results

A first evaluation of the analytical results for the buckling stress τ_{cr} from equation (4.31) is performed by comparing the present method with the normalized buckling stresses reported by Starnes. For this purpose, four different sets of analytical predictions are considered. One, the normalized buckling stresses determined by employing the solution from Chapter 4 with the shape function suggested by Starnes (denoted as Analytical in the figures below). Two, the same as one, but with a modified displacement function where quadratic terms of the radial coordinate r are included in the displacement function (Analytical extended). Three, the normalized buckling stresses which have been reported by Starnes in his dissertation in Table IV (Starnes Table). Four, the normalized buckling stresses computed with the matrix components presented by Starnes in his Ph.D. dissertation on pages 50 to 53 (Starnes Matrix). The buckling stresses are normalized with the classical buckling stress τ_{cl} of the pristine shell, see equation (3.63). All four cases are visualized in Figure 6.1 where the normalized buckling stress is plotted against the curvature parameter μ from equation (2.5).

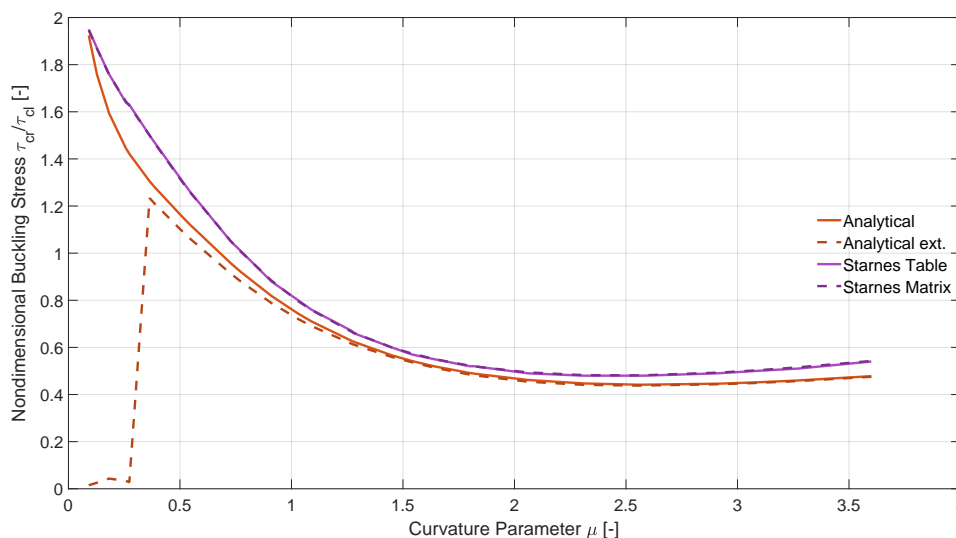


Figure 6.1: Analytical predictions for the normalized buckling stress of isotropic shells.

As identified by Starnes and regardless of the solution method, the normalized buckling stresses all fall onto a single curve as long as the horizontal axis is proportional to a/\sqrt{Rt} . Initially, increasing the cutout size causes a significant decrease of the buckling stress. This rapid decline transitions to a range of μ where the buckling load remains approximately constant independent of the radius of the circular opening. Interestingly enough, if the cutout size is increased further, the shell appears to be able to carry more load once again before it buckles.

Figure 6.1 raises two important questions. First, what is the reason for the discrepancy between the buckling stresses predicted by Starnes' solution and the estimates computed with the present method? Second, why does the extended analytical solution not behave like the other solutions for small values of μ ?

Focusing on the former concern first, an explanation can be found by looking at the derivation of the eigenvalue problem, more specifically by inspecting the calculation of the boundary value problem coefficients. Starnes reported

$$b'_2 = \frac{Et}{4RB^3} \left[A_0 e^{-Ba} (B^2 a + B) - A_2 B^3 a^2 \text{Ei}_1(Ba) + C_0 e^{-Ba} (B^2 a^2 + 2Ba + 2) - C_2 e^{-Ba} (B^2 a^2 + Ba) \right] \quad (6.1)$$

whereas

$$b'_2 = \frac{Et}{4RB^3} \left[A_0 e^{-Ba} (B^2 a + B) - A_2 B^3 a^2 \text{Ei}_1(Ba) + C_0 e^{-Ba} (B^2 a^2 + 2Ba + 2) - C_2 B^2 a^2 e^{-Ba} \right] \quad (6.2)$$

is obtained from the analysis in Chapter 4, see Appendix A.2. The underscored term in Starnes' b'_2 is missing in equation (6.2). Other than that, Starnes' membrane stress function terms k_{12} and k_{32} are equivalent to those in Appendix A.3. Substituting equations (6.1) and (6.2) in the expressions for the corresponding stress resultants demonstrates that the boundary conditions $N_r(r=a) = 0$ and $N_{r\theta}(r=a) = 0$ are not satisfied by Starnes' version of b'_2 . Consequently, his solution is offset by some value that depends on the product of the decay parameter B and the cutout radius a .

Furthermore, Starnes' solution for the particular solution term h_0 is exactly negative of what is presented in equation (4.20). The effects of these two differences are investigated by modifying the present solution accordingly, i.e. Starnes' b'_2 as well as his alternative definition of h_0 are incorporated in the analytical solution. The new buckling stress predictions are computed and subsequently illustrated in Figure 6.2 which shows the normalized buckling stress on the vertical and μ on the horizontal axis.

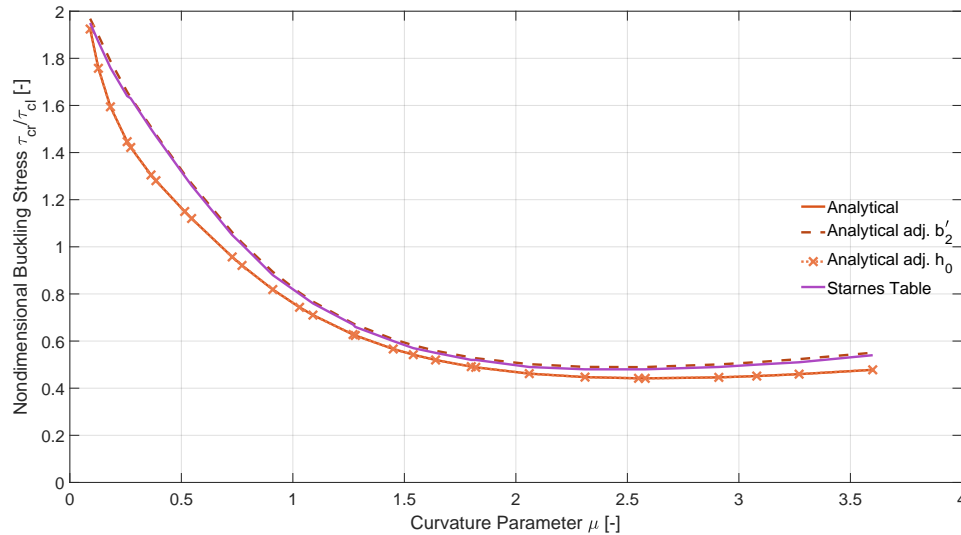


Figure 6.2: Normalized buckling stress predictions after modification of the present solution.

Clearly, adding the extra term in b'_2 impacts the buckling stress estimates considerably. In contrast, altering h_0 does not appear to have any effect. The latter is a direct consequence of the membrane strain energy formulation in equation (4.4). All stress resultants are squared, and therefore the sign of h_0 does not influence the final expressions for the matrix components of \mathbf{K}^M and \mathbf{K}^G .

Further insight can be gained by evaluating the different solution methods with respect to each other. Figure 6.3 shows a plot where the normalized buckling stresses from Starnes' Table IV are taken as a baseline. Since Starnes rounded his results to the nearest one-hundredth, the apparent discontinuities for each curve may be explained with a fluctuation of the reference values of up to 1%. It can be seen that Starnes' results do not coincide perfectly with the present adjusted analysis which is attributed to a number of smaller discrepancies between the two solutions. In any case, it is evident that the additional term in b'_2 accounts for most of the gap between the present analysis and Starnes' version in Figure 6.1.

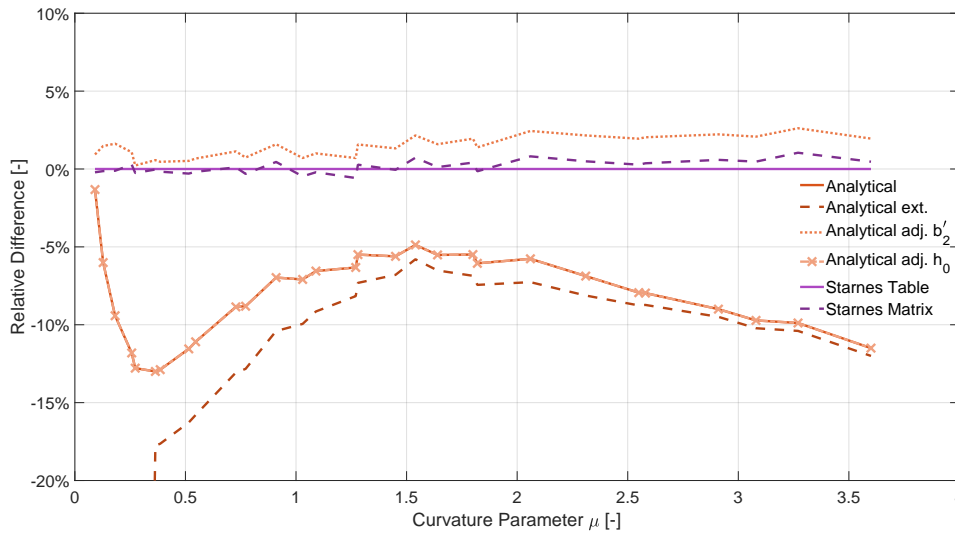


Figure 6.3: Comparison between the different analytical solutions.

Figure 6.3 also verifies what has been suggested earlier when the Ritz method was introduced. Increasing the DOFs of the shape function by adding extra powers of r leads to a lower buckling stress because the Ritz method converges to the exact solution while overestimating the stiffness of the structure. Hence, the trend from the standard to the extended analytical solution makes sense.

Coming back to the second question raised by Figure 6.1 regarding the reason for the low buckling stresses predicted by the extended analytical solution when cylindrical shells with small μ are considered, it is helpful to plot the buckling τ_{cr} stress as a function of the decay parameter B as depicted in Figure 6.4. Therein, the functions of the two shells I1.2 and I1.6 from Table 5.1 are visualized.

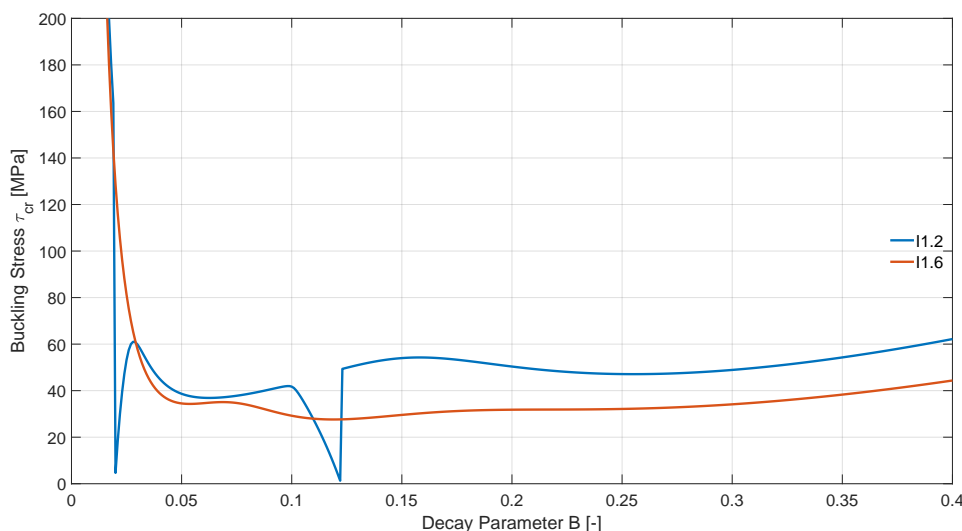


Figure 6.4: Buckling stress τ_{cr} versus decay parameter B .

While the curve representing the shell containing the larger cutout is smooth, the blue one features downwards spikes that appear to be somewhat out of place. These are the reason for the low buckling stresses

observed in Figure 6.1. Even when the standard solution is considered, the matrices \mathbf{K}^M and \mathbf{K}^G are ill-conditioned. The condition number for inversion, which is calculated as the ratio between the largest matrix element and the smallest one, is of the order 10^8 for this case and certain products of Ba . Incorporating higher order terms of r in the displacement function w worsens the problem. For quadratic r terms, that is $M = 2$ in equation (4.43), the worst-case condition number increases to approximately $1.5 \cdot 10^{13}$. Since Matlab uses 16 digits of precision by default [77], the number of significant digits is substantially reduced and the computation of the eigenvalues is susceptible to numerical noise which manifests itself in the spikes depicted in Figure 6.4. Adding even higher order terms of r in the displacement function exacerbates the issue such that the calculated buckling stresses are meaningless regardless of the cutout radius. As a result, convergence cannot be studied past quadratic terms of r or when the argument of the trigonometric function features a factor of θ larger than two for the reasons discussed in Section 4.5.

Three options for overcoming the first restriction are increasing the numerical precision, choosing an eigenvalue extraction algorithm that can cope with severely ill-conditioned matrices, and identifying the problematic regions in Figure 6.4 in order to exclude them from the domain of admissible results. Increasing the number of significant digits is not further investigated. Employing the QZ-algorithm instead of the standard procedure does not improve the numerical predictions even though the Matlab documentation suggests otherwise [71]. One reason could be that documentation refers to a different type of condition number, in particular the ratio between the largest and the smallest eigenvalue which is not an issue. Finally, limiting the solution space does not resolve the underlying issue. Furthermore, it is not reliable because numerical noise might deteriorate parts of the function $\tau_{cr} = f(B)$ where the global minimum would be found if no noise was present.

Consequently, only the cases $M = 1$ and $M = 2$ can be considered for convergence. A reduction of the buckling stress between 0.5% and 5.5% depending on the curvature parameter μ is observed which indicates that the original displacement function is indeed a reasonable choice. Nevertheless, convergence is not achieved for all possible shell configurations from Table 5.1.

One may also vary the input values of the Young's modulus and the Poisson's ratio to determine the sensitivity of the solution to these variables. Altering the material stiffness does not have any effect on the nondimensionalized buckling stresses. In other words, the plot in Figure 6.1 is always the output of the analysis regardless of the choice of E . Hence, the results are independent of the Young's modulus as should be expected when a nondimensionalization is performed. However, this is not the case for the Poisson's ratio ν as shown in Figure 6.5 which suggests that μ is not an appropriate choice for the nondimensional curvature parameter. Since curvature is a geometric property, one might suspect that removing the dependency of μ on ν resolves the issue. Still, plotting the nondimensional buckling stress against α yields a graph that is very similar to Figure 6.5. Evidently, a nondimensional curvature parameter that maps all shell configurations onto a single design curve is not yet available. Of course, a potential explanation for the dependency on ν is the possibility that the analytical solution does not accurately model the shell response, but the results from FE simulations indicate trends similar to those in Figure 6.5.

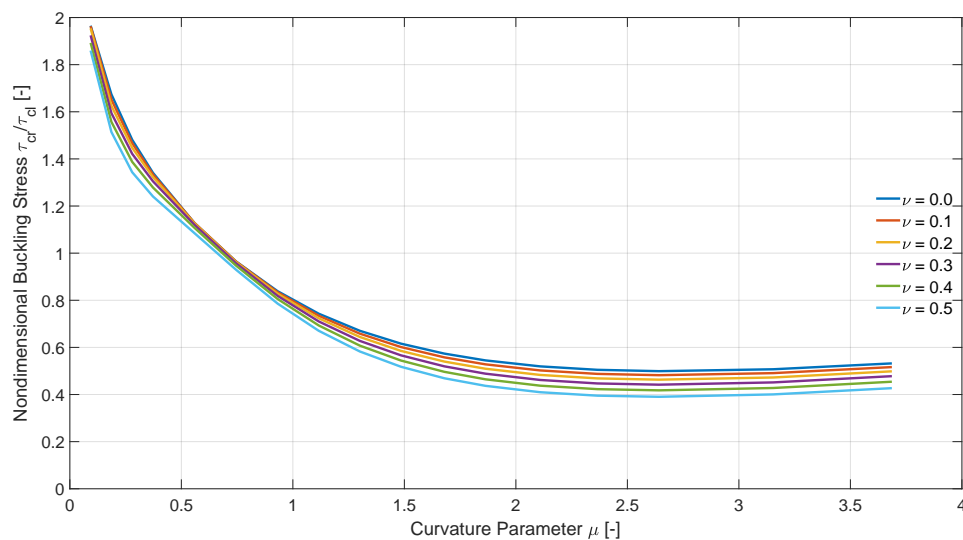


Figure 6.5: Normalized buckling stress for various values of the Poisson's ratio ν .

6.2. Numerical Results and Verification

FE analyses for the shell configurations I1.1 to I1.12, I2.10 to I2.12, I4.8, and I4.9 from Table 5.1 are run to verify the analytical results and to gain a better understanding of the buckling behavior of cylindrical shells with circular cutouts. Three different types of numerical procedures are considered, namely linear bifurcation analyses (LBA), nonlinear static (NLS), as well as a nonlinear dynamic (NLD) simulations.

Since the analytical solution predicts local buckling, the same phenomenon must be identified in the numerical simulations. To make a distinction between local and global buckling, the idea of initial and maximum buckling is introduced. Initial buckling corresponds to the load step where a minimum tangent stiffness is encountered for the first time. A relative threshold value invalidates negligible stiffness changes and thereby eliminates the influence of numerical noise during the automated post-processing. When a tangent stiffness of zero or less is calculated and the first condition has not been fulfilled yet, then initial buckling is assumed to have occurred regardless. Maximum buckling simply refers to the limit load of the structure.

Consequently, one may distinguish between two cases. Either the requirements for initial and maximum buckling are met simultaneously which suggests that the cylindrical shell buckles without experiencing a stable local buckling configuration, or initial buckling is followed by maximum buckling which indicates that the shell can be loaded after an initial loss of stiffness.

6.2.1. Comparison of Modeling Alternatives

Various modeling alternatives for the shell are assessed by comparing the respective buckling loads which depend on mesh size, element type, load application, and, for dynamic simulations, damping. Hence, up to 24 numerical analyses need to be performed per shell configuration and analysis type to account for all possible permutations. To reduce this number, a reference model with S4R elements, displacement loading, and default quasi-static damping settings is considered. The influence of each parameter is subsequently evaluated by varying one setting with respect to the reference model. Thus, the number of required simulations per shell configuration is reduced to either 9 or 12 depending on the analysis type. Mesh convergence is not plotted in the figures below for reasons of clarity and conciseness. In short, only the smallest cutout size demands a characteristic mesh size of 1 mm whereas a value of 2 mm is sufficient for all other cases.

A LBA cannot differentiate between initial and maximum buckling. Hence, the curves in Figure 6.6 provide all available and necessary information to investigate the effects of the element type and the load application. Each curve is labeled with the used element, i.e. S4 or S4R, as well as the load application type, that is D for displacement loading and F for force loading.

The numerical results for the models loaded with a uniform shell-end displacement agree well with each other. In contrast, the buckling loads of the force-loaded cylindrical shells seem to diverge from the reference model with increasing μ . The discontinuities in the curve representing the force-loaded shell correspond to jumps between different ratios of R/t . Overall, the shells discretized with S4R elements and subjected to a displacement load can be considered as representative of all modeling variants even though a maximum relative difference of 4% is not ideal.

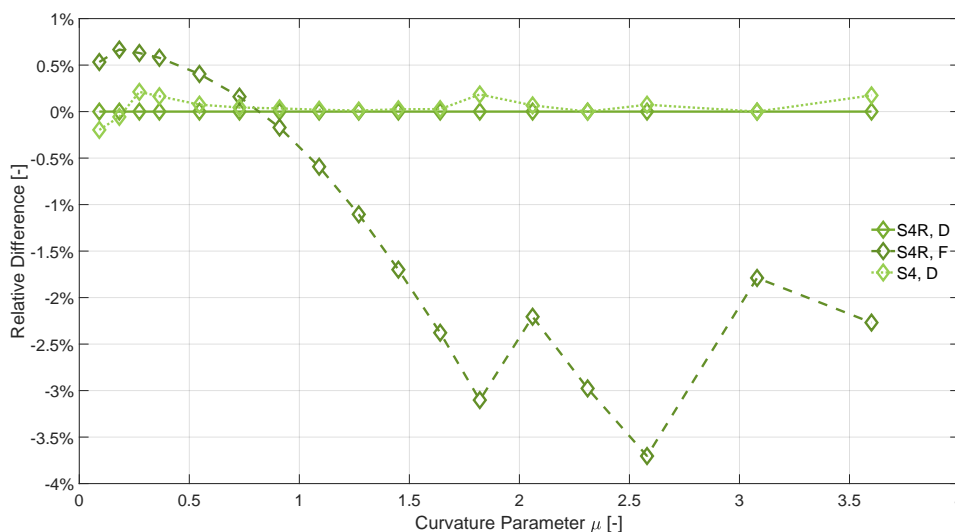


Figure 6.6: Relative difference of initial/maximum buckling load estimates for various modeling alternatives considering a LBA.

Figures 6.7 and 6.8 are concerned with the numerical predictions of nonlinear static analyses where a distinction between initial and maximum buckling is required since the structural response is evidently not the same. While the maximum buckling loads shown in Figure 6.8 are practically independent of element type, load application and the curvature parameter μ , the same cannot be said for the initial buckling load curves shown in Figure 6.7. Again, a change of the R/t ratio at $\mu = 2$ and $\mu = 3$ coincides with an increase of the relative difference of the buckling loads. However, the maximum deviation is only approximately 2% and therefore small enough to deem the predictions obtained from the model with S4R elements and displacement loading as typical.

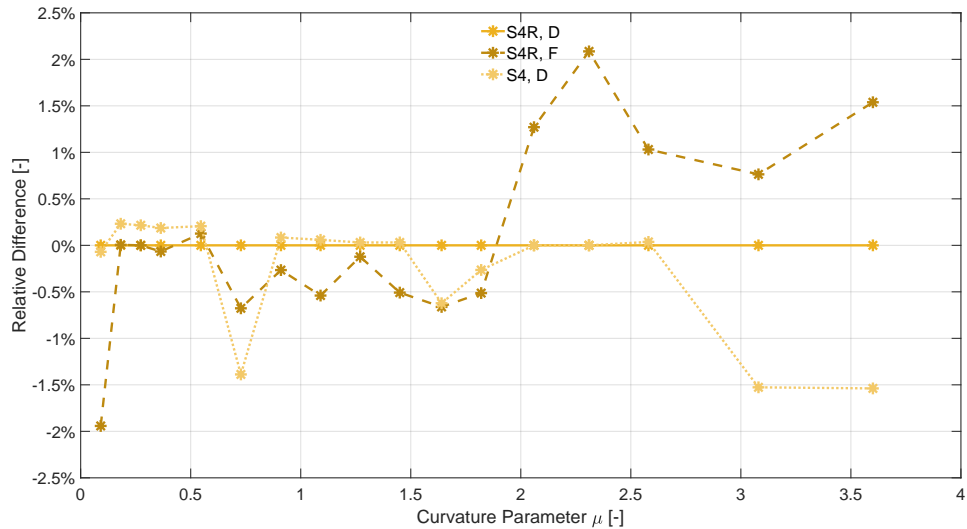


Figure 6.7: Relative difference of initial buckling load estimates for various modeling alternatives considering a NLS simulation.

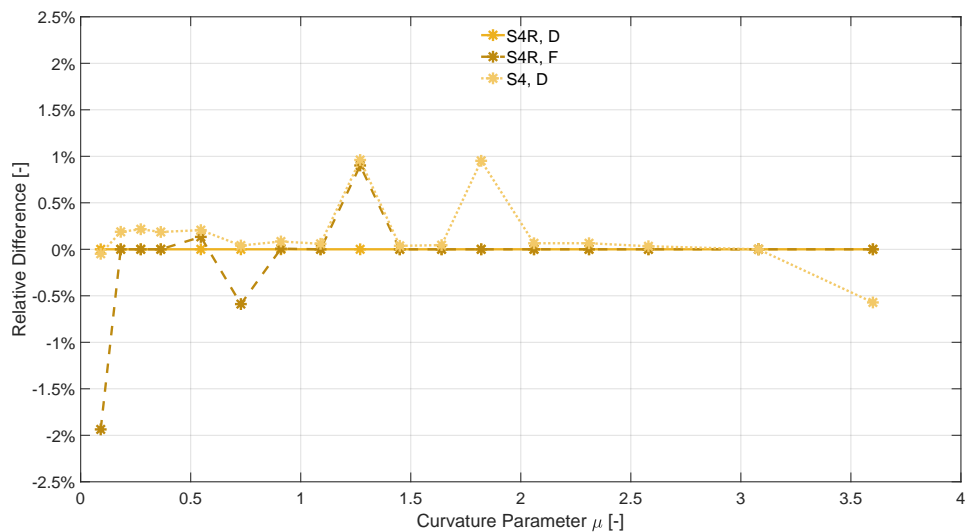


Figure 6.8: Relative difference of maximum buckling load estimates for various modeling alternatives considering a NLS analysis.

As mentioned before, the nonlinear dynamic analyses include damping effects. Hence, a fourth curve is added in Figures 6.9 and 6.10 which quantifies the influence of maximum numerical damping with respect to the reference model that uses default quasi-static settings. The relative difference of the initial buckling load displayed in Figure 6.9 follows similar trends as observed for the nonlinear static case, i.e. the variation increases once shell configurations with different R/t are considered. In contrast to Figure 6.8, Figure 6.10 features an offset between shells subjected to displacement and force loading. While the NLS simulation aborts when dynamic events occur because no numerical stabilization is used, the iterations of the NLD procedure may converge and therefore postbuckling equilibrium configurations are calculated. To reach the postbuckling domain, the reaction forces at the constrained nodes have to increase for force loading while

this is not required for displacement loading which explains the higher maximum buckling loads of the curve corresponding to the former case. Again, the largest relative difference of the two buckling load definitions is about 2% and consequently the S4R model with displacement loading is representative of the other options.

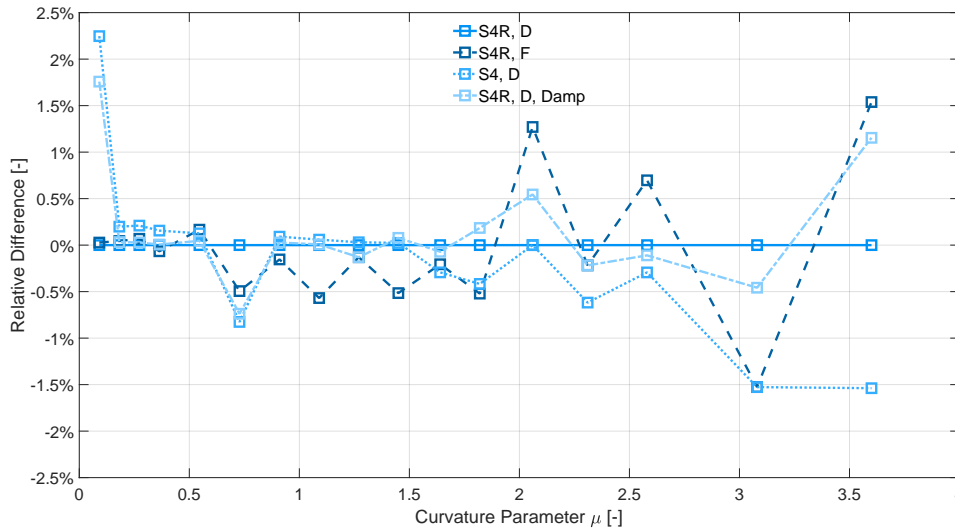


Figure 6.9: Relative difference of initial buckling load estimates for various modeling alternatives considering a NLD simulation.

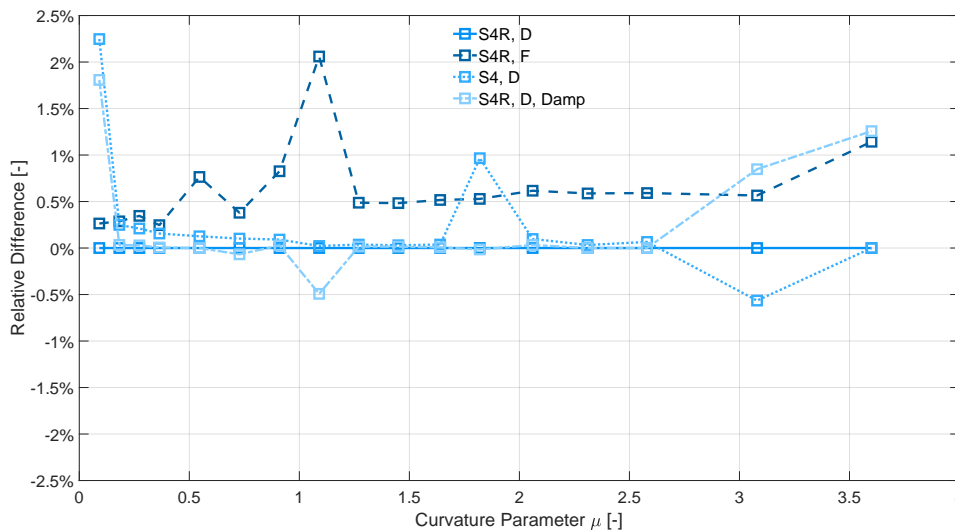


Figure 6.10: Relative difference of maximum buckling load estimates for various modeling alternatives considering a NLD analysis.

For every type of analysis, the buckling load predictions of cylindrical shells discretized with S4R elements and subjected to a uniform shell-end displacement yield reasonably close results compared to the investigated alternatives. Hence, they are referred to in the following when numerical results are mentioned.

6.2.2. Buckling Loads

A comparison between the numerically obtained buckling loads and those predicted with the analytical solution serves as a starting point for the verification of the method presented in Chapter 4. Figure 6.1 is reproduced and the results from the LBA, NLS, as well as the NLD analyses are added which yields the extra curves in Figure 6.11. Here, the normalized buckling load is the ratio between the sum of all reaction forces at the bottom shell edge at buckling F_{cr} and the classical buckling load F_{cl} which is computed by multiplying τ_{cl} with $2\pi Rt$. It has been stated before that a distinction between initial and maximum buckling is only meaningful for the nonlinear simulations because the linear eigenvalue analyses cannot differentiate between the two cases. Furthermore, the analytical solution assumes local buckling, so it should be evaluated with respect to

this type of structural response. Unstable local buckling that immediately leads to global buckling cannot be distinguished from global buckling without an unstable local buckling mode in Figure 6.11. However, stable local buckling configurations are clearly visible as the curves for the nonlinear simulations separate.

Although the exact values differ for each analysis type, the numerical predictions in Figure 6.11 suggest that the buckling load is initially constant, then drops off and finally reaches a level where it stabilizes again. The buckling load that corresponds to this second plateau seems to depend on the R/t ratio of the respective shell. Furthermore, the results of the nonlinear analyses coincide which indicates that dynamic effects do not play a major role until the isotropic cylindrical shells buckle globally. Finally, the nonlinear procedures also predict that a stable local buckling configuration exists beyond a certain value of the curvature parameter μ .

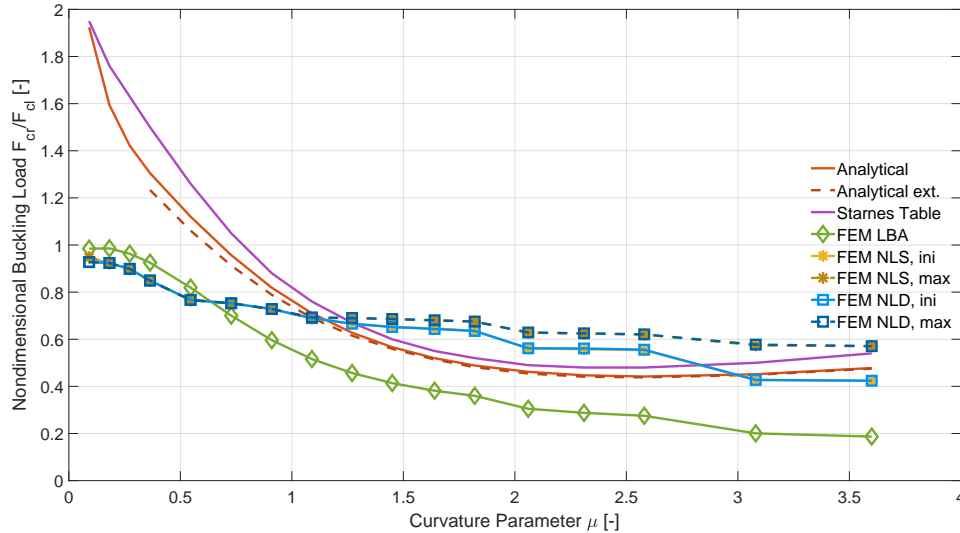


Figure 6.11: Normalized buckling loads of isotropic shells.

It is not surprising that the buckling loads of the LBA and the analytical solution follow similar trends since an eigenvalue analysis is performed in both cases. Obviously, there is an offset between the LBA and the analytical procedure which is more pronounced for extreme values of μ . The higher buckling loads calculated with the method presented in Chapter 4 are mainly caused by two limitations of the analysis. Firstly, the prebuckling stress distribution in the shell is approximated with the flat plate solution of Kirsch [1] as stated in Section 4.2 and therefore the stress field quantified by \mathbf{K}^G is underestimated. Consequently, the eigenvalues that lead to critical stress states must be larger. Secondly, the Ritz method converges to the exact solution by overestimating the stiffness of the structure which also increases the calculated buckling loads.

The large difference between the two methods for small μ is explained with the fact that the LBA anticipates the global buckling in this domain whereas the analytical procedure always prescribes local buckling. Hence, local buckling constitutes a higher order buckling mode which naturally corresponds to higher critical buckling loads. Predictions also diverge for large μ which are obtained by decreasing the shell wall thickness. Apparently, the disproportional bending stiffness reduction promotes lower buckling loads which is counterintuitive because the bending stress contribution decreases for smaller thicknesses t . Since the analytical procedure does not capture the effects of bending stresses, it cannot predict this behavior.

Before comparing the nonlinear numerical simulations with the analytical solution, it is pointed out that the relation between the LBA and the nonlinear procedures inverts at approximately $\mu = 0.65$. This is surprising because buckling loads obtained from nonlinear analyses are typically lower than those from a LBA. Figure 6.12 illustrates the prebuckling stress distribution in terms of the von Mises stress shortly before initial buckling occurs assuming linear and nonlinear geometric behavior. The stress field predicted by a linear static analysis yields some insight into the stress distribution considered by the LBA. As the curvature parameter increases, the maximum stress for the nonlinear analysis rises more rapidly because large displacements in the cutout area cause additional bending stresses. The same out-of-plane deflections also reduce the axial stiffness in the cutout region which results in a stress redistribution away from the opening as the cross-section above and below the cutout becomes devoid of stresses for larger μ . Evidently, nonlinearities can play an important role in the buckling behavior of shells with cutouts. The LBA cannot account for their influence in \mathbf{K}^M and \mathbf{K}^G which leads to the aforementioned inversion of the buckling load in Figure 6.11.

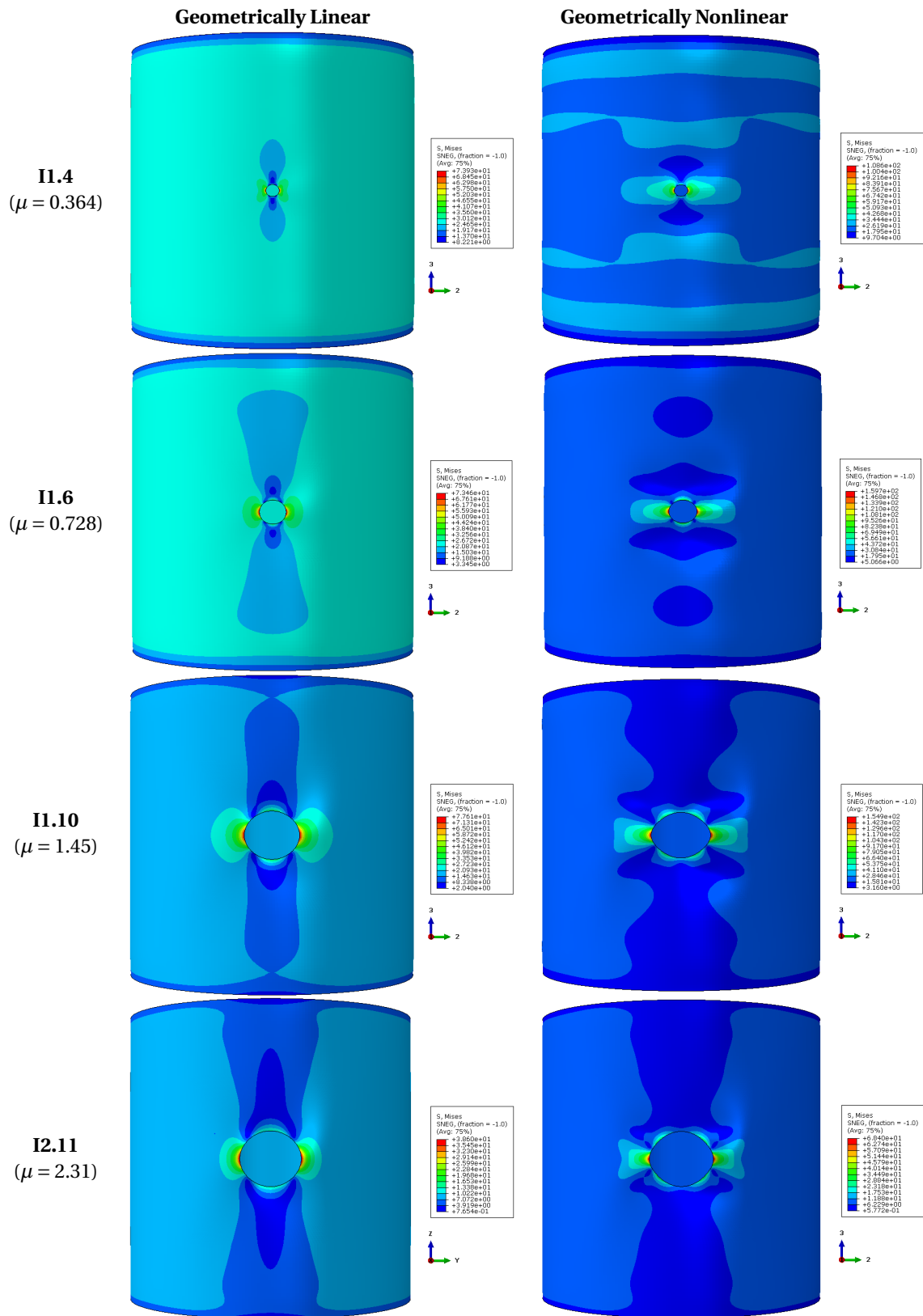


Figure 6.12: Prebuckling distribution of the von Mises stress as computed by geometrically linear and nonlinear procedures.

Since the working principles of the LBA and the analytical procedure are similar, the differences between the analytical solution and the nonlinear analyses can be explained with the ideas just described. Compared to the LBA, constant nondimensional buckling loads are observed over a larger range of the curvature parameter μ as large displacements cause a stress redistribution inside the cylindrical shell. Again, there appears to be some dependence of the nonlinear buckling loads on R/t which is more pronounced for initial than for maximum buckling. This suggests that the global buckling configuration is less sensitive to the emerging displacement and stress fields.

Additionally, the analytical solution is assessed with respect to its ability to predict buckling loads when material parameters are changed. Since the normalized buckling loads are independent of the Young's modulus, the Poisson's ratio is varied. More specifically, numerical simulations with the limiting cases of $\nu = 0$ and $\nu = 0.5$ as well as $\nu = 0.3$ are run. The results are plotted in Figure 6.13. Like the analytical buckling load estimates, the FE analyses indicate the normalized buckling loads do not fall onto a single curve. This confirms that the curvature parameter μ and its dependence on ν is not an effective parameter when the goal is to obtain an unambiguous design curve from which the engineer can predict the buckling load of a real structure by multiplying the nondimensional parameter with material constants and geometric properties.

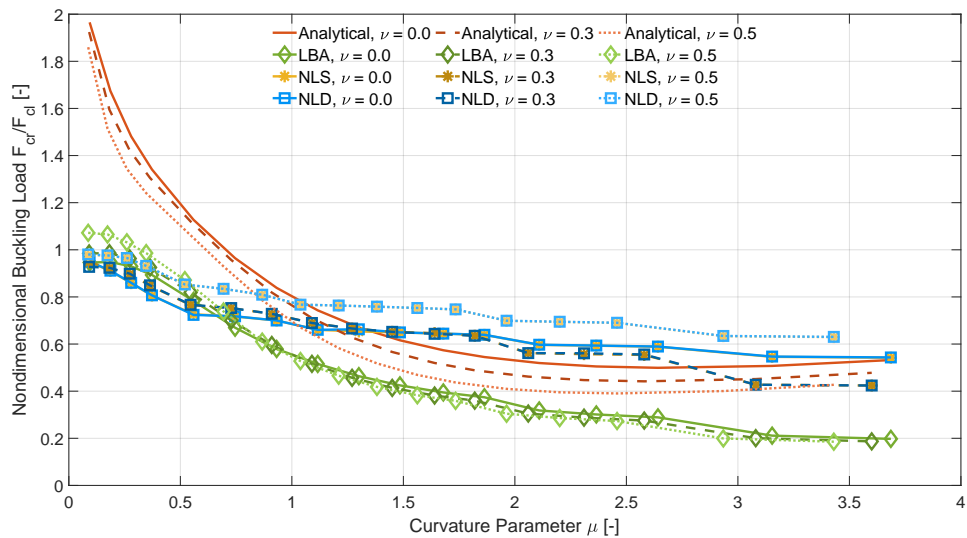


Figure 6.13: Effect of the Poisson's ratio on the normalized maximum buckling loads.

The trends in Figure 6.13 are not identical for different values of ν when comparing the considered analysis types. In fact, one obtains a different order of buckling loads sorted from highest to lowest that depends on the Poisson's ratio for the linear and nonlinear analyses. For example, the nonlinear simulations indicate that the buckling load is at its maximum when the material is incompressible whereas the opposite is the case according to the analytical solution. Moreover, there are some trend inversions for the LBA as well as the NLS and NLD procedures. Consequently, it is questionable whether the method presented in Chapter 4 is suitable for comparing materials with different values of the Poisson's ratio.

6.2.3. Buckling Mode Shapes

A second output of the generalized eigenvalue problem are eigenvectors which are typically interpreted as the displacement pattern at buckling. Again, the working principles of the analytical solution and the LBA are very similar as buckling mode shapes are predicted in the same way. Eigenvectors can be scaled to an arbitrary length which means that even though the displacement patterns are represented accurately within the limitations of a linear buckling analysis, their amplitude is impossible to determine. In most cases the magnitude of the largest deflection is normalized to unity and all other displacements are adjusted accordingly.

Figure 6.14 shows the buckling mode shapes obtained from various analyses. AN1 and AN2 refer to the analytical solution and its extended version, respectively. The displacement patterns of the LBA correspond to the lowest calculated eigenvalue. One should note that the gap between the first and second lowest eigenvalue of the LBA decreases as the curvature parameter μ becomes smaller. Closely spaced eigenvalues are often observed in LBAs for pristine cylindrical shells which buckle globally. A tendency towards global dis-

placement pattern is also observed for shells with small cutouts which explains this phenomenon as multiple, somewhat global, buckling configurations yield similar buckling loads.

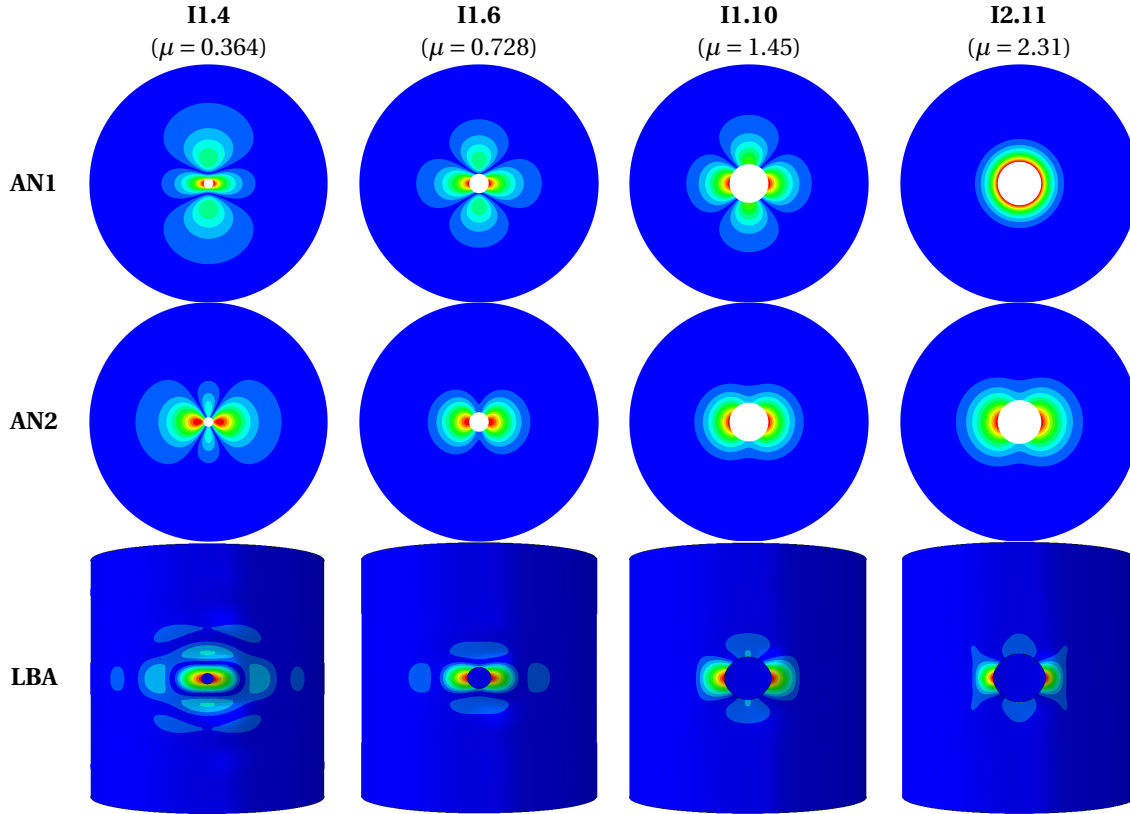


Figure 6.14: Initial buckling patterns of isotropic shells.

Unsurprisingly, the buckling mode shapes of the analytical procedure are restricted to the cutout vicinity. Adding an extra r term in the shape function improves the displacement pattern for large μ but dampens the deflections above and below the opening compared to the LBA. Overall, the buckling patterns of the linear procedures are relatively similar if μ is above a certain threshold value. When the curvature parameter is small, then the LBA buckling mode shape becomes more global even though the highest displacement amplitudes are still located at the cutout edge. Furthermore, the estimated buckling patterns are clearly dominated by the destabilizing effects of compressive stresses since the highest deflection amplitudes are located where stress concentrations are expected.

6.2.4. Buckling Mode Shape Evolution

To better understand the mechanisms that govern the buckling behavior of cylindrical shells with circular cutouts, the process of buckling itself is investigated in more detail. The numerical nonlinear dynamic procedure is the most general of the considered analysis types and therefore evaluated in this subsection. Load-displacement curves such as those shown in Figure 6.15 provide some insight into the shell response when the structure is subjected to a uniform end shortening. The axial reaction force at the bottom of the shell RF3 and the axial displacements at the top of the shell U3 are normalized with quantities derived from the classical buckling stress τ_{cl} assuming linear relations. F_{cl} has been defined at the beginning of Subsection 6.2.2. The reference buckling displacement u_{cl} is calculated with equation (6.3).

$$u_{cl} = \frac{1}{\sqrt{3(1-\nu^2)}} \frac{Lt}{R} \quad (6.3)$$

Figure 6.15 suggests that nonlinear geometric effects influence the shell response more and more as the curvature parameter μ increases. Shells with small cutouts deform linearly until a maximum load is reached and lose a considerable percentage of their load-carrying capability afterwards. Cylindrical shells with larger

μ exhibit a configuration where the structural stiffness is significantly reduced. However, this event is not critical as the cylindrical shell recovers part of its initial stiffness and can be loaded further until a second stiffness loss occurs. Both the initial and the maximum load at which a loss of stiffness is observed decreases when the value of μ is increased.

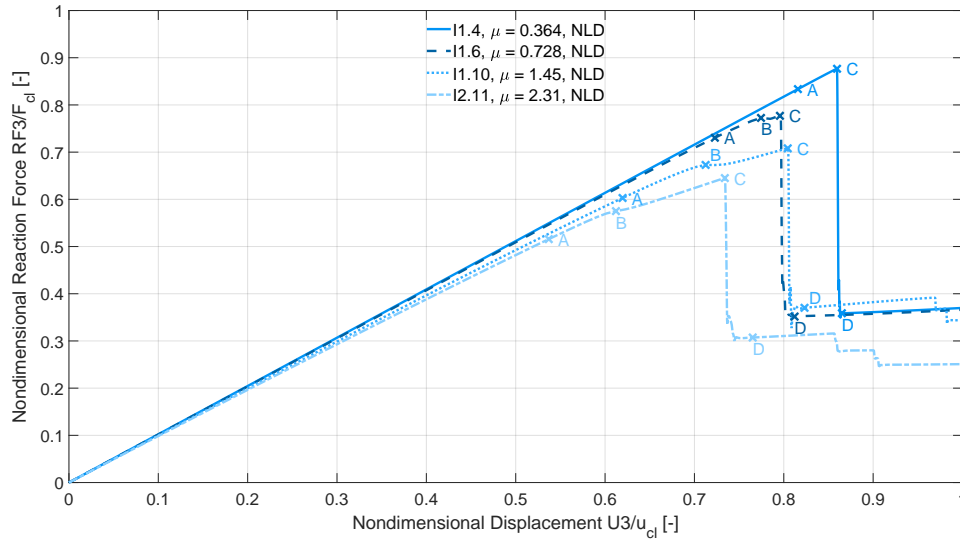


Figure 6.15: Normalized load-displacement curves for various isotropic shells.

Naturally, one would expect that some sort of buckling can be observed at these characteristic points. Hence, radial displacements scaled up by factor five are depicted in Figure 6.16 as a measure of the out-of-plane deformation to verify this suspicion. Images labeled with an *A* are taken in the prebuckling domain. The letter *B* refers to equilibrium states where large displacements are limited to the cutout area, i.e. local buckling. *C* denotes the displacement field just before global buckling and *D* indicates the global buckling pattern. For reference, the maximum displacements at local buckling correspond to deformations inwards equal to 1.73 mm, 3.80 mm, and 2.64 mm for the shells I1.6, I1.10, and I2.11, respectively. It should be noted that shell I2.11 is only half as thick as the other ones. After global buckling, the maximum displacements are 2.25 mm, 2.39 mm (both outwards), 8.30 mm, and 5.32 mm (both inwards). Shells with small openings do not buckle locally and therefore the related field is empty for shell I1.4 in Figure 6.16.

The shape of the prebuckling configuration *A* in Figure 6.16 looks relatively similar for all shells and it is conceivable how the local buckling mode *B* of shells I1.6, I1.10, and I2.11 emerges. However, it is difficult to extrapolate from the shape of *A* to the global buckling displacement pattern *D*. When comparing the buckling mode evolution of shell I1.6 with its initial and maximum buckling load in Figure 6.11 as well as with the load-displacement curve in Figure 6.15, one can see that the critical loads for local and global buckling are almost indistinguishable. The shell also buckles globally shortly after the onset of local buckling, the prebuckling response is almost completely linear, and the displacement pattern of the global buckling configuration of shell I1.6 is similar to that of I1.4. Additionally, the growth of the out-of-plane deflection from state *B* to *C* is negligible. Starnes suggested in his Ph.D. dissertation [18] that global buckling for certain values of the curvature parameter μ is triggered by the disturbance of the stress redistribution at the onset of local buckling. The present data for shell I1.6 supports this conclusion. Thus, predicting local buckling in this domain is equivalent to determining the global buckling load of the cylindrical shell.

Increasing μ further significantly changes the buckling behavior of the cylindrical shells. The local buckling configurations in rows *B* and *C* become stable as the initial and maximum buckling loads in Figure 6.11 separate. The same information can be obtained from the load-displacement curve in Figure 6.15. Furthermore, the local buckling pattern evolves as the two buckles above and below the cutout split horizontally into two parts. In addition, the out-of-plane displacement amplitude grows to a great extent from state *B* to *C* for the shells I1.10 and I2.11. As a result, the structure buckles globally when the individual buckles interfere with each other which yields the global buckling configuration in row *D*.

Figure 6.16 also allows relating the linear buckling mode shapes from Figure 6.14 to the nonlinear ones. In fact, the displacement patterns obtained from the NLD procedure differ considerably from the linear eigenvalue analyses. Small openings trigger a global buckling configuration that is only marginally influenced by

the presence of a cutout. Apparently, the influence of geometric nonlinearities relieves the severity of the stress field in the area around the opening if the cutout is sufficiently small which explains the different buckling modes for small μ . The transition from global to local buckling features a symmetric mode shape that is not predicted by the linear eigenvalue analyses. Buckling mode shapes for larger curvature parameters resemble those of the linear procedures in the sense that the largest displacement amplitudes can be found on the left and the right side of the opening where stress concentration peaks are located. However, the nonlinear simulations indicate that four additional diamond-shaped buckles are positioned around the cutout.

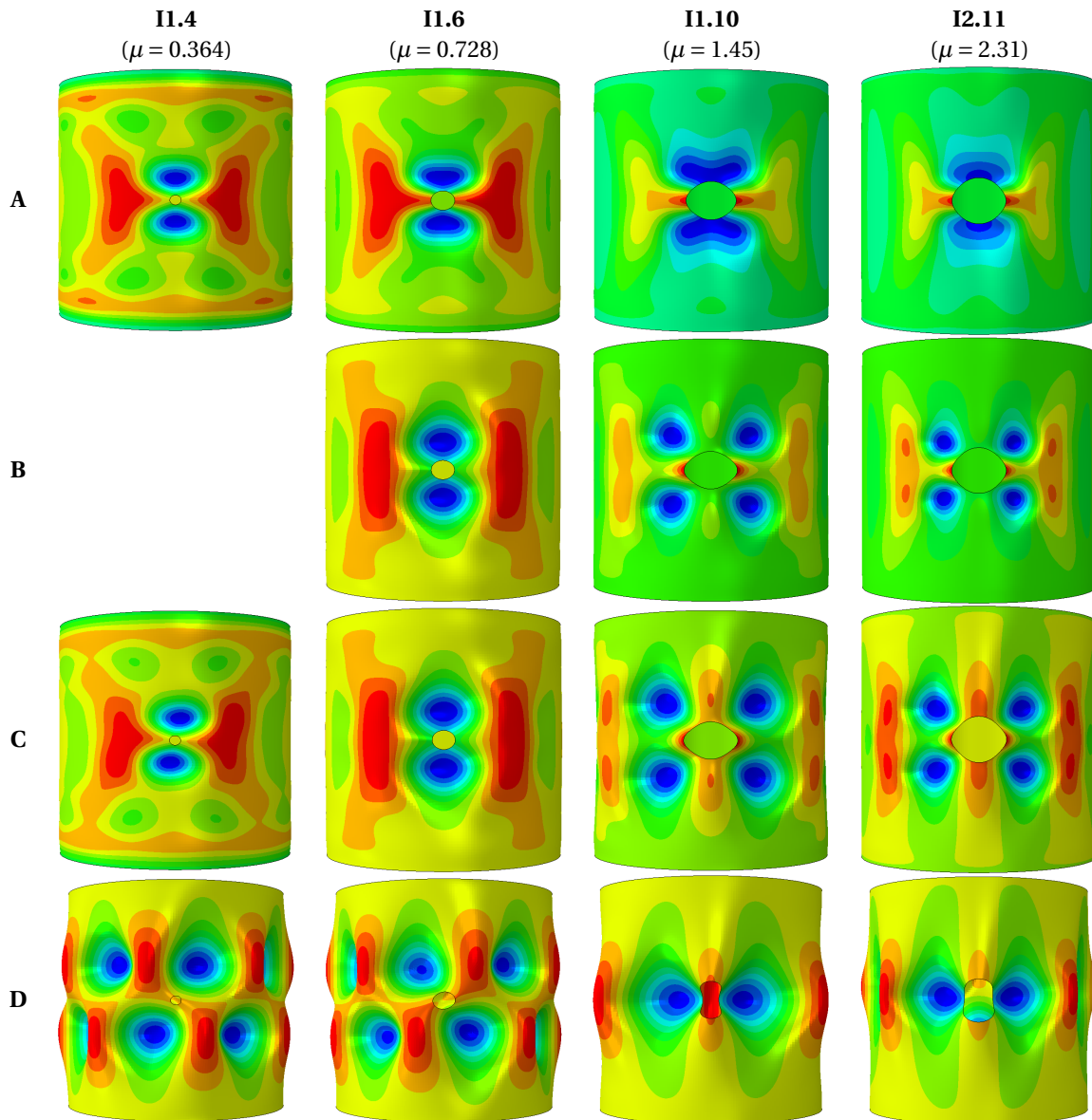


Figure 6.16: Radial displacements amplified by factor 5 during loading (A), at stable local buckling (B), before (C), and after (D) global buckling of isotropic shells.

6.2.5. Initial Geometric Imperfections

It is well known that pristine cylindrical shells are sensitive to initial geometric imperfections. Different kinds of imperfections have already been discussed in Subsection 2.3.4 where their respective influence on the buckling behavior of shells with and without cutouts is quantified in Table 2.1. Incorporating thickness variations and nonuniform loading usually requires imperfection data measured on real specimens. Generally speaking, the same is true for mid-surface variations, but a popular approach is to assume them in the shape of buckling mode shapes as it is presumed that these imperfections are the most detrimental to the structure's

buckling resistance. Hence, mid-surface variations are introduced in the NLD analyses by superimposing the displacement patterns obtained from the LBA and scaling them relative to the shell wall thickness.

Comparing the buckling patterns in Figures 6.14 and 6.16 indicates that the predictions from the LBA do not necessarily agree with the NLD procedure. However, higher order buckling mode shapes calculated with the LBA are reasonably similar to the displacement patterns computed with NLD analyses. Criteria for the selecting mode shapes are their type (local or global) as well as position, number, and orientation of buckling waves. Global buckling displacement fields are considered for the shells I1.4 and I1.6 since they buckle without experiencing a stable local buckling configuration. Shell 1.10 exhibits stable local and global buckling which is why displacement patterns for both instabilities are introduced.

Nondimensional load-displacement curves are displayed in Figure 6.17 for shell I1.4 and varying imperfection amplitudes. Raising the imperfection amplitude results in a continuous and significant reduction of the buckling load where the shape of the load-displacement curve only starts to deviate from the ideal reference shell when relatively large imperfection amplitudes are taken into account.

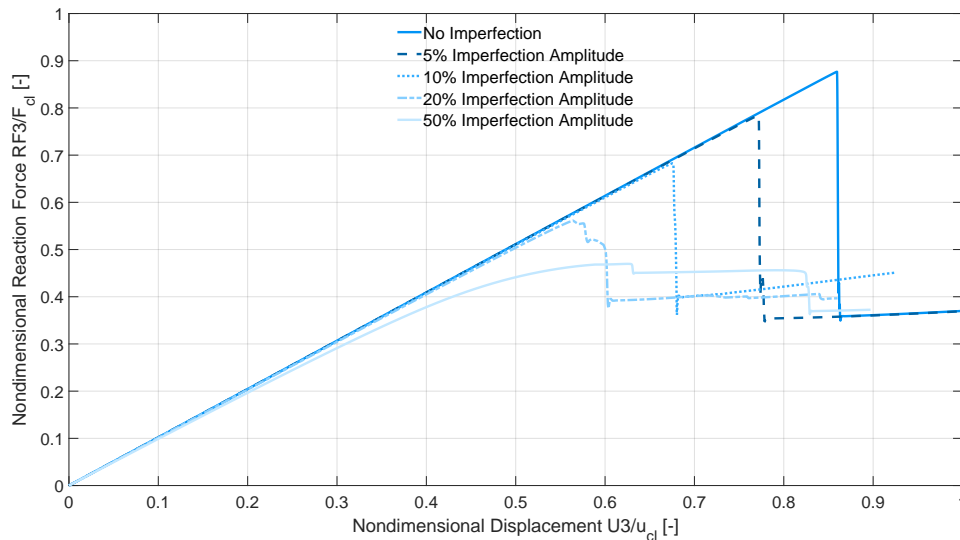


Figure 6.17: Normalized load-displacement curves considering an imperfect geometry of shell I1.4 ($\mu = 0.364$).

A similar effect can be observed for slightly larger cutouts in Figure 6.18 where the unstable local buckling event acts as a threshold until the imperfection amplitude is sufficiently large. An identical imperfection amplitude as in the previous case results in less of a buckling load reduction, see Table 6.1.

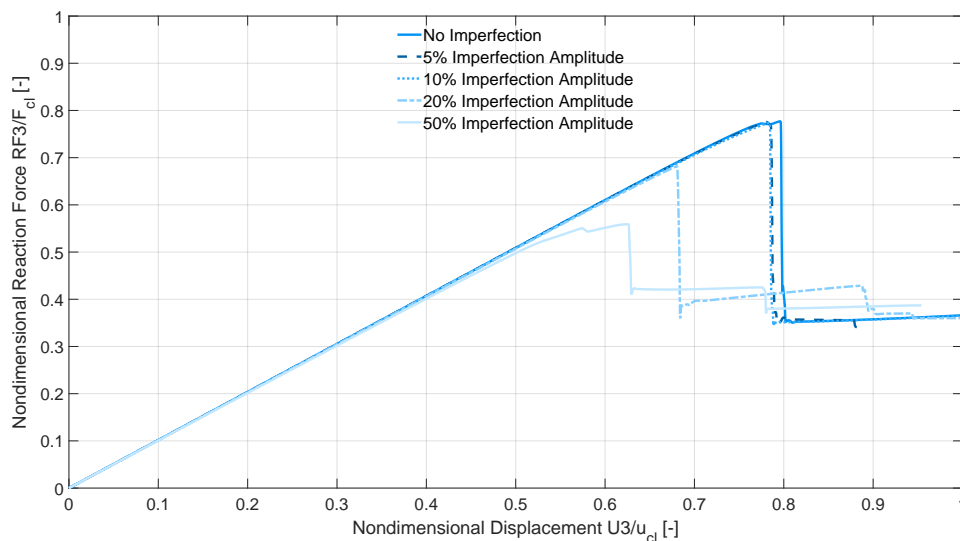


Figure 6.18: Normalized load-displacement curves considering an imperfect geometry of shell I1.6 ($\mu = 0.728$).

Comparing mid-surface imperfections in the shape of local and global buckling modes is interesting since the load-displacements curves in Figures 6.19 and 6.20 differ greatly. Imperfections that resemble the local buckling pattern have practically no influence on the buckling load as shown in Figure 6.19. It is probably unrealistic that imperfections increase the buckling load of a structure, but this result shows that certain imperfection shapes are less detrimental than others. An explanation for low sensitivity of the shell response to local buckling mode imperfection could be the natural presence of this imperfection shape due to the growth of large out-of-plane displacements in the vicinity of the cutout.

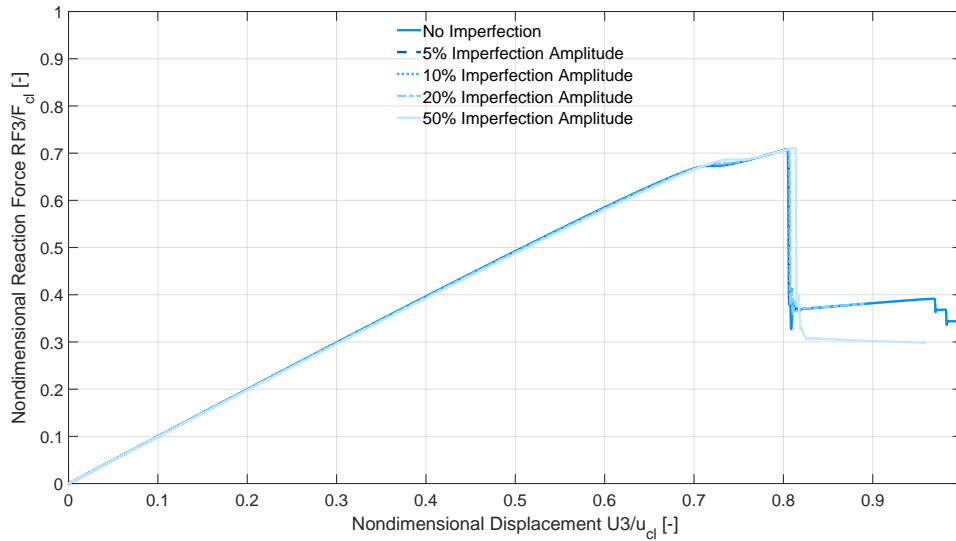


Figure 6.19: Normalized load-displacement curves considering an imperfection in the shape of the local buckling mode for shell II.10 ($\mu = 1.45$).

In contrast, imperfections that correspond to the global buckling mode lead to load-displacement curves more akin to those in Figures 6.17 and 6.18. However, this type of imperfection completely changes the buckling behavior of the cylindrical shell as the stable local buckling configuration ceases to exist for an imperfection amplitude of 5%. It returns for larger amplitudes, but the maximum sustainable buckling load is reduced considerably which suggests that the overall shell response is completely different than that of the ideal reference shell. As such, it could be the case that a suboptimal imperfection shape was selected, but the importance of the corresponding choice is once again highlighted.

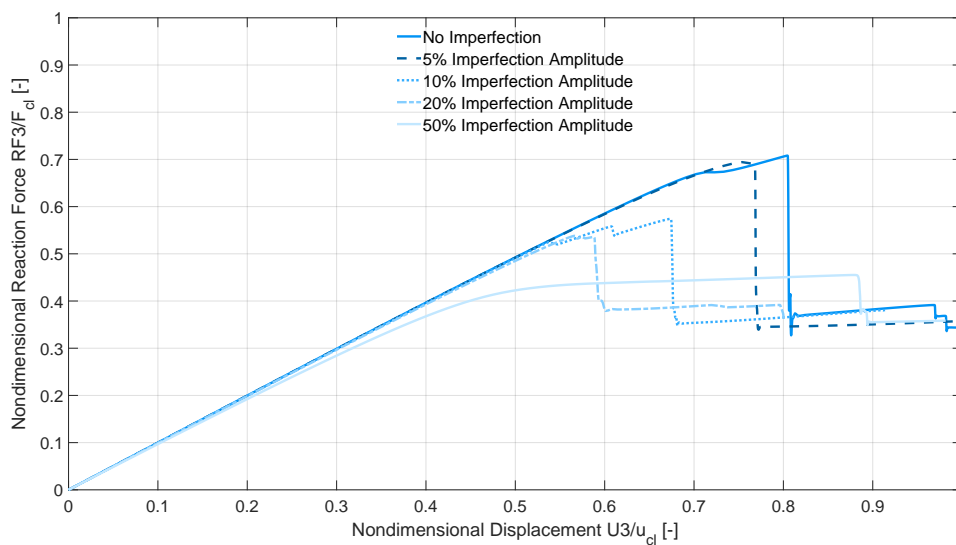


Figure 6.20: Normalized load-displacement curves considering an imperfection in the shape of the global buckling mode for shell II.10 ($\mu = 1.45$).

The normalized (Norm.) maximum buckling loads from the above figures are summarized in Table 6.1. Additionally, the relative (Rel.) change with respect to the buckling load of the ideal shell is listed. Considering the limited number of data points and the fact that the mid-surface imperfection patterns vary with the cutout size, the overall results of this brief investigation on the influence of imperfections on the buckling behavior of cylindrical shells with cutouts are somewhat inconclusive. The sensitivity of the buckling load with respect to a given imperfection amplitude decreases with increasing μ as long as imperfections in the shape of the initial buckling configurations are incorporated in the nonlinear simulation. Furthermore, imperfections can theoretically increase the maximum buckling load as indicated in Table 2.1. Whether imperfections in the form of local or global buckling modes are assumed heavily influences the numerical predictions.

Imperfection Amplitude [-]	I1.4 ($\mu = 0.364$)		I1.6 ($\mu = 0.728$)		I1.10, local ($\mu = 1.45$)		I1.10, global ($\mu = 1.45$)	
	Norm. [-]	Rel. [-]	Norm. [-]	Rel. [-]	Norm. [-]	Rel. [-]	Norm. [-]	Rel. [-]
0%	0.877	100%	0.777	100%	0.708	100%	0.708	100%
5%	0.784	89.4%	0.776	99.8%	0.708	100%	0.694	98.0%
10%	0.683	77.9%	0.774	99.6%	0.708	100%	0.574	81.1%
20%	0.561	64.0%	0.682	88.3%	0.709	100.1%	0.538	76.0%
50%	0.470	53.6%	0.559	71.9%	0.711	100.4%	0.455	64.3%

Table 6.1: Normalized and relative maximum buckling loads for several isotropic shells and imperfection amplitudes.

6.2.6. Shell Failure

Up to this point, one of the main concerns has been estimating the limit load of isotropic cylindrical shells with cutouts due to buckling. It is then interesting to evaluate whether the buckling load is reached before the structure fails because it exceeds the material strength to determine which of these cases is critical and drives the design. Hence, the concept of Figure 6.16 is repurposed to indicate the current stress level in the shell. Mylar is a ductile material and therefore a reasonable choice for the stress measure is the von Mises stress.

Before discussing aspects of strength in more detail, Figure 6.21 yields some insight regarding the assumption related to equation (4.26) which states that the in-plane stress resultants far away from the cutout are negligible. Row *B* shows that this is a reasonable approximation, but the stresses are not actually equal to zero. As a consequence, the assumption associated with equation (4.26) introduces a small error in the analytical solution. It would be more accurate to prescribe a far-field stress that is equal to the buckling stress. However, this cannot be realized without an iterative solution process because the buckling load is not known before the analysis is performed. Additionally, the formulation of the eigenvalue problem requires splitting the stiffness matrix into two parts where one scales with the applied load which renders the described boundary condition obsolete.

Figure 6.21 also shows that the stress maxima are found on the left and right side of the cutout regardless of whether the shell is being loaded or in the process of buckling. The opening acts as a stress raiser which explains these positions. Another contributing factor for the observed location of maximum stress are bending stresses which become more significant as the out-of-plane deflections grow with increasing μ .

The prebuckling stress distribution depicted in Figure 6.12 is equivalent to row *A* in Figure 6.21. Hence, the previously discussed effects that are observed before any sort of buckling event occurs are also visible here. In addition, it may be noted that bending stresses divide the stress field above and below the cutout into two parts as their share of the total stress at a given point increases with larger μ . Shell configurations with stable local buckling modes feature four buckles compared to the two for unstable local buckling. It seems like the split of the stress field in the prebuckling domain is a good indicator as to what type of local buckling mode can be expected if the cylindrical shell is loaded further.

Furthermore, the stress redistribution associated with local buckling is visualized in row *B* of Figure 6.21. The character of the stress field changes dramatically compared to row *A*. While the cutout area remains heavily loaded, regions further away from the opening that were previously unstressed start to contribute to the load transfer in the shell. The stress field after global buckling depends on whether a stable local buckling configuration exists for a given shell. If it does not, then unstable local buckling leads to a stress distribution that is comparable to that of the cylindrical shell that fails globally without any kind of local buckling.

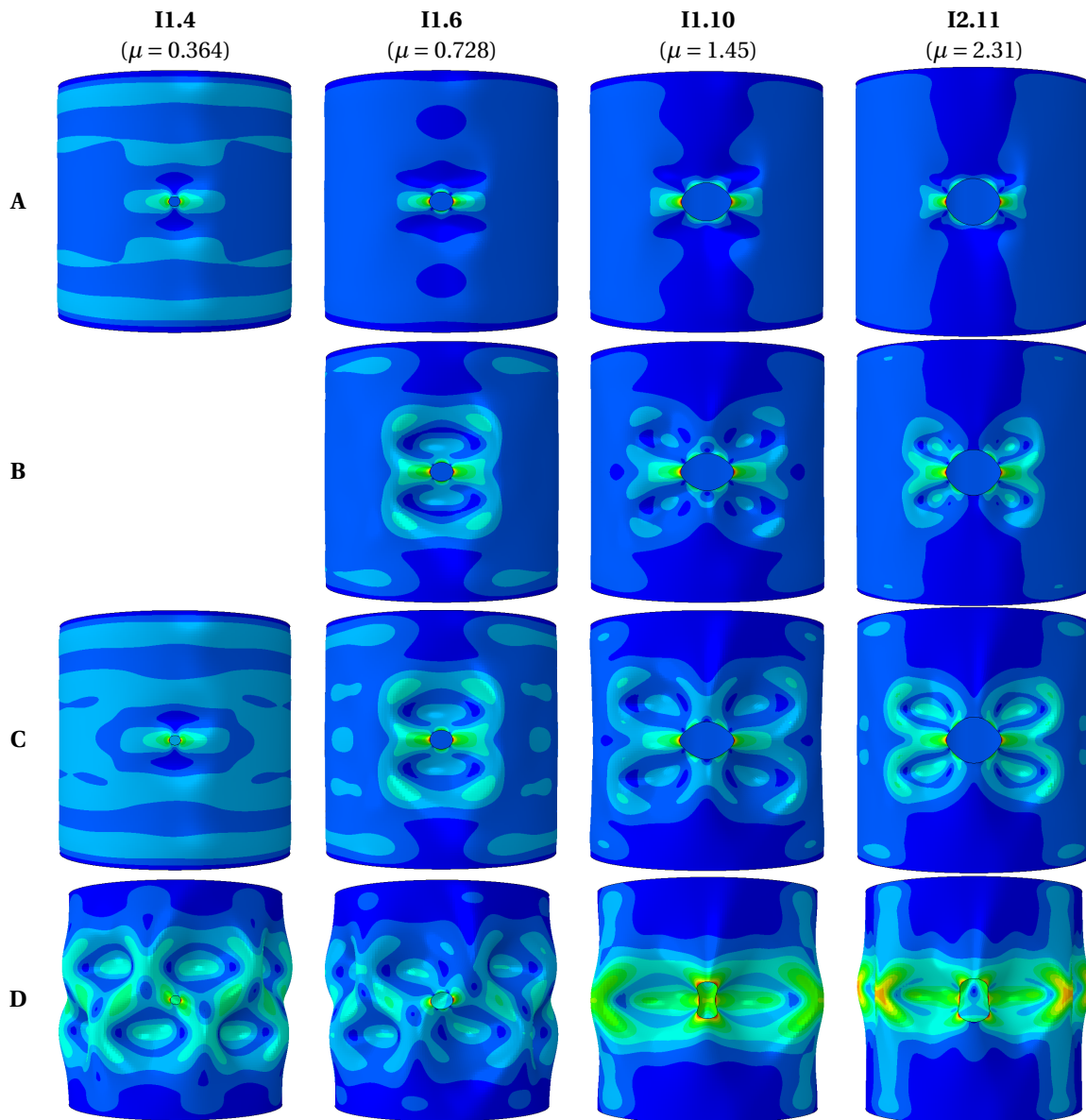


Figure 6.21: Von Mises stress distribution in isotropic shells during loading (A), at local buckling (B), before (C), and after (D) global buckling.

The maximum von Mises stresses from Figure 6.21 are quantified in Table 6.2.

	I1.4 ($\mu = 0.364$)	I1.6 ($\mu = 0.728$)	I1.10 ($\mu = 1.45$)	I2.11 ($\mu = 2.31$)
A	108.6 MPa	159.7 MPa	154.9 MPa	68.4 MPa
B		185.7 MPa	174.4 MPa	72.4 MPa
C	119.5 MPa	143.8 MPa	183.7 MPa	74.3 MPa
D	162.0 MPa	194.9 MPa	120.7 MPa	51.4 MPa

Table 6.2: Maximum von Mises stress during loading (A), at local buckling (B), before (C), and after (D) global buckling.

Reference [73] recommends using the stress at 1% offset of 115.8 MPa for structures that are loaded in compression since Mylar does not yield. The ultimate compressive stress is reported as 206 MPa. Hence, buckling is critical for shells I1.4, I1.6, and I1.10 while strength is not a concern. Neither buckling nor strength drives the design of the thinner shells (I2.xx, I3.xx, I4.xx) from Table 5.1.

6.3. Experimental Results and Validation

Finally, the analytical and numerical predictions are validated with the experimental buckling loads that Starnes reported in his Ph.D. dissertation [18]. Testing is influenced by numerous factors and therefore it is not surprising that no distinct curves, but rather a scatter band of the maximum buckling loads was obtained. Additionally, Starnes documented the force at which local and global buckling was observed for some experimental setups and shell configurations. In particular, the results for Starnes' shells 6, 17, and 20 are relevant because the boundary conditions and load application of these specimens are similar to those described in Chapter 5. Adding the buckling data of all shells to Figure 6.11 makes the plot somewhat convoluted. Therefore, only the local and global buckling loads of shell 6 are included in Figure 6.22.

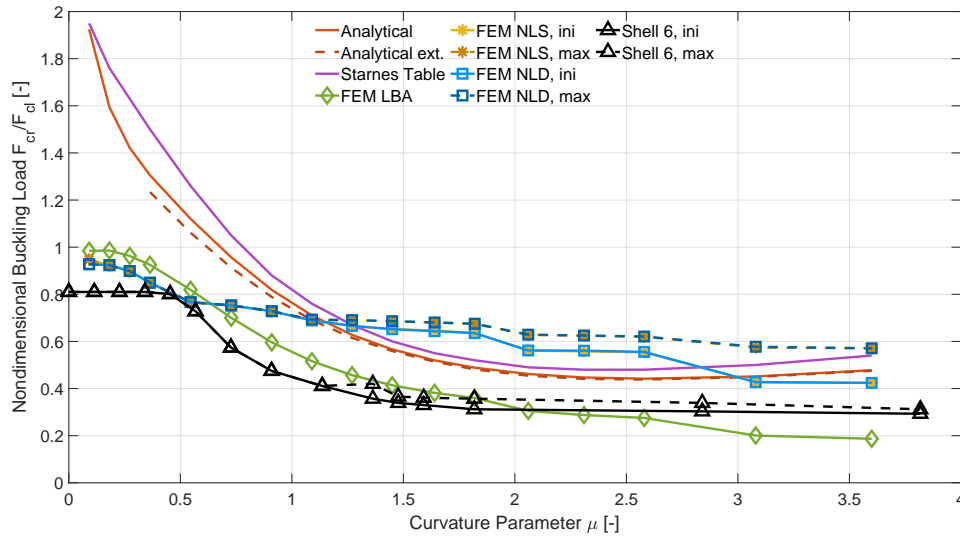


Figure 6.22: Normalized buckling loads of isotropic shells including experimental data.

Clearly, there are significant discrepancies between the buckling load predictions presented in this chapter and the experimental measurements by Starnes. Starting with a comparison between the analytical solution and the test data, it has already been argued that the analysis from Chapter 4 is based on some simplifying assumptions, e.g. the prebuckling behavior is linearized and the corresponding stress field is idealized with that of a flat plate. Furthermore, the shape function always predicts local buckling and therefore the buckling load estimates for small μ are overly conservative since the actual structure buckles globally as if no opening was present. The application of the Ritz method also introduces an error as the procedure approaches the exact solution while overestimating the stiffness of the structure. A quantification of this error is difficult because the infinite series for the displacement function is terminated rather early. Consequently, no conclusive convergence study of the analytical buckling load predictions could be performed.

The LBA shares the limitation of linearizing the shell prebuckling response with the analytical solution which is not necessarily a reasonable assumption since Starnes observed large deformations for sufficiently large cutouts. Figure 6.16 shows that these nonlinear geometric effects are also predicted by the nonlinear FE procedures. Hence, the proximity of the black and green curves in Figure 6.22 is, to some extent, the result of chance. Nonetheless, the linear eigenvalue analyses capture the general response trends of the real structure, i.e. an initial reduction of the buckling load which levels off when the curvature parameter, or the cutout size, becomes sufficiently large. The discontinuities of the buckling load curve at $\mu = 1.8$ and $\mu = 2.8$ have already been explained with the modification of the shell geometry. The wall thickness of Shell 6 is constant, so abrupt changes in the buckling load curve due to changing bending stress contributions should not occur.

Normally, one would expect that the NLS and NLD procedures provide estimates closer to the experimental measurements than the LBA. While the nonlinear algorithms seem to predict the emergence of a stable local buckling mode for the same value of μ , the normalized buckling loads differ greatly from the test data. Thus, the general buckling behavior of the cylindrical shells seems to be captured. Yet, some modeling choices cause the nonlinear numerical buckling load predictions to be unconservative.

Mylar has been idealized as an isotropic material, but the data sheet [73] indicates that it would be more accurate to treat its constitutive relations as transversely isotropic. Transverse stiffness is positively correlated with buckling resistance and therefore it is suspected that changing the material properties could account for some of the discrepancy between numerical and experimental predictions. Also, the length-to-radius ratio in the FE models is slightly smaller than the one that Starnes reported for Shell 6. Figure 2.16 suggests that this corresponds to a buckling load reduction with respect to the pristine shell of approximately five percentage points.

It has been mentioned before that cylindrical shells with cutouts buckle globally when the opening is sufficiently small. Hence, the initial slope of the experimental data curve in Figure 6.22 is zero as the buckling behavior is independent of the cutout size. It is well known that shell buckling is dominated by initial geometric imperfections in the structure. These are not modeled except in Subsection 6.2.5 and therefore these effects are not accounted for in the numerical results.

Incorporating the effects of mid-surface imperfections may explain some of the discrepancies between the nonlinear numerical and the experimental results. Of course, one could conclude from Table 6.1 that a sufficiently large imperfection amplitude is the reason for the entire gap. However, Starnes' specimens are described as being of high quality by Jullien et al. [25]. Hence, it is more likely that the low experimental buckling loads are the result of some other type of imperfection, namely nonuniform loading. Table 2.1 suggests that this imperfection may have a major impact on the sustainable load that cylindrical shells with cutouts can carry before they buckle. In fact, Starnes manufactured his shells from roll stock sheets that were cut to size and placed on a mandrel. Subsequently, an adhesive material was applied to bond the circumferential shell ends with a lap joint. Naturally, the stiffness of this cross-sectional area differs from the rest of the shell and therefore the assumption of a uniform load introduction in the structure may be overly simplifying. More importantly, Starnes also reported that load misalignments could result in significantly reduced buckling loads.

As such, idealizing shells with circular cutouts as perfect structures enables the engineer to estimate the type of buckling, i.e. global, unstable, or stable local buckling, but accurately predicting buckling loads requires precise information about the real geometry. In this sense the analytical solution serves the same purpose as the numerical simulations because its outputs are qualitatively correct which makes it suitable for preliminary design applications.

7

Quasi-Isotropic, Symmetric, Composite Cylindrical Shells

The investigation of the buckling behavior of isotropic cylindrical shells with cutouts from the previous chapter is extended to quasi-isotropic, symmetric, composite shells on the following pages. After a brief discussion on the choice of a suitable curvature parameter in Section 7.1, the predictions from the modified analytical solution are presented in Section 7.2. Three different laminate stacking sequences are considered, namely $[0, \pm 45, 90]_S$, $[\pm 45, 0, 90]_S$, and $[90, \pm 45, 0]_S$. The analytical results are verified with numerical simulations in Section 7.3 which covers the influence of the cutout on buckling loads, buckling patterns, shell failure, as well as the effects of initial geometric imperfections.

7.1. Curvature Parameters

Several nondimensional curvature parameters have been introduced in Chapter 2, namely Lur's α in equation (2.3) which is based on geometric quantities only, Lekkerkerker's μ in (2.5) which also accounts for the material properties of isotropic cylindrical shells, and finally Hilburger's C in equation (2.19) which fulfills the same purpose as μ , but for composite cylindrical shells. Since many plots in Chapter 6 feature μ , an appropriate curvature parameter for composites has to be selected. C is an intuitive choice, but the context of its derivation differs from that of μ . An equivalent expression for the μ of composite cylindrical shells should be obtained by following the same approach that Lekkerkerker used to arrive at equation (2.4). Since such a derivation is out of scope, it is noted that the expression for μ of isotropic materials is similar to that of the Batdorf parameter Z in equation (3.64). Assuming that the relation between μ and Z should remain the same for composite cylindrical shells yields

$$\mu = \frac{1}{2} \sqrt[4]{\frac{A_{11}A_{22} - A_{12}^2}{A_{11}\sqrt{D_{11}D_{22}}} \frac{a}{\sqrt{R}}} \quad (7.1)$$

after modifying the equivalent Batdorf parameter of a composite shell as given by Nemeth et al. [67] accordingly. The new expression for μ in terms of C is given by

$$\mu = \frac{1}{4} \sqrt[4]{12} \sqrt[3]{\frac{A_{22}}{A_{11}}} \sqrt{C} \quad (7.2)$$

when equating the circumferential width of the circular and the rectangular cutout ($2a = b$). If furthermore $A_{11} = A_{22}$, then the ratio between μ and \sqrt{C} is approximately 0.4653. The factor $1/\sqrt{t}$ from α is implicitly included in μ as the bending stiffness terms scale with t^3 whereas the membrane ones are proportional to t .

The investigation on the influence of ν on the buckling load predictions with analytical and numerical methods in Figures 6.5 and 6.13 suggests that the isotropic μ is not an ideal choice for the nondimensional curvature parameter because the normalized buckling loads are not mapped onto a single design curve. By extension, it should not be expected that the composite μ meets this criterion. However, defining it according to equation (7.1) allows drawing some parallels with the results from the previous chapter.

7.2. Analytical Results

After adapting the analytical solution as described in Section 4.4, it is possible to estimate the buckling loads of quasi-isotropic, symmetric, composite cylindrical shells with circular cutouts. The curvature parameter μ from equation (2.5) is replaced with the expression given in (7.1). Furthermore, the equation for the classical buckling stress in (3.63) is not valid for composite cylindrical shells. Instead, the analytical and numerical results are normalized with τ_{cl} from equation (3.66) as derived by Nemeth et al. [67]. Table 7.1 summarizes the buckling stresses calculated with this method for the pristine reference shells. Naturally, the ply stacking sequence becomes an additional design variable.

R/t [-]	$[0, \pm 45, 90]_S$			$[\pm 45, 0, 90]_S$			$[90, \pm 45, 0]_S$		
	m [-]	n [-]	τ_{cl} [MPa]	m [-]	n [-]	τ_{cl} [MPa]	m [-]	n [-]	τ_{cl} [MPa]
100	1	6	273.5	1	5	363.5	14	0	250.4
200	1	7	131.9	1	6	178.7	20	0	125.1
400	1	8	65.30	1	8	86.23	29	0	62.48
800	1	10	32.10	1	9	42.28	41	0	31.24

Table 7.1: Number of buckling waves m and n as well as the corresponding buckling stresses for pristine composite shells.

Appendix B presents the matrix elements that govern the generalized eigenvalue problem for composite cylindrical shells. Since these are populated differently than the matrix entries for the analysis of isotropic cylindrical shells, only $M = N = 1$ in the general shape function (4.43) provides meaningful results due to the effects of ill-conditioned matrices for the case of additional r terms.

Figure 7.1 plots the analytical buckling stress τ_{cr} normalized with the reference stress τ_{cl} against the new curvature parameter μ for each layup and R/t combination. One can see that the data points for different values of R/t do not coincide when the laminate stacking sequence is either $[0, \pm 45, 90]_S$ or $[\pm 45, 0, 90]_S$. The separation is not the result of the modified constitutive relations. Instead, it is caused by the buckling stresses that are used to normalize the analytical predictions. Comparing the latter in Table 7.1 for the first two laminates reveals that halving the shell thickness reduces the buckling stress by a factor that is slightly larger than two. However, the analytical buckling stress for the shell with a cutout is exactly halved when R/t is doubled. Only when the buckling mode of the pristine reference shell is axisymmetric, i.e. $n = 0$ which is also assumed during the derivation of the buckling stress of isotropic cylindrical shells, the two values change proportionally so that a single curve is obtained as for the layup $[90, \pm 45, 0]_S$.

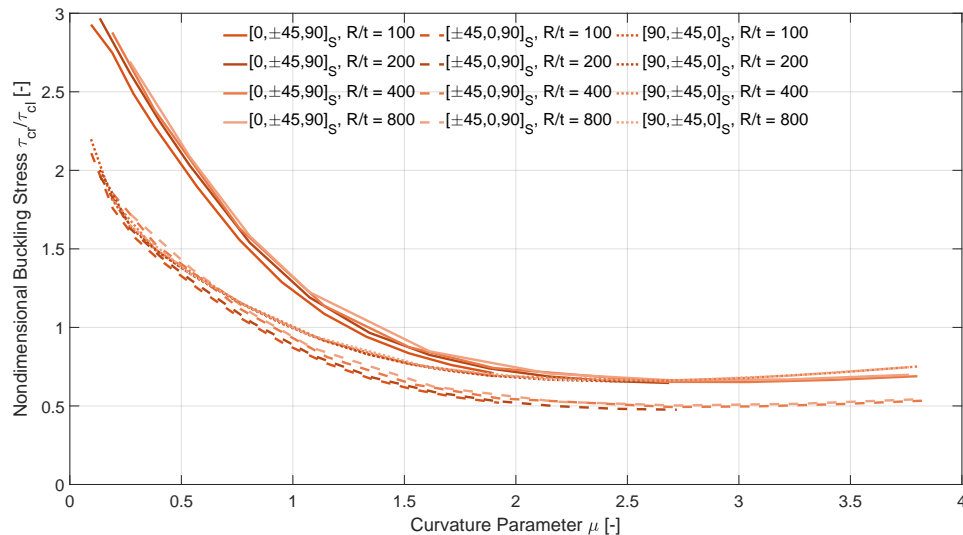


Figure 7.1: Analytically predicted normalized buckling stresses for quasi-isotropic laminates.

The $[0, \pm 45, 90]_S$ laminate appears to be the most sensitive to an increase of the cutout size, followed by the $[\pm 45, 0, 90]_S$ layup and finally the composite with a $[90, \pm 45, 0]_S$ stacking sequence. Initially, the last one provides a low buckling resistance, but it is able to deal with larger cutout sizes more efficiently. As for

isotropic materials, the buckling stress decreases rapidly at first and then stabilizes at approximately $\mu = 2$. If the curvature parameter is sufficiently large, a small increase in the normalized buckling stress is observed again. The normalized buckling stress of the $[0, \pm 45, 90]_S$ layup is relatively large compared to the predictions for the isotropic shell displayed in Figure 6.1 while the estimates for the other two laminates are more in line with those for the isotropic case.

Since the buckling stresses are normalized with different reference values, it is also interesting to look at the absolute numbers illustrated in Figure 7.2. Results are presented for $R/t = 400$ as it covers a large range of the curvature parameter. The order of laminates from the most to the least effective stacking sequences is the same as the previously mentioned one. All layups perform similarly well for large cutout dimensions. In contrast to the buckling stresses of the pristine shells indicated in Table 7.1 where the $[\pm 45, 0, 90]_S$ stacking sequence performs the best, the $[0, \pm 45, 90]_S$ laminate provides the highest buckling resistance for cylindrical shells with cutouts. The membrane response of all shells is identical, and the structure is loaded in axial compression. Hence, it is conceivable that adding more axial bending stiffness is the most beneficial in terms of increasing the buckling stress when bending stresses are neglected.

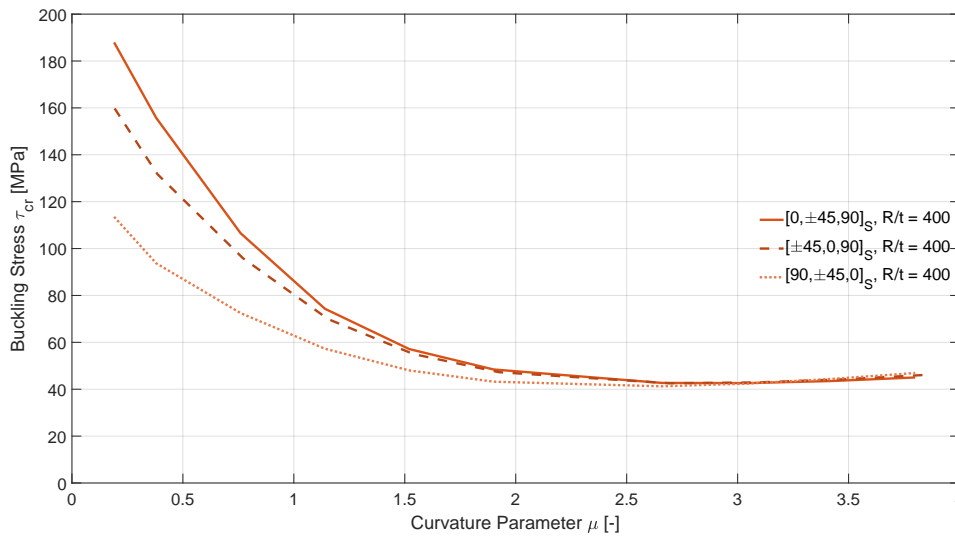


Figure 7.2: Absolute buckling stresses for quasi-isotropic composite shells predicted by the analytical solution.

7.3. Numerical Results and Verification

As in Chapter 6, the analytical results are verified with numerical predictions. Mesh and loading convergence studies are conducted again and yield similar results as for the isotropic case, i.e. a mesh size of 2 mm is sufficient for most shell geometries and the type of load application has a negligible effect on the buckling load estimates. Without checking it is assumed that the conclusions from the investigations regarding the influence of the element type and numerical damping are still valid.

One should note that the NLS simulations struggle to overcome the sudden change in stiffness associated with local buckling for the three considered layups. The generated load-displacement curves indicate that zero tangents cannot explain this behavior for all cases and therefore it is suspected that the structural response of composite cylindrical shells during local buckling could be of dynamic nature. In any case, the NLS procedure aborts early which is why it is not discussed further in this section.

7.3.1. Buckling Loads

First, the analytically predicted buckling loads are compared with the results from the FE simulations. The buckling load estimates from the LBA are plotted in Figure 7.3 for all shell configurations from Table 5.2. Nondimensional buckling loads F_{cr}/F_{cl} greater than unity for the $[0, \pm 45, 90]_S$ layup are caused by τ_{cl} underestimating the load-carrying capability of the pristine composite shells compared to predictions of the LBA for the same structure. The numerical buckling loads for the other two laminate stacking sequences are slightly lower than their analytical counterparts. Furthermore, the number of axial and circumferential (half)-waves is overestimated in Table 5.2, especially for higher R/t .

Anyhow, it can be seen that the buckling resistance of composite cylindrical shells in Figure 7.3 is quite different from that shown in Figure 7.1. The buckling loads decrease continuously in every case due to an increasing influence of the bending stresses as suggested by Figure 2.1. Furthermore, the individual buckling load curves separate for all considered layups and therefore the normalization with the reference buckling loads cannot be the sole origin of this behavior. A similar trend is observed in Figure 6.11 where it has been argued that a changing relation between membrane and bending stresses in combination with varying sensitivities of the specific buckling modes to these variations causes the buckling loads to drop for higher R/t . The fact that the order of the R/t curves in Figure 7.3 changes approximately at values of μ where different buckling patterns emerge appears to support this conclusion.

As in Figure 7.1, the $[0, \pm 45, 90]_S$ layup performs best, followed by the $[\pm 45, 0, 90]_S$ composite. The stacking sequence $[90, \pm 45, 0]_S$ yields the lowest nondimensional buckling loads for a given R/t . Overall, the three layups are almost equally sensitive to an increase of μ . If one were to plot Figure 7.3 with absolute buckling loads, then the order of the preferred stacking sequences would be the same as in Table 5.2.

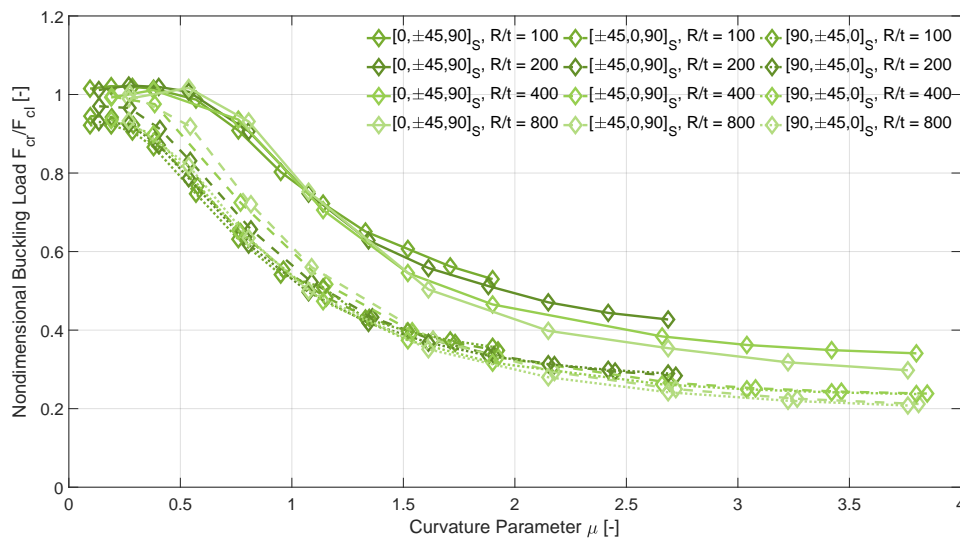


Figure 7.3: Normalized buckling loads for various stacking sequences predicted with a LBA.

Figures 7.4 and 7.5 depict the initial and maximum buckling loads determined with the NLD procedure. The sequence of the layups in terms of the largest buckling load generally agrees with the analytical solution, but trend inversions occur at different values of μ due to the limitations of the linear eigenvalue analysis. The displacement fields shown in Subsection 7.3.3 indicate that buckling loads decrease rapidly when unstable local buckling modes are present. These mode shapes are different for each stacking sequence and they relate to a varying sensitivity to unstable local buckling.

When the initial buckling load recovers and the maximum one remains approximately constant, the displacement patterns of all three composites are similar. Hilburger, Starnes, and Nemeth [31–33] found that adding 90° plies around the cutout as a reinforcement against stable local buckling is more beneficial than doing so with 0° laminas. Similarly, the $[90, \pm 45, 0]_S$ layup resists local buckling to a greater extent than the $[0, \pm 45, 90]_S$ one. Apparently, decreasing the axial bending stiffness to lower the corresponding bending stresses in the vicinity of the opening is more effective than increasing the bending stiffness in an attempt to limit the out-of-plane displacements.

Initial buckling loads in Figure 7.4 are larger for thicker shells because thinner shells are more susceptible to large out-of-plane displacements as well as the associated stress redistribution and its consequences due to the disproportional bending stiffness reduction. The initial buckling loads recover after some value of μ as predicted by the analytical solution. This critical value is a function of the stacking sequence and R/t , while the individual layup curves are closely spaced for small μ . Like in Figure 2.9 where the buckling load curve branches off depending on R/t , the curvature parameter μ is not sufficient to describe the shell response adequately. Naturally, nonlinear effects must be the cause of this response because the LBA does not predict comparable trends. It is suspected that the stress redistribution associated with the large prebuckling displacements is responsible for the observed behavior even though there are no obvious stress field patterns discernible in Subsection 7.3.5.

The analytical solution also suggests that there is an increase of the initial buckling load for large μ , but it cannot account for nonlinearities. Therefore, the corresponding trend in Figure 7.1 is better explained with the change of the local buckling displacement pattern as shown in Subsection 7.3.2. This manifests itself mathematically through the jump of the global minimum of the buckling stress function plotted in Figure 6.4 towards higher values of the decay parameter B .

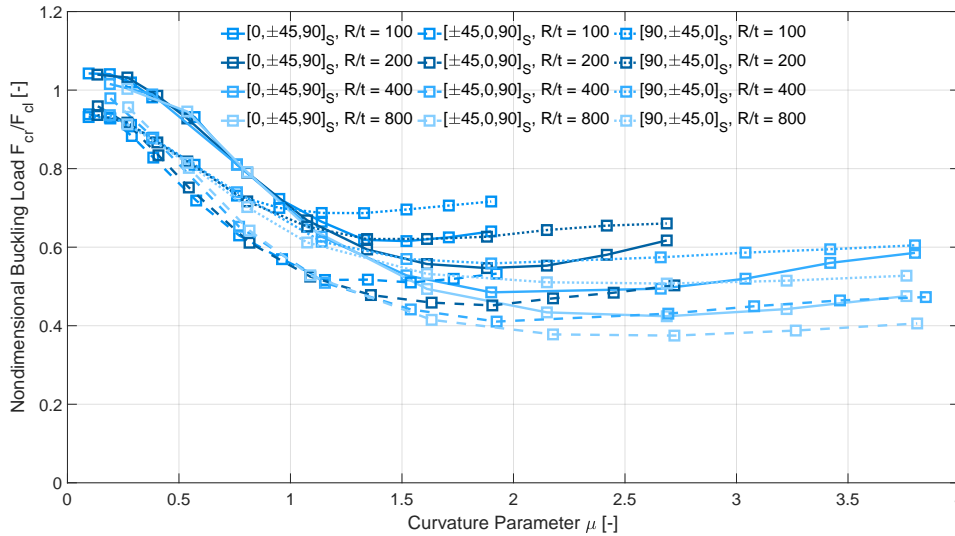


Figure 7.4: Normalized initial buckling loads for various stacking sequences predicted with a NLD analysis.

In contrast to the diverging curves representing the initial buckling load in Figure 7.4, the maximum buckling load in Figure 7.5 can be characterized by μ for all R/t , but there is still some dependency on the stacking sequence of the laminate. In fact, higher R/t are advantageous which is reasonable because bending stresses are lower for thinner shells. Additionally, the load-displacement curves in Subsection 7.3.3 indicate that thinner shells also feature a higher nondimensional stiffness after local buckling. Finally, the spacing of the curves in Figure 7.5 compared to Figure 7.4 implies that the mechanisms that govern the local and global buckling of shells with large μ are inherently different which supports the argument from Chapter 6 that the two buckling modes are sensitive to distinct characteristics of the respective displacement and/or stress fields.

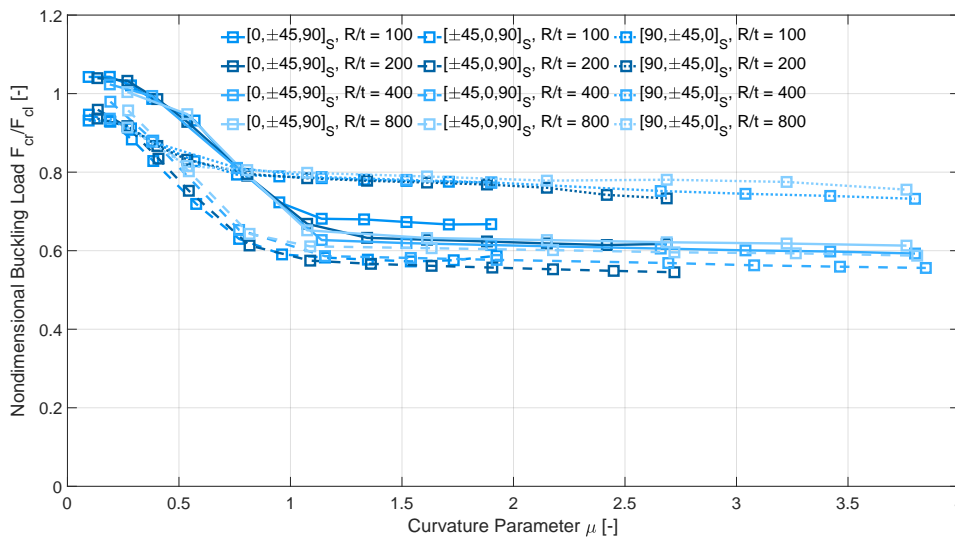


Figure 7.5: Normalized maximum buckling loads for various stacking sequences predicted with a NLD analysis.

Again, $R/t = 400$ is selected to analyze the results from the various analyses because it covers the largest range of μ . Figure 7.6 summarizes the analytical predictions, those of the LBA and initial buckling loads from NLD simulations. Some observations that were made for isotropic shells are also valid for composite

cylindrical shells. For example, the buckling load estimates by the analytical solution are too high for small cutout sizes because it is assumed that local buckling always occurs, while the numerical simulations predict global buckling in this domain. Furthermore, the LBA buckling loads are initially higher than those for the NLD which is expected, but the trend inverts as soon as nonlinear geometric effects have to be considered. The fact that the trend inversion of the $[90, \pm 45, 0]_S$ laminate occurs rather early is partly caused by the relation between the reference buckling stresses from Table 7.1, but it also suggests that nonlinear effects are more important for this stacking sequence than for the other two which goes hand in hand with the idea that large radial displacements are more endurable than the effects of higher stress concentrations.

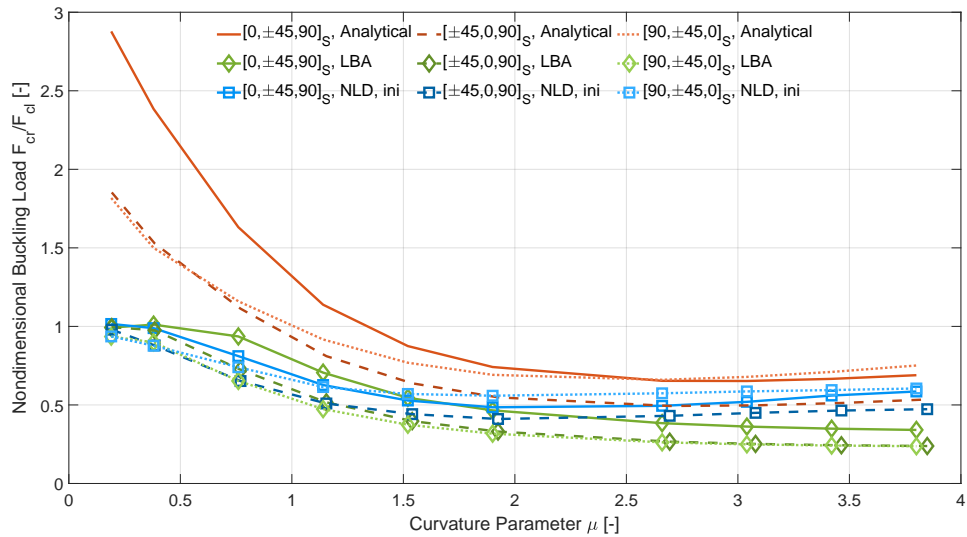


Figure 7.6: Normalized (initial) buckling loads of quasi-isotropic shells for $R/t = 400$.

It is noted that the curves that represent the analytical buckling load prediction intersect in the same order as those of the NLD procedure which cannot be said for the LBA. Hence, one could argue that nonlinear geometric effects as well as the actual shell prebuckling stress distribution are reasonably well approximated by the linearized structural response in combination with the assumption of the flat plate prebuckling stress field. The analytical solution predicts the largest buckling loads due to the underestimation of the prebuckling stress distribution and certain characteristics of the Ritz method.

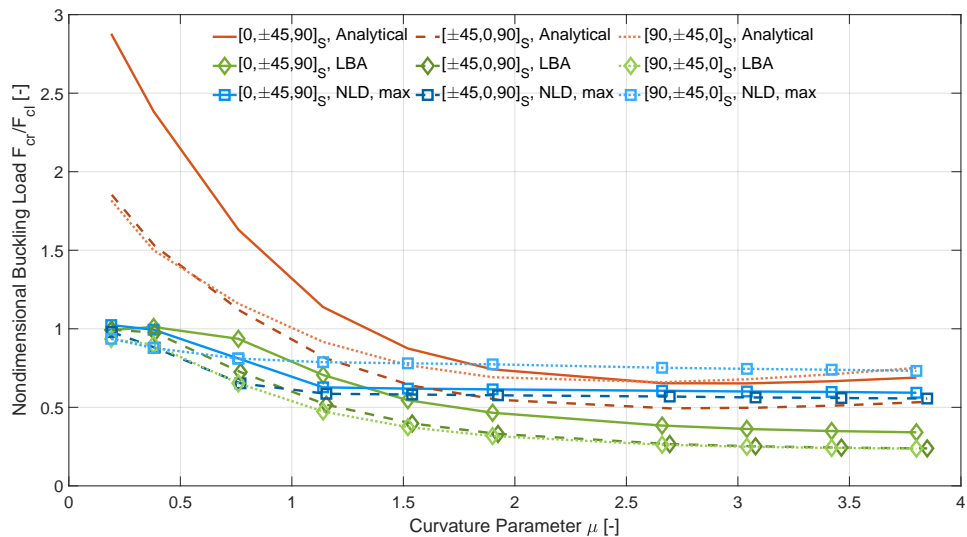


Figure 7.7: Normalized (maximum) buckling loads of quasi-isotropic shells for $R/t = 400$.

As mentioned earlier, the analytical procedure is best evaluated against the initial buckling load predictions from the NLD simulations because the maximum buckling mode shapes are always global which is not

modeled in Chapter 4. Nonetheless, such a comparison is made in Figure 7.7. Important changes relative to Figure 7.6 are that the NLD maximum buckling loads remain constant from smaller μ onwards and that the analytical predictions underestimate the numerical buckling loads.

Due to the varying reference buckling loads from Table 7.1, it is helpful to investigate absolute values as in Figure 7.2. Hence, Figure 7.8 is a version of Figure 7.7 that is adapted accordingly. It is noted that the $[\pm 45, 0, 90]_S$ laminate provides the highest numerical buckling loads for small μ which is consistent with the predictions from Table 7.1. The LBA estimates that the $[90, \pm 45, 0]_S$ layup performs significantly worse than the other two stacking sequences which is not the case for the NLD procedure. Here, the $[\pm 45, 0, 90]_S$ composite outperforms its counterparts, but due to the low sensitivity to an increase of the cutout size the $[90, \pm 45, 0]_S$ laminate is the next best choice for large cutouts.

The curves predicted with the analytical solution agree reasonably well. However, the buckling resistance of the $[0, \pm 45, 90]_S$ is significantly overestimated. This is probably the result of neglecting the bending stresses in the problem setup. Placing 0° plies on the outside of the cylindrical shell considerably increases the bending stiffness which is accounted for in \mathbf{K}^M . However, the corresponding detrimental effects on the bending stress distribution are not quantified in \mathbf{K}^G .

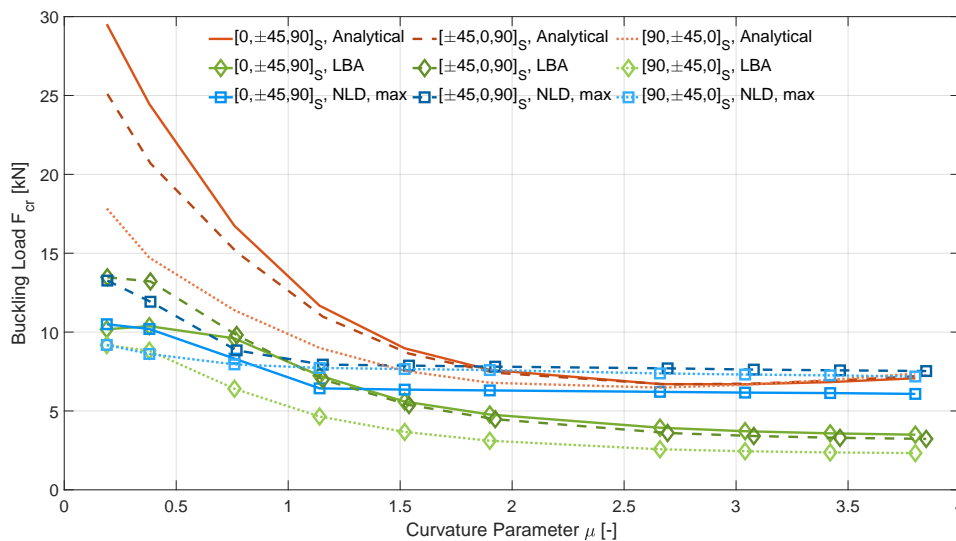


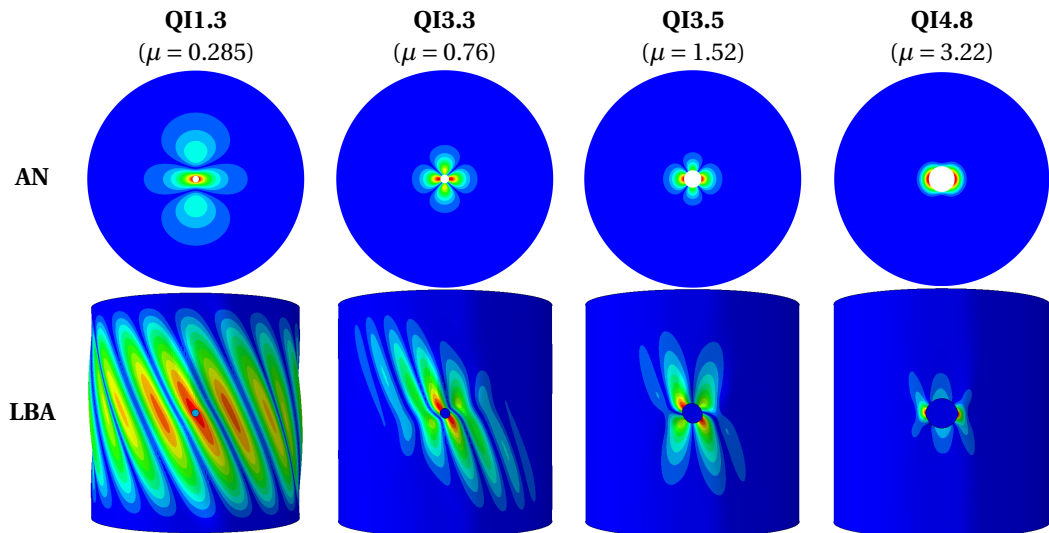
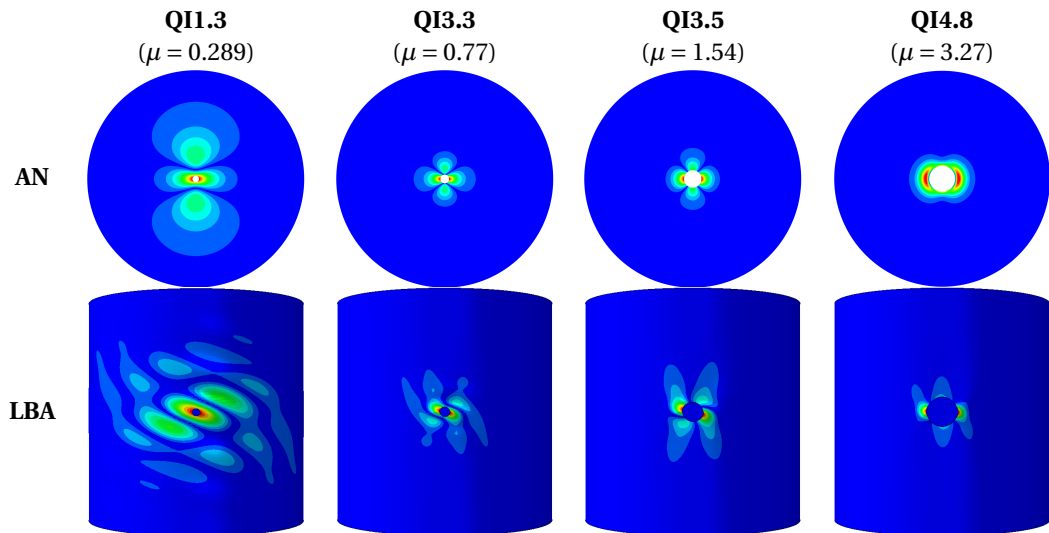
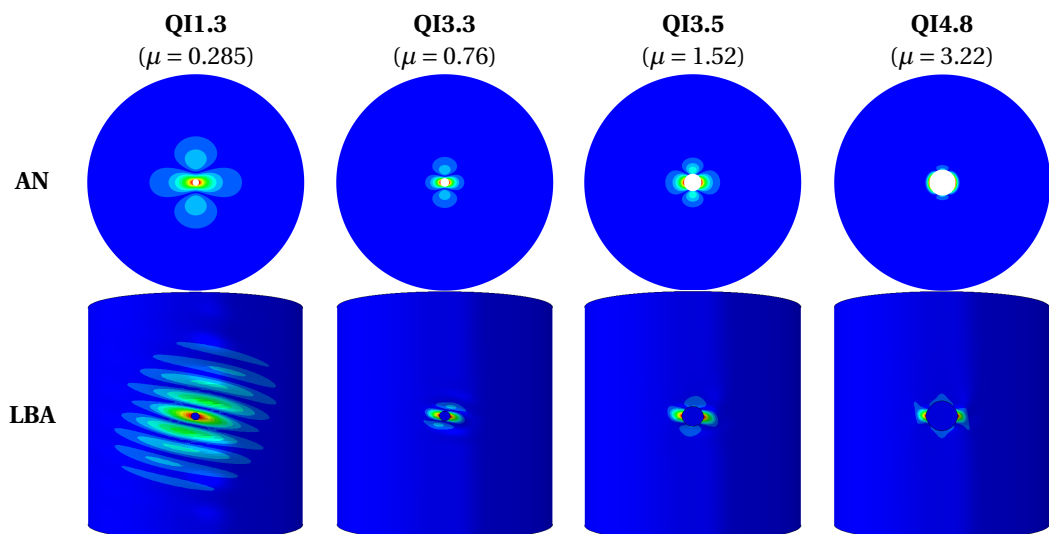
Figure 7.8: Absolute buckling loads of quasi-isotropic shells for $R/t = 400$.

7.3.2. Buckling Mode Shapes

Next, the buckling mode shapes predicted with analytical and numerical methods are evaluated for the considered laminates. AN in Figures 7.9, 7.10, and 7.11 refers to the eigenmodes obtained from the analytical solution. Since the shape function (4.1) does not include cosine terms with arguments that feature factors larger than two for θ , it is not possible to model the rotated buckles that are predicted by the numerical simulations. As such, the analytical buckling mode shapes for the quasi-isotropic shells resemble those of the isotropic cylindrical shells from Subsection 6.2.3. Furthermore, there is little variance between the buckling modes of the different composite layups, yet the buckling load predictions in the previous segment follow distinct trends.

Looking only at the LBA, one can see how the buckling mode shapes are influenced by the respective laminate stacking sequence. The buckles are oriented axially for the $[0, \pm 45, 90]_S$ layup and small μ , they are skewed for the $[\pm 45, 0, 90]_S$ composite, and almost horizontal for the $[90, \pm 45, 0]_S$ laminate. Apparently, the alignment of the buckling pattern follows the orientation of the outermost ply of each laminate which makes sense because these layers provide the highest bending stiffness. All buckling mode shapes transition to the localized displacement pattern. While the change of the buckling mode is rather continuous for the $[0, \pm 45, 90]_S$ layup, it is much more abrupt for the other two, especially for the $[90, \pm 45, 0]_S$ composite. This suggests that the corresponding stress fields vary in a similar pattern which is confirmed in Subsection 7.3.5.

Evidently, the initial buckling patterns predicted with the LBA are vastly different compared to the analytical solution due to the limitations of the displacement function. Exceptions are cylindrical shells with large μ where the mode shapes resemble those of the isotropic shells.

Figure 7.9: Initial buckling patterns of the $[0, \pm 45, 90]_S$ layup.Figure 7.10: Initial buckling patterns of the $[\pm 45, 0, 90]_S$ layup.Figure 7.11: Initial buckling patterns of the $[90, \pm 45, 0]_S$ layup.

7.3.3. Buckling Mode Shape Evolution

After discussing the shape of the initial buckling modes, the structural response of composite cylindrical shells is investigated in more detail by evaluating the results from the nonlinear dynamic simulations. The load-displacement curves shown in Figures 7.12, 7.13, and 7.14 correspond to the radial displacement fields illustrated in Figures 7.15, 7.16, and 7.17. Again, *A*, *B*, *C*, and *D* denote the configurations before any type of buckling occurs, at local buckling, as well as before and after global buckling, respectively. The load-displacement curves depend on the nondimensional reaction force RF3 at the unloaded shell edge which is plotted against the normalized uniform shell-end displacement $U3$. The normalization of RF3 is performed as explained in Section 6.2.2, whereas the reference displacement at buckling u_{cl} is calculated according to equation (7.3) assuming a linear shell membrane response. τ_{cl} is taken from Table 7.1.

$$u_{cl} = \tau_{cl} \frac{A_{11}}{A_{11}^2 - A_{12}^2} Lt \quad (7.3)$$

The loading history of the $[0, \pm 45, 90]_S$ layup is depicted in Figures 7.12 and 7.15. Shell QI1.3 does not exhibit a local buckling configuration which is why point *B* is missing on the respective load-displacement curve. In fact, none of the investigated QI1.3 shells feature a local buckling mode. Unlike for the isotropic shell I1.6 in Figure 6.16, a local buckling configuration does not stand out for shell QI3.3 at first glance because the load-displacement curve only contains a single point where the structure's stiffness changes drastically. However, the displacement pattern in Figure 7.15 depicts large displacements before the shell buckles globally which is an indicator of local buckling.

In contrast, the load-displacement curves of shells QI3.5 and QI4.8 include multiple points after which a stiffness loss is observed. The earlier ones correspond to stable local buckling configurations as the post-buckling stiffness is positive. The first local buckling displacement pattern is shown in row *B* of Figure 7.15. The counterclockwise rotation around the cutout from row *B* to row *C* takes place during the second local buckling event. It is noted that the normalized postbuckling stiffness of shell QI4.8 is higher than that of QI3.5. While the local buckling mode shapes in Figure 7.15 are similar, the out-of-plane displacements are restricted to the cutout vicinity which explains the increased stiffness as the effective carrying width of the shell is larger. Additionally, the transition from one configuration to the other is gradual for shell QI3.5, whereas an abrupt change is observed for shell QI4.8.

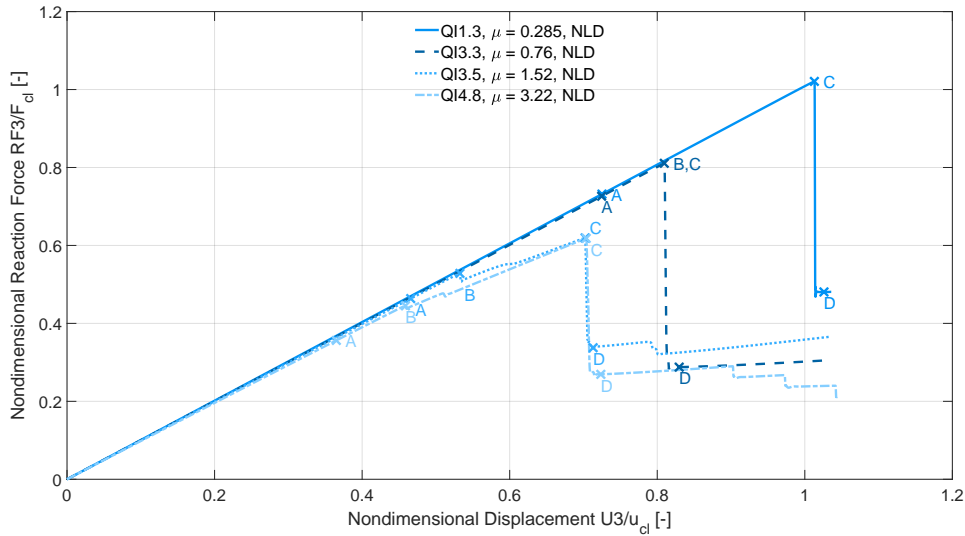


Figure 7.12: Load-displacement curves for some configurations of the $[0, \pm 45, 90]_S$ laminate.

Figures 7.13 and 7.16 relate to the $[\pm 45, 0, 90]_S$ layup. Overall, the structural response of this laminate is relatively similar to the previous one. Again, there is no distinct local buckling event visible in Figure 7.13 for shell QI3.3, but the displacement field in Figure 7.16 implies its existence and the shell configurations QI3.5 and QI4.8 feature two stable stiffness reductions each just like the layup discussed before. Similarly, the second stiffness loss corresponds to the rotation of the buckling pattern. One may also notice that the nondimensional displacement at global buckling is slightly larger for shell QI4.8 than for QI3.5 which suggests that a critical stress state is reached later due to the larger effective carrying width of the structure.

Like the isotropic shell, the unstable local buckling mode of the $[\pm 45, 0, 90]_S$ cylindrical shell features a different shape than the stable one. While the prebuckling displacement field resembles that of the $[0, \pm 45, 90]_S$ layout, the diametrically opposed buckles combine into a single distortion directly on top of the cutout. The out-of-plane deflections shown in Figure 7.16 increase substantially over a very short time frame. Consequently, the events denoted by points B and C essentially coincide on the load-displacement curve.

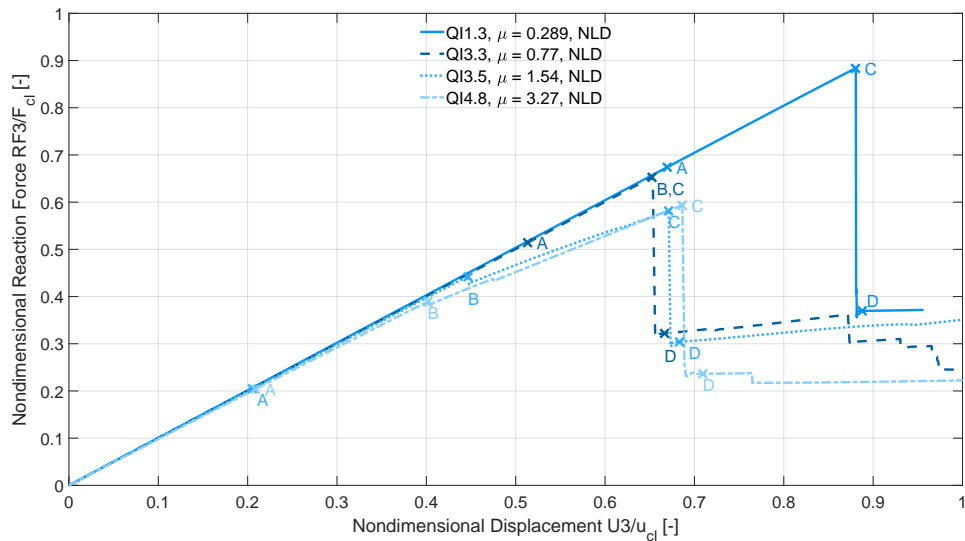


Figure 7.13: Load-displacement curves for some configurations of the $[\pm 45, 0, 90]_S$ laminate.

The plot in Figure 7.14 and the images in Figure 7.17 represent the structural response of the $[90, \pm 45, 0]_S$ laminate. As the load-displacement curve indicates, this layout is less sensitive to an increase of the curvature parameter. Local buckling occurs at slightly higher nondimensional load levels. Furthermore, the shell can sustain more additional load between local and global buckling. Comparing the postbuckling characteristics in Figures 7.12, 7.13, and 7.14 with the respective stiffness properties reveals that the higher D_{11} , the smaller the gap between points B and C on the load-displacement curves. Hence, one could argue that the shell response after local buckling is dominated by the ability of the structure to withstand axial bending stresses. Since the relative contribution of bending stresses is reduced when the shell thickness decreases, it makes sense that these configurations generally show better results for the maximum buckling load in Figure 7.5.

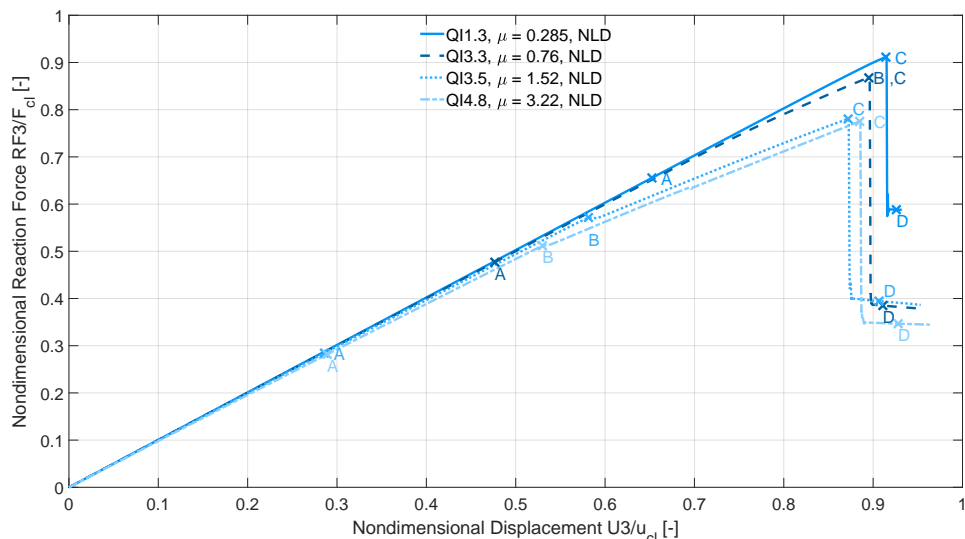


Figure 7.14: Load-displacement curves for some configurations of the $[90, \pm 45, 0]_S$ laminate.

Compared to the response of isotropic cylindrical shells depicted in Figure 6.16, the prebuckling stiffness of composite shells appears to be less nonlinear since the laminated cylindrical shells buckle locally at re-

duced nondimensional buckling loads. Consequently, large prebuckling displacements do not have as much time to develop. The superior postbuckling stiffness of shells with larger μ is also visible for the isotropic case. Hence, one can expect that the trends depicted in Figure 7.5 are also valid for the isotropic cylindrical shells even though it cannot be directly inferred from the previous chapter since no distinction between different R/t has been made.

As Figures 7.15, 7.16, and 7.17 naturally contain the initial buckling modes of the NLD simulations, one may also evaluate them against the linear mode shapes from Subsection 7.3.2. First, the initial buckling modes for shell QI1.3 are global as predicted by the LBA. While the displacement patterns do not agree exactly with the LBA, they also change their shape depending on the layup. For large μ the buckling modes have a similar shape regardless of the composite stacking sequence. However, when the local buckling mode is unstable as for shell QI3.3, then the mode shapes are a function of the layup again. The unstable displacement pattern in Figure 7.9 evolves naturally into the buckling modes for larger μ . The same is not true for the other two laminates which implies that the sensitivity of the buckling load to the cutout size shown in Figure 7.4 may be caused by the respective stress distribution.

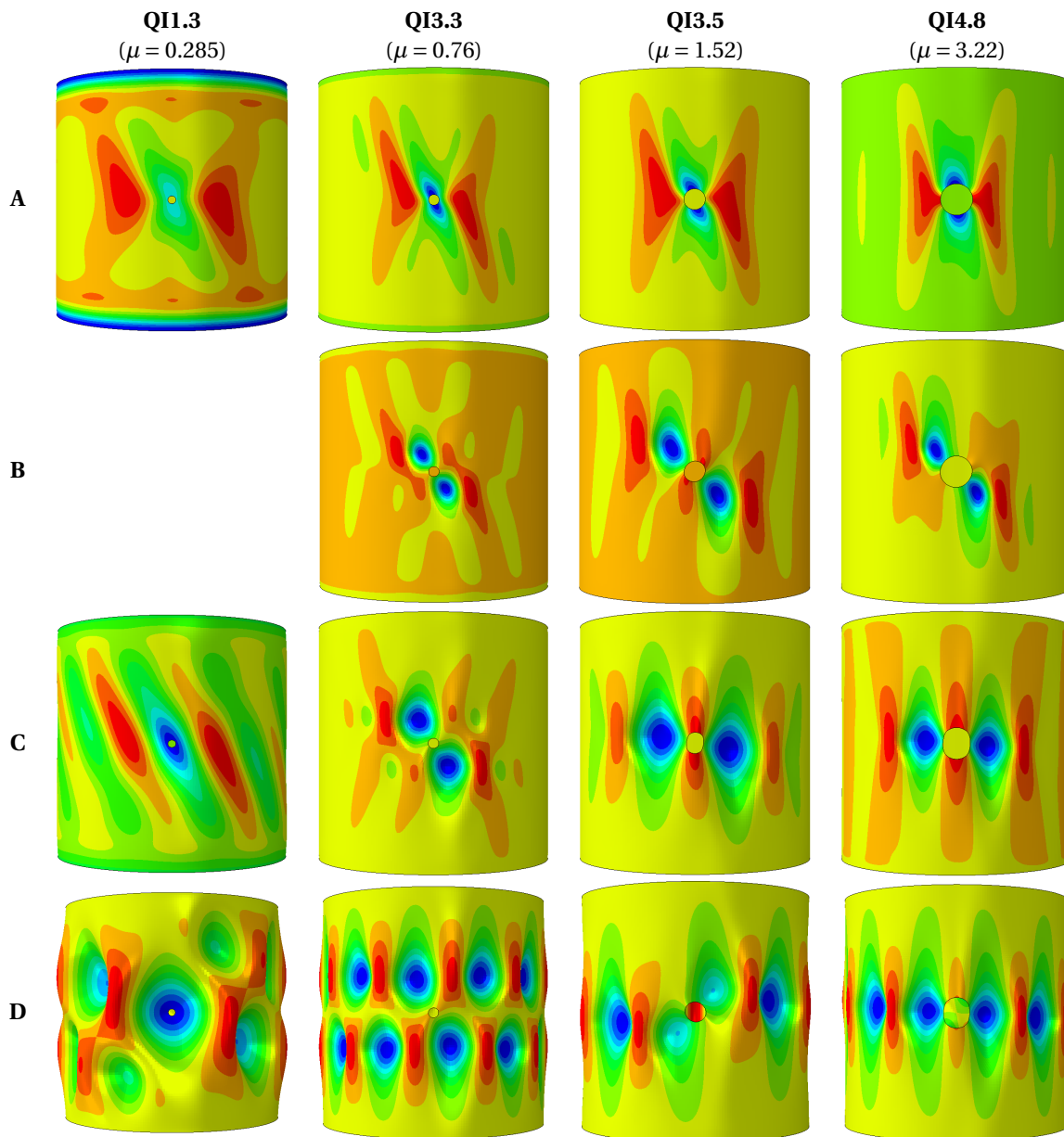


Figure 7.15: Radial displacements of a $[0, \pm 45, 90]_S$ laminate calculated with a NLD analysis during loading (A), at local buckling (B), before (C), and after (D) global buckling. Amplification factor 5.

To provide some perspective regarding the magnitude of the displacements in Figures 7.15, 7.16, and 7.17, the following list contains the maximum radial deflections of the configurations *B* and *D*, i.e. at local and after global buckling, for the considered layups. They all point inwards which means that they relate to the color blue in the images. The order of the deflections is equal to the order of the shell names in the figures.

- $[0, \pm 45, 90]_S$; *B*: n.a., 0.933 mm, 1.45 mm, 0.764 mm, *D*: 6.18 mm, 2.10 mm, 3.42 mm, 2.11 mm
- $[\pm 45, 0, 90]_S$; *B*: n.a., 0.165 mm, 0.305 mm, 0.162 mm, *D*: 4.84 mm, 3.12 mm, 3.33 mm, 1.73 mm
- $[90, \pm 45, 0]_S$; *B*: n.a., 0.594 mm, 0.763 mm, 0.428 mm, *D*: 4.57 mm, 1.67 mm, 1.90 mm, 1.44 mm

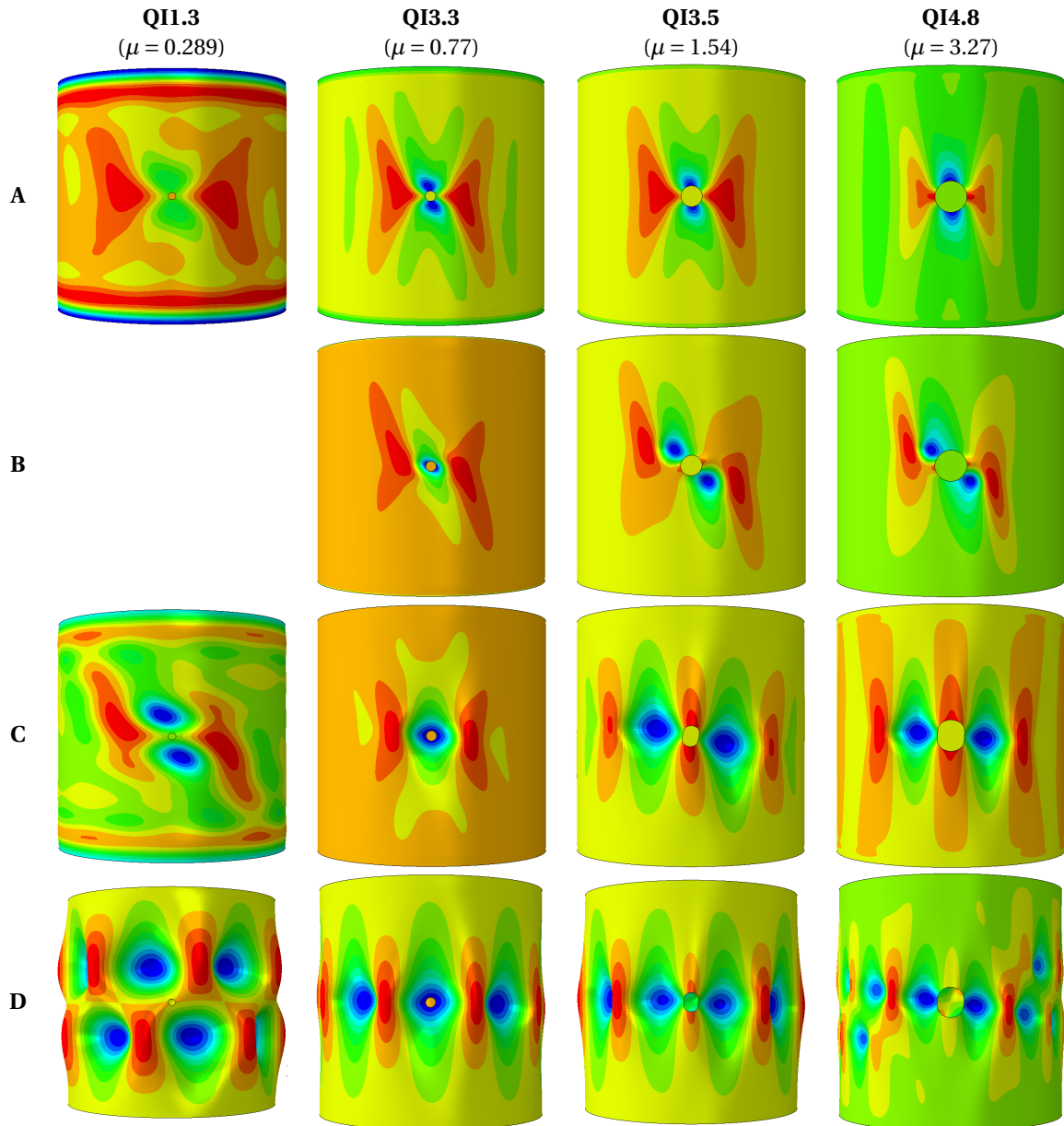


Figure 7.16: Radial displacements of a $[\pm 45, 0, 90]_S$ laminate calculated with a NLD analysis during loading (A), at local buckling (B), before (C), and after (D) global buckling. Amplification factor 5.

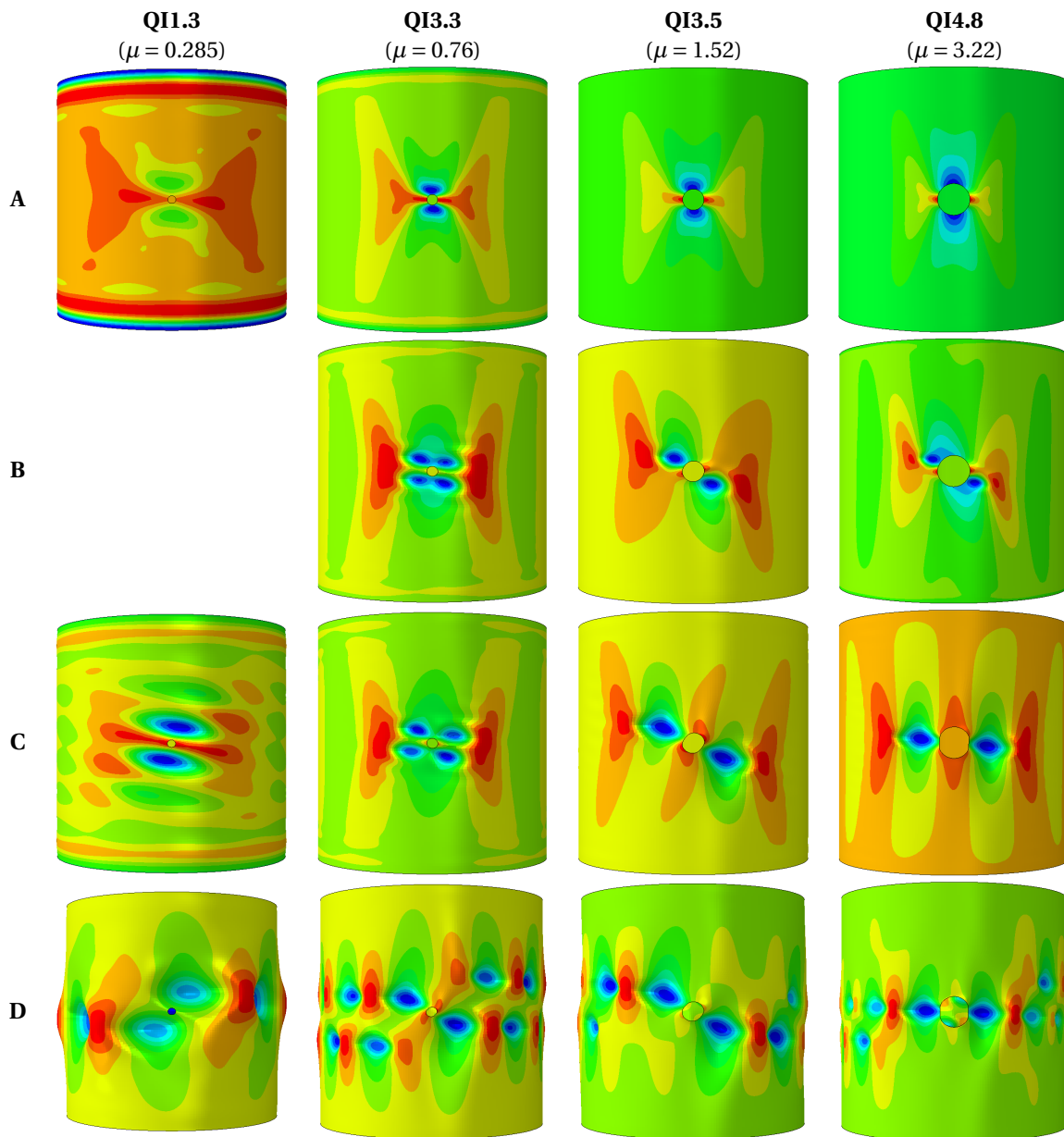


Figure 7.17: Radial displacements of a $[90, \pm 45, 0]_S$ laminate calculated with a NLD analysis during loading (A), at local buckling (B), before (C), and after (D) global buckling. Amplification factor 5.

7.3.4. Initial Geometric Imperfections

The effects of mid-surface imperfections are studied by superimposing buckling mode shapes computed with the LBA and scaling them relative to the shell wall thickness. Global buckling patterns are considered for shells QI1.3, QI3.3, and QI3.5. Additionally, imperfections in the form of local buckling modes are modeled for shell QI3.5 because it exhibits a stable local buckling configuration. All imperfection patterns are selected to match the nonlinear displacement fields illustrated in the previous subsection. Higher order buckling modes from the LBA provide reasonable approximations for every possible permutation of shell configuration, stacking sequence, and buckling mode type with the exception of the global buckling pattern for shell QI3.5 with a $[90, \pm 45, 0]_S$ layup. None of the first 30 LBA eigenvectors correspond to the displacement field in row D of Figure 7.17. The superposition of two linear buckling modes is used as an approximation instead. Figures 7.18, 7.19, and 7.20 contain exemplary load-displacement curves for some selected shell and stacking sequence combinations. More information regarding the influence of the imperfection amplitude on the maximum buckling load for the various laminates is available in Tables 7.2, 7.3, and 7.4.

The graph in Figure 7.18 is concerned with the $[0, \pm 45, 90]_S$ version of shell Q11.3. Like for isotropic cylindrical shells, it can be seen that the inclusion of mid-surface imperfections results in a significant reduction of the load that the shell can sustain before it buckles globally. The prebuckling response is mostly linear except for very large imperfection amplitudes where nonlinearities begin to emerge. Buckling leads to a considerable reduction of the shells' load-carrying capability with the exception of the shell that is modeled with an imperfection amplitude of 50%. For this configuration a positive postbuckling stiffness is observed which indicates that a stable local buckling mode can also exist for cylindrical shells with small μ .

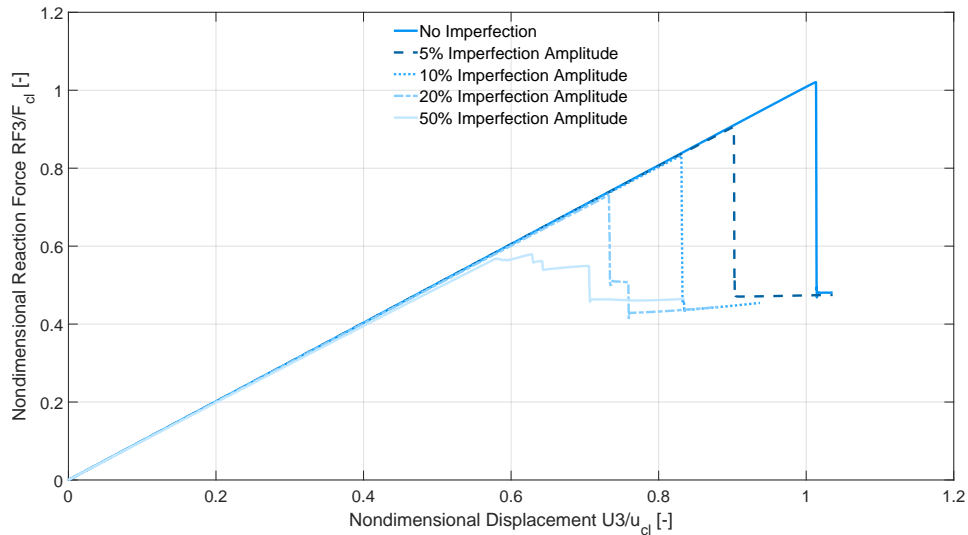


Figure 7.18: Normalized load-displacement curves for shell Q11.3 with a $[0, \pm 45, 90]_S$ layup and varying imperfection amplitudes.

The trends of the $[\pm 45, 0, 90]_S$ layup for shell Q13.3 in Figure 7.19 agree with their isotropic counterparts to a lesser degree. In Figure 6.18 it was observed that the unstable local buckling mode acts as a threshold as it prohibits large imperfection amplitudes to impact the load-carrying capability of the structure. Such an effect is, if at all, only present for the smallest considered imperfection amplitude. Higher ones alter the structural response of the shell in a way that promotes stable local buckling modes. Especially the load-displacement curve for an imperfection amplitude of 20% is reminiscent of those for shell Q13.5 as it features two instabilities before global buckling occurs.

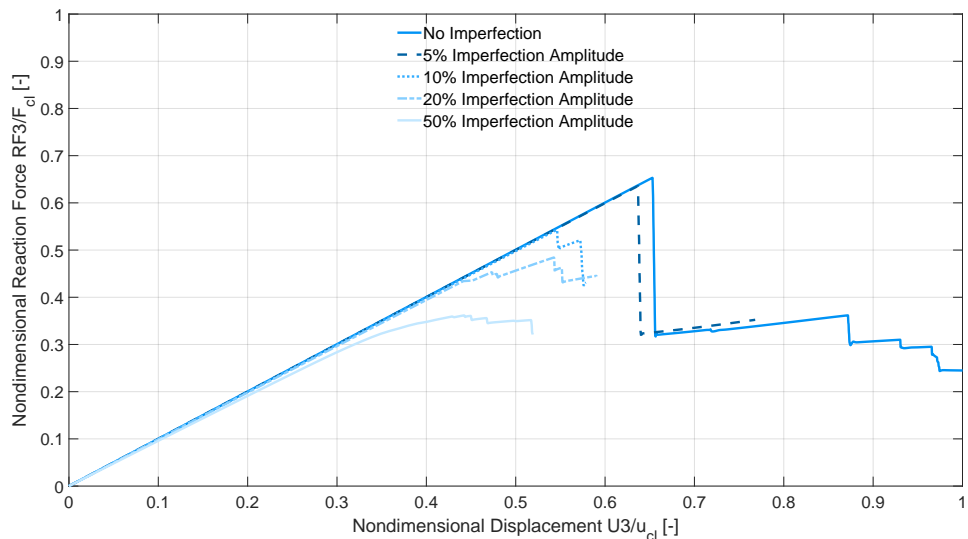


Figure 7.19: Normalized load-displacement curves for shell Q13.3 with a $[\pm 45, 0, 90]_S$ layup and varying imperfection amplitudes.

The load-displacement curves for shell Q13.5 and a stacking sequence of $[90, \pm 45, 0]_S$ that account for local imperfection patterns are shown in Figure 7.20. Like for the isotropic cylindrical shells, this type of imperfec-

tion has almost no effect on the structure's ability to carry loads. If cylindrical shells with an imperfection in the shape of a stable local buckling mode could be manufactured, one would be able completely remove the local buckling event from the shell response at the expense of a negligible portion of the prebuckling stiffness.

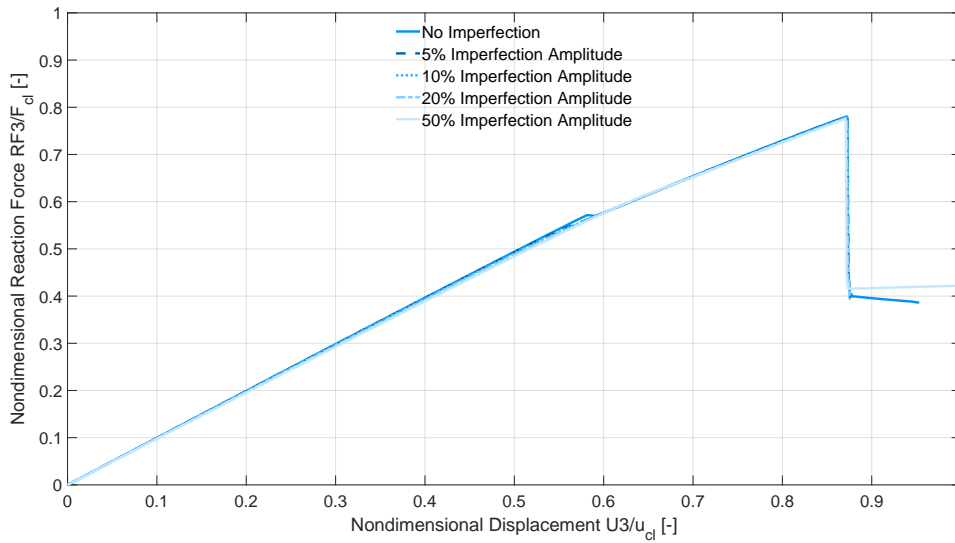


Figure 7.20: Normalized load-displacement curves for shell QI3.5 with a $[90, \pm 45, 0]_S$ layup and varying local mid-surface imperfection amplitudes.

As mentioned before, multiple imperfection patterns obtained from a LBA are superpositioned in an attempt to capture the global buckling mode shape of shell QI3.5 in Figure 7.17. Figure 7.21 illustrates the corresponding load-displacement curves which are uncharacteristic when taking the overall trends from Tables 7.2, 7.3, and 7.4 into account. It appears that the inclusion of two buckling patterns triggers a nonlinear structural response before any type of buckling occurs. This is not the case for the other two laminates. As such, it is debatable whether the described modeling choice is appropriate.

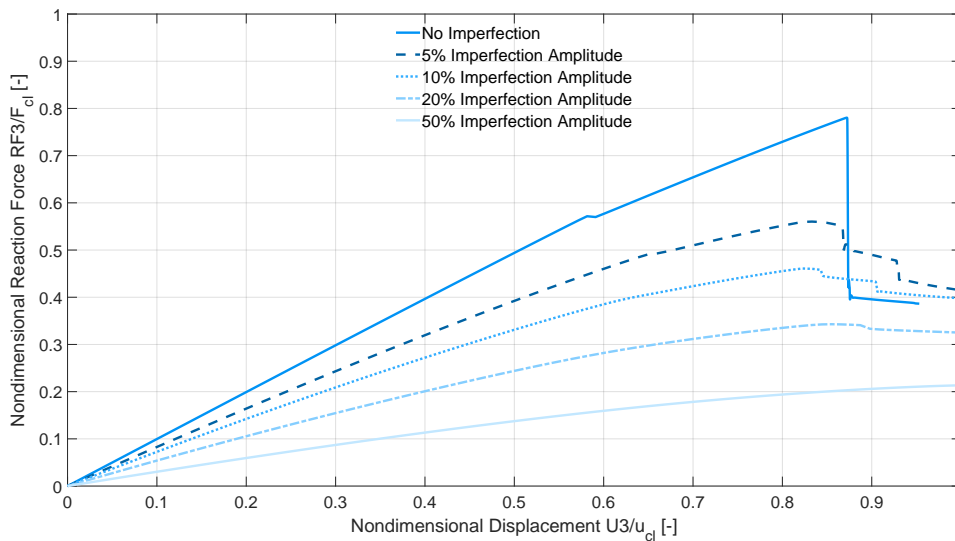


Figure 7.21: Normalized load-displacement curves for shell QI3.5 with a $[90, \pm 45, 0]_S$ layup and a combination of local and global mid-surface imperfections at varying amplitudes.

Normalized and relative nondimensional maximum buckling loads are summarized in the tables below in the same way as in Subsection 6.2.5. It is especially interesting to compare the relative maximum buckling loads because they relate to the sensitivity of a given laminate and shell configuration to mid-surface imperfections. The results in Subsection 7.3.1 indicate that the stacking sequences $[0, \pm 45, 90]_S$ and $[\pm 45, 0, 90]_S$ are approximately equally sensitive to an increase of μ . Similarly, the relative normalized maximum buckling

loads in Tables 7.2 and 7.3 are comparable for shells QI1.3 and QI3.3. In contrast, the values in Table 7.4 for these shells are less effected by an increase of the imperfection amplitude. This makes sense because the LBA predicts mode shapes that are dominated by the stress field in the cylindrical shell because it cannot account for geometric nonlinearities. One may argue that superimposing the LBA displacement patterns on the pristine shell geometry creates regions that are even more susceptible to bending stresses. Naturally, the layup with the smallest axial bending stiffness experiences the least amount of additional detrimental stresses and therefore it is able to resist higher imperfection amplitudes more efficiently.

Imperfection Amplitude [-]	QI1.3 ($\mu = 0.285$)		QI3.3 ($\mu = 0.76$)		QI3.5, local ($\mu = 1.52$)		QI3.5, global ($\mu = 1.52$)	
	Norm. [-]	Rel. [-]	Norm. [-]	Rel. [-]	Norm. [-]	Rel. [-]	Norm. [-]	Rel. [-]
0%	1.02	100%	0.811	100%	0.619	100%	0.619	100%
5%	0.906	88.8%	0.751	92.6%	0.620	100.1%	0.577	93.1%
10%	0.833	81.6%	0.612	75.4%	0.620	100.1%	0.554	89.5%
20%	0.730	71.3%	0.454	56.0%	0.621	100.2%	0.473	76.3%
50%	0.579	56.7%	0.381	46.9%	0.620	100.2%	0.352	56.8%

Table 7.2: Normalized and relative maximum buckling loads for a $[0, \pm 45, 90]_S$ laminate considering mid-surface imperfections.

Imperfection Amplitude [-]	QI1.3 ($\mu = 0.289$)		QI3.3 ($\mu = 0.77$)		QI3.5, local ($\mu = 1.54$)		QI3.5, global ($\mu = 1.54$)	
	Norm. [-]	Rel. [-]	Norm. [-]	Rel. [-]	Norm. [-]	Rel. [-]	Norm. [-]	Rel. [-]
0%	0.883	100%	0.653	100%	0.581	100%	0.581	100%
5%	0.740	83.8%	0.635	97.3%	0.581	99.9%	0.605	104.1%
10%	0.638	72.3%	0.543	83.1%	0.581	99.9%	0.574	98.8%
20%	0.529	59.8%	0.484	74.2%	0.580	99.8%	0.568	97.7%
50%	0.406	45.9%	0.361	55.4%	0.578	99.5%	0.456	78.5%

Table 7.3: Normalized and relative maximum buckling loads for a $[\pm 45, 0, 90]_S$ laminate considering mid-surface imperfections.

Imperfection Amplitude [-]	QI1.3 ($\mu = 0.285$)		QI3.3 ($\mu = 0.76$)		QI3.5, local ($\mu = 1.52$)		QI3.5, global ($\mu = 1.52$)	
	Norm. [-]	Rel. [-]	Norm. [-]	Rel. [-]	Norm. [-]	Rel. [-]	Norm. [-]	Rel. [-]
0%	0.911	100%	0.867	100%	0.780	100%	0.780	100%
5%	0.847	93.0%	0.796	91.8%	0.779	99.9%	0.560	71.8%
10%	0.840	92.2%	0.794	91.5%	0.778	99.8%	0.461	59.1%
20%	0.826	90.7%	0.791	91.1%	0.777	99.6%	0.343	43.9%
50%	0.791	86.8%	0.761	87.7%	0.775	99.3%	0.215	27.5%

Table 7.4: Normalized and relative maximum buckling loads for a $[90, \pm 45, 0]_S$ laminate considering mid-surface imperfections.

Columns six and seven in each table confirm that the influence of mid-surface imperfections in the shape of stable local buckling configurations on the shell response is negligible for all considered layups.

7.3.5. Shell Failure

A simple criterion to determine the strength of a composite laminates is the maximum stress failure theory. It neglects interaction effects between the stress tensor components which means that failure may occur in multiaxial stress states even though it is not yet predicted by the simplified analysis. Camanho et al. [74] provide mean failure stresses of Hexcel IM7-8552 plies which are interpreted as the maximum stress allowables without calculating A- and B-basis values due to the relatively small number of tested specimens. In addition to information regarding the shell failure modes, the evaluation of the stress fields can also provide some insight into the mechanisms that govern the shell buckling response.

X_T , X_C , Y_T , and Y_C represent the maximum allowable ply stresses in the direction of the fibers (X) as well as perpendicular to them (Y). S denotes the maximum allowable shear stress. The properties depend on whether the structure experiences tensile (T) or compressive (C) stresses. Hence, the reserve factors in equation (7.4) are calculated with the corresponding absolute stress components in the local coordinate system of the laminas.

$$\frac{\tau_{11}}{X_T}, \frac{\tau_{11}}{X_C}, \frac{\tau_{22}}{Y_T}, \frac{\tau_{22}}{Y_C}, \frac{|\tau_{12}|}{S} \quad (7.4)$$

The average measured ply strengths reported by Camanho et al. [74] are rounded and listed in Table 7.5.

X_T	X_C	Y_T	Y_C	S
2325 MPa	1200 MPa	62 MPa	200 MPa	92 MPa

Table 7.5: Average stress allowables of Hexcel IM7-8552 [74].

Three stacking sequences, four shell configurations with eight plies each, five strength allowables and four characteristic points on the load-displacement curve requires checking a total of 1920 reserve factors. They are not quantified at this point for the sake of clarity. A qualitative summary is that shell QI1.3 fails due to excessive compression of the fibers regardless of the layup before the buckling load is reached. Transverse matrix properties as well as the maximum allowable shear stress are also exceeded, but not to the extent of the fiber compression. Thinner shells lose their load-carrying capability due to the onset of global buckling and not because of strength concerns.

The stress distribution in fiber direction of the innermost ply of each laminate is plotted on the shell surface in Figures 7.22, 7.23, and 7.24. This lamina is chosen because it allows comparing the stress field for various ply orientations. Furthermore, the true stress is at its maximum there according to Lekkerkerker's prediction in Figure 2.1a where a positive bending stress causes compression on the inside of the cylindrical shell due to tension which means that a negative bending stress results in compression on the inside as well when the structure is compressed axially. Previous observations suggest that the bending response of each laminate is characteristic for the shell's resistance against buckling, so taking a look at the plies furthest away from the middle of the composite also makes sense. Since both compressive and tensile stresses are illustrated, the color blue indicates large compressive stresses, whereas red denotes tension.

While the prebuckling displacements for the three layups are quite similar, the stress fields in Figures 7.22, 7.23, and 7.24 show characteristic differences. Of course, one reason for this is that they are orientated differently. Anyhow, it is notable that the $[0, \pm 45, 90]_S$ composite features high destabilizing compressive stresses on the left and the right side of the cutout. The position of the stress concentrations rotates counter-clockwise for the $[\pm 45, 0, 90]_S$ layup and the stacking sequence $[90, \pm 45, 0]_S$ generates a tensile stress field where the first laminate sees compression. The effect becomes more pronounced with an increase of the curvature parameter μ . Due to the high axial membrane and bending stiffness, additional displacement loading is more detrimental for the $[0, \pm 45, 90]_S$ composite than for the other two. Apparently, it is beneficial to minimize stress concentrations to optimize the normalized buckling load of shells that are susceptible to local buckling which is achieved by selecting a layup that features minimal axial stiffness.

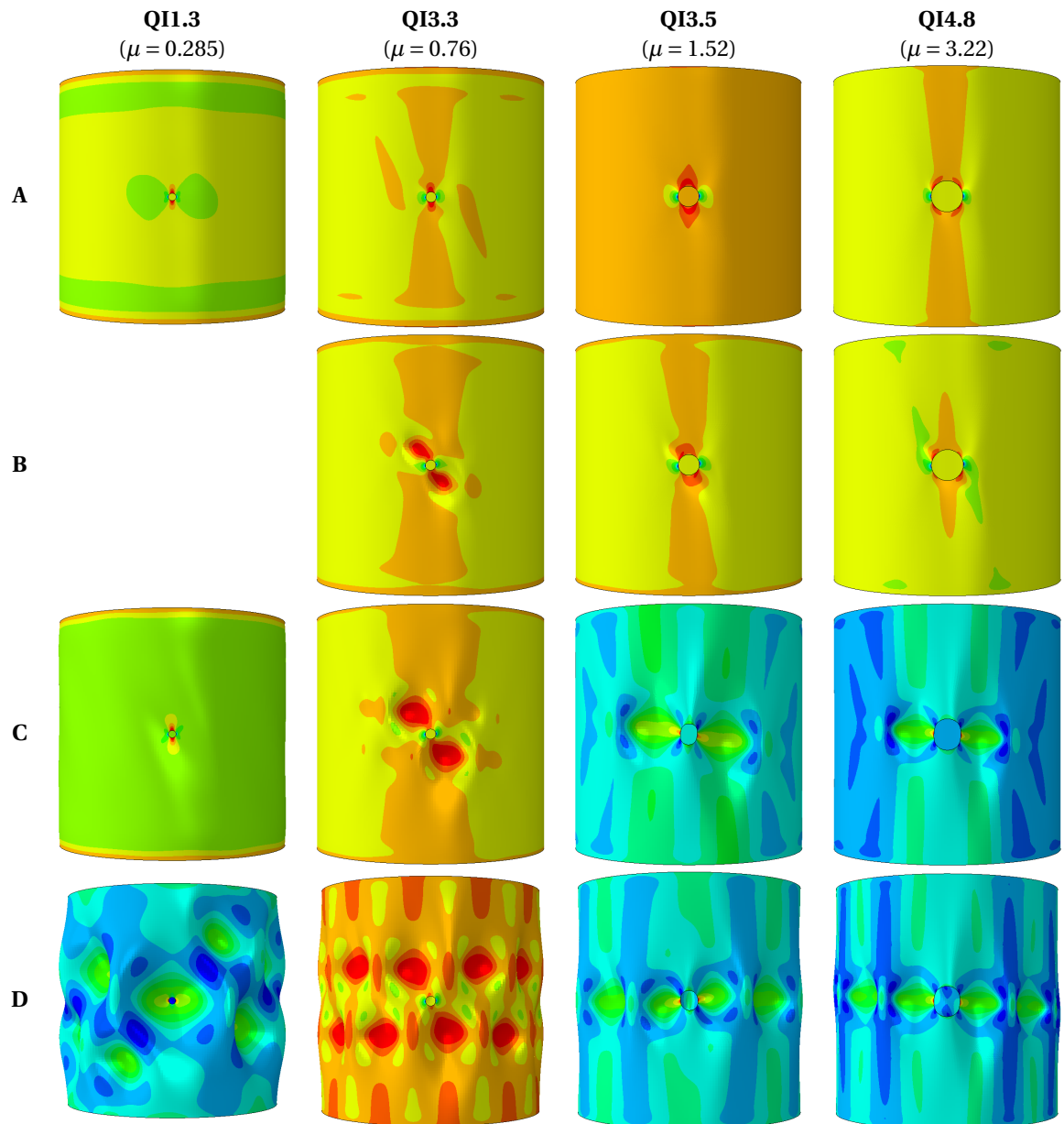


Figure 7.22: Stresses along the fiber direction of the innermost ply in a $[0, \pm 45, 90]_S$ laminate during loading (A), at local buckling (B), before (C), and after (D) global buckling.

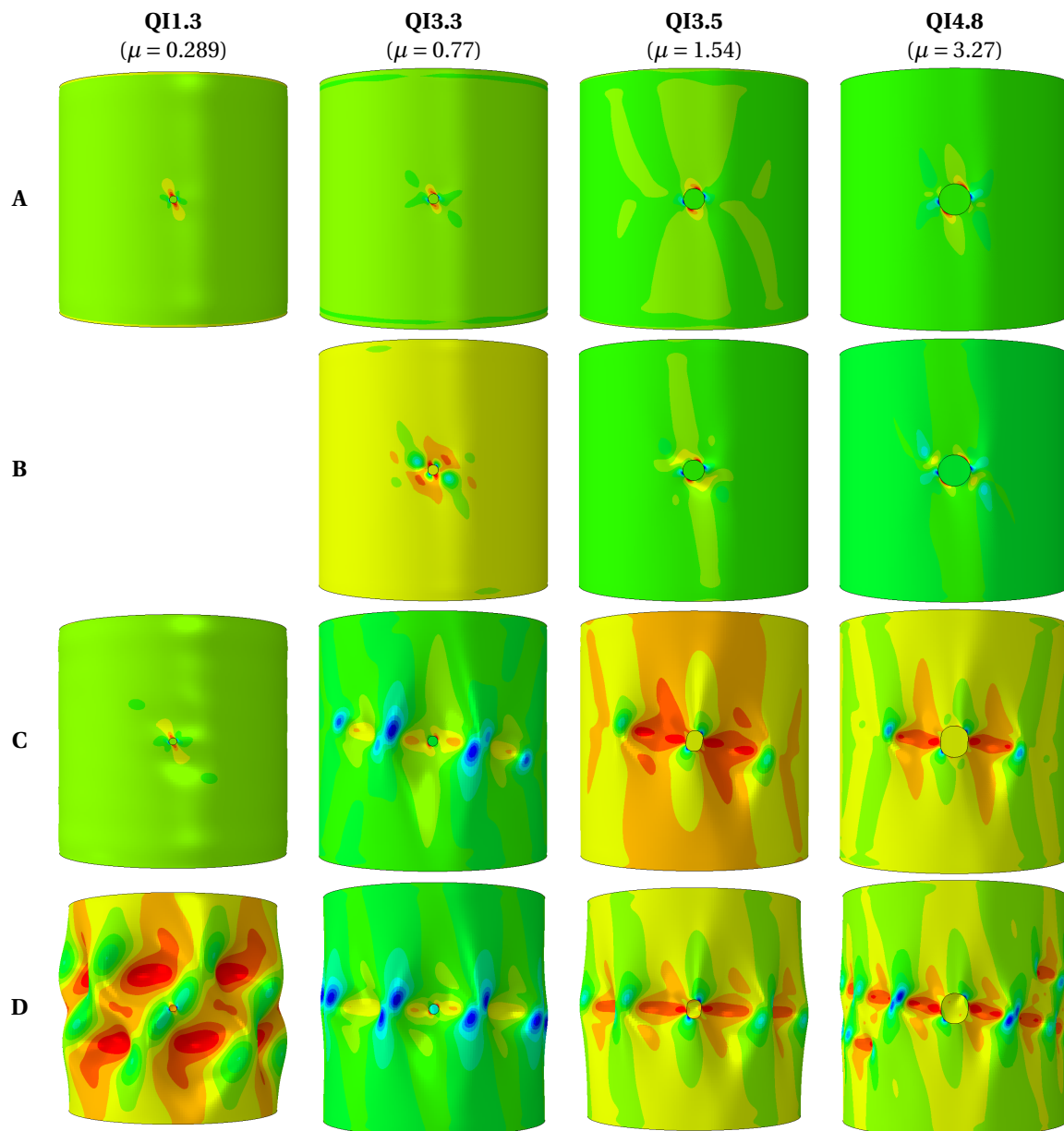


Figure 7.23: Stresses in fiber direction in the innermost ply of a $[\pm 45, 0, 90]_S$ laminate during loading (A), at local buckling (B), before (C), and after (D) global buckling.

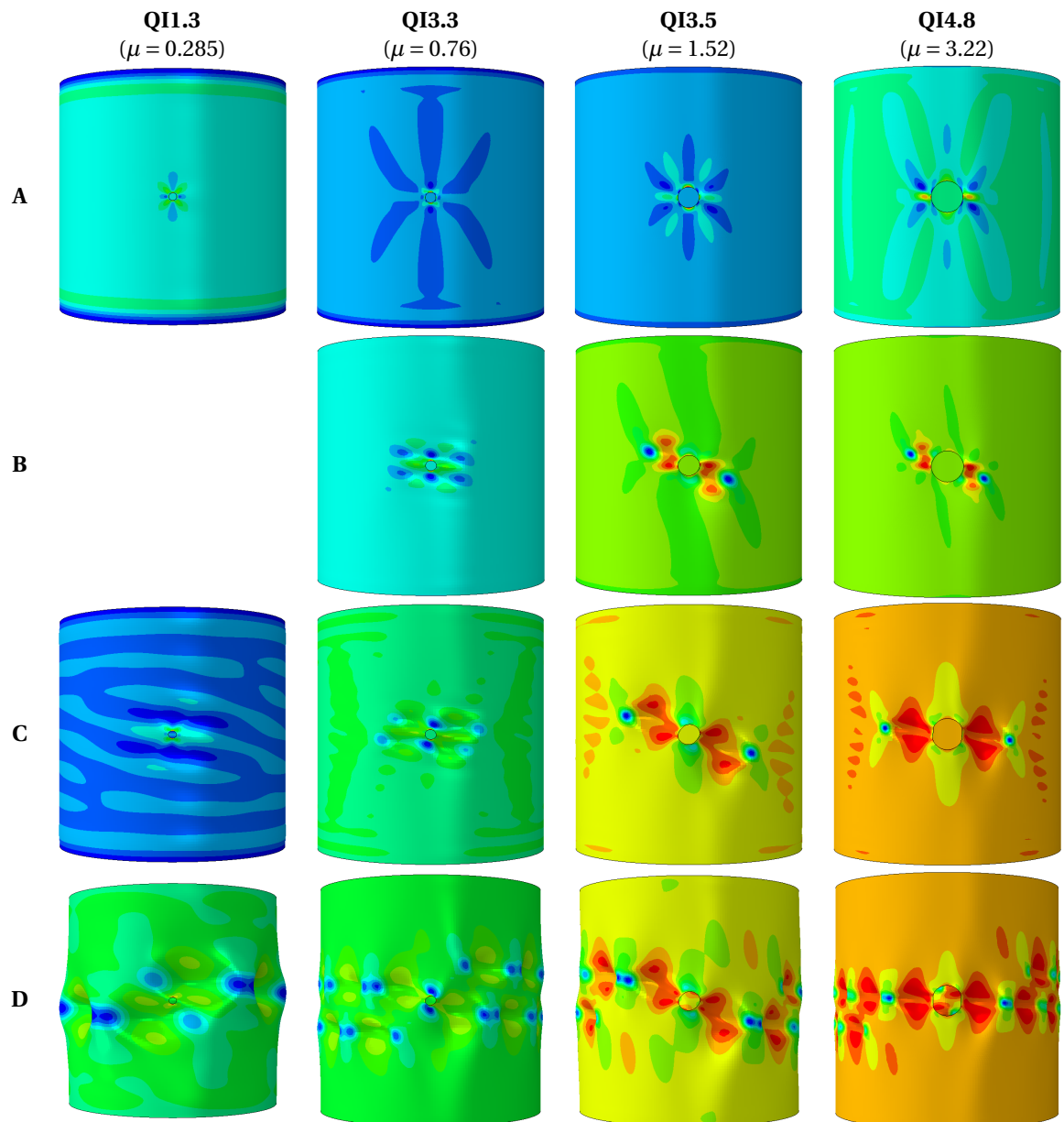


Figure 7.24: Stresses in fiber direction in the innermost ply of a $[90, \pm 45, 0]_S$ laminate during loading (A), at local buckling (B), before (C), and after (D) global buckling.

8

Conclusion and Recommendations for Future Work

The buckling behavior of isotropic and quasi-isotropic composite cylindrical shells with circular cutouts has been investigated. After reviewing existing literature, the principle of minimum total energy is combined with the theory of shallow shells as well as classical lamination theory to develop an analytical procedure for predicting the linear buckling load of cylindrical shells subjected to a uniform axial edge load. Finite element models are created and solved with linear eigenvalue, nonlinear static, as well as nonlinear dynamic simulations to verify the analytical approach. Mylar and composite laminates made from Hexcel IM7-8552 are idealized as isotropic and composite materials, respectively. Three laminate stacking sequences are assessed analytically and numerically, namely $[0, \pm 45, 90]_S$, $[\pm 45, 0, 90]_S$, and $[90, \pm 45, 0]_S$. In addition to the primary verification purpose, the numerical simulations are evaluated with respect to the evolution of the buckling mode shapes, the influence of initial geometric imperfections, and shell failure.

The results of the investigation are summarized in Section 8.1, whereas recommendations for future work are provided in the second part of the chapter, Section 8.2.

8.1. Conclusion

Special attention is given to the buckling behavior of isotropic and quasi-isotropic composite cylindrical shells with circular cutouts in Subsection 8.1.1 and to the benefits and limitations of the analytical solution in Subsection 8.1.2 of this section.

8.1.1. Buckling Behavior of Cylindrical Shells with Circular Cutouts

The buckling behavior of isotropic and quasi-isotropic composite shells with circular cutouts may be characterized with a nondimensional curvature parameter as long as it is proportional to $\alpha = a/\sqrt{Rt}$ where a is the cutout radius, R is the shell radius, and t is the shell thickness. More elaborate curvature parameters also account for material properties. For example, μ , which is a function of the Poisson's ratio ν and α , is available for isotropic shells, and both C as well as the equivalent μ for composite materials depend on extensional and flexural laminate stiffness terms. When the analytical or numerical buckling load is normalized with the buckling load of a pristine reference shell, this quantity can be plotted against any curvature parameter for a given material (and stacking sequence) to obtain maximum buckling load curves that are closely spaced regardless of the ratio R/t . These plots may be studied to predict the buckling load of a shell with different geometric properties, but with an identical nondimensional curvature parameter.

Shells buckle globally if the cutout is comparatively small. The buckling load is virtually constant in this domain and independent of the cutout size, i.e. the shell approximately behaves as if it was pristine. When the radius of the opening is increased beyond a critical point, the buckling load begins to decrease drastically. Now, the shell exhibits an unstable local buckling event restricted to the cutout area that induces a stress redistribution which constitutes a sufficient disturbance in the structure such that it leads to global buckling. The corresponding critical curvature parameter as well as the sensitivity to the cutout size depend on the layup stacking sequence when composite cylindrical shells are considered. Shells experience both of the aforementioned buckling modes without encountering large lateral prebuckling displacements.

Significant out-of-plane deflections can be observed before buckling occurs for large openings. This effect is more pronounced for Mylar shells than for the stiffer composite cylindrical shells. In any case, the large displacements lead to a stress redistribution away from the cutout which results in a stable local buckling mode as well as a reduced axial stiffness. Interestingly enough, the load that can be sustained before the local buckling event triggers increases after a critical cutout size is exceeded. Isotropic cylindrical shells only feature one stable local buckling mode, but composite shells may exhibit multiple of these events. After being subjected to further force or displacement loading, the shell buckles globally. This global buckling load slightly decreases with an increasing cutout size, but it can be approximated as being constant. All buckling modes are caused by destabilizing compressive stress fields in the area around the cutout in combination with, if applicable, large lateral prebuckling deformations.

Shells with cutouts always exhibit bending stresses when subjected to a uniform axial load due to the discrepancy between the centroid of the structure and the applied load. Consequently, changing the stacking sequence of a laminate influences the buckling resistance of the shell significantly. Layups that reduce the overall stress concentrations in the vicinity of the opening are less sensitive to an increase of the cutout size than those that attempt to restrict large bending displacements by increasing the corresponding stiffness parameters. Out of the three considered layups, the stacking sequence $[\pm 45, 0, 90]_S$ yields the highest buckling loads regardless of the cutout size.

The shape of the buckling modes depends on the material as well as the layup of the laminate. Additionally, each type of buckling, i.e. global, unstable local followed by global, and stable local followed by global, features its own characteristic displacement pattern.

The influence of mid-surface imperfections that resemble global buckling modes generally diminishes the larger an opening becomes. Furthermore, the less a given layup promotes axial bending stresses, the less it is affected by these mid-surface imperfections. Nonetheless, imperfections are still highly relevant for the buckling resistance of shells with circular cutouts as they can reduce the sustainable buckling load considerably. Particularly detrimental imperfections are those that cause a nonuniform loading of the shell.

Curvature parameters cannot be applied in every case, for example when the shell contains very large openings, i.e. $\alpha > 7$. Here, the nondimensional buckling load becomes a function of R/t . Similarly, stable local buckling modes emerge for varying α depending on the shell-radius-to-thickness ratio. Finally, even though μ and C imply the ability to evaluate different material properties, this is not the case. Hence, α should be used as the preferred curvature parameter for design purposes.

8.1.2. Analytical Solution

The analytical solution provides a reasonable prediction for the buckling load of isotropic and quasi-isotropic composite cylindrical shells with circular cutouts when local buckling is considered. For large cutouts and global buckling, geometric nonlinearities play an important role such that the linear buckling loads are not necessarily conservative. However, the analytical solution follows the general trends of experimental and numerical buckling loads for both cases.

Major assumptions during the derivation are the local nature of the buckling event and the approximation of the prebuckling stress distribution in the shell with the stress field around a circular cutout in an infinite flat plate. In addition, a linear material response is prescribed by performing a linear eigenvalue analysis. Hence, the analytical buckling load should follow the trends of the numerical predictions only up to moderately large cutouts, but it also estimates the local buckling load for higher curvature parameters to a reasonable degree even though large out-of-plane prebuckling displacements are observed in this case.

A comparison of the numerical linear buckling analysis and its analytical equivalent indicates that the neglected bending stresses can have a significant impact on the buckling load estimates for composite materials and should therefore be included in the analysis. The dismissal of bending stress in the analytical solution is also the reason why normalized buckling loads fall onto a single design curve when plotting them against any curvature parameter as long as the reference buckling load is calculated assuming an axisymmetric displacement pattern.

A reason for the upper bound nature of the analytical buckling load estimates is the application of the Ritz method to minimize the energy of the structure. Furthermore, the approximation of the prebuckling stress distribution with the flat plate solution underestimates the stress field, and therefore the analytical buckling loads are overestimated. The chosen shape function is suitable for isotropic materials but does not contain sufficient degrees of freedom to model the buckling modes of quasi-isotropic composite laminates.

The main benefit of analytically estimating the shell buckling load is the significant reduction in computational time per buckling load prediction. It is approximately 350 times faster than a numerical linear

eigenvalue analysis, more than 7,900 times faster than a nonlinear static procedure, and over 15,900 times faster than a nonlinear dynamic simulation with meshes of approximately 200,000 degrees of freedom. At the same time, the analytical solution provides reasonably accurate buckling loads.

Overall, there is some discrepancy between absolute analytical and numerical predictions, but also between numerical and experimental measurements due to the effects of initial geometric imperfections which were neglected in most simulations. Nonetheless, the analytical solution is well suited to serve as a tool during preliminary design to estimate the consequences of changing material or geometric properties because it can predict general trends as long as the bending stress contribution in the axial direction of the cylindrical shell is not significant.

8.2. Recommendations for Future Work

Naturally, the information presented in this document cannot explain every aspect concerning the buckling behavior of isotropic and composite cylindrical shells with cutouts. However, it provides a number of answers, some of which raise interesting new questions. Consequently, recommendations for future research are discussed hereafter.

There are a few opportunities to extend the analytical solution from Chapter 4. As mentioned in the previous subsection, it is desirable to model the actual prebuckling stress field of the shell that includes bending stresses. Unfortunately, a closed-form solution does not appear to be publicly available for any type of constitutive relation. Unless advancements in this field are made, employing semi-analytical approaches is probably most likely to result in other practical solutions. Of course, obtaining more accurate predictions with semi-analytical procedures comes at the cost of increased computational time per buckling load estimation which diminishes one of the major advantages of an analytical method. While enhancing the analytical solution certainly has its merits, one should take into account that sophisticated semi-analytical methods for the prediction of linear buckling loads of cylindrical shells with cutouts already exist, for example the one developed by Madenci et al. [15].

Anyhow, Lekkerkerker's solution [5] could be automated numerically to determine the prebuckling stress distribution for a given geometry. This allows a more precise quantification of the potential energy due to external forces which in turn leads to more realistic buckling load predictions.

Modeling the stress distribution in a quasi-isotropic laminate becomes even more inefficient. Following the idea of van Tooren et al. [13], it should be possible to compute the membrane and bending stress fields for a given stacking sequence separately by computing the equivalent properties of an orthotropic material. Evaluating the approach proposed by Ashmarin [11] twice yields a suitable stress field for energy minimization purposes.

Extending the analytical solution to composites that are symmetric and balanced, but not quasi-isotropic, requires solving a significantly more complex version of the compatibility equation in polar coordinates. A solution for transversely isotropic materials has been developed by Cairns [78] in his Ph.D. dissertation and could perhaps be extended to the more general orthotropic case which is sufficient to model the membrane response of a laminated shell.

Instead of expanding the applicability range of the analytical solution, one may also incorporate new algorithms to improve the computational efficiency of the current solution. For example, a gradient-based algorithm could be introduced to determine minimum eigenvalues more quickly. Moreover, algorithms that reduce the condition number for inversion exist [79] and they should be made available for the generalized eigenvalue problem in order to make use of the full potential of the assumed displacement function.

A second area of interest is the continuing investigation of the buckling behavior of cylindrical shells with cutouts. An explanation for the, somewhat counterintuitive, increased stable local buckling load of thicker shells has been proposed, but it should be verified or validated by a third party.

Furthermore, it would be interesting to incorporate imperfection data from an imperfection data bank to more realistically predict the effects of initial geometric imperfections. This approach could also account for the influence of nonuniform loading. Corresponding research has already been conducted, for example by Starnes et al. [34], but a parametric study for as big of a sample size as in the present study has not been performed yet.

In accordance with the extension of the analytical solution to balanced and symmetric composites, it makes sense to investigate buckling loads, buckling mode shape evolutions, as well as the imperfection sensitivity of such laminates with linear and nonlinear FE simulations to verify the analytical results and to gain further insights regarding to governing buckling mechanisms of these structures.

A

Expressions Used During the Analysis of an Isotropic Shell With a Circular Cutout

Equations and expressions that are helpful for understanding the analysis presented in Chapter 4 are summarized in this appendix.

A.1. General Stress Resultants

Stress resultants for the discussion of the boundary conditions (4.25a) through (4.26c) in Subsection 4.3.6. The terms after the summations depend on the assumed displacement function.

$$\begin{aligned} N_r = & a_0 r^{-2} + 2b_0 + c_0 (1 + 2\ln r) + 2d_0 \theta \\ & + a_1'' r^{-1} \cos \theta + (2b_1 r - 2a_1' r^{-3} + b_1' r^{-1}) \cos \theta - c_1'' r^{-1} \sin \theta + (2d_1 r - 2c_1' r^{-3} + d_1' r^{-1}) \sin \theta \\ & - \sum_{n=2}^{\infty} \left\{ \left[(n^2 - n) a_n r^{n-2} + (n^2 - n - 2) b_n r^n + (n^2 + n) a_n' r^{-n-2} + (n^2 + n - 2) b_n' r^{-n} \right] \cos n\theta \right\} \\ & - \sum_{n=2}^{\infty} \left\{ \left[(n^2 - n) c_n r^{n-2} + (n^2 - n - 2) d_n r^n + (n^2 + n) c_n' r^{-n-2} + (n^2 + n - 2) d_n' r^{-n} \right] \sin n\theta \right\} \\ & + \frac{\partial \Phi_p}{\partial r} r^{-1} + \frac{\partial^2 \Phi_p}{\partial \theta^2} r^{-2} \end{aligned} \quad (\text{A.1a})$$

$$\begin{aligned} N_\theta = & -a_0 r^{-2} + 2b_0 + c_0 (2 + \ln r) + 2d_0 \theta \\ & + (6b_1 r + 2a_1' r^{-3} + b_1' r^{-1}) \cos \theta + (6d_1 r + 2c_1' r^{-3} + d_1' r^{-1}) \sin \theta \\ & + \sum_{n=2}^{\infty} \left\{ \left[(n^2 - n) a_n r^{n-2} + (n^2 + 3n + 2) b_n r^n + (n^2 + n) a_n' r^{-n-2} + (n^2 - 3n + 2) b_n' r^{-n} \right] \cos n\theta \right\} \\ & + \sum_{n=2}^{\infty} \left\{ \left[(n^2 - n) c_n r^{n-2} + (n^2 + 3n + 2) d_n r^n + (n^2 + n) c_n' r^{-n-2} + (n^2 - 3n + 2) d_n' r^{-n} \right] \sin n\theta \right\} \\ & + \frac{\partial^2 \Phi_p}{\partial r^2} \end{aligned} \quad (\text{A.1b})$$

$$\begin{aligned} N_{r\theta} = & -d_0 + a_0' r^{-2} + (2b_1 r - 2a_1' r^{-3} + b_1' r^{-1}) \sin \theta + (2d_1 r - 2c_1' r^{-3} + d_1' r^{-1}) \cos \theta \\ & + \sum_{n=2}^{\infty} \left\{ \left[(n^2 - n) a_n r^{n-2} + (n^2 + n) b_n r^n - (n^2 + n) a_n' r^{-n-2} - (n^2 - n) b_n' r^{-n} \right] \sin n\theta \right\} \\ & + \sum_{n=2}^{\infty} \left\{ \left[(n^2 - n) c_n r^{n-2} + (n^2 + n) d_n r^n - (n^2 + n) c_n' r^{-n-2} - (n^2 - n) d_n' r^{-n} \right] \cos n\theta \right\} \\ & - \frac{\partial}{\partial r} \left(\frac{\partial \Phi_p}{\partial \theta} r^{-1} \right) \end{aligned} \quad (\text{A.1c})$$

A.2. Boundary Value Problem Constants

Nonzero constants of the solution for the Airy stress function (4.27) determined from the boundary conditions in Subsection 4.3.6 and assuming the shape function (4.1).

$$a_0 = \frac{Et}{4RB^3} \left[2A_0 e^{-Ba} (B^2 a + B) - A_2 B^3 a^2 \text{Ei}_1(Ba) + 2C_0 e^{-Ba} (B^2 a^2 + 2Ba + 2) - C_2 B^2 a^2 e^{-Ba} \right] \quad (\text{A.2a})$$

$$\begin{aligned} a'_2 = & -\frac{Et}{8RB^5} \left[A_0 e^{-Ba} (2B^4 a^3 + 6B^3 a^2 + 12B^2 a + 12B) - A_2 e^{-Ba} (B^4 a^3 + 3B^3 a^2 + 6B^2 a + 6B) \right. \\ & - A_2 B^5 a^4 \text{Ei}_1(Ba) + C_0 e^{-Ba} (2B^4 a^4 + 8B^3 a^3 + 24B^2 a^2 + 48Ba + 48) \\ & \left. - C_2 e^{-Ba} (2B^4 a^4 + 4B^3 a^3 + 12B^2 a^2 + 24Ba + 24) \right] \end{aligned} \quad (\text{A.2b})$$

$$b'_2 = \frac{Et}{4RB^3} \left[A_0 e^{-Ba} (B^2 a + B) - A_2 B^3 a^2 \text{Ei}_1(Ba) + C_0 e^{-Ba} (B^2 a^2 + 2Ba + 2) - C_2 B^2 a^2 e^{-Ba} \right] \quad (\text{A.2c})$$

$$\begin{aligned} a'_4 = & -\frac{Et}{8B^7 R} e^{-Ba} \left[A_2 (B^6 a^5 + 5B^5 a^4 + 20B^4 a^3 + 60B^3 a^2 + 120B^2 a + 120) \right. \\ & \left. + C_2 (B^6 a^6 + 6B^5 a^5 + 30B^4 a^4 + 120B^3 a^3 + 360B^2 a^2 + 720Ba + 720) \right] \end{aligned} \quad (\text{A.2d})$$

$$b'_4 = \frac{Et}{8RB^5} e^{-Ba} \left[A_2 (B^4 a^3 + 3B^3 a^2 + 6B^2 a + 6) + C_2 (B^4 a^4 + 4B^3 a^3 + 12B^2 a^2 + 24Ba + 24) \right] \quad (\text{A.2e})$$

A.3. Stress Resultant Coefficients

Stress resultants computed by operating (3.61) on the Airy stress function (4.27) in Subsection 4.3.6. The terms are obtained assuming the displacement function (4.1).

$$k_{11} = -\frac{Et}{4RB^3 r^2} \left[2A_0 e^{-Br} (B^2 r + B) - A_2 B^3 r^2 \text{Ei}_1(Br) + 2C_0 e^{-Br} (B^2 r^2 + 2Br + 2) - C_2 B^2 r^2 e^{-Br} \right] + \frac{a_0}{r^2} \quad (\text{A.3a})$$

$$\begin{aligned} k_{12} = & -\frac{Et}{4B^5 r^4} \left[2A_0 e^{-Br} (B^4 r^3 + 7B^3 r^2 + 18B^2 r + 18B) - A_2 e^{-Br} (3B^4 r^3 + 9B^3 r^2 + 18B^2 r + 18B) \right. \\ & + A_2 B^5 r^4 \text{Ei}_1(Br) + 2C_0 e^{-Br} (B^4 r^4 + 8B^3 r^3 + 32B^2 r^2 + 72Br + 72) \\ & \left. - 2C_2 (B^4 r^4 + 6B^3 r^3 + 18B^2 r^2 + 36Br + 36) \right] - 6 \frac{a'_2}{r^4} - 4 \frac{b'_2}{r^2} \end{aligned} \quad (\text{A.3b})$$

$$\begin{aligned} k_{13} = & -\frac{Et}{4RB^7 r^6} e^{-Br} \left[A_2 (B^6 r^5 23 + B^5 r^4 + 146B^4 r^3 + 546B^3 r^2 + 1200B^2 r + 1200B) \right. \\ & \left. + C_2 (B^6 r^6 + 24B^5 r^5 + 192B^4 r^4 + 984B^3 r^3 + 3384B^2 r^2 + 7200Br + 7200) \right] - 20 \frac{a'_4}{r^6} - 18 \frac{b'_4}{r^4} \end{aligned} \quad (\text{A.3c})$$

$$\begin{aligned} k_{21} = & \frac{Et}{4RB^3 r^2} \left[2A_0 e^{-Br} (B^3 r^2 + B^2 r + B) - A_2 B^3 r^2 e^{-Br} + A_2 B^3 r^2 \text{Ei}_1(Br) \right. \\ & \left. + 2C_0 e^{-Br} (B^3 r^3 + B^2 r^2 + 2Br + 2) - C_2 e^{-Br} (B^3 r^3 - B^2 r^2) \right] - \frac{a_0}{r^2} \end{aligned} \quad (\text{A.3d})$$

$$\begin{aligned} k_{22} = & \frac{Et}{4RB^5 r^4} \left[2A_0 e^{-Br} (B^5 r^4 + 3B^4 r^3 + 9B^3 r^2 + 18B^2 r + 18B) \right. \\ & - A_2 e^{-Br} (2B^5 r^4 + 3B^4 r^3 + 9B^3 r^2 + 18B^2 r + 18B) + A_2 B^5 r^4 \text{Ei}_1(Br) \\ & + 2C_0 e^{-Br} (B^5 r^5 + 3B^4 r^4 + 12B^3 r^3 + 36B^2 r^2 + 72Br + 72) \\ & \left. - 2C_2 e^{-Br} (B^5 r^5 + B^4 r^4 + 6B^3 r^3 + 18B^2 r^2 + 36Br + 36) \right] + 6 \frac{a'_2}{r^4} \end{aligned} \quad (\text{A.3e})$$

$$\begin{aligned} k_{23} = & \frac{Et}{4RB^7 r^6} e^{-Br} \left[A_2 (B^7 r^6 + 7B^6 r^5 + 41B^5 r^4 + 182B^4 r^3 + 582B^3 r^2 + 1200B^2 r + 1200B) \right. \\ & \left. + C_2 (B^7 r^7 + 7B^6 r^6 + 48B^5 r^5 + 264B^4 r^4 + 1128B^3 r^3 + 3528B^2 r^2 + 7200Br + 7200) \right] \\ & + 20 \frac{a'_4}{r^6} + 6 \frac{b'_4}{r^4} \end{aligned} \quad (\text{A.3f})$$

$$k_{31} = 0 \quad (\text{A.3g})$$

$$k_{32} = -\frac{Et}{4RB^5r^4} \left[4A_0e^{-Br} \left(B^4r^3 + 4B^3r^2 + 9B^2r + 9B \right) - A_2e^{-Br} \left(3B^4r^3 + 9B^3r^2 + 18B^2r + 18B \right) \right. \\ \left. - A_2B^5r^4\text{Ei}_1(Br) + 4C_0e^{-Br} \left(B^4r^4 + 5B^3r^3 + 17B^2r^2 + 36Br + 36 \right) \right. \\ \left. - 4C_2e^{-Br} \left(B^4r^4 + 3B^3r^3 + 9B^2r^2 + 18Br + 18 \right) \right] - 6\frac{a'_2}{r^4} - 2\frac{b'_2}{r^2} \quad (\text{A.3h})$$

$$k_{33} = -\frac{Et}{RB^7r^6}e^{-Br} \left[A_2 \left(B^6r^5 + 8B^5r^4 + 41B^4r^3 + 141B^3r^2 + 300B^2r + 300B \right) \right. \\ \left. + C_2 \left(B^6r^6 + 9B^5r^5 + 57B^4r^4 + 264B^3r^3 + 864B^2r^2 + 1800Br + 1800 \right) \right] - 20\frac{a'_4}{r^6} - 12\frac{b'_4}{r^4} \quad (\text{A.3i})$$

A.4. Generalized Eigenvalue Problem Matrices

The setup of the generalized eigenvalue problem as defined in equation (4.31) in Subsection 4.3.7. The matrices \mathbf{K}^M and \mathbf{K}^G are given by

$$\mathbf{K}^M = \begin{bmatrix} K_{11}^M & K_{12}^M & K_{13}^M & K_{14}^M \\ K_{12}^M & K_{22}^M & K_{23}^M & K_{24}^M \\ K_{13}^M & K_{23}^M & K_{33}^M & K_{34}^M \\ K_{14}^M & K_{24}^M & K_{34}^M & K_{44}^M \end{bmatrix} \quad (\text{A.4})$$

as well as

$$\mathbf{K}^G = \begin{bmatrix} K_{11}^G & K_{12}^G & K_{13}^G & K_{14}^G \\ K_{12}^G & K_{22}^G & K_{23}^G & K_{24}^G \\ K_{13}^G & K_{23}^G & K_{33}^G & K_{34}^G \\ K_{14}^G & K_{24}^G & K_{34}^G & K_{44}^G \end{bmatrix} \quad (\text{A.5})$$

with the entries

$$K_{11}^M = \frac{3}{16} \frac{E}{R^2B^2} e^{-2Ba} (2Ba + 1) + \frac{Et^2B^2}{24(1-v^2)} \left[e^{-2Ba} (2Ba + 1 - 4v) + 4\text{Ei}_1(2Ba) \right] \quad (\text{A.6a})$$

$$K_{12}^M = -\frac{E}{8R^2B^2} \left[e^{-2Ba} (2Ba + 5) - 8e^{-Ba}\text{Ei}_1(Ba) (Ba + 1) + 8\text{Ei}_1(2Ba) \right] \quad (\text{A.6b})$$

$$K_{13}^M = \frac{3}{16} \frac{E}{R^2B^3} e^{-2Ba} (2B^2a^2 + 2Ba + 1) \\ + \frac{Et^2B}{24(1-v^2)} \left\{ e^{-2Ba} \left[2B^2a^2 - 2Ba(1+2v) + 1 + 4v \right] - 4\text{Ei}_1(2Ba) \right\} \quad (\text{A.6c})$$

$$K_{14}^M = -\frac{E}{8R^2B^3} e^{-2Ba} (2B^2a^2 - 2Ba - 1) \quad (\text{A.6d})$$

$$K_{22}^M = \frac{E}{64R^2B^2} \left[e^{-2Ba} (14Ba + 7) - 48B^2a^2\text{Ei}_1^2(Ba) \right] \\ + \frac{Et^2}{48(1-v^2)a^2} \left\{ e^{-2Ba} \left[2B^3a^3 + B^2a^2(1-4v) - 32Bav + 48 - 16v \right] + 36B^2a^2\text{Ei}_1(2Ba) \right\} \quad (\text{A.6e})$$

$$K_{23}^M = -\frac{E}{8R^2B^3} \left[e^{-2Ba} (2B^2a^2 + 6Ba + 11) - e^{-Ba}\text{Ei}_1(Ba) (B^2a^2 + 2Ba + 2) + 2\text{Ei}_1(2Ba) \right] \quad (\text{A.6f})$$

$$K_{24}^M = \frac{E}{64R^2B^3} \left[e^{-Ba} (14B^2a^2 + 14Ba + 7) - 48B^2a^2\text{Ei}_1(Ba) \right] \\ + \frac{Et^2}{48(1-v^2)a} \left\{ e^{-2Ba} \left[2B^3a^3 - 2B^2a^2(1+2v) + Ba(17-14v) \right] - 36\text{Ei}_1(2Ba) \right\} \quad (\text{A.6g})$$

$$K_{33}^M = \frac{3}{32} \frac{E}{R^2 B^4} e^{-2Ba} (4B^3 a^3 + 6B^2 a^2 + 6Ba + 3) + \frac{Et^2}{48(1-\nu^2)} \left\{ e^{-2Ba} [4B^3 a^3 - 2B^2 a^2 (5+4\nu) + 2Ba(5+8\nu) - 3 - 8\nu] + 8 \text{Ei}_1(2Ba) \right\} \quad (\text{A.6h})$$

$$K_{34}^M = -\frac{E}{16R^2 B^4} e^{2-Ba} (4B^3 a^3 - 2B^2 a^2 - 2Ba - 1) \quad (\text{A.6i})$$

$$K_{44}^M = \frac{E}{128R^2 B^4} e^{-2Ba} (28B^3 a^3 - 54B^2 a^2 + 42Ba + 21) + \frac{Et^2}{96(1-\nu^2)} \left\{ e^{-2Ba} [4B^3 a^3 - 2B^2 a^2 (5+4\nu) + 6Ba(1-8\nu) + 45 + 24\nu] + 72 \text{Ei}_1(2Ba) \right\} \quad (\text{A.6j})$$

and

$$K_{11}^G = \frac{1}{4} e^{-2Ba} (2Ba + 1) - B^2 a^2 \text{Ei}_1(2Ba) \quad (\text{A.7a})$$

$$K_{12}^G = -\frac{1}{8} e^{-2Ba} (4B^3 a^3 - 2B^2 a^2 - 6Ba - 3) + B^2 a^2 \text{Ei}_1(2Ba) (B^2 a^2 - 2) \quad (\text{A.7b})$$

$$K_{13}^G = B a^2 \text{Ei}_1(2Ba) \quad (\text{A.7c})$$

$$K_{14}^G = \frac{1}{4B} e^{-2Ba} (2Ba + 1) \quad (\text{A.7d})$$

$$K_{22}^G = -\frac{1}{8} e^{-2Ba} (14Ba + 9) + \frac{1}{2} \text{Ei}_1(2Ba) (7B^2 a^2 + 4) \quad (\text{A.7e})$$

$$K_{23}^G = \frac{1}{4B} e^{-2Ba} (8B^3 a^3 - 4B^2 a^2 - 2Ba - 1) - 4B a^2 \text{Ei}_1(2Ba) (B^2 a^2 - 1) \quad (\text{A.7f})$$

$$K_{24}^G = \frac{1}{B} e^{-2Ba} (2Ba + 1) - \frac{7}{2} B a^2 \text{Ei}_1(2Ba) \quad (\text{A.7g})$$

$$K_{33}^G = \frac{1}{8B^2} e^{-2Ba} (4B^2 a^2 + 2Ba + 1) - a^2 \text{Ei}_1(2Ba) \quad (\text{A.7h})$$

$$K_{34}^G = -\frac{1}{16B^2} e^{-2Ba} (12B^3 a^3 - 14B^2 a^2 + 2Ba + 1) + \frac{3}{2} B^2 a^4 \text{Ei}_1(2Ba) \quad (\text{A.7i})$$

$$K_{44}^G = \frac{1}{16B^2} e^{-2Ba} (4B^2 a^2 + 18Ba + 9) + \frac{3}{2} a^2 \text{Ei}_1(2Ba) \quad (\text{A.7j})$$

B

Generalized Eigenvalue Problem Matrix Elements for the Quasi-Isotropic Case

The elements of the generalized eigenvalue problem matrices (4.31) for quasi-isotropic, symmetric laminates as derived in Section 4.4. They have the same form as indicated in Appendix A.4. Major differences are apparent in the bending contribution terms of \mathbf{K}^M . The membrane response only changes in so far as that the isotropic membrane stiffness terms are replaced with equivalent composite ones. Consequently, the thickness t cannot be eliminated in \mathbf{K}^G as a comparison between (A.7) and (B.2) shows. The new matrix entries are given by

$$K_{11}^M = \frac{3}{16} \frac{A_{11}^2 - A_{12}^2}{A_{11} R^2 B^2} e^{-2Ba} (2Ba + 1) + \frac{B^2}{16} \left\{ e^{-2Ba} [2Ba(3D_{11} + 2D_{12} + 3D_{22} + 4D_{66}) - D_{11} - 22D_{12} - D_{22} + 20D_{66}] + 4\text{Ei}_1(2Ba)(3D_{11} + 2D_{12} + 3D_{22} + 4D_{66}) \right\} \quad (\text{B.1a})$$

$$K_{12}^M = -\frac{A_{11}^2 - A_{12}^2}{8A_{11} R^2 B^2} \left[e^{-2Ba} (2Ba + 5) - 8e^{-Ba} \text{Ei}_1(Ba)(Ba + 1) + 8\text{Ei}_1(2Ba) \right] - \frac{B}{8a} (D_{11} - D_{22}) \left[e^{-2Ba} (2B^2 a^2 - 3Ba - 8) + 12Ba\text{Ei}_1(2Ba) \right] \quad (\text{B.1b})$$

$$K_{13}^M = \frac{3}{16} \frac{A_{11}^2 - A_{12}^2}{A_{11} R^2 B^3} e^{-2Ba} (2B^2 a^2 + 2Ba + 1) + \frac{B}{16} \left\{ e^{-2Ba} [2B^2 a^2 (3D_{11} + 2D_{12} + 3D_{22} + 4D_{66}) - 2Ba(5D_{11} + 14D_{12} + 5D_{22} - 4D_{66}) + 7D_{11} + 26D_{12} + 7D_{22} - 12D_{66}] - 4\text{Ei}_1(2Ba)(3D_{11} + 2D_{12} + 3D_{22} + 4D_{66}) \right\} \quad (\text{B.1c})$$

$$K_{14}^M = -\frac{A_{11}^2 - A_{12}^2}{8A_{11} R^2 B^3} e^{-2Ba} (2B^2 a^2 - 2Ba - 1) - \frac{B}{8} (D_{11} - D_{22}) \left[e^{-2Ba} (2B^2 a^2 - 6Ba - 1) - 12Ba\text{Ei}_1(2Ba) \right] \quad (\text{B.1d})$$

$$K_{22}^M = \frac{A_{11}^2 - A_{12}^2}{64A_{11} R^2 B^2} \left[e^{-2Ba} (14Ba + 7) - 48B^2 a^2 \text{Ei}_1^2(Ba) \right] + \frac{1}{64a^2} \left\{ e^{-2Ba} [2B^3 a^3 (7D_{11} + 2D_{12} + 7D_{22} + 4D_{66}) - B^2 a^2 (13D_{11} + 22D_{12} + 13D_{22} - 84D_{66}) - 64Ba(D_{11} + 6D_{12} + D_{22} - 4D_{66}) + 256D_{11} + 256D_{22} + 512D_{66}] + 36B^2 a^2 \text{Ei}_1(2Ba)(7D_{11} + 2D_{12} + 7D_{22} + 4D_{66}) \right\} \quad (\text{B.1e})$$

$$K_{23}^M = -\frac{A_{11}^2 - A_{12}^2}{8A_{11}R^2B^3} \left[e^{-2Ba} (2B^2a^2 + 6Ba + 11) - e^{-Ba} \text{Ei}_1(Ba) (B^2a^2 + 2Ba + 2) + 2\text{Ei}_1(2Ba) \right] \\ - \frac{1}{8a} (D_{11} - D_{22}) \left[e^{-2Ba} (2B^3a^3 - 6B^2a^2 + 3Ba + 8) - 12Ba\text{Ei}_1(2Ba) \right] \quad (\text{B.1f})$$

$$K_{24}^M = \frac{A_{11}^2 - A_{12}^2}{64A_{11}R^2B^3} \left[e^{-Ba} (14B^2a^2 + 14Ba + 7) - 48B^2a^2\text{Ei}_1(Ba) \right] \\ + \frac{1}{64a} \left\{ e^{-2Ba} [2B^3a^3 (7D_{11} + 2D_{12} + 7D_{22} + 4D_{66}) - 2B^2a^2 (17D_{11} + 14D_{12} + 17D_{22} - 36D_{66})] \right. \\ \left. + Ba (75D_{11} - 326D_{12} + 75D_{22} + 244D_{66}) + 288D_{11} + 192D_{12} + 288D_{22} + 384D_{66} \right] \\ - 36Ba\text{Ei}_1(2Ba) (7D_{11} + 2D_{12} + 7D_{22} + 4D_{66}) \left. \right\} \quad (\text{B.1g})$$

$$K_{33}^M = \frac{3}{32} \frac{A_{11}^2 - A_{12}^2}{A_{11}R^2B^4} e^{-2Ba} (4B^3a^3 + 6B^2a^2 + 6Ba + 3) \\ + \frac{1}{64} \left\{ e^{-2Ba} [4B^3a^3 (3D_{11} + 2D_{12} + 3D_{22} + 4D_{66}) - 2B^2a^2 (19D_{11} + 34D_{12} + 19D_{22} + 4D_{66})] \right. \\ \left. + 2Ba (23D_{11} + 58D_{12} + 23D_{22} - 12D_{66}) - 17D_{11} - 54D_{12} - 17D_{22} + 20D_{66} \right] \\ + 8\text{Ei}_1(2Ba) (3D_{11} + 2D_{12} + 3D_{22} + 4D_{66}) \left. \right\} \quad (\text{B.1h})$$

$$K_{34}^M = -\frac{A_{11}^2 - A_{12}^2}{16A_{11}R^2B^4} e^{-2Ba} (4B^3a^3 - 2B^2a^2 - 2Ba - 1) \\ - \frac{1}{8} (D_{11} - D_{22}) \left[e^{-2Ba} (2B^3a^3 - 9B^2a^2 + 9Ba - 7) + 12\text{Ei}_1(2Ba) \right] \quad (\text{B.1i})$$

$$K_{44}^M = \frac{A_{11}^2 - A_{12}^2}{128A_{11}R^2B^4} e^{-2Ba} (28B^3a^3 - 54B^2a^2 + 42Ba + 21) \\ + \frac{1}{128} \left\{ e^{-2Ba} [4B^3a^3 (7D_{11} + 2D_{12} + 7D_{22} + 4D_{66}) - 2B^2a^2 (55D_{11} + 34D_{12} + 55D_{22} - 60D_{66})] \right. \\ \left. + 6Ba (41D_{11} - 38D_{12} + 41D_{22} + 60D_{66}) + 243D_{11} + 618D_{12} + 243D_{22} + 468D_{66} \right] \\ + 72\text{Ei}_1(2Ba) (7D_{11} + 2D_{12} + 7D_{22} + 4D_{66}) \left. \right\} \quad (\text{B.1j})$$

and

$$K_{11}^G = t \left[\frac{1}{4} e^{-2Ba} (2Ba + 1) - B^2a^2\text{Ei}_1(2Ba) \right] \quad (\text{B.2a})$$

$$K_{12}^G = -t \left[\frac{1}{8} e^{-2Ba} (4B^3a^3 - 2B^2a^2 - 6Ba - 3) - B^2a^2\text{Ei}_1(2Ba) (B^2a^2 - 2) \right] \quad (\text{B.2b})$$

$$K_{13}^G = tBa^2\text{Ei}_1(2Ba) \quad (\text{B.2c})$$

$$K_{14}^G = \frac{t}{4B} e^{-2Ba} (2Ba + 1) \quad (\text{B.2d})$$

$$K_{22}^G = -t \left[\frac{1}{8} e^{-2Ba} (14Ba + 9) - \frac{1}{2}\text{Ei}_1(2Ba) (7B^2a^2 + 4) \right] \quad (\text{B.2e})$$

$$K_{23}^G = t \left[\frac{1}{4B} e^{-2Ba} (8B^3a^3 - 4B^2a^2 - 2Ba - 1) - 4Ba^2\text{Ei}_1(2Ba) (B^2a^2 - 1) \right] \quad (\text{B.2f})$$

$$K_{24}^G = t \left[\frac{1}{B} e^{-2Ba} (2Ba + 1) - \frac{7}{2}Ba^2\text{Ei}_1(2Ba) \right] \quad (\text{B.2g})$$

$$K_{33}^G = t \left[\frac{1}{8B^2} e^{-2Ba} (4B^2a^2 + 2Ba + 1) - a^2\text{Ei}_1(2Ba) \right] \quad (\text{B.2h})$$

$$K_{34}^G = -t \left[\frac{1}{16B^2} e^{-2Ba} (12B^3a^3 - 14B^2a^2 + 2Ba + 1) - \frac{3}{2}B^2a^4\text{Ei}_1(2Ba) \right] \quad (\text{B.2i})$$

$$K_{44}^G = t \left[\frac{1}{16B^2} e^{-2Ba} (4B^2a^2 + 18Ba + 9) + \frac{3}{2}a^2\text{Ei}_1(2Ba) \right] \quad (\text{B.2j})$$

Bibliography

- [1] C. Kirsch, "Die Theorie der Elastizität und die Bedürfnisse der Festigkeitslehre," *Zeitschrift des Vereines Deutscher Ingenieure*, vol. 42, pp. 797–807, 1898.
- [2] S. G. Lekhnitskii, *Anisotropic Plates*. Gordon and Breach, 1968.
- [3] G. N. Savin, *Stress Distribution around Holes*. NASA TT F-607, 1970.
- [4] A. I. Lur'e, *Statics of Thin-Walled Shells*. State Publishing House of Technical and Theoretical Literature, 1947.
- [5] J. G. Lekkerkerker, "On the Stress Distribution in Cylindrical Shells Weakened by a Circular Hole," PhD Dissertation, Delft University of Technology, 1965.
- [6] P. Van Dyke, "Stresses about a circular hole in a cylindrical shell," *AIAA Journal*, vol. 3, no. 9, pp. 1733–1742, 1965.
- [7] N. J. I. Adams, "Stress concentration in a cylindrical shell containing a circular hole," *Journal of Engineering for Industry*, vol. 93, no. 4, pp. 953–961, 1971.
- [8] R. C. Tennyson, "The effects of unreinforced circular cutouts on the buckling of circular cylindrical shells under axial compression," *Journal of Engineering for Industry*, vol. 90, no. 4, pp. 541–546, 1968.
- [9] M. V. V. Murthy, K. P. Rao, and A. K. Rao, "On the stress problem of large elliptical cutouts and cracks in circular cylindrical shells," *International Journal of Solids and Structures*, vol. 10, no. 11, pp. 1243–1269, 1974.
- [10] O. M. Guz, "The stress concentration near a circular opening stiffened with a rigid pipe in a cylindrical orthotropic shell," *Dop. Akad. Nauk Ukr. SSR*, vol. 12, pp. 1594–1597, 1962.
- [11] Y. A. Ashmarin, "Stress concentration around a circular opening in an orthotropic cylindrical shell," *International Applied Mechanics*, vol. 2, no. 2, pp. 26–28, 1966.
- [12] A. N. Guz, I. S. Chernyshenko, and K. I. Shnerenko, "Stress concentration near openings in composite shells," *International Applied Mechanics*, vol. 37, no. 2, pp. 139–181, 2001.
- [13] M. J. L. van Tooren, I. P. M. van Stijn, and A. Beukers, "Curvature effects on the stress distribution in sandwich cylinders with a circular cut-out," *Composites Part A: Applied Science and Manufacturing*, vol. 33, no. 11, pp. 1557–1572, 2002.
- [14] E. Oterkus, E. Madenci, and M. P. Nemeth, "Stress analysis of composite cylindrical shells with an elliptical cutout," *Journal of Mechanics of Materials and Structures*, vol. 2, no. 4, pp. 695–727, 2007.
- [15] E. Madenci and A. Barut, "The influence of geometric irregularities on the linear buckling of cylindrical shells with an elliptical cutout," in *44th AIAA/ASME/ASCE/AHS/ASC Structures, Structural Dynamics, and Materials Conference*, 2003, p. 1929.
- [16] M. P. Nemeth, *A Buckling Analysis for Rectangular Orthotropic Plates with Centrally Located Cutouts*. NASA TM-86263, 1984.
- [17] C. Kassapoglou, "Composite plates with two concentric layups under compression," *Composites Part A: Applied Science and Manufacturing*, vol. 39, no. 1, pp. 104–112, 2008.
- [18] J. H. Starnes, "The Effect of a Circular Hole on the Buckling of Cylindrical Shells," PhD Dissertation, California Institute of Technology, 1970.

- [19] M. W. Hilburger, "Numerical and Experimental Study of the Compression Response of Composite Cylindrical Shells with Cutouts," PhD Dissertation, University of Michigan, 1998.
- [20] M. W. Hilburger, J. H. Starnes, and A. M. Waas, "The response of composite cylindrical shells with cutouts and subjected to internal pressure and axial compression loads," in *39th AIAA/ASME/ASCE/AHS/ASC Structures, Structural Dynamics, and Materials Conference and Exhibit*, 1998, p. 1768.
- [21] J. H. Starnes, "Effect of a slot on the buckling load of a cylindrical shell with a circular cutout." *AIAA Journal*, vol. 10, no. 2, pp. 227–229, 1972.
- [22] S. Toda, "The Effects of Elliptic and Rectangular Cutouts on the Buckling of Cylindrical Shells loaded by Axial Compression," Thesis for the Degree of Aeronautical Engineer, California Institute of Technology, 1975.
- [23] P. Montague and M. R. Horne, "The behaviour of circular tubes with large openings subjected to axial compression," *Journal of Mechanical Engineering Science*, vol. 23, no. 5, pp. 225–242, 1981.
- [24] S. Toda, "Buckling of cylinders with cutouts under axial compression," *Experimental Mechanics*, vol. 23, no. 4, pp. 414–417, 1983.
- [25] J. E. Jullien and A. Limam, "Effects of openings of the buckling of cylindrical shells subjected to axial compression," *Thin-Walled Structures*, vol. 31, no. 1-3, pp. 187–202, 1998.
- [26] C. Zhao, J. Niu, Q. Zhang, C. Zhao, and J. Xie, "Buckling behavior of a thin-walled cylinder shell with the cutout imperfections," *Mechanics of Advanced Materials and Structures*, vol. 26, no. 18, pp. 1536–1542, 2019.
- [27] C. Bisagni, "Buckling tests of sandwich cylindrical shells with and without cut-outs," in *Proceedings of American Society for Composites: 31st Technical Conference and ASTM Committee D30 Meeting*, 2016, pp. 1–10.
- [28] A. Shirkavand, F. Taheri-Behrooz, and M. Omid, "Orientation and size effect of a rectangle cutout on the buckling of composite cylinders," *Aerospace Science and Technology*, vol. 87, pp. 488–497, 2019.
- [29] R. Khakimova, R. Degenhardt, and D. Wilcken, "Experimental and numerical investigation of CFRP cylinders with circular cutouts under axial compression," *Thin-Walled Structures*, vol. 147, p. 106526, 2020.
- [30] P. Jiao, Z. Chen, F. Xu, X. Tang, and W. Su, "Effects of ringed stiffener on the buckling behavior of cylindrical shells with cutout under axial compression: Experimental and numerical investigation," *Thin-Walled Structures*, vol. 123, pp. 232–243, 2018.
- [31] M. W. Hilburger and J. H. Starnes, *Buckling Behavior of Compression-loaded Composite Cylindrical Shells with Reinforced Cutouts*. NASA/TM-2004-212656, 2004.
- [32] M. W. Hilburger and M. P. Nemeth, "Buckling and failure of compression-loaded composite cylindrical shells with reinforced cutouts," in *46th AIAA/ASME/ASCE/AHS/ASC Structures, Structural Dynamics and Materials Conference*, 2005.
- [33] M. W. Hilburger, "Buckling and failure of compression-loaded composite laminated shells with cutouts," in *48th AIAA/ASME/ASCE/AHS/ASC Structures, Structural Dynamics, and Materials Conference*, 2007, p. 2227.
- [34] J. H. Starnes, M. W. Hilburger, and M. P. Nemeth, "The effects of initial imperfections on the buckling of composite cylindrical shells," in *Composite Structures: Theory and Practice*. ASTM International, 2000, pp. 529–550.
- [35] F. Taheri-Behrooz, M. Omid, and M. M. Shokrieh, "Experimental and numerical investigation of buckling behavior of composite cylinders with cutout," *Thin-Walled Structures*, vol. 116, pp. 136–144, 2017.
- [36] B. O. Almroth, F. A. Brogan, and M. B. Marlowe, "Stability analysis of cylinders with circular cutouts," *AIAA Journal*, vol. 11, no. 11, pp. 1582–1584, 1973.

- [37] M. W. Hilburger, A. M. Waas, and J. H. Starnes, "Response of composite shells with cutouts to internal pressure and compression loads," *AIAA Journal*, vol. 37, no. 2, pp. 232–237, 1999.
- [38] M. Shariati and M. M. Rokhi, "Numerical and experimental investigations on buckling of steel cylindrical shells with elliptical cutout subject to axial compression," *Thin-Walled Structures*, vol. 46, no. 11, pp. 1251–1261, 2008.
- [39] H. Han, J. Cheng, F. Taheri, and N. Pegg, "Numerical and experimental investigations of the response of aluminum cylinders with a cutout subject to axial compression," *Thin-Walled Structures*, vol. 44, no. 2, pp. 254–270, 2006.
- [40] K. N. Salloomi, L. A. Sabri, Y. M. Hamad, and S. Al-Sumaidae, "Nonlinear buckling analysis of steel cylindrical shell with elliptical cut-out subjected to longitudinal compressive load," *International Journal of Automotive and Mechanical Engineering*, vol. 16, no. 2, pp. 6723–6737, 2019.
- [41] M. Shariati and M. M. Rokhi, "Buckling of steel cylindrical shells with an elliptical cutout," *International Journal of Steel Structures*, vol. 10, no. 2, pp. 193–205, 2010.
- [42] Y. Wang, C. Feng, Z. Zhao, and J. Yang, "Buckling of graphene platelet reinforced composite cylindrical shell with cutout," *International Journal of Structural Stability and Dynamics*, vol. 18, no. 3, p. 1850040, 2017.
- [43] F. A. Brogan and B. O. Almroth, "Buckling of cylinders with cutouts," *AIAA Journal*, vol. 8, no. 2, pp. 236–240, 1970.
- [44] B. O. Almroth and A. M. C. Holmes, "Buckling of shells with cutouts, experiment and analysis," *International Journal of Solids and Structures*, vol. 8, no. 8, pp. 1057–1071, 1972.
- [45] S. Shi, Z. Sun, M. Ren, H. Chen, and X. Hu, "Buckling response of advanced grid stiffened carbon-fiber composite cylindrical shells with reinforced cutouts," *Composites Part B: Engineering*, vol. 44, no. 1, pp. 26–33, 2013.
- [46] E. Brunesi and R. Nascimbene, "Effects of structural openings on the buckling strength of cylindrical shells," *Advances in Structural Engineering*, vol. 21, no. 16, pp. 2466–2482, 2018.
- [47] A. Tafreshi, "Buckling and post-buckling analysis of composite cylindrical shells with cutouts subjected to internal pressure and axial compression loads," *International Journal of Pressure Vessels and Piping*, vol. 79, no. 5, pp. 351–359, 2002.
- [48] C. A. Schenk and G. I. Schuëller, "Buckling analysis of cylindrical shells with cutouts including random boundary and geometric imperfections," *Computer Methods in Applied Mechanics and Engineering*, vol. 196, no. 35–36, pp. 3424–3434, 2007.
- [49] A. Orifici and C. Bisagni, "Perturbation-based imperfection analysis for composite cylindrical shells buckling in compression," *Composite Structures*, vol. 106, pp. 520–528, 2013.
- [50] M. A. Arbelo, A. Herrmann, S. G. P. Castro, R. Khakimova, R. Zimmermann, and R. Degenhardt, "Investigation of buckling behavior of composite shell structures with cutouts," *Applied Composite Materials*, vol. 22, no. 6, pp. 623–636, 2015.
- [51] M. Alfano and C. Bisagni, "Chaos theory applied to buckling analysis of composite cylindrical shell," in *30th Congress of International Council of the Aeronautical Sciences*. International Council of the Aeronautical Sciences, 2016, pp. 1–8.
- [52] M. Alfano and C. Bisagni, "Probability-based methodology for buckling investigation of sandwich composite shells with and without cut-outs," *International Journal for Computational Methods in Engineering Science and Mechanics*, vol. 18, no. 1, pp. 77–90, 2017.
- [53] A. E. H. Love, *A Treatise on the Mathematical Theory of Elasticity*. Cambridge University Press, 1892.
- [54] V. V. Novozhilov, *The Theory of Thin Elastic Shells*. P. Noordhoff, 1964.

- [55] E. Ventsel and T. Krauthammer, "Thin plates and shells: theory, analysis, and applications," *Applied Mechanics Reviews*, vol. 55, no. 4, pp. B72–B73, 2002.
- [56] L. H. Donnell, *Stability of thin-walled tubes under torsion*. NACA Report No. 479, 1933.
- [57] K. M. Mushtari, "Certain generalizations of the theory of thin shells," *Izv Fiz Mat ob-va pri Kazan Univ*, vol. 11, no. 8, 1938.
- [58] V. Vlasov, *General Theory of Shells and its Application in Engineering*. NASA TT F-99, 1964.
- [59] M. P. Nemeth, *Nondimensional Parameters and Equations for Buckling of Symmetrically Laminated Thin Elastic Shallow Shells*. NASA TM-104060, 1991.
- [60] R. M. Jones, *Buckling of Bars, Plates, and Shells*. Bull Ridge Corporation, 2006.
- [61] W. Ritz, "Über eine neue Methode zur Lösung gewisser Variationsprobleme der mathematischen Physik." *Journal für die reine und angewandte Mathematik*, vol. 1909, no. 135, pp. 1–61, 1909.
- [62] L. H. Donnell, "A new theory for the buckling of thin cylinders under axial compression and bending," *American Society of Mechanical Engineers*, vol. 56, pp. 795–806, 1934.
- [63] S. B. Batdorf, *A Simplified Method of Elastic-stability Analysis for Thin Cylindrical Shells*. NACA Report 874, 1947.
- [64] W. T. Koiter, "The Stability of Elastic Equilibrium," PhD Dissertation, Delft University of Technology, 1945.
- [65] L. H. Donnell and C. C. Wan, "Effect of imperfections on buckling of thin cylinders and columns," *Journal of Applied Mechanics*, vol. 17, pp. 73–83, 1950.
- [66] V. I. Weingarten, P. Seide, and J. P. Peterson, *Buckling of Thin-Walled Circular Cylinders*. NASA SP-8007, 1968.
- [67] M. P. Nemeth and M. M. Mikulas Jr., *Simple Formulas and Results for Buckling-resistance and Stiffness Design of Compression-loaded Laminated-composite Cylinders*. NASA/TP-2009-215778, 2009.
- [68] C. Kassapoglou, *Modeling the Effect of Damage in Composite Structures: Simplified Approaches*. John Wiley & Sons, 2015.
- [69] Y. C. Fung, *Foundations of Solid Mechanics*. Prentice-Hall, Inc., 1965.
- [70] M. Abramowitz and I. A. Stegun, *Handbook of Mathematical Functions with Formulas, Graphs, and Mathematical Tables*. Dover Publications, 1965.
- [71] MathWorks, "Eig." [Online]. Available: <https://www.mathworks.com/help/matlab/ref/eig.html> [Accessed: 2020-07-05]
- [72] C. Kassapoglou, *Design and Analysis of Composite Structures With Applications to Aerospace Structures*. John Wiley & Sons, 2013.
- [73] DuPont Teijin Films, *Mylar, Physical-thermal Properties*. Hopewell, VA, USA, 2017.
- [74] P. P. Camanho, P. Maimí, and C. G. Dávila, "Prediction of size effects in notched laminates using continuum damage mechanics," *Composites Science and Technology*, vol. 67, no. 13, pp. 2715–2727, 2007.
- [75] Dassault Systèmes, *Abaqus Theory Guide*. Providence, RI, USA, 2016.
- [76] Dassault Systèmes, *Abaqus Analysis User's Guide*. Providence, RI, USA, 2016.
- [77] MathWorks, "Precision of numeric calculations." [Online]. Available: <https://www.mathworks.com/help/symbolic/increase-precision-of-numeric-calculations.html> [Accessed: 2020-07-07]
- [78] D. S. Cairns, "Impact and Post-impact Response of Graphite/Epoxy and Kevlar/Epoxy Structures," PhD Dissertation, Massachusetts Institute of Technology, 1987.
- [79] MathWorks, "Equilibrate." [Online]. Available: <https://www.mathworks.com/help/matlab/ref/equilibrate.html> [Accessed: 2020-11-10]